DIFFRACTION INVESTIGATIONS OF CEMENT CLINKER AND TRICALCIUM SILICATE USING RIETVELD ANALYSIS

Vanessa Kate Peterson

Bachelor of Applied Science (Honours) in Chemistry with First Class Honours

Department of Chemistry, Materials and Forensic Sciences
University of Technology, Sydney

August 2003

Submitted for the Degree of Doctor of Philosophy

CERTIFICATE OF AUTHORSHIP / ORIGINALITY

I certify that the work in this thesis has not previously been submitted for a degree nor has it been submitted as part of requirements for a degree except as fully acknowledged within the text.

I also certify that the thesis has been written by me. Any help that I have received in my research work and the preparation of the thesis itself has been acknowledged. In addition, I certify that all information sources and literature used are indicated in the thesis.

Signature of Candidate

Vanessa Peterson

ACKNOWLEDGMENTS

I am grateful to Dr Brett Hunter from the Australian Nuclear Science and Technology Organisation (ANSTO) for help and guidance during his role as supervisor. Thanks to Bragg Institute staff of ANSTO, for various discussions, and to A/Prof. Abhi Ray from the University of Technology, Sydney (UTS). I also thank Dr Ray Withers from the Australian National University for help with work involving structural modulation.

This work was supported by an Australian Ph.D. award and a postgraduate research award from the Australian Institute of Nuclear Science and Engineering (AINSE). Thanks to the UTS for use of thermal analysis facilities. Use of neutron facilities at the ANSTO was funded by the AINSE. Thanks to the ANSTO for the use of other equipment. Facility use at the Australian National Beamline Facility, Japan, was funded by the Australian Synchrotron Research Program. Facility use at Brookhaven National Laboratories, U.S.A., was funded by the Access to Major Research Facilities program of the ANSTO.

I would like to thank those listed below, responsible for support to attend schools, conferences, meetings, and congresses. I was able to attend many during my doctoral candidature, and it is through these events that opportunities for the student to enter the research world as a working scientist begin.

- ANSTO.
- UTS.
- School on symmetry of crystals organising committee.
- International Union of Crystallography.
- Australian X-ray Analytical Association.
- Professor Brian O'Connor.
- Australian Institute of Physics.
- National Institute of Standards and Technology
- Society of Crystallographers in Australia and New Zealand.
- Australian synchrotron project.

Thanks to my mum and to all of my friends, especially Dr Mikl Law. Final thanks goes to the world of rock climbing, which kept me inspired as a scientist.

TABLE OF CONTENTS

LIST OF FULLY REFEREED PUBLICATIONS

LIST OF FIGURES

CHAPTER 2

CHAPTER 3

CHAPTER 6

APPENDIX B

LIST OF TABLES

APPENDIX B

LIST OF ABBREVIATIONS

AINSE	Australian Institute of Nuclear Science and Engineering
AIP	Australian Institute of Physics
ANBF	Australian National Beamline Facility (KEK)
ANSTO	Australian Nuclear Science and Technology Organisation
AM	Alumina Modulus
AMRF	Access to Major Research Facilities
ASRP	Australian Synchrotron Research Program
AXAA	Australian X-ray Analytical Association
BCE	Before Christian Era
BNL	Brookhaven National Laboratories
C_2S	Dicalcium silicate
C_3A	Tricalcium aluminate
C_3S	Tricalcium silicate
C_4AF	Tetracalcium aluminoferrite (brownmillerite)
CTL	Construction Technology Laboratories
C-S-H	Calcium silicate hydrate
DTA	Differential Thermal Analysis
ECM	European Crystallography Meeting
FOM	Figures of Merit
FWHM	Full Width at Half Maximum
GSAS	General Structure Analysis System
GUI	Graphical User Interface
HIFAR	High Flux Australian Reactor
HRPD	High Resolution Powder Diffractometer (HIFAR)
HRTEM	High Resolution Transmission Electron Microscopy
ICCC	International Congress on the Chemistry of Cement
ICNS	International Conference on Neutron Scattering
IUCr	International Union of Crystallography
IMS	Incommensurately Modulated Structures
KEK	High-Energy Accelerator Research Organisation
LSF	Lime Saturation Factor
MPC	Microscope Point Counting

NCNR	National Centre for Neutron Research
NIST	National Institute of Standards and Technology
NSLS	National Synchrotron Light Source
OPC	Ordinary Portland Cement
PCA	Portland Cement Association
PSD	Position Sensitive Detector
QPA	Quantitative Phase Analysis
SAD	Selected Area Diffraction
SCANZ	Society of Crystallography in Australia and New Zealand
SEM	Scanning Electron Microscopy
SOF	Site Occupancy Factor
SR	Silica Modulus
SSC	School on Symmetry of Crystals
SXPD	Synchrotron X-ray Powder Diffraction
TEM	Transmission Electron Microscopy
USA	United States of America
UTS	University of Technology, Sydney
XRD	X-ray Diffraction
XRF	X-ray Fluorescence
XRPD	X-ray Powder Diffraction

ABSTRACT

Cement is the world's most popular building material, yet surprisingly its composition is not fully understood. Due to the complex nature of cement constituents, there is currently no reliable method to quantitatively determine the composition of cement. Partly this arises from the fact that the crystal structure of the main component of cement, tricalcium silicate, has not been fully determined.

There has been an increase in the use of Rietveld refinement of powder diffraction data for the analysis of cement in recent years. The method has emerged as a valuable tool for the quantitative determination of the composition of cement. A further advantage of the method is its ability to refine complex crystal structures, such as tricalcium silicate. Despite the increased application of this method, few publications exist concerning the evaluation or improvement of the method for the purpose of cement analysis.

In this work, the Rietveld method has been critically investigated as a tool for the identification and quantification of the different phases in cement clinker. Laboratory X-ray, synchrotron, neutron, and combined diffraction data are all used in the investigations. For the first time, comparisons of analysis results using various sources are made, rather than comparing the results from various methods. Inconsistencies in the results were found, and their causes were investigated and identified. The reliability of this method was shown to be dependent on the quality of the diffraction data, both in terms of the counting statistics and the resolution, and on the ability of the structures used in the Rietveld model to describe the phases in the sample.

The only previously existing structural model for triclinic tricalcium silicate is shown, in this work, inadequate as a description of the form found in cement. Consequently, the triclinic crystal structures of tricalcium silicate were re-investigated. Using synchrotron powder diffraction data, the lattice dynamics during the T_1–T_2 transition were observed in detail for the first time. Superstructure reflections were observed for the two structures. The first model for the average sub-structure of the T_2 form is presented. Structural modulation in the T_1 form was re-investigated. The parent sub-structure, suitable for Rietveld refinement, corresponding modulation wave-vector, and superspace group of the superstructure, were identified.

CHAPTER 1

RESEARCH OBJECTIVES AND THESIS OVERVIEW

1.1 Introduction

Despite the long history of cement as the most popular building material in the world, integral to our way of life, it is surprising to find that the exact composition of such an important product is poorly understood. Partly this is because the main component of cement, tricalcium silicate, does not have its structure fully determined. It is the arrangement of atoms, particular to each of the many components of cement, that give cement its characteristic and useful properties. Although the atomic composition of cement can be determined, it is disturbing that there currently exists no reliable method for the quantitative determination of the components of cement.

Recent advances in investigative tools and new technologies, such as the Rietveld method and powder diffraction instrumentation, allow more information about the component structure of cement to be revealed. As one of the more reliable tools for the quantitative determination of the components in cement, the Rietveld method has emerged as a powerful technique for the structural determination of cement components. Although significant gains have been made in understanding cement component structure and chemistry, there are unexpected gaps in the literature.

Diffraction sources used in the industrial analysis of cement are often inferior to those available in research. Hence, industrially obtained data usually does not reveal as much information about the sample as the data used in the research analysis of cement. The analysis methods developed from research using higher resolution sources may therefore not be appropriate for use with data obtained from lower resolution laboratory X-ray sources, as used in industry. The difference between results obtained from Rietveld analysis using various diffraction sources, in terms of both the quality of the data and diffraction mechanism (type of data), is therefore of interest. Such comparisons are made for the first time in this thesis, and the deficiencies of the Rietveld method for the quantitative analysis of clinker in industry are highlighted.

Tricalcium silicate has a number of polymorphs that commonly exist simultaneously in cement. There currently exists no method to quantify these polymorphs in clinker. The main reason for this is that structures have not been determined for some of the known polymorphs. Deciphering the atomic arrangement of unknown tricalcium silicate forms will allow a better crystallographic description of the phases in cement. Tricalcium silicate is the principle hydraulic component of cement, responsible for strength development. Each polymorph of tricalcium silicate has a different strength property. The incorporation of more accurate phase descriptions into a Rietveld model will allow the reliable quantification of all phases, including tricalcium silicate forms, in cement. Hence, structural solutions for tricalcium silicate forms are of immense potential benefit to industry.

A knowledge of the limitations of the Rietveld method and incorporation of better structural models will promote more efficient methods of producing optimised cement products in industry.

1.2 Research issues and investigations

The key issue addressed in this thesis is the identification and quantification of cement clinker components. Addressing this research issue involved extracting diffraction data from cement samples and analysing it to yield information about the sample composition. Structural information was derived using technologies such as powder diffraction, coupled with computer modelling techniques that interpret the data qualitatively and quantitatively, such as Rietveld analysis. Prior to the work in this thesis, the reliability of the result obtained using the Rietveld method was unclear. Previously, quantitative analysis had never been performed for the polymorphs of tricalcium silicate. Quantitative identification of the phases present in the cement sample, rather than their atomic composition alone, was determined in this thesis.

The three primary investigations of the thesis are outlined as follows:

1. *Investigation of the quantitative phase analysis of cement clinker using the current best crystallographic method and observing its deficiencies.*
   Currently the Rietveld method is the most reliable method for the quantitative analysis of clinker components, and the only method allowing a quantitative identification of the tricalcium silicate polymorphic modifications. This is the first study to compare the results obtained using data from different diffraction sources and of varying quality. Quantitative results for the tricalcium silicate polymorphs in a clinker are compared for the first time.

2. *Identification of the causes of inconsistencies in the method.*
   It was hypothesised that the limitations of the method may be induced by variation in data, resulting in variation of the resulting composition or quantities obtained. The deficiencies of the method that were observed were investigated, and their cause(s) identified. This investigation promoted awareness of the limitations of the method, particularly for lower quality data.

3. *Resolution of identified problems to improve the current method.*
   New structures for tricalcium silicate polymorphs were investigated, with a focus on the triclinic polymorphs. Superstructure reflections were observed for two tricalcium silicate forms, and found to cause problems with the Rietveld analysis of data containing these polymorphs. The transition mechanics for the first triclinic transition were investigated, and a new average structure for a previously undetermined form was established. The superstructure of the pure tricalcium silicate form at ambient temperature was discussed in terms of the structural modulation of a pseudotrigonal parent group.

1.3 Structure of the thesis

The thesis begins with a literature review that initiated the three investigations of the thesis, which then unfold in the chapters that follow.

Chapters 2 and 3 report on the current knowledge, as reported in the available literature, of cement and the common tools for its investigation. Chapter 2 gives an overview of the past research on cement structure and the current analysis practices. The Rietveld method is an important tool for the quantitative phase analysis of cement. However, a lack of literature comparing the quantitative phase analysis results obtained using different diffraction sources was noticed. Chapter 3 outlines the theory and use of the tools used in the investigations reported in this study.

Chapters 4, 5, and 6 present the three main investigations of this work, as outlined in section 1.2. Chapter 4 investigated gaps in the literature highlighted in chapter 2, using the tools outlined in chapter 3. Chapters 5 and 6 build upon the results of the previous chapter. As each investigation yielded results, they were published in reviewed journals and proceedings. These publications are included as the primary part of chapters 4, 5, and 6. Chapters 4 and 5 each contain two publications. Chapter 6 contains one publication, and includes results that have not yet been published elsewhere. A description of the need for, and research performed, in chapters 4, 5, and 6 is included in the introduction to each chapter. The introduction is followed by a description of the exact research details of the investigation and the publications from the investigations. Chapters 5 and 6 are broken into smaller investigations that have separate descriptions. The results of these investigations are summarised at the end of the chapters.

Conclusions and recommendations for future research into the identification and quantification of cement clinker components are included at the end of chapter 6.

Appendix A contains structural information of clinker components that were used in the Rietveld refinements. Crystal constants and atomic positional and displacement parameters from references are reproduced. Appendix B contains information on the materials used and results from investigations not presented elsewhere. Crystal constants and atomic positional and displacement parameters of new structures, or those structures differing significantly from the literature, are also included in this appendix.

References for all chapters are listed at the end of the thesis, although references for publications are listed within the publication.

CHAPTER 2

CEMENT STRUCTURE AND CHEMISTRY

2.1 Introduction

Cements are powdered mixtures of inorganic compounds which, when mixed with water, undergo a chemical hydration reaction and harden. Natural cement was being created when the earth was undergoing intense geological changes, and cement has existed for at least 12 million years. Precursors of modern cements were lime-based materials used by the Greeks and Romans six centuries BCE. Improvements in cement technology led to the invention of "Portland" cement in the early 19^{th} century. This material and the basic process by which it was formed were subsequently refined and developed, resulting in the well-controlled material used to form the matrix of vast amounts of modern mortars, concretes, and special composites.

Global production of Portland cements currently exceeds 800 million metric tonnes annually (Portland Cement Association). It is produced from raw materials derived from some of the earth's most abundant elements. When cement is mixed with water, fine aggregate such as sand, and coarse aggregate such as gravel or crushed stone, it forms concrete, the world's most popular building material.

2.2 Crystal chemistry of Portland Cement

Ordinary Portland Cement (OPC) consists of ground cement clinker mixed with approximately 3-5 wt. % gypsum. Clinker is produced from heating approximately 80 wt. % limestone and 20 wt. % clay, or other source of SiO_2, with additives such as iron ore to above 1500 °C (Taylor, 1997). At these temperatures the main constituents of cement, calcium silicates such as tricalcium and dicalcium silicate, form. Stoichiometry and texture of the clinker phases are determined through the thermodynamic and kinetic phenomena of the firing process. The principal characteristics of this process include the rate of heating after limestone decomposition and the time of residence in the clinkering zone (approximately 1300–1450 °C). The rate of cooling to 1100 °C is also important.

Process control is dependant on factors that include constraints imposed by the raw feed mineralogy, such as particle size distribution, and site specific process conditions.

Clinker phases crystallise from a partly melted composition containing the main elements Ca, Si, Al, and Fe, with various other elements as impurities. OPC clinker typically has a composition of approximately 67% CaO, 22% SiO_2, 5% Al_2O_3, 3% Fe_2O_3 and 3% of other components (Taylor, 1997). Clinker contains the four main crystalline components alite, belite, aluminate phase, and ferrite phase. Several other phases, such as alkali sulfates and calcium oxide, are normally present in minor amounts. Alites are solid solutions of tricalcium silicate, Ca_3SiO_5, and belite is Ca_2SiO_4. Tricalcium aluminate, $Ca_3Al_2O_6$, and tetracalcium aluminoferrite, $Ca_2(Al_xFe_{1-x})_2O_5$, constitute the interstitial phase. This phase is liquid at the clinkering temperature and crystallises between the alite and belite crystals during cooling.

Cement chemistry notation is commonly used to represent the formulae for the phases in clinker. In this notation tricalcium silicate is represented as C_3S, dicalcium silicate as C_2S, tricalcium aluminate as C_3A, and tetracalcium aluminoferrite as C_4AF, where C = CaO, S = SiO_2, F = FeO_2, and A = Al_2O_3. The minor elements are non-uniformly distributed in the four main phases and their amounts have been shown to be at least 4 % in alite, 6 % in belite, 10 % in C_4AF, and 13 % in C_3A, (Regourd, 1986).

Cement is produced from clinker by the addition of gypsum (calcium sulphate dihydrate, $Ca_2SO_4.2H_2O$), which is included as a source of sulphate ions. The sulphate ions slow the extremely exothermic hydration reaction of the tricalcium aluminate phase. Hence, the gypsum controls the setting rate of the resultant cement.

2.3 Crystal modifications of clinker components

Clinker is a non-equilibrium, multi-component system of solid solutions. The crystal structures of the components in cement clinker vary with clinkering temperature and processing conditions. Some of the crystal forms that exist in the high temperature clinkering process may be stabilised at room temperature by metal ions present in minor amounts in the solid solution. The crystal structure and modifications of the four main phases in clinker are discussed in the following sections.

2.3.1 Tricalcium silicate modifications

The polymorphism of C_3S as a function of temperature is complicated by numerous, extremely similar modifications, and by the very small transformation enthalpies. C_3S has been reported to have seven polymorphs, many of which have similar structures. Three crystal systems are encountered in the C_3S polymorphs. These are the trigonal, monoclinic, and triclinic systems. Table 2.1 summarises the information available in the literature. The trigonal form of C_3S is known as rhombohedral, as the other polymorphs are described as a deformation of the basal plane in the rhombohedral setting of this form. The reversible phase transitions of C_3S have been detected by a combination of Differential Thermal Analysis (DTA), high temperature X-Ray Diffraction (XRD) and high-temperature light microscopy (Bigaré *et al,* 1967). Some C_3S forms have also been recognised to have superstructure present (Urabe *et al,* 2000) (Urabe *et al,* 2002).

Table 2.1: Modifications of C_3S.

Transition temperature (°C)	Polymorph	Type	Space group	Structure Reference and temperature (°C)
1070	R(a,c)	Trigonal	*R*3*m*	Jeffery (1952) (Ideal structure at ambient temp.)
	R(a,c)	Trigonal	*R*3*m*	Nishi and Takéuchi (1984). (1200 °C)
	R(a,c)	Trigonal	*R*3*m*	Il'inets *et al* (1985) (20 °C)
	R(2a,c)	Trigonal	*R*3*m*	Referenced by Il'inets *et al* (1992). (details not known, doubled a-axis)
1060	M_3 super-cell	Monoclinic	*C*1*m*1	Nishi *et al* (1985)
	M_3 sub-cell	Monoclinic	*C*1*m*1	Mumme (1995)
990	M_2	Monoclinic		Unknown structure
980	M_1	Monoclinic		Unknown structure
920	T_3	Triclinic		Unknown structure
620	T_2	Triclinic		Unknown structure
Ambient	T_1	Triclinic	$P\bar{1}$	Golovastikov *et al* (1975)

Many researchers have investigated the crystal chemistry of tricalcium silicate (Singh, 1976) and there is clear evidence to suggest at least seven distinct polymorphs. A fourth triclinic structure, T_4, was noted by Il'inets and Bikbau (1992) who suggested that this form existed in addition to the T_1, T_2, and T_3 modifications. Il'inets and Bikbau (1992) list the lattice parameters of the T_4 polymorph, attributed to Golovastikov *et al* (1975), incorrectly by using the numerical decimal equivalent of degrees and minutes without conversion. Taylor *et al* (2000) also listed the T_4 polymorph, however, in this work Il'inets and Bikbau (1992) were referenced as their source. Viani *et al* (1998) stated that the T_4 structure was actually the T_1 structure and clarified that the only three triclinic forms known to exist are the T_1, T_2 and T_3 forms.

The high-temperature modification of tricalcium silicate possesses true rhombohedral symmetry. On cooling, the symmetry is reduced; many reflections in the powder pattern split into groups. They represent small deformations in the rhombohedral structure. The structural deviations in the polymorphs affect the coordination of the Ca^{2+} ions and the O atoms of the SiO_4^{4-} tetrahedra. For each polymorph there are thought to exist several crystallographically distinct Ca sites, each having a different coordination. For a given site the coordination is believed to vary between individual atoms due to the orientational disorder in the surrounding SiO_4^{4-} tetrahedra. The mean coordination number of the Ca can therefore be used to distinguish the polymorphs, if the abnormally long bonds are excluded. The mean coordination of the calcium has been determined as 5.66 in the R form, 6.15 in the M_3 form, and 6.21 in the T_1 form (Maki, 1986). Polymorphic transformations occur in the following order during heating (Taylor, 1997).

$$T_1 \xleftrightarrow{620\,^\circ C} T_2 \xleftrightarrow{920\,^\circ C} T_3 \xleftrightarrow{980\,^\circ C} M_1 \xleftrightarrow{990\,^\circ C} M_2 \xleftrightarrow{1060\,^\circ C} M_3 \xleftrightarrow{1070\,^\circ C} R$$

Bigaré *et al* (1967) summarised the DTA diagrams for three different studies on tricalcium silicate polymorphism and considered the transformations observed by DTA to be definitively established. Despite this, there exist some anomalies in some DTA curves in the literature, where features remain unexplained or only speculated about. Recent investigations, using DTA on a pure C_3S sample by Viani *et al* (1998), showed that variation in the transitions temperatures listed above exist in the literature.

At approximately 1070 ºC a change in symmetry from R to M_3 is noted (Taylor, 1997), occurring via inversion (Mumme, 1995). The characteristic hexagonal reflections $\bar{2}01$, $\bar{2}04$, and 220 split progressively. The deformation occurs in the basal plane of the hexagonal cell (Bigaré *et al*, 1967). Urabe *et al* (2000) list the M_3-R transition temperature as 739.4 ºC, although the referenced source (Maki and Chromý, 1978) reports the transition temperature as 1070 ºC.

Urabe *et al* (2002) state that the M_3 modification appears between M_2 and R and the M_3-M_2 transition is only detectable by a change in optical properties, citing Maki and Chromý (1978). Urabe *et al* (2002) report the M_2-R transition temperature as 1050 ºC. At approximately 1060 ºC, the transition from M_2-M_3 takes place (Taylor, 1997). At 990 ºC the transformation M_2-M_1 occurs (Taylor, 1997) (Urabe, 2002), via inversion (Mumme, 1995). During this transition, the triplet of reflections $\bar{2}01$, $\bar{2}04$, and 220 become clearly separated (Bigaré *et al*, 1967). In addition to the deformation of the hexagonal basal plane, an inclination of the c axis occurs in the $1\bar{2}10$ plane (Bigaré *et al*, 1967). The monoclinic phases in particular have been observed to have complicated superstructures (Mumme, 1995).

At temperatures up to approximately 980 ºC there is a sequence of three triclinic phases that eventually invert to monoclinic forms (Mumme, 1995). Below this temperature there is a change of symmetry from M_1 to T_3 (Taylor, 1997) (Urabe, 2002). The doublets of the three reflections $\bar{2}01$, $\bar{2}04$, and 220 become narrow triplets and the pseudohexagonal axes a and b are doubled to 14 Å; the c axes remains unaltered (Bigaré *et al*, 1967). At 920 ºC the transition T_3 to T_2 occurs (Taylor, 1997) (Urabe, 2002). The triplets $\bar{2}01$, $\bar{2}04$, and 220 separate progressively (Bigaré *et al*, 1967). At 620 ºC the transition T_2 to T_1 occurs (Taylor, 1997) (Urabe *et al*, 2002). The slight discontinuous separation in the triplets that occurs is thought to be caused by changes in the axes a and b as c shows no discontinuity. Two weak lines with *d* values of 14 Å and 8 Å were interpreted by Bigaré *et al* (1967) as a second doubling of a and b to 28 Å.

A foreign ion that is introduced into the C_3S crystal lattice can substitute for Ca^{2+} or Si^{4+}, or can occupy a hole (Hahn *et al*, 1969.) The lattice energy is modified and one of the polymorphic forms can be stabilised at room temperature.

All polymorphic forms of C_3S could theoretically be present at room temperature. Regourd *et al* (1986) noted using XRD that the mutual interaction of foreign elements such as Al, Fe, Mg, K, and Na permitted the stabilisation of T_1, T_2, and M_3 at room temperature. Numerous other studies on the substitution of ions into the tricalcium silicate structure have noted similar stabilisations (Singh, 1976).

All polymorphs have their lattice parameters of the basal plane determined as pseudohexagonal and/or pseudo-orthohexagonal (Bigaré *et al*, 1967) (Taylor, 1997), however, the internal structures of the M_2, M_1, T_3, and T_2 polymorphs remain unsolved. R, M_3, and T_1 have determined structures (Nishi and Takéuchi, 1984) (Il'inets *et al*, 1985) (Jeffery, 1952) (Nishi *et al*, 1985) (Mumme, 1995) (Golovastikov *et al*, 1976). Structural information for these polymorphs is listed in appendix A.

Deformations that occur in the basal plane, hexagonal in appearance, of the trigonal form in the rhombohedral setting of pure tricalcium silicate are represented in figures 2.1-2.4 (Bigaré *et al*, 1967). In figures 2.1-2.3, the hexagonal, monoclinic, and triclinic basal plane of the cell are shown, respectively. The hexagonal basal plane in these figures is represented as trigonal in the rhombohedral setting. Figure 2.4 shows the pseudohexagonal and pseudo-orthohexagonal basal plane in the trigonal-rhombohedral setting, where a_1, b_1, d_1 are the pseudohexagonal axes and a_2, b_2, and c_2 are the pseudo-orthohexagonal axes.

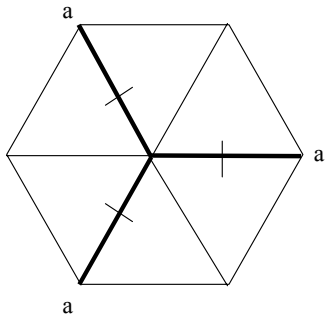

Figure 2.1: Hexagonal basal plane of the cell in pure Ca_3SiO_5.

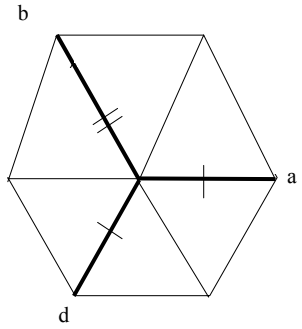

Figure 2.2: Monoclinic deformation of the hexagonal basal plane in pure Ca_3SiO_5.

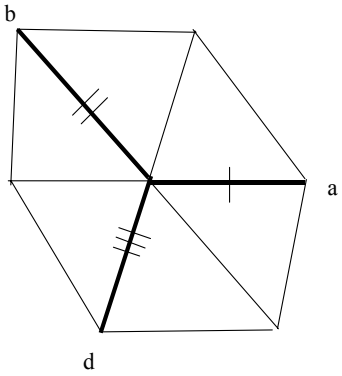

Figure 2.3 Triclinic deformation of the hexagonal basal plane in pure Ca_3SiO_5.

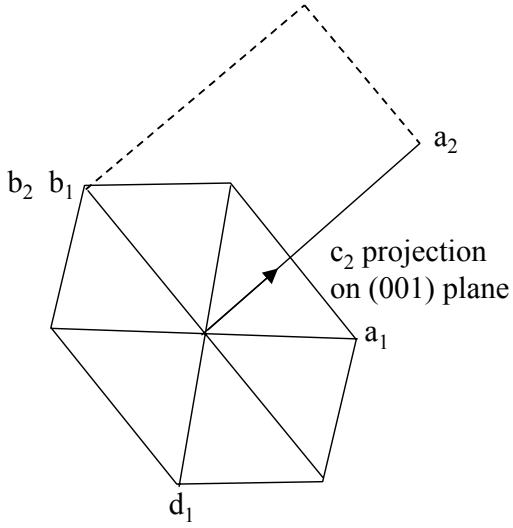

Figure 2.4 Pseudohexagonal and pseudo-orthohexagonal axes deformation of the hexagonal basal plane in pure Ca_3SiO_5.

In figures 2.6 – 2.20, the known structures of tricalcium silicate are atomically represented using the program Atoms (Dowty, 1999). Silicon-oxygen tetrahedra with central silicon atoms are shown in red, calcium atoms are dark blue, or dark blue and white where statistical disorder is represented, and oxygen atoms are shown in turquoise. Poly-ligand oxygen atoms that form SiO_4 tetrahedra are shown with small radii, whilst those that form part of Ca-O bonds are of larger radii. Unit cells are outlined with black.

The crystal is represented in three ways, one with crystal arrangement as shown in the left hand side of figure 2.5, another looking through the c axis of this arrangement as shown in the right hand side of figure 2.5. A third arrangement is presented in the non-rhombohedral forms. In the third arrangement, the distorted basal plane, common to all forms, was located and highlighted in yellow within the displayed unit cell. In this case the crystal axes arrangement differs between forms, and is identified inset in the appropriate figures.

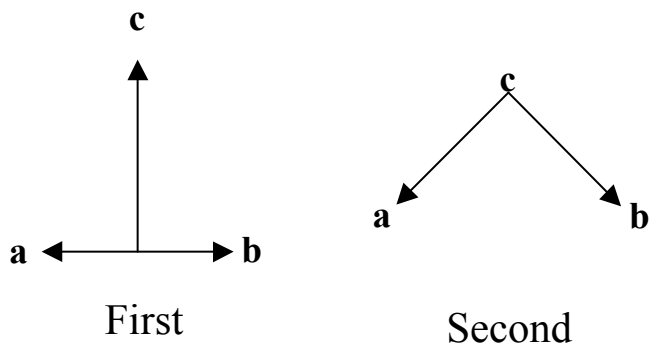

Figure 2.5 Crystal axes arrangement of the first and second representations of the each C_3S modification.

The rhombohedral form of C_3S was first studied by Jeffery (1952) as a pseudorhombohedral structure with hexagonal axes a = 7.0 Å and b = 25.0 Å. The space group was determined to be *R*3*m* with Z = 9. This form is shown in figures 2.6 and 2.7, where figure 2.7 shows the basal plane in the hexagonal setting of the trigonal symmetry group.

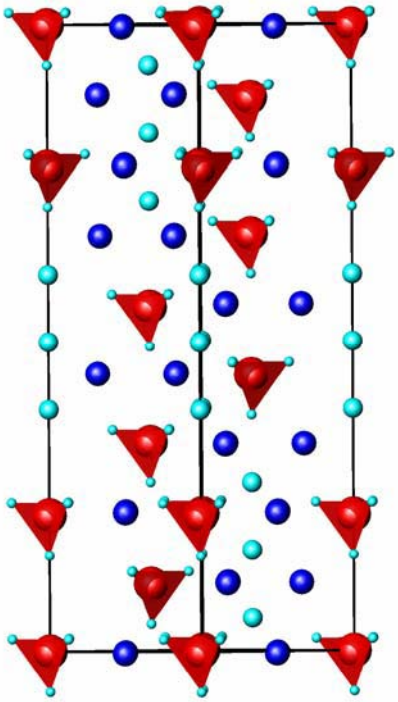

Figure 2.6: First unit cell representation of structure in C_3S type R (Jeffery, 1952).

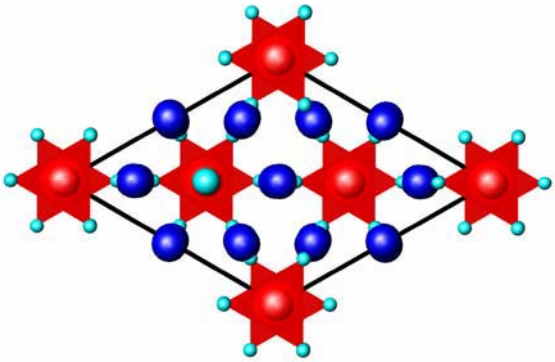

Figure 2.7: Second unit cell representation of structure in C_3S type R (Jeffery, 1952).

The rhombohedral form of C_3S was also studied by Nishi and Takéuchi (1984). The high temperature form was studied by heating Al_2O_3 stabilised M_1 tricalcium silicate crystals above the inversion. Cell parameters were shown to be a = 7.135 Å and c = 25.586 Å, when a trigonal cell in the hexagonal setting was used, and space group determined as *R*3*m*. This structure is represented in figures 2.8 and 2.9.

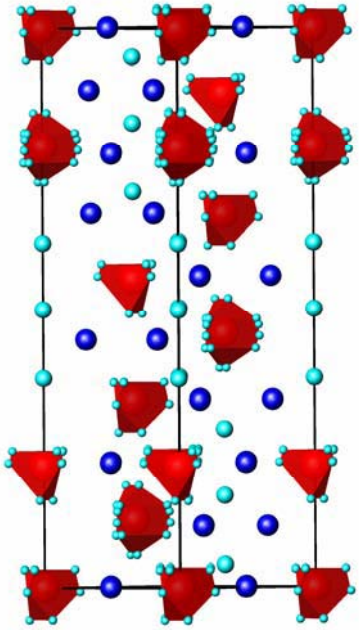

Figure 2.8: Fist unit cell representation of structure in C_3S type R (Nishi and Takéuchi, 1984).

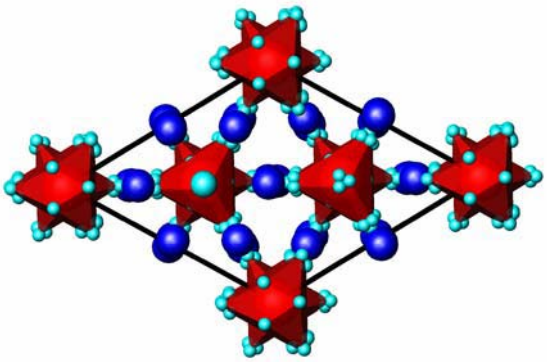

Figure 2.9: Second unit cell representation of structure in C_3S type R (Nishi and Takéuchi, 1984).

In figures 2.8 and 2.9, one of three independent tetrahedra points 70 % of the time in the opposite c direction. The apical directions of all the tetrahedra that are parallel to the threefold axis in the statistical structure are tilted with respect to the axis. This structure was determined at 1200 °C. Odd-shaped SiO_4 tetrahedra represent statistical disorder in the structure, represented as partial occupancy of some O positions.

Il'inets *et al* (1985) re-investigated the rhombohedral modification of C_3S about the same time as Nishi *et al* (1985), and solved the structure for an ion-stabilised rhombohedral modification at ambient temperature. These are shown in figure 2.10 and 2.11. Space group was established as *R*3*m*, with lattice parameters a = 7.057 Å and c = 24.974 Å.

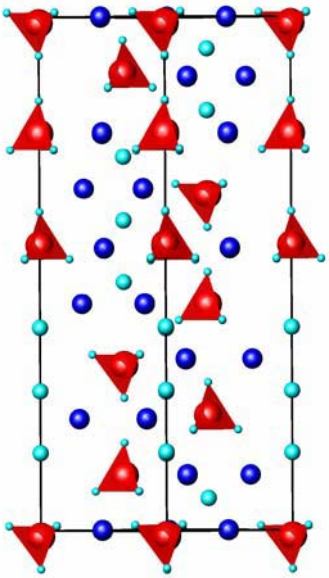

Figure 2.10: First unit cell representation of structure in C_3S type R (Il'inets *et al*, 1985).

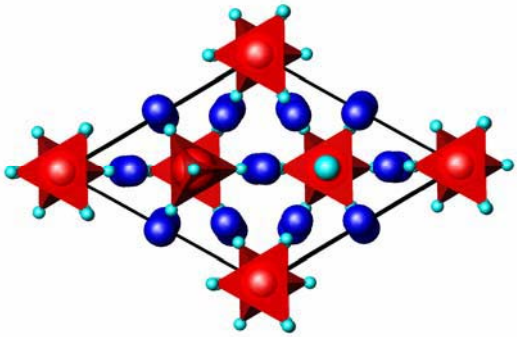

Figure 2.11: Second unit cell representation of structure in C_3S type R (Il'inets *et al*, 1985).

The monoclinic form of C_3S was first determined by Jeffery (1952) using an alite sample with composition $54CaO.16SiO_2.Al_2O_3.MgO$. The form was shown to have 18 molecules of $3CaO.SiO_2$, where two silicon atoms had both been replaced by aluminium, with one magnesium atom entering the lattice to balance the charge. This

monoclinic form was shown to have space group *Cm* with lattice parameters of a = 33.08 Å, b = 7.07 Å, c = 18.56 Å, and β = 94°10′.

Monoclinic C_3S has also been studied by Nishi *et al* (1985) who determined the M_3 superlattice structure as a large unit cell (4312 $Å^3$), shown in figures 2.12-2.14. The structure was originally determined by following the rhombohedral structure into its monoclinic sub-cell. Single crystal diffraction of this phase enabled the extremely complicated superstructure reflections to be determined. These were found to correspond to those of the crystal whose average monoclinic structure was determined by Jeffery (1952). Untwinned crystals of the M_3 form were stabilised at ambient temperature using MgO. Of the two possible space groups, *C*2/*m* and *Cm*, the *Cm* was adopted for structural analysis as it is a subgroup of *R*3*m* and was used by Jeffery (1952) in the first monoclinic structure determination.

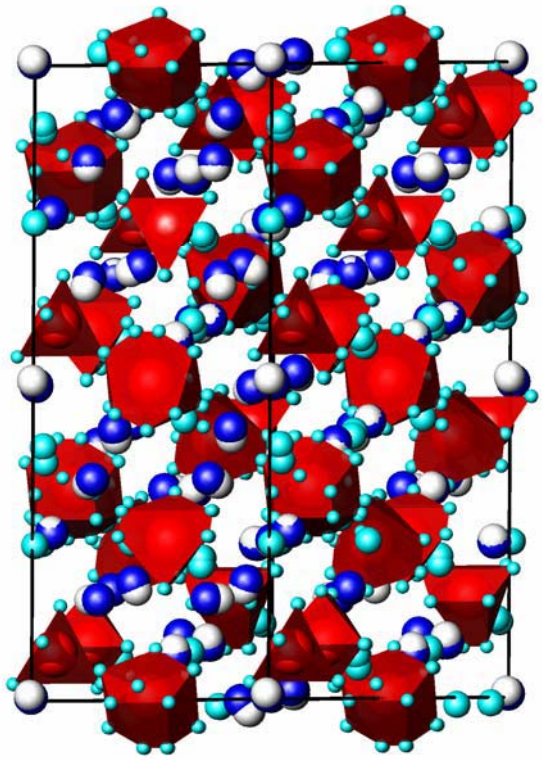

Figure 2.12: First unit cell representation of structure of C_3S type M_3 (Nishi and Takéuchi, 1985).

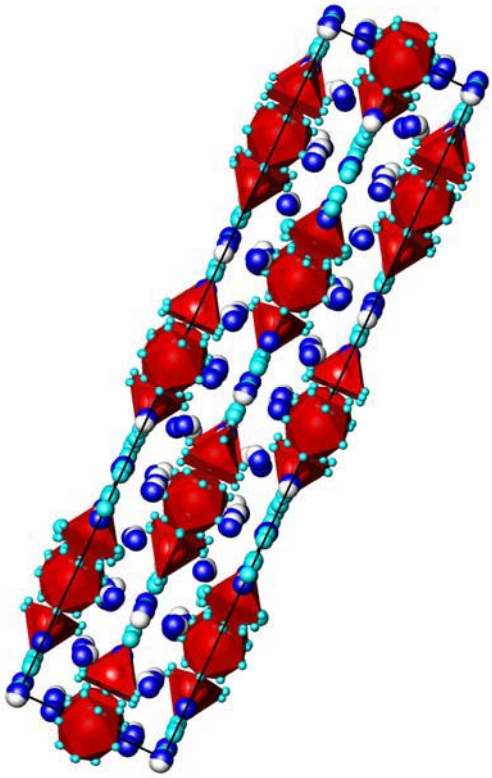

Figure 2.13: Second unit cell representation of structure in C_3S type M_3 (Nishi and Takéuchi, 1985).

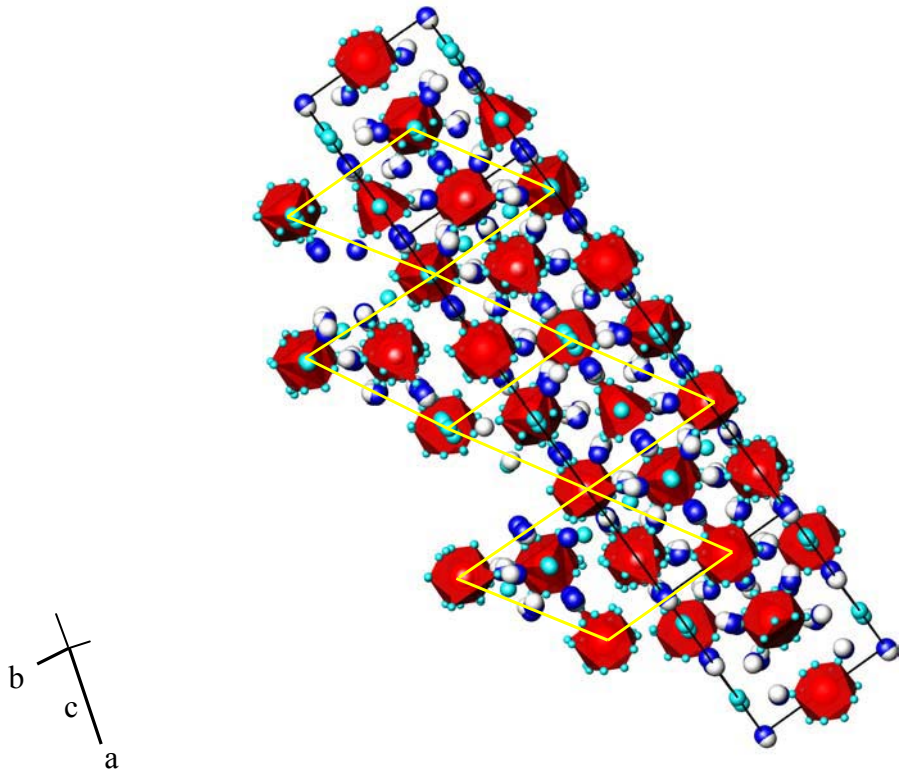

Figure 2.14: Third unit cell representation showing common basal plane within C_3S type M_3 (Nishi and Takéuchi, 1985), with crystal axes arrangement shown.

In figures 2.12-2.14, the various positions of the Ca atoms are represented as either dark blue or white. X-ray structural solution specifies the position of 36 Ca atoms and 36 associated O atoms in the asymmetric unit as "split", describing them as occupying, with equal possibilities, two adjacent sites. The cell parameters were reported as a = 33.083 Å, b = 7.027 Å, c = 18.499 Å, and β = 94.12°.

The structure in figures 2.12-2.14 has 36 Ca_3SiO_5 units per unit cell, and is complicated by statistical disorder. The disorder arises from the orientation of 18 SiO_4 tetrahedra in an asymmetric unit, some of which may statistically occupy three different orientations. Tetrahedral disorder is represented by polyhedra. Depending on the orientation of SiO_4 in the polyhedra, the Ca atoms can occupy various positions.

Mumme (1995) studied the M_3 sub-lattice structure, on which the super-lattice structure of Nishi and Takéuchi is based. This work has the advantage of being performed on a clinker crystal, and is therefore more applicable to cement structure studies. This structure is represented in figures 2.15-2.17 with cell parameters reported as a = 12.235 Å, b = 7.073 Å, c = 9.298 Å, and β = 116.31°. Space group was determined as *Cm*.

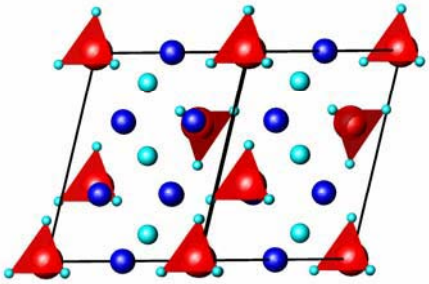

Figure 2.15: First unit cell representation of structure in C_3S type M_3 (Mumme, 1995).

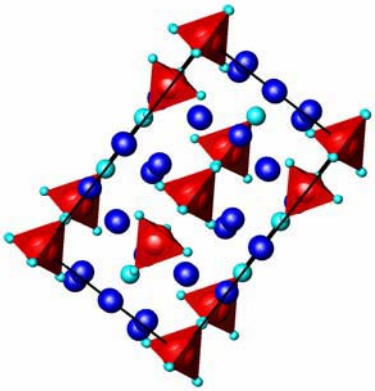

Figure 2.16: Second unit cell representation of structure in C_3S type M_3 (Mumme, 1995).

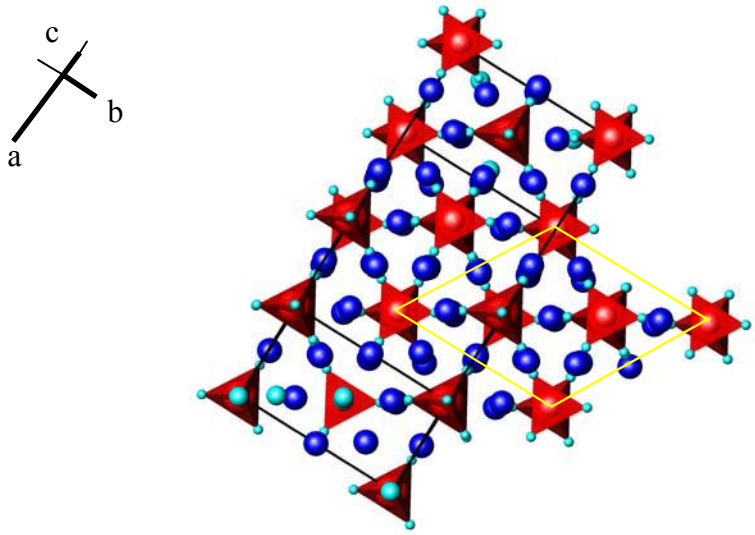

Figure 2.17: Third unit cell representation showing common basal plane within monoclinic C_3S type M_3 (Mumme, 1995), with crystal axes arrangement shown.

One form of triclinic C_3S has been characterised, but it is likely that other forms will have a similar structure. Golovastikov *et al* (1975) designated the type to be T_1, and their structure is represented in figures 2.18-2.20.

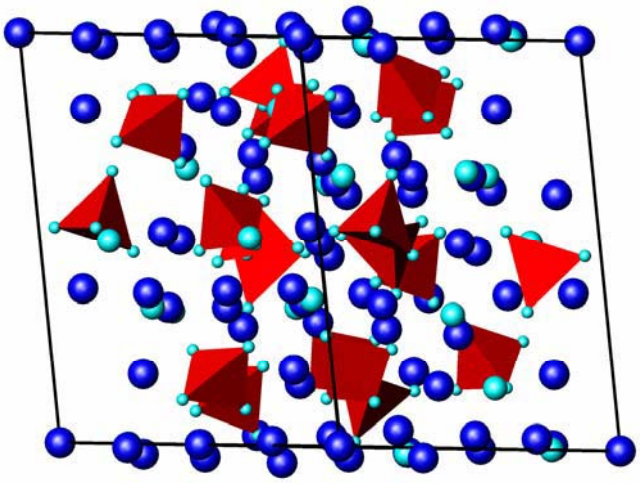

Figure 2.18: First unit cell representation of structure in C_3S type T_1 (Golovastikov *et al*, 1975).

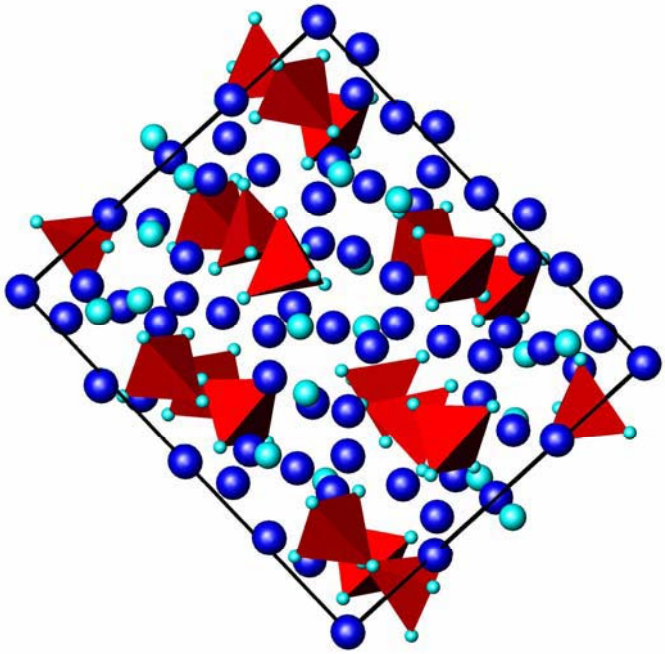

Figure 2.19: Second unit cell representation of structure in C_3S type T_1 (Golovastikov *et al*, 1975).

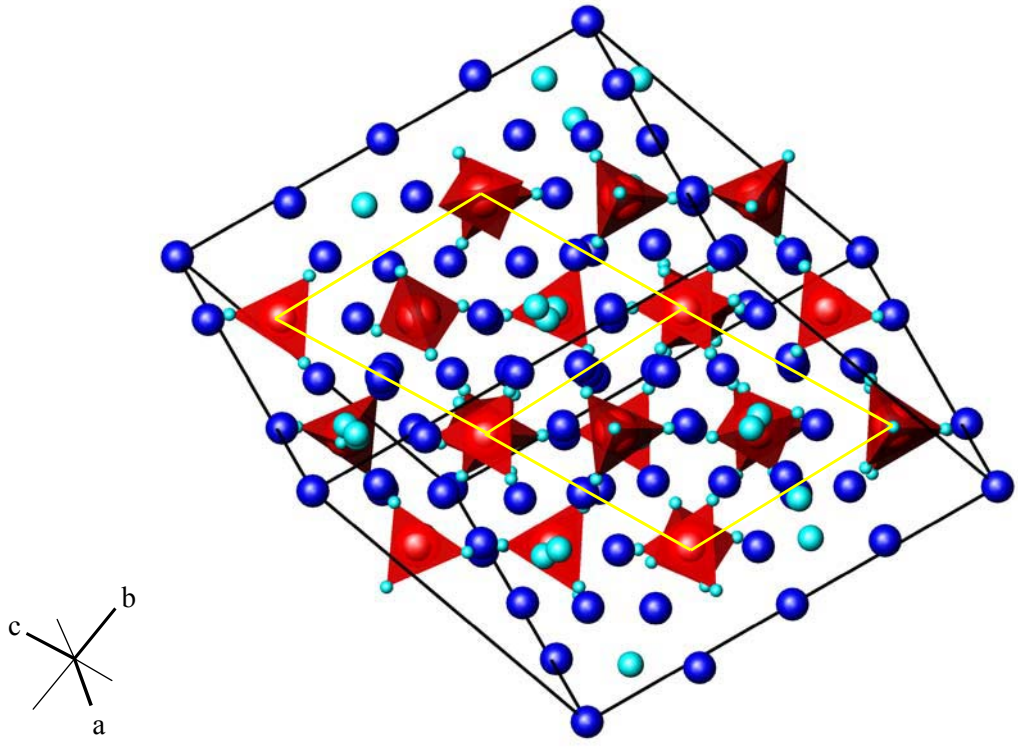

Figure 2.20: Third unit cell representation showing common basal plane within C_3S type T_1 (Golovastikov *et al*, 1975), with crystal axes arrangement shown.

The unit cell, as represented in figures 2.18-2.20, has lattice parameters of a = 11.67 Å, b = 14.24 Å, c = 13.72 Å, α = 105°30′, β = 94°20′, and γ = 90°. The space group was determined as $P\bar{1}$.

The structure proposed by Golovastikov *et al* (1975) was studied by Urabe *et al* (2000). A pseodotrigonal sub-cell, in the hexagonal setting, was introduced with lattice parameters of a = 7.081 Å, b = 7.043 Å, c = 25.230 Å, α = 89.97°, β = 90.37°, and γ = 119.44°.

A T_1 supercell was reported by Guinier and Regourd (1968), using High Resolution Transmission Electron Microscopy (HRTEM). The cell parameters for the triclinic super-cell were reported as a = 28.160 Å, b = 28.294 Å, c = 25.103 Å, α = 90.30°, β = 89.77°, and γ = 119.53°. No structural solution was given. The relationship between this structure and the structure of Golovastikov *et al* (1975) is uncertain as no data exists concerning the observation of superstructure by Guinier and Regourd (1968).

Recently Viani *et al* (1998) observed C_3S polymorphs using XRD of heated pure and Mg-stabilised forms of C_3S, but were only able to identify the T_1 and M_3 forms already characterised.

Pérez-Méndez *et al* (1984) studied the CaO-SiO_2-CaF_2 system that can occur in some clinker raw materials. They postulated a structure for the fluorine-stabilised aristotype of Ca_3SiO_5, in the hexagonal setting of $P6_3/mmc$. Another fluorine containing phase, $KF.2[Ca_6(SO_4)(SiO_4)_2O]$, was identified in some clinkers. Its structure was determined by Fayos *et al* (1985) as being similar to Jeffery's (1952) structure (Taylor and Aldridge, 1993a).

Jeffery (1952) first noted the appearance of satellite reflections in the diffraction pattern from Mg-doped C_3S. He noted that the pure rhombohedral ambient form, with no rhombohedral distortion, did not possess these satellite reflections. From this, it was concluded the satellite reflections were caused not by periodic variations in density caused by substitution, but to a periodic distortion of the rhombohedral lattice.

Urabe and Yamamoto (1996) investigated the reflections from tricalcium silicate using electron diffraction. They noted that the T_1 phase has a superstructure caused by a structural modulation normal to the ($\bar{2}$, 3, 2) plane of the basic rhombohedral cell with hexagonal axes. Main reflections were considered to arise from the sub-cell, and satellite reflections were the result of structural modulation. Later, Shirakami *et al* (1999) synthesised monoclinic C_3S and investigated the superstructure of a monoclinic form using electron diffraction.

Recently, Urabe *et al* (2000, 2002) investigated the reflections from C_3S forms using Selected Area Diffraction (SAD). In their work, the C_3S forms were studied as modulated structures. Structural modulations of the T_1, M_1, M_2, and M_3 modifications were observed. The modulations were identified as one-dimensional types of pseudotrigonal sub-cells in the hexagonal setting, modulated to form super-cells. The modulation waves were detected and the direction of the structural modulation was identified for these types, with respect to the chosen sub-cell. Modulation waves in the T_2 form were also observed, however, the modulation was not fully characterised (Urabe *et al*, 2002).

The results of Urabe *et al* (2000, 2002) are listed in table 2.2. Structural modulations in C_3S were shown to be in some cases commensurate, and incommensurate in another case.

Table 2.2: Known structural modulations in C_3S (Urabe *et al,* 2000) (Urabe *et al,* 2002).

Modification	Direction of modulation (the normal is given)	Sequence of modulation Where *d* = interplanar spacing	Type (1-dimensional)
T_1	122	6 x *d*(122)	Commensurate
M_1	$\bar{2}\,2\,\bar{7}$	5.4 x *d*($\bar{2}\,2\,\bar{7}$)	Incommensurate
M_2	$\bar{1}\,1\,\bar{5}$	5 x *d*($\bar{1}\,1\,\bar{5}$)	Commensurate
M_3	$\bar{1}17$	6 x *d*($\bar{1}17$)	Commensurate
R	Unmodulated	-	-

The relationship between the structural modulations of known C_3S forms and their transformation mechanism is currently unknown. Despite the identification of modulation, and its direction in some cases, no further characterisation of the sub-cell structure was published. Existing models for C_3S forms now known to possess structural modulations are not full solutions for the structures. Published structures for all modulated (non-rhombohedral) C_3S forms are averages of the structures, or models that only approximate the true, unknown structure.

2.3.2 Dicalcium silicate modifications

C_2S has been reported to have five polymorphs distributed in hexagonal, orthorhombic, and monoclinic forms. Table 2.3 summarises the structural information available in the literature.

Table 2.3: Modifications of C_2S.

Transition temperature (°C)	Form	Type	Space group	Reference
1425	α	Hexagonal	*P*63/*mmc*	Mumme *et al* (1996) Mumme *et al* (1995) Udagawa *et al* (1977)
1160	α'_H	Orthorhombic	*Pnma*	Catti *et al* (1984) Sr-stabilised
780-860 (heating from γ) 690 (heating from β)	α'_L	Orthorhombic	*Pna*2$_1$	Il'nets and Bikbau, (1990) Udagawa *et al* (1979)
630-680 (cooling from α'_L)	β	Monoclinic	*P*2$_1$/*n*	Mumme *et al* (1995) Jost *et al* (1977)
<500 (cooling from β)	γ	Orthorhombic	*Pbnm*	Czaya *et al* (1971)

The accepted transformation for the polymorphs of C_2S at ordinary pressures occur as follows:

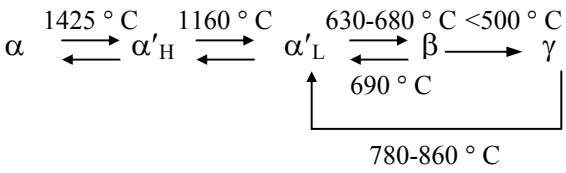

The β modification of C_2S is metastable, forming only during cooling, and has been shown not to be produced from the γ form upon heating (Mumme *et al,* 1996). Unless the β form is stabilised during cooling, the α and α′ polymorphs revert to the stable γ form.

C_2S consists of Ca^{2+} and SiO_4^{4-} ions. The γ form differs from the others as it is lower in density than the other polymorphs. The lower density of this form causes the β form to crack and fall to a powder of higher volume upon cooling. This process is known as "dusting". Yannaquis and Guinier (1959) noted that if the crystallites of the β form are sufficiently small, the transformation to the γ form does not take place, even if no stabiliser is present.

The structures of the α'_H, α'_L, and β polymorphs were derived from that of the α form by progressive decreases in symmetry arising from the changes in the SiO_4^{4-} tetrahedra, as well as small movements of the Ca^{2+} ions. The structures for the α, α'_H, and β form are closely related in their Ca^{2+} and SiO_4^{4-} ionic arrangements, as shown in figures 2.21-2.23. Figure 2.24 shows the γ form. In figures 2.21-2.24 the large open circles represent calcium atoms and the small closed circles represent silicon atoms. The triangular formations represent silicon-oxygen tetrahedra. Atomic heights are given as hundredths of the cell height.

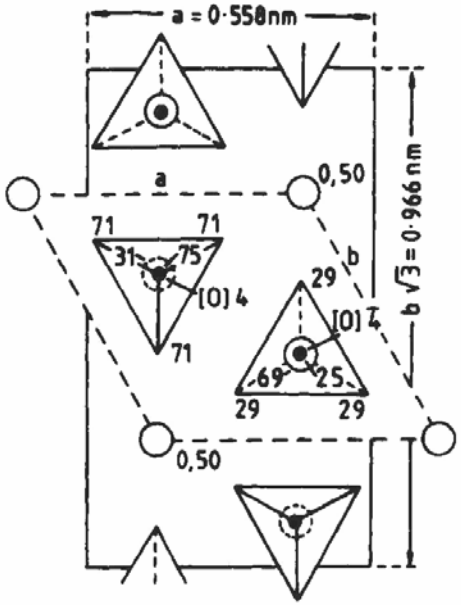

Figure 2.21: Crystal structure of α C_2S (Taylor, 1997).

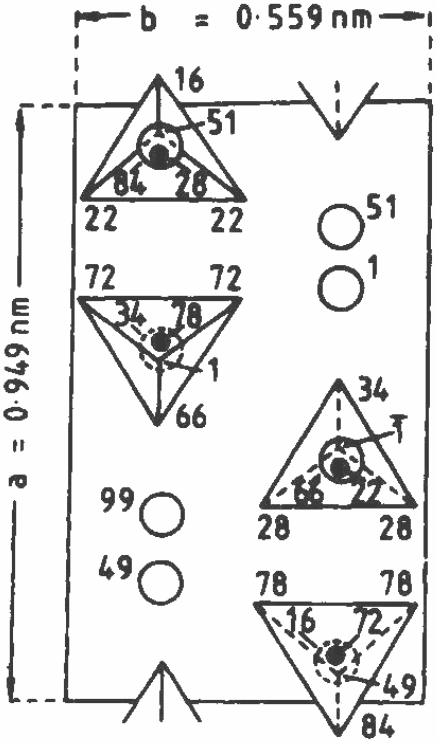

Figure 2.22: Crystal structure of α'_H C_2S (Taylor, 1997).

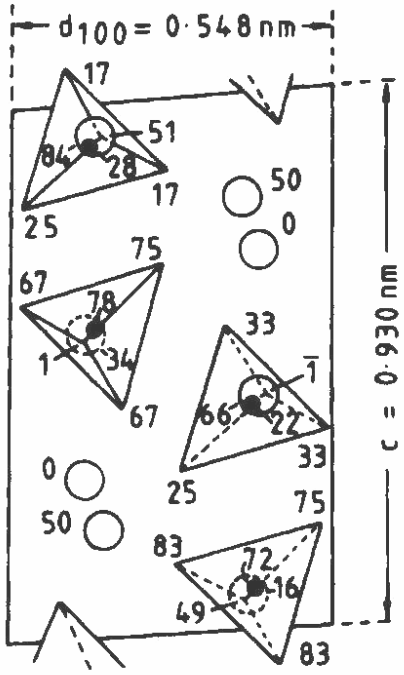

Figure 2.23: Crystal structure of β C_2S (Taylor, 1997).

The space group of the α form may vary according to stabiliser, as well as the temperature. α'_L is a generic term for complex variants of α'_H, as two different super-lattices have been found to occur (Taylor, 1997). The polymorphs of C_2S can also be identified by the coordination of the Ca^{2+} ions. In the β form some Ca^{2+} are 7 coordinated and some are 8 coordinated, to O atoms within 0.288 nm (Jost *et al,* 1977).

In the γ form, the calcium is octahedrally coordinated. The unit cell and the arrangement of the Ca^{2+} and SiO_4^{4-} ions show some similarities to the other polymorphs, as shown in figure 2.24.

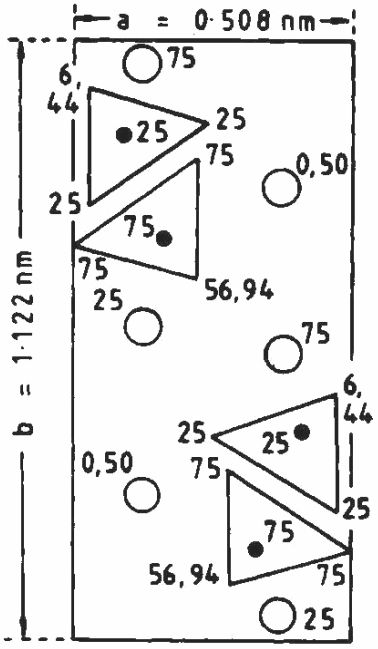

Figure 2.24: Crystal structure of γ C_2S (Taylor, 1997).

Single crystal high temperature XRD evidence has indicated that transformations involving the γ form occur with definite crystallographic orientation relative to the starting material, but fragment because of the large volume change (Taylor, 1997). Interestingly, γ C_2S barely reacts with water at ambient temperature.

Miyakazi *et al* (1998) investigated a new "x C_2S" form of C_2S, synthesised at 600 º C, and reported it as a monoclinic type with space group $P2_1/c$.

2.3.3 Tricalcium aluminate modifications

Pure C_3A does not exhibit polymorphism. Moore (1967) and Maki and Sugimura (1970) postulated the existence of a ring consisting of six AlO_4 tetrahedra in pure C_3A. Mondal and Jeffery (1975) first determined the structure as cubic, with lattice parameter a = 1.5263 nm, space group *Pa*3, and Z = 24. The ring structure was shown to be of formula $Al_6O_{18}^{18-}$. The $Ca_9Al_6O_{18}$ ($Ca_3Al_2O_6$) structure is built of hollow rings of six corner sharing AlO_4 tetrahedra. The Al_6O_{18} ring of Mondal and Jeffery (1975) is shown in the C_3A structure in figure 2.25.

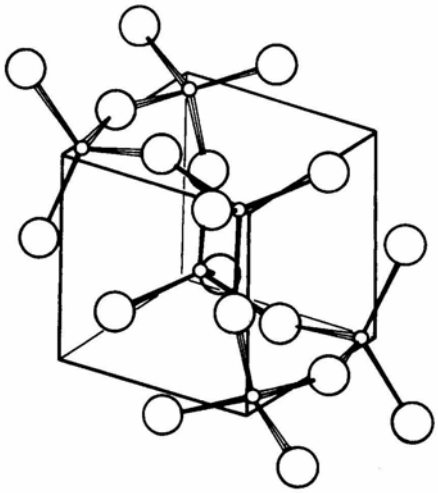

Figure 2.25: Unit cell of C_3A showing the Al_6O_{18} ring structure of Mondal and Jeffery (1975) (Taylor, 1997).

The unit cell is composed of 64 (4^3) sub-cells, of which 8 are occupied by Al_6O_{18} rings, whilst the Ca^{2+} are located near the body centres of some of the remaining sub-cells, and near the corners of the others. The Ca^{2+} coordination of those at the body centre of the sub-cells is irregular, with either 5 or 6 oxygen atoms within 0.28 nm, and those at the corners are octahedrally coordinated.

C_3A can incorporate ions such as Na^+ through substitution with Ca^{2+} and inclusion of a second Na^+ in an otherwise vacant site, giving solid solutions of general formula $Na_{2x}Ca_{3-x}Al_2O_3$ (Taylor, 1997). X-ray emission spectroscopy on $Ca_9Al_6O_{18}$ (Day, 1963) shows the Al to be tetrahedrally coordinated in the crystalline phases of the $Ca_9Al_6O_{18}$-Na_2O solid solution occurring in Portland cement. Nishi and Takéuchi (1975) noted that

as the Al:O ratio in this series is 1:3, the AlO_4 tetrahedra in their structures must be joined to form a certain type of aluminate radical. Investigations of the modifications of the C_3A structure with the general formula $Na_{2x}Ca_{3-x}Al_2O_6$ have shown that a relationship between the amount of Na_2O within the compound and the crystal form that exists. These are shown in table 2.4.

Table 2.4: Modifications of C_3A of general formula $Na_{2x}Ca_{3-x}Al_2O_6$ (Takéuchi *et al*, 1980).

% Na_2O	Compositional Range (x)	Type	Space group	Designation
0 - 1.0	0 – 0.04	Cubic	*Pa*3	C_I
1.0 - 2.4	0.04 - 0.10	Cubic	$P2_13$	C_{II}
2.4 - 3.7	0.10 - 0.16	-	-	C_{II} + O
3.7 - 4.6	0.16 - 0.20	Orthorhombic	*Pbca*	O
4.6 - 5.7	0.20 - 0.25	Monoclinic	$P2_1/a$	M

Both C_I and C_{II} structures are very similar, with C_I existing as a minor variant of the latter with lower symmetry. C_I and C_{II} are impossible to distinguish by XRD without precise lattice determinations, where a = 15.248 Å in C_{II}. In these forms the additional Na^+ ions are situated at the centre of the Al_6O_{18} rings. The O crystal form was studied by Nishi and Takéuchi (1975). The O structure is composed of pseudocubic sub-cells, although this form has a different Al_6O_{18} ring arrangement.

Takéuchi *et al* (1980) refined the structures of cubic, orthorhombic, and monoclinic C_3A. They found the orthorhombic and monoclinic structures to be very similar. The M structure ($Na_{1.50}Ca_{8.25}Al_6O_{18}$) is a slightly distorted variant of the O structure, and was shown to have lattice constants a = 10.877 Å, b = 10.854 Å, c = 15.135 Å, and β = 90.1 °, with Z = 4.

Substitution of calcium with strontium was investigated as the synthetic series $Ca_{3-x}Sr_xAl_2O_6$ by Prodjosantoso *et al* (2000). They noted that within the series of isostructural compounds of space group $Pa\bar{3}$, there is a strong preference for the Ca^{2+} to occupy the six-coordinated sites, and for the Sr^{2+} to occupy the seven to nine-coordinated sites.

2.3.4 Tetracalcium aluminoferrite modifications

The C_4AF phase in cement is sometimes referred to as brownmillerite, which is the mineral name (Hansen *et al*, 1928) given to the compound with oxide composition $(CaO)_4$-$(Al_2O_3)(Fe_2O_3)$, present in an Al/Fe solid solution form, sometimes with various minor substitutions. In the absence of oxide components other than CaO, Al_2O_3, and Fe_2O_3, the ferrite phase can be prepared with any composition in the solid solution series $Ca_2(Al_xFe_{1-x})_2O_5$, where $0<x<0.7$. The crystal data for these ferrites are listed in table 2.4, where the unit cell is orthorhombic, and Z = 4.

Table 2.5: Crystal data for the solid solution series $Ca_2(Al_xFe_{1-x})_2O_5$ (Taylor, 1997).

x	a (Å)	b (Å)	c (Å)	Space group
0	5.5980	14.7687	5.4253	*Pcmn*
0.285	5.588	14.61	5.380	*Ibm*2
0.36	5.583	14.58	5.374	*Ibm*2
0.5	5.5672	14.521	5.349	*Ibm*2
1	5.41	14.45	5.23	*Ibm*2

Several Ca_2Al/Fe_2O_5 compounds, isostructural with brownmillerite, are known to exist (Anderson *et al,* 1993). In the orthorhombic unit cell, layers of Al/FeO_3 octahedra alternate with layers of Al/FeO_2 tetrahedra, and Ca^{2+} cations occupy the spaces between. The difference in symmetry between $Ca_2Fe_2O_5$ with space group Pcmn (Bertaut *et al*, 1959) and Ca_2FeAlO_5 with space group *Ibm*2 (Colville and Geller, 1972), involves different patterns of tetrahedra orientation.

The distinct preference of Al atoms for tetrahedral sites and Fe for octahedral ones was first proposed by Smith (1962). The structure determined by Colville and Geller (1972) is shown in figure 2.26 (Jupe *et al,* 2001), where octahedral Fe/Al are shown as large black spheres in layers, and are linked by oxygen atoms (grey spheres) to the tetrahedrally coordinated Al/Fe layers (shown as small black spheres). Light spheres represent the Ca atoms.

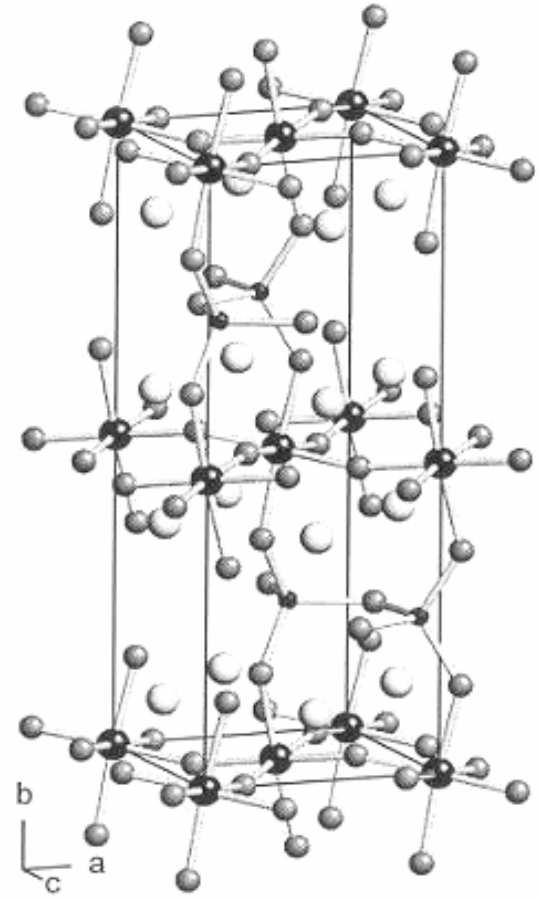

Figure 2.26: Colville and Geller (1972) structure of brownmillerite (Jupe *et al*, 2001).

Jupe *et al* (2001) investigated for the first time the nature of atomic substitutions in brownmillerite. They demonstrated that for the form 2.7:1 Fe/Al, a preference for octahedral/tetrahedral (respectively) occupation is obtained. The trend was reflected in Mg-doped brownmillerite, which showed that Mg exhibited a distinct preference for octahedral sites rather than a disordered occupation between the octahedral/tetrahedral sites.

2.3.5 Phases of Portland cement

In clinker C_3S always crystallises from the melt in trigonal form. The stabilisation factors during the cooling process determine which stable modification at ambient temperature is formed. For this reason C_3S forms morphologically trigonal pseudomorphs in clinker. Interpretation of data on intensity and growth rate can help microscopically determine which combination of types of C_3S are likely to be present in a clinker, but not how much. Microscopy is useful at using sample features such as

birefringence and type of twinning to distinguish C_3S forms. The M_3 form has two times higher birefringence than M_1; T_2 is characterised by the lowest birefringence and inverse polysynthetic twinning. Polymorphs can be reliably identified by high temperature microphotometry, which determines the variation of birefringence as a function of temperature.

The C_3S polymorphs with known structures can also be reliably identified by XRD. Quantification of C_3S polymorphs using XRD would be possible given adequate structural models for their description. Taylor *et al* (2000) stated the importance of including C_3S polymorphs in the Rietveld model for the reliable phase quantification of all cement clinker components.

It has been established that alites are true solid solutions of Ca_3SiO_5, represented by definite phase regions in the appropriate multi-component systems (Hahn *et al*, 1969). Maki and Chromý (1978) found that after optical examination of 30 kinds of industrial clinkers, that alites are mainly monoclinic, M_1 and M_3, and rarely T_2. Taylor (1997) concluded that on present evidence it was probable that the only alite polymorphs found in production clinkers approximate to M_3, M_1, or occasionally, T_2. Taylor (1997) also conceded that some alites formed in the presence of fluorides may stabilise the R form. Taylor *et al* (2000) doubted the polymorphic conclusions above, based on X-ray data and Rietveld analysis, and presented the T_1 polymorph as the main crystal form of alite in clinker.

Thermal stability of the monoclinic forms are dependent on the amount of MgO in the clinker. The stabilisation of M_3 is dependant on the amount of MgO and SO_3 in the clinker (Maki and Kato, 1982). With amounts of MgO > 1.2 %, M_3 is a stable form. With amounts MgO = 0.8 % - 1.2 %, alite crystals are zoned, composed of M_3 and M_1. All polymorphic modifications of C_3S can be stabilised. Hence, it is possible that all forms of C_3S may be present in a clinker and multiple forms may be present simultaneously.

XRD evidence shows that in the majority of production clinkers the C_2S form is predominantly the β form, although the presence of both α, and an α′ form (of non-specific type) have been reported (Taylor, 1997). Characterisation of the polymorphic

type in cement clinker is difficult due to the similarities between the alite and C_2S patterns in XRD data. The C_2S phase in cement clinker varies usually only in terms of its texture, and not its polymorph. Types I and II have been denoted to represent respectively: round grains typically 20 to 40 μm in diameter, with several sets of parallel striations, and irregular grains with only one set of striations. Type II C_2S is rare.

Two crystalline forms of C_3A are typically found in cements, the cubic studied by Mondal and Jeffery (1975), and the orthorhombic form which is stabilised by the presence of alkalis in the clinker feedstocks. Takéuchi *et al* (1980) found that these modifications can occur in clinkers by stabilisation with Na, Fe, and Si as impurities.

The analysis of C_4AF in clinkers is made difficult by the variable Al/Fe ratio over a considerable range. C_4AF in real cement is more complex as a result of additional minor substitutions for Fe and Al by Mg, Si, and Ti (Harrisson *et al,* 1985) (Bergstrom *et al*, 1994). Typical real cement ferrite phases have compositions such as $Ca_2Fe_{0.8}Al_{0.8}Mg_{0.2}Si_{0.15}Ti_{0.05}O_5$ (Gollop and Taylor, 1994), suggesting that Fe and Al are replaced to the same degree. Despite this, difficulties in synthesising brownmillerite with these degrees of substitutions have been reported (Maki *et al,* 1995) (Neubauer *et al*, 1996).

2.4 Phase quantification of cement clinker

It is necessary to determine a complete mineralogy of clinker cement to correctly understand, interpret, and predict the outcome of any plant production process. Quantitative Phase Analysis (QPA) of cement clinker is difficult due to the complexity of phases.

The cement industry standard method for estimating mineralogical composition of clinker, a procedure known as the Bogue calculation (Bogue, 1929), provides approximate concentrations of alite, C_2S, C_3A, and the ferrite phases. This method transforms chemical analysis oxide figures into mineral phase percentages, assuming certain chemical formulae for each of the minerals. This method has the disadvantage that the phase composition is calculated by the chemical composition, as even if the

chemical composition of the four main phases is well known, thermal equilibrium has to be assumed. As the technical process in clinker production does not guarantee this, the Bogue composition often varies from the actual phase composition. The Bogue method assumes the mineralogy of the clinker rather than measuring it and the result is dependent on the chemical formulae assumed for the particular minerals. The actual minerals are often impure, and phase formulae may differ between samples. The different mineral formula of each phase are sometimes also similar, so there is a danger that the formulae used may not provide a unique and correct answer.

Other approaches to QPA of cement clinker are also based on estimation from chemical analysis such as wet chemical analysis methods. Examples of these are the Lime Saturation Factor (LSF), and the alumina and silica moduli (AR and SR respectively).

QPA of clinker has been done directly from XRD or optical microscopy data. A consistently reliable method for quantification of the mineral phases present in cement clinker is by Microscope Point Counting (MPC). However, this method requires special skills in representative sampling and recognising phases under the reflecting microscope, and it is very labour intensive. Generally the optical methods are too slow and expensive to be used on a large scale.

Attempts have been made to quantify cement phases with XRD analysis using traditional integrated intensity methods. However, because of the concentration and superposition of the strong lines of these minerals in a narrow angular range of the pattern, this approach to phase quantification makes reliable quantification too difficult. Similar difficulties are also encountered with neutron diffraction methods.

In the last few years, advances in powder diffraction methods have meant that Rietveld analysis of powder diffraction data is being favoured in some cases for QPA of cement clinker (Scarlett *et al,* 2002) (Füllmann *et al*, 2001) (Taylor *et al*, 2000) (Feret and Feret, 1999). Rietveld analysis uses each point of the profile step-scan as a data point, rather than the integrated intensities of the individual lines. This alleviated the line superposition problem and gave up to several thousand data points per pattern. Powder diffraction analysis of cement clinker has the major advantage over other analysis methods of allowing polymorphic identification of the clinker components. This is

exceptionally important with the main alite phase, whose different polymorphs have a wide range of compressive strengths.

2.4.1 Amorphous clinker component

Clinker contains both crystalline and amorphous components, although the quantity of amorphous constituent in clinkers is a highly debated topic in the literature. Most researchers agree that the crystalline component of cement is of primary abundance, with the amorphous component comprising less than 10 % in typical clinker materials.

Yang (1996) concluded from the modified Ruland method that clinker components prepared as pure crystalline phases were less than 95 % crystalline, and found some clinker materials with less than 90 % crystallinity by this method.

Taylor *et al* (2000) reported a minimal quantity of non-diffracting components in the clinker NIST standards 8486, 8487, and 8488. This result was evidenced by their own XRD results, and a summary of the literature given by Taylor (1997). In the summary, Taylor (1997) states that quantitative XRD, Scanning Electron Microscopy (SEM), or X-ray microanalysis does not support the view that modern clinkers contain significant quantities of glass, except in rare cases. Taylor *et al* (2000) suggest a corundum spike method for amorphicity testing, but remark that this method would not be suited to systems where crystallinity was less than 92.5 %.

Suhermann *et al* (2002) recently investigated the phase fraction of non-diffracting components of the same NIST clinkers as Taylor *et al* (2000), and found weight percentages of greater than 5 wt. % non-diffracting (amorphous) phase in these clinkers.

The amount of amorphous material in clinker remains speculative. QPA of clinker by the Rietveld method assumes 100 % crystallinity of the sample and results are based on a constraint of the total composition of components being modelled to 100%. Upon investigating an unknown clinker using only the Rietveld method, it is important to consider this bias. In an investigation comparing the QPA of a sample using various diffraction sources where the results are produced using identical Rietveld methods, bias is assumed systematic and consistent.

2.5 Hydration of Portland cement

Although the general process by which OPC cures is known, it is still not completely understood. The hydration reactions involved in the setting of cement are complicated by the variety of material present during cement hydration (Mindess and Young, 1981). The hydration of cement is often simplified by considering the hydration of each compound separately. Although this is not an entirely accurate description of the hydration of cement, this approach has been used in many publications as an approximation to the actual reactions (Mindess and Young, 1981) (Taylor, 1997) (Skalny and Young, 1980).

More detailed mechanisms than those presented in this chapter appear controversial and reaction theory varies between publications. Amorphous reaction products often exist, with highly variable composition. Although much research has been done concerning the structure and composition of reaction products (Young, 1988) (Berliner *et al,* 1998) classical cement chemistry notation is necessary for representing reactions where product variation exists.

Variation in the composition of hydrating cement has been noted as functions of cure temperature, amount of water present, as well as with the addition of supplementary cementitious materials. Plots of the rate of heat evolution with time of hydrating cement, as shown in figure 2.27, are useful for the investigation of hydration mechanisms in cement.

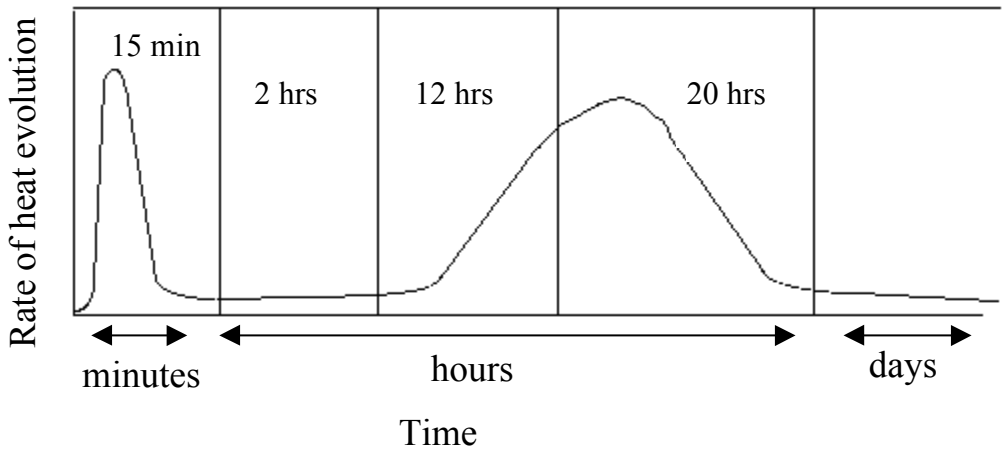

Figure 2.27: Calorimetric plot of the rate of heat evolution with time for the hydration of OPC.

In order to assess the effect of these variables on the composition of hydrating cement, it is better to consider the cementitious system as a series of hydrating components.

2.5.1 Hydration of calcium silicates

The reaction between C_3S and water is the main factor in the setting and hardening of OPC. This reaction has been studied primarily with the aim of obtaining a detailed understanding of the mechanism of strength evolution in cement. However, both the kinetics and reaction stoichiometry are both poorly understood.

When calcium silicate grains in OPC are mixed with water a rapid release of calcium and hydroxide ions from each grain surface results. The production of hydroxide ions causes the pore fluid solution pH to rise above 12 within the first few minutes (Skalny and Young, 1980). In this process, calcium silicates hydrate to form amorphous calcium silicate hydrate (C-S-H), known as tobermorite gel, and calcium hydroxide, as in reactions 2.1 and 2.2.

$$2C_3S + 7H \rightarrow C\text{-}S\text{-}H + 3CH \quad (2.1)$$

Similarly,

$$2C_3S + 5H \rightarrow C\text{-}S\text{-}H + CH \quad (2.2)$$

Amorphous calcium silicate hydrate is of variable composition. The ratio of C:S varies with the concentration of released hydroxide ions. The number of water molecules bound to the produced hydrate gel is also variable. It was believed that most calcium hydroxide is crystalline and of fixed composition, however amorphous calcium hydroxide was found by Taylor (1997) in a cementitious system.

The overall hydration process proceeds with several reaction steps. These steps are summarised in standard chemistry notation in reaction 2.3.

$$Ca_3SiO_5 + (3 + y - x)H_2O \rightarrow (CaO)_x(SiO_2)\bullet(H_2O)_y + (3 - x)Ca(OH)_2 \quad (2.3)$$

In the summary reaction 2.3, *x* determines the Ca to Si ratio of the C-S-H and *y* is the sum of the hydroxyl ions and bound water molecules that are incorporated into the C-S-H structure. Both *x* and *y* vary throughout the reaction and it is through this mechanism that the C-S-H can vary its composition (FitzGerald *et al,* 1998).

The composition of the C-S-H gel is very important as is believed to be responsible for the strength of the cured paste. Reaction 2.3 consists of three separate sub-reactions. Reaction 2.4 outlines the first of these, the irreversible exothermic dissolution of the C_3S.

$$Ca_3SiO_{5(s)} + 3H_2O \rightarrow 3Ca^{2+}_{(aq)} + 4OH^-_{(aq)} + H_2SO_4^{2-}{}_{(aq)} \quad (2.4)$$

Formation of the C-S-H gel then occurs through reaction 2.5.

$$H_2SO_4^{2-}{}_{(aq)} + x Ca^{2+}_{(aq)} + (2x - 2)OH^-_{(aq)} + (y - x)H_2O_{(l)} \rightarrow (CaO)_x(SiO_2)\bullet(H_2O)_y \quad (2.5)$$

The Ca/Si ratio of the C-S-H has been shown to vary as functions of hydration time and temperature (Skalny and Odler, 1972) (Odler, 1973) (Bentur *et al*, 1979). The ratio varies from approximately 1 – 2, and is always less than 3. Hence, a Ca^{2+} rich solution results. Reaction 2.6 shows the $Ca(OH)_2$ precipitation that results from this once the critical concentration of Ca^{2+} has been reached.

$$Ca^{2+}_{(aq)} + 2(OH)^-_{(aq)} \rightarrow [Ca(OH)_2]_{(s)} \quad (2.6)$$

The mechanisms that guide the formation of products from hydrating cement vary between publications. The literature agrees, however, on the rate mechanisms that control the hydration reactions. These can be divided into five stages. In the literature, disagreements arise with issues concerning the overlapping of concurrent stages and their exact occurrence and interdependency. It is easier to consider the stages as non-concurrent, with only brief reference to those that are interdependent. The five stages are presented in table 2.6. Figure 2.28 also shows a calorimetric plot of the rate of heat evolution with time, featuring five divisions representing each of the reaction stages.

Table 2.6: Hydration sequence of calcium silicates (Taylor, 1997).

Reaction stage	Description	Rate control mechanism	Approximate rate
1	Initial hydrolysis	Chemical	Rapid
2	Induction period	Nucleation	Slow
3	Acceleration	Chemical	Rapid
4	Deceleration	Chemical and diffusion	Slow
5	Steady-state	Diffusion	Slow

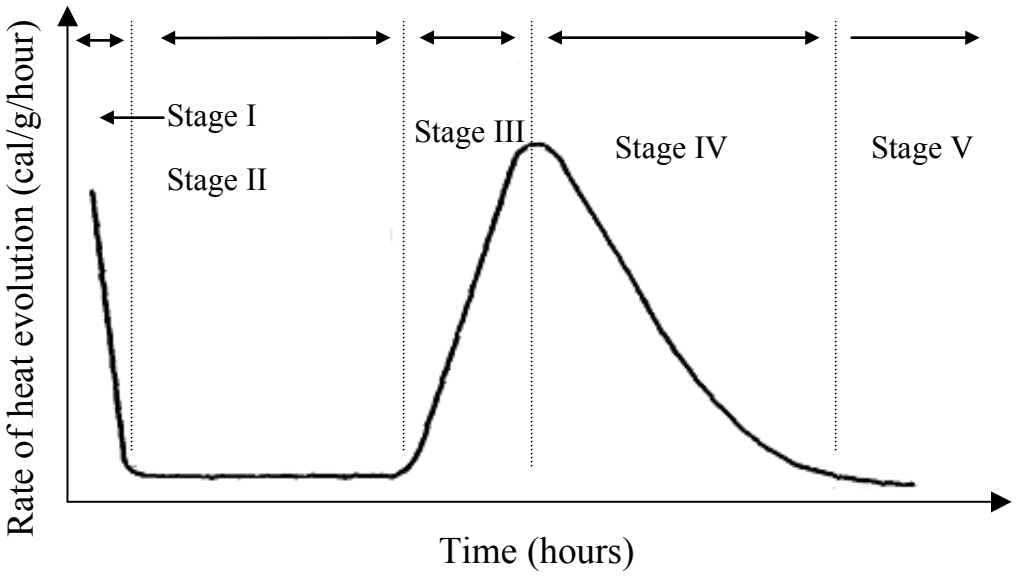

Figure 2.28: Calorimetric plot of the rate of heat evolution with time for the hydration of C_3S (Young, 1983).

The rate of the first stage, or initial hydrolysis, is chemically controlled. The concentrations of Ca^{2+} and OH^- released during the early stages of reaction represented by reactions 2.1 and 2.2, rise towards a critical value, a point at which calcium hydroxide begins to crystallise. The first stage is both rapid and temperature sensitive.

The second stage, induction, is nucleation controlled. The induction stage refers to the stage in reactions 2.1 and 2.2 where the ionic concentrations build toward that required for crystal nuclei formation, from which the hydration products form. The dependency of stage 1 on stage 2 has been widely discussed in the literature (de Jong *et al,* 1967) (Shpynova *et al*, 1968) (Fujii and Kondo, 1968).

The third stage begins once nucleation is achieved. This stage is a period of reaction acceleration, where the calcium silicate grains once again react rapidly as the hydration rate reverts to chemical control. This step is most sensitive to changes in temperature. As the C_3S grains hydrate, they become covered with a calcium silicate hydrate coating. This continues until the hydration product around each non-reacted grain thickens, and water must diffuse through the deposited layer to the shrinking grain before further reaction can occur.

The fourth rate involves a deceleration of the reaction rate. Deceleration continues to a point where the rate of grain hydration becomes purely dependent on the rate of water diffusion through the hydrated layer.

The final rate step is a slow, diffusion-controlled process, and is not temperature sensitive below approximately 100 °C. Diffusion controlled hydration finally approaches completion asymptotically.

The chemistry of hydration changes significantly at temperatures greater than approximately 100 °C and is not discussed in the thesis (Taylor, 1997).

2.5.2 Strength of hydrated tricalcium silicate

Tricalcium silicate is the fundamental hydraulic component of cement and has been shown responsible for the development of strength in the cement paste. The essential step in the hydration of C_3S is the transfer of protons from the water to the solid. The reactivities of the oxygen atoms towards protonation depends on their basicity, or the magnitudes of their localised charges, as the water in this case is acting as a Brønsted acid. Any structural feature that draws electrons away from the O atoms renders them less reactive, and the basicities depend on the electronegativities of the atoms with which they are associated. Although the nearest neighbours are the most important in these effects, those further away cannot be discounted as negligible.

In relation to reactivity towards water, the coordination of the oxygen atoms is possibly more important than that of the Ca. The O atoms attached to atoms of a single element will be less reactive as the electronegativity of that element increases. As C_3S contains

O atoms linked to Ca, if the electronegativity of the Ca is decreased, then the O becomes more reactive.

Quantification of the polymorphs of C_3S has the potential to be extremely useful to industrial applications. Harada *et al* (1977) showed that each polymorph of C_3S has a different rate of hydration, which was reflected in their resultant strength properties. Mascolo *et al* (1977) noted that the compressive strength of the polymorphs appeared to be related to the type of stabilising ion entering the lattice. Recently a link between C_3S polymorphism and strength of cement was demonstrated by Staněk and Sulovský (2002), although no reference to the earlier works of Harada *et al* (1977) or Moscolo *et al* (1977) was made.

2.5.3 Hydration of tricalcium aluminate

It is essential to quantify the amount of C_3A present in a clinker in order to add the desired amount of gypsum required for control of the hydration rate of this phase. Understanding the mechanisms of C_3A hydration are thought to lead to a better understanding of the role of gypsum has in the control of the setting rate of the cement. Reaction 2.7 represents the primary initial reaction of C_3A with water in the presence of gypsum, the formation of ettringite.

$$C_3A + 3C\bar{S}H_2 + 26H \rightarrow C_6A\bar{S}_3H_{32} \qquad (2.7)$$

Ettringite is a stable hydration product only when there is an ample supply of sulfate available. If the solution concentration of SO_4^{2-} drops, then ettringite is converted to monosulfate, as shown by reaction 2.8.

$$2C_3A + C_6A\bar{S}_3H_{32} + 4H \rightarrow 3C_4A\bar{S}H_{12} \qquad (2.8)$$

The overall reaction of C_3A can be represented as in reaction 2.9.

$$C_3A + C\bar{S}H_2 + 10H \rightarrow C_4A\bar{S}H_{12} \qquad (2.9)$$

Ettringite has a specific composition in the general group of AFt, the Al_2O_3 - Fe_2O_3 - trisulfate, phases. In the AFt phases, Al can be partly or totally replaced by Fe, and SO_4^{2-} by other anions. Ettringite is, however, often used as a synonym for AFt. Similarly, monosulfate is one particular composition in the group of AFm, the Al_2O_3 - Fe_2O_3 - monosulfate, phases.

Both steps in the hydration of C_3A are exothermic. The hydration of C_3A is slowed as ettringite forms a diffusion barrier around the C_3A grain, analogous to the C-S-H formed around the calcium silicate grains. The conversion of ettringite to monosulfate causes the barrier to be broken down and the C_3A is free to hydrate again. The evolved heat for C_3A is much greater than that for the calcium silicates.

The more gypsum there is, the longer the ettringite will remain stable. The formation of monosulfate occurs because of a deficiency of sulfate ions necessary to form ettringite from all the available hydroxyaluminate ions. When monosulfate is bought into contact with a new source of sulfate ions, ettringite can be formed once again, as in reaction 2.10.

$$C_4A\bar{S}H_{12} + 2C\bar{S}H_2 + 16H \rightarrow C_6A\bar{S}_3H_{32} \qquad (2.10)$$

The vigorous initial reaction of C_3A with water can lead to flash setting of the clinker. Flash setting is caused by the rapid formation of calcium aluminate hydrates, as represented in reaction 2.11. Gypsum is added to the clinker to dampen the vigorous reaction.

$$2C_3A + 21H \rightarrow C_4AH_{13} + C_2AH_8 \qquad (2.11)$$

The products of reaction 2.11 are unstable AFm products, and convert to hydrogarnet as in reaction 2.12.

$$C_4AH_{13} + C_2AH_8 \rightarrow 2C_3AH_6 + 9H \qquad (2.12)$$

The high heat evolution accompanying reaction 2.11 means that the temperature of a hydrating C_3A paste can easily rise several tens of °C. Above 30 °C, reaction 2.12 is very rapid, but once hydrogarnet has nucleated crystal growth can readily occur below this temperature. Direct formation of hydrogarnet, as in reaction 2.13, can only occur when temperatures exceed 80 °C.

$$C_3A + 6H \rightarrow C_3AH_6 \quad (2.13)$$

When quite small amounts of gypsum are present there may still be un-reacted C_3A left after all the ettringite has been converted to monosulfate. In this case AFm phases having compositions between $C_4A\bar{S}H_{12}$ and C_4AH_{13} are formed as in reaction 2.14, either as mixtures or as solid solutions.

$$C_4A\bar{S}H_{12} + C_3A + CH + 12H \rightarrow 2[C_4A(\bar{S},H)H_{12}] \quad (2.14)$$

Table 2.6 shows the formation of hydration products from C_3A with varying amounts of gypsum.

Table 2.7: Formation of C_3A hydration products with varying amounts of $C\bar{S}H_2$.

$C\bar{S}H_2/C_3A$ molar ratio	Stable hydration products formed
3.0	$C_6A\bar{S}_3H_{32}$
3.0 - 1.0	$C_6A\bar{S}_3H_{32} + C_4A\bar{S}H_{12}$
1.0	$C_4A\bar{S}H_{12}$
< 1.0	$C_4A\bar{S}H_{12}$ - C_4AH_{13} solid solution
0	C_3AH_6

2.5.4 States of water in cement pastes

Water molecules exist in a number of states in a hydrating cement paste. They exist as non-evaporable bound water, such as in crystalline phases, in gel spaces, or adsorbed on surfaces. Water can also exist as free water, such as in capillary pores between 10 and

100 nm, or in macropores greater than 100 nm (Livingston, 1995). The distribution of the water molecules among different sites within the hydrated structure is uncertain.

A complete determination of the distribution of water among these various sites has been hampered by the amorphous nature of C-S-H, which renders XRD difficult. The standard method for measuring water in different phases of cement has been weight loss during drying either by oven heating or by equilibration with very low water vapour pressure atmospheres. These methods can cause shifts in the fractions of bound and unbound water. Quasi-elastic neutron scattering methods are currently being used to investigate this topic.

CHAPTER 3

THEORETICAL BACKGROUND AND EXPERIMENTAL METHODS

3.1 Introduction

Diffraction is an important tool in the study of crystal structures and phase transitions. Current technologies have expanded this tool for use in complex phase identification and quantification. Consequently, diffraction techniques have been successfully applied to the investigation of many complex materials. Cement and its components are sufficiently complex to require such technologies and these materials have been increasingly investigated using diffraction tools in recent years. Quantitative phase analysis of cements, structural analysis of cement clinker components, and the mechanism of cement component hydration, have all been investigated using diffraction technologies.

Recent advances are yielding more and/or improved data containing increased sample information. Radiation sources used in diffraction experiments are more intense and have higher resolution, such as advanced 3rd generation synchrotron sources. Data collection strategies have also improved, with diffraction instrumentation leading to better source quality and detector systems. Data analysis techniques, such as Rietveld refinement, have also been implemented in powerful programs that allow a better extraction of the sample information from the diffraction data.

Due to the complexity of cement, other analysis techniques are often used in conjunction with diffraction to provide complimentary information about cement and its components. X-ray fluorescence is used to establish atomic composition, whilst differential thermal analysis is used to investigate thermal behaviour during kinetic phenomena such as phase transitions.

All of these techniques and tools are used in the investigations described in this thesis. The theory behind and concepts of these are reported in this chapter.

3.2 Crystal Structure

A solid with an arrangement of atoms in a pattern that is periodic in three dimensions is a crystal. Amorphous solids do not possess periodicity. An ideal crystal is constructed by the infinite repetition in space of identical structural units. In the simplest crystals the structural unit is a single atom, however, in many materials the structural unit can be several atoms or molecules.

The structure of all crystals is described in terms of a lattice with a group of atoms, called the basis, attached to each lattice point. The crystal structure is then the repetition of the basis in space. An ideal crystal is composed of atoms arranged on a lattice defined by the three fundamental translation vectors, $\mathbf{a_1}$, $\mathbf{a_2}$, and $\mathbf{a_3}$. The origin of the repeating units is immaterial, it is only the magnitude and direction of the repeating displacements that is important.

The smallest volume, which when periodically repeated forms the crystal, is called the unit cell. This is defined by the three fundamental translation vectors and the unit cell volume, v_c, which is given in equation 3.1 (Ashcroft and Mermin, 1981) (Zachariasen, 1945) (Cullity, 1978).

$$v_c = \mathbf{a_1} \cdot \mathbf{a_2} \times \mathbf{a_3} \tag{3.1}$$

It can be assumed that the different atoms in the unit cell are numbered 1, 2, 3, … , n, and that the vectors that relate to the cell origin are given by the cell vectors $\mathbf{r}_1$, $\mathbf{r}_2$, $\mathbf{r}_3$, …, $\mathbf{r}_n$. Similarly, the different unit cells can be designated by the three integers m_1, m_2, and m_3, such that the cell $m_1m_2m_3$ is the one whose origin is displaced from the crystal origin by $m_1\mathbf{a}_1 + m_2\mathbf{a}_2 + m_3\mathbf{a}_3$. The position of the atom of type n in the unit cell $m_1m_2m_3$ is given by the vector in equation 3.2. Figure 3.1 depicts in two dimensions the periodic property of a crystal.

$$m_1\mathbf{a}_1 + m_2\mathbf{a}_2 + m_3\mathbf{a}_3 + \mathbf{r}_n \tag{3.2}$$

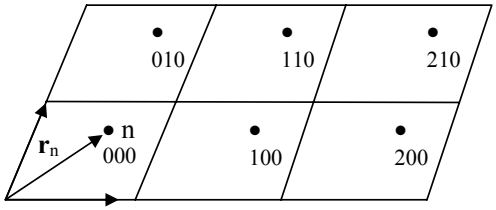

Figure 3.1: Two-dimensional representation of the periodic property in a crystal.

3.3 Diffraction

Diffraction is a scattering phenomenon. A diffracted beam can be defined as a beam composed of a large number of scattered rays mutually reinforcing one another. A single atom scatters an incident beam in all directions in space, but a large number of atoms arranged periodically to form a crystal will scatter an incident beam in only a few directions. The periodic arrangement of atoms causes destructive interference of the scattered rays in all directions, except those predicted by the Bragg law, where reinforcement occurs. The relationship between destructive interference and structural periodicity is most notable by a comparison of the scattering from solids and liquids. The curve of scattered intensity versus 2θ for a crystalline solid is almost zero everywhere except at certain angles where the beam is diffracted, appearing as high and sharp maxima. Both amorphous solids and liquids have structures characterised by an almost complete lack of periodicity or tendency to order. In these structures atoms are tightly packed, showing a statistical preference for a particular interatomic distance. The result is a diffraction pattern consisting only of a few broad maxima.

For diffraction of radiation by a crystal, the essential condition that must be met if diffraction is to occur is given by the Bragg law, given in equation 3.3.

$$n\lambda = 2d\sin\theta \qquad (3.3)$$

In equation 3.3, d is the distance between the parallel planes of atomic arrangement within a crystal, λ is the wavelength of the incident beam of radiation, and θ is the angle of the incident radiation beam on the crystal. The order of reflection, n, may take an

integral value consistent with sinθ not exceeding unity, equal to the number of wavelengths in the path difference between rays scattered by adjacent planes. Equation 3.3 demonstrates conditions where, for fixed values of λ and d, there may be several angles of incidence θ_1, θ_2, θ_3… at which diffraction may occur corresponding to n = 1, 2, 3… By using a monochromatic beam of known λ and measuring θ, the spacing of various planes in a crystal can be determined and a structure elucidated.

3.3.1 Miller indices and Bragg theory

The Bragg diffraction condition considers diffraction in terms of a set of crystallographic planes, *hkl,* with a spacing d_{hkl} between planes. Figure 3.2 gives a graphical definition of the concept (Zachariasen, 1945).

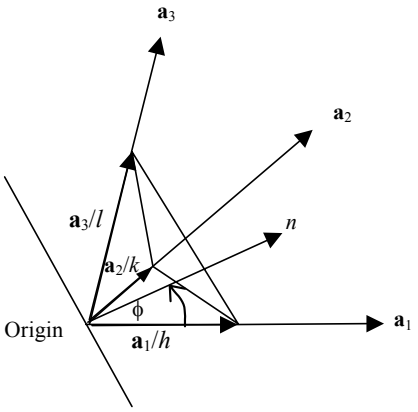

Figure 3.2: Representation of the crystallographic planes *hkl*.

The crystallographic planes *hkl* are a set of parallel, equidistant planes, known as the Miller indices. One passes through the origin and the next nearest makes intercepts on the three crystallographic axes at $\mathbf{a}_1/h$, $\mathbf{a}_2/k$ and $\mathbf{a}_3/l$.

A simple representation of the orientation and spacing of these planes is obtained by introducing the vector $\mathbf{H}_{hkl}$, which is perpendicular to the Miller indices and is the reciprocal of their spacing. Equation set 3.4 shows the reciprocal vectors $\mathbf{b}_1$, $\mathbf{b}_2$, and $\mathbf{b}_3$, defined using the crystal axes $\mathbf{a}_1$, $\mathbf{a}_2$, and $\mathbf{a}_3$.

$$\mathbf{b}_1 = 2\pi\frac{\mathbf{a}_2 \times \mathbf{a}_3}{\mathbf{a}_1 \bullet \mathbf{a}_2 \times \mathbf{a}_3},\ \mathbf{b}_2 = 2\pi\frac{\mathbf{a}_3 \times \mathbf{a}_1}{\mathbf{a}_1 \bullet \mathbf{a}_2 \times \mathbf{a}_3},\ \mathbf{b}_3 = 2\pi\frac{\mathbf{a}_1 \times \mathbf{a}_2}{\mathbf{a}_1 \bullet \mathbf{a}_2 \times \mathbf{a}_3} \tag{3.4}$$

Each vector is perpendicular to the plane defined by the two crystal axes having different indices. Equation 3.5 gives the important scalar product of the two sets of vectors in equation 3.4 when the indices are the same. Equation 3.6 gives their scalar product if they are different.

$$\mathbf{a}_1 \bullet \mathbf{b}_1 = \mathbf{a}_1 \bullet \frac{\mathbf{a}_2 \times \mathbf{a}_3}{\mathbf{a}_1 \bullet \mathbf{a}_2 \times \mathbf{a}_3} = 2\pi \tag{3.5}$$

$$\mathbf{a}_1 \bullet \mathbf{b}_2 = \mathbf{a}_1 \bullet \frac{\mathbf{a}_3 \times \mathbf{a}_1}{\mathbf{a}_1 \bullet \mathbf{a}_2 \times \mathbf{a}_3} = 0 \tag{3.6}$$

As the vector $\mathbf{a}_3 \times \mathbf{a}_1$ is perpendicular to $\mathbf{a}_1$, the trigonometry of their scalar product allows these results to be generalised by the normal and orthogonal conditions between the primary and reciprocal vectors. This is shown in equation 3.7.

$$\mathbf{a}_\mathrm{i} \bullet \mathbf{b}_\mathrm{j} = \begin{cases} 1, \mathrm{i} = \mathrm{j} \\ 0, \mathrm{i} \neq \mathrm{j} \end{cases} \tag{3.7}$$

Equation 3.8 defines the vector $\mathbf{H}_{hkl}$, using the reciprocal vectors and the Miller indices.

$$\mathbf{H}_{hkl} = h\mathbf{b}_1 + k\mathbf{b}_2 + l\mathbf{b}_3 \tag{3.8}$$

Figure 3.2 shows that ($\mathbf{a}_1/h - \mathbf{a}_2/k$) and ($\mathbf{a}_2/k - \mathbf{a}_3/l$) are vectors parallel to the *hkl*-planes. The relationships expressed in equation 3.7 can be used to show that $\mathbf{H}_{hkl}$ is perpendicular to the set of *hkl* planes, since it is perpendicular to the parallel vectors to the planes, as follows:

$$\left(\frac{\mathbf{a}_1}{h} - \frac{\mathbf{a}_2}{k}\right) \bullet \mathbf{H}_{hkl} = \left(\frac{\mathbf{a}_1}{h} - \frac{\mathbf{a}_2}{k}\right) \bullet \left(h\mathbf{b}_1 + k\mathbf{b}_2 + l\mathbf{b}_3\right) = 1 - 1 = 0,$$

$$\left(\frac{\mathbf{a}_2}{k} - \frac{\mathbf{a}_3}{l}\right) \bullet \mathbf{H}_{hkl} = \left(\frac{\mathbf{a}_2}{k} - \frac{\mathbf{a}_3}{l}\right) \bullet \left(h\mathbf{b}_1 + k\mathbf{b}_2 + l\mathbf{b}_3\right) = 1 - 1 = 0.$$

The spacing of the planes is the perpendicular distance between them. From figure 3.2, for the unit vector perpendicular to the planes (**n**), equation 3.9 can be derived.

$$d_{hkl} = \frac{|\mathbf{a}_1|}{h}\cos\phi = \frac{\mathbf{a}_1}{h} \bullet \mathbf{n} \tag{3.9}$$

$\mathbf{H}_{hkl} / |\mathbf{H}_{hkl}|$ can be used to construct **n**, since $\mathbf{H}_{hkl}$ is perpendicular to the *hkl*-planes. The spacing d_{hkl} is now given by equation 3.10.

$$d_{hkl} = \frac{a_1}{h} \bullet \frac{(h\mathbf{b}_1 + k\mathbf{b}_2 + l\mathbf{b}_3)}{|H_{hkl}|} = \frac{2\pi}{|H_{hkl}|} \tag{3.10}$$

If vectors $\mathbf{H}_{hkl}$ are drawn for all indices *hkl*, the terminal points of these vectors form the reciprocal lattice. The reciprocal vectors obtained from equation 3.4 and the crystal axes can be used to create the reciprocal lattice by repetitions of $\mathbf{b}_1$, $\mathbf{b}_2$, and $\mathbf{b}_3$.

3.3.2 Neutron and X-ray scattering

Based on the kinematic theory of diffraction the amplitude of scattering of X-rays or neutrons from a crystal, Y(**Q**), can be represented by equation 3.11 (Lovesey, 1987) (Squires, 1978).

$$Y(\mathbf{Q}) = \sum_{lk} b_k \exp[i\mathbf{Q} \cdot (r(lk) + u(lk))] \tag{3.11}$$

In equation 3.11, b_k is the atomic scattering factor (for X-ray scattering) or the nuclear scattering length (for neutron scattering) for the kth atom, **Q** is the scattering vector, r(lk) is the equilibrium position of the 1th unit cell from a fixed origin in the crystal, and u(lk) is the displacement of the atom (lk). The summation in equation 3.11 is over n atoms in the unit cell and over N unit cells in the crystal. **Q** can also be defined as in equation 3.12.

$$|\mathbf{Q}| = 4\pi\sin\theta/\lambda \tag{3.12}$$

The intensity of scattering into a unit solid angle for a unit incident intensity is known as the total scattering cross-section, $\frac{\partial\sigma}{\partial\Omega}$, and is equal to Y * Y, as shown in equation 3.13 (Squires, 1978).

$$\frac{\partial\sigma}{\partial\Omega} = \sum_{lk}\sum_{l'k'} b_k b_{k'} \exp[i\mathbf{Q}\cdot(r(lk) - r(l'k'))]\langle\exp[i\mathbf{Q}\cdot(u(lk) - u(l'k'))]\rangle \qquad (3.13)$$

The displacements u(lk) are time-dependent. The angle brackets indicate the average value over a period of time that is large, compared with the period of oscillation of an individual atom. The various scattering processes contributing to the differential cross section can be subdivided into elastic (zero order) and inelastic processes. These are processes involving the exchange of energy with the quanta of lattice vibration energy (phonons) of the crystal. The representative cross sections for zero order scattering are expressed in equation 3.14 (Lovesey, 1987) (Squires, 1978) (Willis, 1969).

$$\frac{d\sigma}{d\Omega} = \left(\frac{d\sigma}{d\Omega}\right)_0 + \left(\frac{d\sigma}{d\Omega}\right)_1 + \left(\frac{d\sigma}{d\Omega}\right)_2 + \ldots \qquad (3.14)$$

In equation 3.14, the successive terms on the right hand side represent the cross sections for elastic, one-phonon, two-phonon… etc. scattering.

To develop the expressions 3.13 and 3.14 further, the potential energy (V) of the crystals is considered. The expression is expanded as a Taylor power series in the cartesian components $u_{X1}(lk)$, $u_{X2}(lk)$, and $u_{X3}(lk)$ of the thermal displacements u(lk) of all atoms (Willis, 1969) (Willis and Pryor, 1975).

$$V = V_0 + \sum_{xlk} u_x(lk)\left[\frac{\partial V}{\partial x(lk)}\right]_0 + \sum_{xlk}\sum_{x'l'k'} u_x(lk)\,u_{x'}(l'k')\left[\frac{\partial^2 V}{\partial x(lk)\,\partial x'(l'k')}\right]_0 + \ldots \text{ higher order terms} \qquad (3.15)$$

In equation 3.15, all derivatives are evaluated at the equilibrium positions r(lk) so that the linear term vanishes (Willis, 1969).

In the harmonic approximation, assuming a crystalline material, all the higher order terms after the quadratic term in equation 3.14 are ignored. The cross section for Bragg scattering then reduces to equation 3.16 (Lovesey, 1987) (Squires, 1978) (Willis, 1969) (Willis and Pryor, 1975).

$$\left(\frac{d\sigma}{d\Omega}\right)_0 = \frac{N}{v_c}\sum_{\mathbf{B}}|F(\mathbf{B})|^2\delta(\mathbf{Q}-\mathbf{B}) \tag{3.16}$$

In equation 3.16, v_c is the unit cell volume and **B** is a reciprocal lattice vector. Equation 3.17 defines F(**B**), the structure factor for elastic scattering.

$$F(\mathbf{B}) = \sum_{k=1}^{n} b_k \exp[-W_k(\mathbf{Q})]\exp(i\mathbf{Q}\cdot r(k)) \tag{3.17}$$

In equation 3.17, r(k) is the radius vector from the origin of the unit cell of atom *k*, and $\exp[-W_k(\mathbf{Q})]$ is the Debye-Waller factor accounting for the influence of the thermal motion of the *k*th atom. The delta function $\delta(\mathbf{Q}-\mathbf{B})$ represents the condition that scattering cannot take place unless **Q** = **B**, or $2\sin\theta/\lambda = 1/d$ (the Bragg condition). The delta function is defined by the equation set 3.18.

$$\begin{aligned} &\delta(\mathbf{Q}=\mathbf{B}) = 0 \text{ for } \mathbf{Q} \neq \mathbf{B} \\ &\int\delta(\mathbf{Q}-\mathbf{B})\,dv_z = 1 \end{aligned} \tag{3.18}$$

The integration in equation 3.18 is over the Brillouin zone associated with **B**, and v_z is the volume of the reciprocal unit cell.

Within the harmonic approximation, the exponent of the Debye-Waller factor is given by the equation set 3.19 (Squires, 1978) (Willis, 1969).

$$W_k = \frac{1}{2}\left\langle [\mathbf{Q} \cdot u(lk)]^2 \right\rangle = \frac{1}{2}\mathbf{Q}^2 \left\langle u^2 \right\rangle_{\mathbf{Q}} \tag{3.19}$$

In equation 3.19, $\left\langle u^2 \right\rangle_{\mathbf{Q}}$ is the mean square amplitude of vibration along **Q**, which can be expressed as a symmetrical tensor with a maximum number of six independent components. The number of independent variables needed to describe the thermal motion of an atom depends on the symmetry around that atom. In the simple case of isotropic thermal motion W_k can be written as in equation 3.20.

$$W_k = B_k \sin^2 \theta / \lambda^2 \tag{3.20}$$

In equation 3.20, the isotropic B-factor or temperature-factor (B_k, also known as the atomic displacement parameter) of the *k*th atom is given in equation 3.21.

$$B_k = 8\pi^2 \left\langle u^2(lk) \right\rangle \tag{3.21}$$

The measurement of temperature-factors is important in the study of disordered structures. The contribution of an individual mode of vibration (*j***q**) of a cubic crystal to the mean square displacement $\left\langle u^2(lk) \right\rangle$ in any direction is proportional to equation 3.22 (Squires, 1978) (Willis, 1969).

$$\frac{E_{j(\mathbf{q})}}{\omega_j^2(\mathbf{q})} \tag{3.22}$$

At high temperatures the mode energy $E_{j(\mathbf{q})} = k_B T$, where k_B is Boltzmann's constant and T is the absolute temperature. Provided the frequencies $\omega_j(\mathbf{q})$ are temperature independent, W_k is proportional to the absolute temperature.

The inelastic coherent first-order scattering is governed by the momentum conservation rule, equation 3.23 (Lovesey, 1987) (Squires, 1978) (Willis, 1969).

$$\boldsymbol{k} - \boldsymbol{k}_0 = \mathbf{B} \pm \mathbf{q} \tag{3.23}$$

The sector of equation 3.23 that is zero-order elastic scattering (Bragg scattering) is known as the Laue equation. As $\mathbf{Q} = \boldsymbol{k} - \boldsymbol{k}_0$, by the energy conservation rule equation 3.24 can be extracted from equation 3.23.

$$\frac{\hbar^2}{2\mathrm{m}}\left(\boldsymbol{k}^2 - \boldsymbol{k}_0^2\right) = \pm\hbar\omega_j(\mathbf{q}) \tag{3.24}$$

The minus sign in equation 3.24 corresponds to a phonon absorption process in which the neutron gains energy, while the positive sign corresponds to a phonon emission process in which a neutron loses energy. Because the energy of thermal neutron is comparable with phonon energies, equation 3.23 forms a scattering surface in reciprocal space where this equation is satisfied. The scattering surface is different for phonon absorption and phonon emission and each branch *j* of the phonon dispersion curves can have its own distinct pair of scattering surfaces.

The Ewald sphere (Ewald, 1913) allows for a simple construction in the reciprocal lattice of the diffracted wave vectors associated with a given direction of incidence and a given wavelength to be made (Zachariasen, 1945). The Ewald spheres shown below represent a section of reciprocal lattice with the origin at the point O. The point P is chosen so that the line PO corresponds in direction and magnitude to the incident wave vector, $\boldsymbol{k}$. Since $|\boldsymbol{k}| = |\boldsymbol{k}_0| = 1/\lambda$, it is possible to represent $\boldsymbol{k}$ as a radius vector in a Ewald sphere of radius $1/\lambda$ constructed with the point P as centre.

In the case of Bragg scattering, the vector **B** that satisfies the Laue vector equation, must have its own terminus on the Ewald sphere. It is clear that the sphere in general will not pass through any reciprocal lattice point if $\boldsymbol{k}$ is chosen entirely at random. In order to satisfy the Laue vector equation and produce diffraction maxima, it becomes necessary to adjust the wavelength, or the direction of incidence, so that one or more of the reciprocal lattice points fall on the Ewald sphere. Figure 3.3 is a reciprocal space diagram representing Bragg scattering, where $|\boldsymbol{k}| = |\boldsymbol{k}_0| = 1/\lambda$.

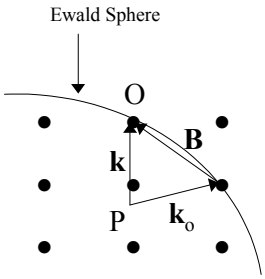

Figure 3.3: Reciprocal space diagram representing Bragg scattering.

3.3.3 Modulated crystal structures

Numerous crystal systems have been found which can be considered as perfect crystals with a periodic distortion. This distortion can be from their basic structural atomic positions (displacive modulation), such as the C_3S system, and/or of the occupation probability of atoms (density modulation).

The presence of periodic distortions is revealed in diffraction spectra by the existence of satellite reflections distributed around the main Bragg reflections. If satellite reflections are labelled with the rational indices in terms of the reciprocal lattice, L^*, of the basic structure, then distortion periods are commensurate with the translation periods of the basic structure. In this case the new lattice, L'^*, containing L^*, can be introduced. The main reflections are known as substructure reflections and the satellites as superstructure reflections. If the position of a satellite reflection varies continuously with respect to L^*, depending on the temperature, it is possible that the satellite reflections can assume non-rational indices. This indicates that the periodic distortions are incommensurable with the translation periods of the basic lattice. These are known as Incommensurately Modulated Structures (IMS).

In the case of a one-dimensionally displacively modulated structure, when the displacement vector field is a harmonic function, in a perfect crystal the *j*th atom in the unit cell is defined by the lattice vector $\mathbf{r_u} = u\mathbf{a} + v\mathbf{b} + w\mathbf{c}$. The *j*th atom is located at $\mathbf{r_{u,}}_j = \mathbf{r}_j^0 + \mathbf{r_u}$. In a harmonically modulated crystal the location of the atom can be expressed as in equation 3.25 (Giacovazzo, 2000).

$$\mathbf{r}_{\mathbf{u},j} = \mathbf{r}_j^0 + \mathbf{r}_\mathbf{u} + \mathbf{g}_j \sin\left[2\pi \boldsymbol{K} \bullet (\mathbf{r}_j^0 + \mathbf{r}_\mathbf{u}) - \phi_j\right] \tag{3.25}$$

In equation 3.25, $\mathbf{r}_j^0$ is the average position of the *j*th atom, $\mathbf{g}_j$ and ϕ_j are its displacement wave amplitude and phase respectively. $\boldsymbol{K}$ is the modulation vector expressed in reciprocal space by equation 3.26.

$$\boldsymbol{K} = k_1\boldsymbol{a}^* + k_2\boldsymbol{b}^* + k_3\boldsymbol{c}^* \tag{3.26}$$

The contribution of the *j*th atom to the structure factor can be given by equation 3.27.

$$\begin{aligned} & b_j(\mathbf{r}^*) \sum_\mathbf{u} \exp 2\pi \mathrm{i}\, \mathbf{r}^* \bullet \{\mathbf{r}_j^0 + \mathbf{r}_\mathbf{u} + \mathbf{g}_j \sin\left[2\pi \boldsymbol{K} \bullet (\mathbf{r}_j^0 + \mathbf{r}_\mathbf{u}) - \phi_j\right]\} \\ & \quad = b_j(\mathbf{r}^*) \exp(2\pi \mathrm{i}\, \mathbf{r}^* \bullet \mathbf{r}_j^0) \sum_\mathbf{u} \exp(2\pi \mathrm{i}\, \mathbf{r}^* \bullet \mathbf{r}_\mathbf{u}) \\ & \quad \times \exp\{2\pi \mathrm{i}\, \mathbf{r}^* \bullet \mathbf{g}_j \sin\left[2\pi \boldsymbol{K} \bullet (\mathbf{r}_j^0 + \mathbf{r}_\mathbf{u}) - \phi_j\right]\} \end{aligned} \tag{3.27}$$

In equation 3.27, b_j is the atomic scattering factor. The last exponential term in equation 3.27 can be re-written using the Jacobi expansion as given in equation 3.28.

$$\exp(\mathrm{i}z \sin\alpha) = \sum_{m=-\infty}^{+\infty} \exp(-\mathrm{i}m\alpha) J_{-m}(z) \tag{3.28}$$

In equation 3.28, J_m is a Bessel function of the first kind with order *m*, satisfying the condition $J_{-m}(z) = (-1)^{\mathrm{m}}\mathrm{J_m(z)}$. This reduces equation 3.28 to equation 3.29.

$$\begin{aligned} & b_j(\mathbf{r}^*) \exp(2\pi \mathrm{i}\, \mathbf{r}^* \bullet \mathbf{r}_j^0) \sum_\mathbf{u} \exp(2\pi \mathrm{i}\, \mathbf{r}^* \bullet \mathbf{r}_\mathbf{u}) \\ & \quad \times \sum_m \exp\{\mathrm{i}m(\phi_j - 2\pi \boldsymbol{K} \bullet (\mathbf{r}_j^0 + \mathbf{r}_\mathbf{u})]\} J_{-m}(2\pi\, \mathbf{r}^* \bullet \mathbf{g}_j) \\ & \quad = b_j(\mathbf{r}^*) \exp(2\pi \mathrm{i}\, \mathbf{r}^* \bullet \mathbf{r}_j^0) \sum_m J_{-m}(2\pi\, \mathbf{r}^* \bullet \mathbf{g}_j) \\ & \quad \times \exp\{\mathrm{i}m(\phi_j - 2\pi \boldsymbol{K} \bullet \mathbf{r}_j^0)\} \sum_\mathbf{u} \exp[\, 2\pi \mathrm{i} \mathbf{r}_\mathbf{u} \bullet (\mathbf{r}^* - m\boldsymbol{K})]. \end{aligned} \tag{3.29}$$

Provided the number of cells in the crystal is large enough, the sum over **u** is equal to $(1/V)\ \delta\ (\boldsymbol{H} - \mathbf{r}^* + m\boldsymbol{K})$, where $\boldsymbol{H} = h\boldsymbol{a}^* + h\boldsymbol{b}^* + h\boldsymbol{c}^*$. Reflections occur for $\mathbf{r}^* = \boldsymbol{H}' = \boldsymbol{H} + m\boldsymbol{K}$; for $m = 0$ there exist main reflections ($\boldsymbol{H}' = \boldsymbol{H}$); for $m \neq 0$ satellites are defined.

Four indices are required for the identification of a diffraction effect. The structure factor of the reflections $\overline{\boldsymbol{H}}$' = (*h, k, l, n*) is defined in equation 3.30.

$$F_{\boldsymbol{H}'} = \sum_{j=1}^{N} b_j(\boldsymbol{H}')\exp(2\pi i\, \mathbf{r}^* \bullet \mathbf{r}_j^0) J_m(2\pi\, \boldsymbol{H}' \bullet \mathbf{g}_j)(-1)^m$$
$$\times \exp(-2\pi i \boldsymbol{K} \bullet \mathbf{r}_j^0) \exp(i m\phi_j). \qquad (3.30)$$

3.4 Powder Diffraction

Powder diffraction is a well-established laboratory tool used principally for phase identification and quantitative analysis (Klug and Alexander, 1974). In the powder diffraction method, the crystal to be examined is reduced to a powder. Each particle in the powder is a tiny crystal, or assemblage of smaller crystals, oriented at random with respect to the incident beam. Some of the crystals will be oriented so that a particular plane of the crystal will reflect the incident beam. As other crystals will reflect other planes, the result is that the mass of powder is equivalent to a single crystal being rotated, about all possible axes. Sometimes suitably large single crystals of a material cannot be obtained, however, a powder of crystals of the material can be. The powder diffraction method is obviously suited to these cases. The method is appropriate for the identification of single or multiple phases, such as in the analysis of cement materials.

Powder patterns, unlike single crystal patterns, are one-dimensional. Corrections are sometimes necessary when dealing with complex powder diffraction patterns. Each Bragg reflection in a powder pattern is defined by a single angle and its intensity. Despite their single dimensional quality, powder patterns provide excellent fingerprints for crystalline substances as each diffraction pattern depends on the cell dimensions, symmetry, and reflection intensity defined by atomic positions.

Instrument configuration is an important consideration in powder patterns. There are two main common experimental configurations. Bragg-Brentano configuration features a flat specimen moving in a θ to 2θ relationship with the counter. Debye-Scherrer configuration features a cylindrical sample is bathed in the radiation beam.

There are several factors affecting the relative intensity of the reflections in a powder pattern. These are the polarisation, structure, multiplicity, Lorentz, absorption, and temperature factors. Preferred orientation may also affect the reflection intensities.

The reflection peak profile is dependent on the characteristics of the instrument used and structural imperfections in the sample. Instrumental peak profiles arise from the distribution of wavelength in the incident beam, convoluted with several functions to compensate for instrument geometry including source size, beam divergence, slit width, and residual misalignment. The profiles vary continuously with $\sin\theta/\lambda$. For Bragg-Brentano configurations, peak profiles are approximately 50 % Gaussian and 50 Lorentzian at low angles.

The angle dependant corrections for powder diffraction include the Lorentz factor, for neutrons and X-rays, and the polarisation factor, for X-rays only. The polarisation factor, P, arises if the incident beam is unpolarised. It is common to all intensity calculations and is given in equation 3.31.

$$P = (1 + \cos^2(2\theta)) / 2 \tag{3.31}$$

The Lorentz factor is given in equation 3.32.

$$L = [P + (1-P)\cos^2\theta] / [2\sin^2\theta \cos\theta] \tag{3.32}$$

The amount of polarisation (polarisation fraction) in a beam has been shown to vary between radiation sources (Giacovazzo *et al*, 2000 p.240). CuKα laboratory X-rays are typically unpolarised and synchrotron X-rays are almost completely polarised.

The reflection multiplicity is determined for the space group of the crystal. The resultant wave scattered by all the atoms in a unit cell is called the structure factor, F. F describes how the atomic arrangement, given by *uvw* for each atom, affects the scattered beam. Equation 3.33 shows the structure factor for the *hkl* reflection, which is a very important relation in crystallography as it allows calculation of the intensity of any *hkl* reflection from a knowledge of atomic positions.

$$F_{hkl} = \sum_{1}^{N} f_n e^{2\pi i(hu_n + kv_n + lw_n)} \tag{3.33}$$

The summation in equation 3.33 extends over all N atoms of the unit cell. The intensity of the beam diffracted by all the atoms in the unit cell, in all directions predicted by the Bragg law, is proportional to the square of the amplitude of the resultant beam ($|F|^2$). $|F|^2$ is obtained by multiplying equation 3.33 by its complex conjugate.

Absorption involves the removal of radiation by the sample. The absorption factor is affected by the shape and size of the specimen and the experimental configuration. Each configuration requires a different mathematical correction for absorption. Equation 3.34 (Sabine *et al*, 1998) can be used to compensate for absorption in cylindrical samples.

$$A_k = A_B(\mu R)\cos^2\theta_k + A_L(\mu R)\sin^2\theta_k \tag{3.34}$$

In equation 3.34, The absorption, A_k, is calculated from the Bragg and Laue absorption terms, A_B and A_L, where R is the radius of the cylindrical sample, and μ is the linear absorption coefficient. For a flat plate system the absorption can be corrected using equation 3.35 (Hermann and Ermrich, 1987).

$$A_k = (1 - P_0 - P_s(\theta)) = 1 - P_0(1 + \alpha_0(\tau/\sin(\theta) (1 - \tau /\sin(\theta)) -1)) \tag{3.35}$$

In equation 3.35, τ describes the surface roughness, α_0 is the packing fraction of the bulk material, and P_0 and P_s describe the absorption correction caused by bulk porosity and surface roughness, respectively.

Preferred orientation arises when there is a stronger tendency for the crystallites in a specimen to be oriented more one way, or one set of ways, than for others. An analysis with neutrons usually involves using larger specimens, a larger fraction of the diffracting crystallites are farther from the bounding surfaces and their orientations are therefore less influenced by those surfaces. Consequently, preferred orientation is less problematic in neutron than in X-ray Powder Diffraction (XRPD).

Complex patterns arise from multiple Bragg reflections contributing to a single observed peak. The observed intensity, $y(2\theta)_j$, at some point $2\theta_j$ in a powder diffraction pattern is the sum of the contributions from all the neighbouring reflections, $h_j(2\theta)$, plus the background, $b(2\theta_j)$, at that point. The observed intensity is expressed mathematically in equation 3.36.

$$y(2\theta)_j = \sum h_j(2\theta_j) + b(2\theta_j) \tag{3.36}$$

3.5 Radiation sources

Ideally, the type of information that needs to be extracted should dictate the type of radiation that is used in a powder experiment. Intense international competition for beam time at some facilities results in higher experimental cost at these facilities. Consequently, some facilities can be difficult to access, although they may be the best solution experimentally.

The three radiation sources used in the investigations of this thesis are outlined in sections that follow. These sources are laboratory X-ray, synchrotron, and neutron sources.

3.5.1 Laboratory X-ray sources

Scattering of X-rays occurs primarily due to interaction with the electrons that surround the atomic nucleus, giving the positions of electron density. The strength of a scattered X-ray depends on the number of electrons surrounding the atomic nucleus and consequently is a function of atomic number (Z). Interference in this scattering type takes place between X-rays from different parts of an atom.

X-ray scattering lengths increase with Z, are dependent on the number of electrons in an atom, and decrease with $\sin\theta/\lambda$. The value of the scattering factor at $\sin\theta/\lambda = 0$ is the value of Z for neutral atoms.

The most widely used source of radiation is the conventional sealed X-ray tube, primarily due to its low cost relative to other sources. The wavelength choice depends on the reciprocal space range targeted and the sample composition. Commonly Cu is used as a source resulting in CuKα and CuKβ radiation. This radiation can cause X-ray diffraction patterns to be complicated by the presence of paired α-β lines with Lorentzian components.

3.5.2 Synchrotron sources

Synchrotron radiation is produced from charged particles, in particular electrons or positrons. When these particles are forced to move in a circular orbit, they emit photons. At relativistic velocities when the particles are moving at close to the speed of light these photons are emitted in a narrow cone in the forward direction, at a tangent to the orbit. In a high-energy electron or positron storage ring these photons are emitted with energies ranging from infra-red to energetic (short wavelength) X-rays.

Synchrotron radiation has a number of unique properties including high brightness with extremely intense radiation, hundreds of thousands of times higher than conventional X-ray tubes. The radiation is highly collimated, covering a broad energy spectrum with a wide range of energies, allowing a beam of any energy to be produced. The radiation is also highly polarised.

Typically, synchrotron facilities have access programs for international users and research organisations can fund an instrument in exchange for beam time. There are several synchrotron facilities available to Australian users; the two used in the investigations presented in this thesis are outlined.

The Australian National Beamline Facility (ANBF) is a multi-capability hard X-ray beam line installed at the 2.5 GeV Photon Factory, a second-generation synchrotron light source (ANBF website). The ANBF is located at the High-Energy Accelerator Research Organisation (KEK) in Tsukuba Science City in Japan.

The ANBF is installed on a bending magnet port, beam line 20B, at the Photon Factory. It delivers monochromatic synchrotron X-rays in the energy range 4.5-20 keV to two

experimental stations in a single hutch. The primary instrument is a multi-configuration vacuum diffractometer that uses image plates as its primary detector system. The diffractometer, when configured as an X-ray camera in Debye-Scherrer geometry, is capable of high-resolution powder diffraction including time resolved powder diffraction.

The National Synchrotron Light Source (NSLS) at Brookhaven National Laboratory (BNL) in New York, USA is a US national user research facility. The NSLS operates two electron storage rings including an X-ray ring. X7A is a beam line developed for powder diffraction experiments at the NSLS, offering hard X-rays at the energy range 5-45 keV (X7A website).

The X7A beam line is equipped with a standard four-circle Huber diffractometer and a channel-cut double-crystal monochromator for experiments in the vertical scattering plane. Because the diffractometer is mounted on a horizontal arm, which can be moved on airpads, horizontal scattering angles of up to 25° are possible. The wavelength range is 0.7-2.0 Å, however, experiments down to 0.5 Å are feasible when a linear Position Sensitive Detector (PSD) is used. The best instrumental resolution is obtained if a crystal-analyser is mounted in the diffracted beam (~ 0.01°), see figure 3.4, but much faster counting rates can be obtained with the linear PSD with more modest resolution (~ 0.03°).

A furnace for temperature dependence studies in the range of 10-900 K is also available for use on beam line X7A.

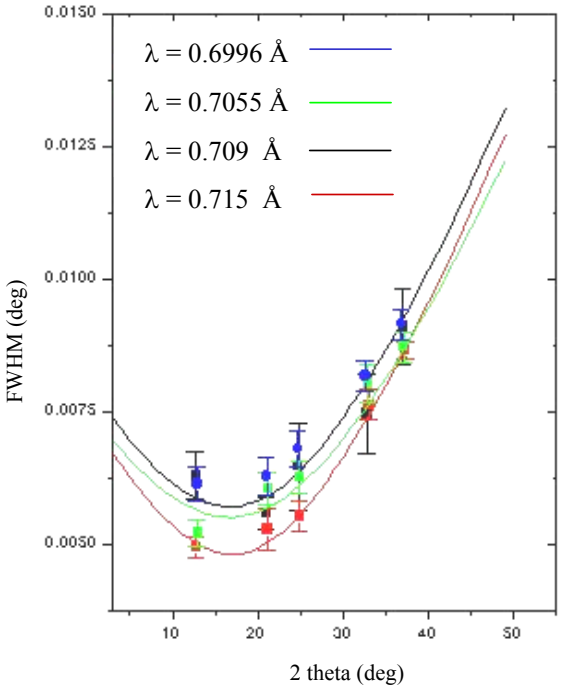

Figure 3.4: X7A resolution function using Si(111) / Ge(220) double crystal monochromator and analyser (X7A external website).

3.5.3 Neutron sources

Neutron methods of analysis, although similar to, have several advantages over X-ray methods. Neutrons are strongly penetrating and are scattered weakly or absorbed by most materials. The 1/e penetration depth for neutrons from dry cement is about 3 cm, compared to 30 μm using Cu Kα X-rays (Berliner *et al*, 1997). A larger sample can therefore be used for analysis by neutrons than for X-rays, providing a more representative sample for heterogeneous systems such as cement. Consequently, uniform particle size is less important for neutron analysis of larger samples.

Neutron scattering details are dependent on nuclear isotope configuration, as the scattering process involves an interaction between the nucleus itself and the neutron.

Scattering lengths are a function of nuclear parameters and vary significantly across the periodic table, while remaining constant with $\sin\theta/\lambda$. As a result, neutrons are better suited to the study of systems containing lighter elements (lower Z). This phenomena is of particular use for the oxygen atom, where neutron diffraction data is much more sensitive to oxygen atom than X-ray data. This is useful for the study of materials in which the atomic positions of oxygen is important, such as tricalcium silicate. Scattering of X-rays and neutrons is compared in figure 3.5.

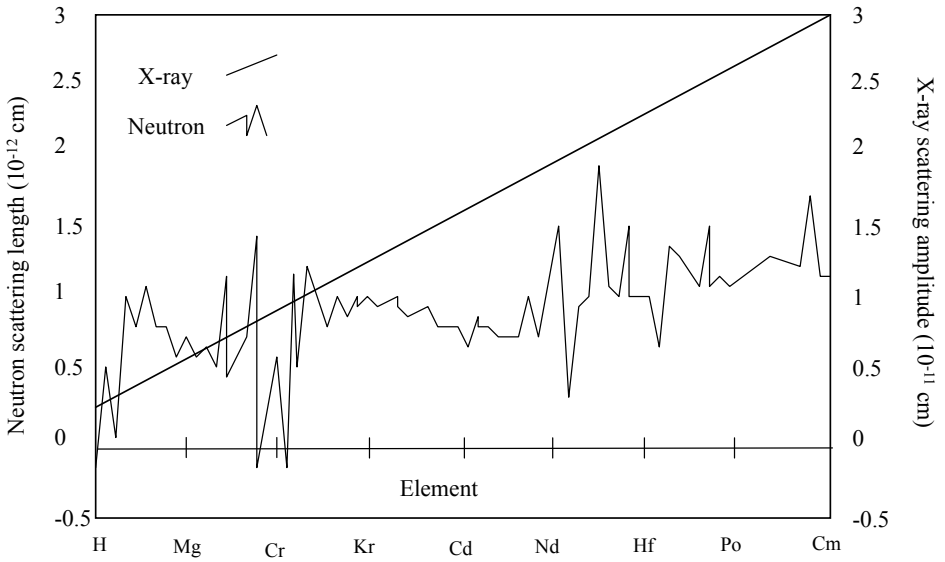

Figure 3.5: X-ray and neutron nuclear scattering amplitudes.

As neutrons are primarily scattered by atomic nuclei, there is only isotropic point scattering. Nuclear scattering is also a combination of scattering by short-range nuclear forces and resonance scattering, resulting in neutron scattering lengths that vary erratically across the periodic table and between isotopes. Thus the nuclear (atomic) scattering factors for thermal neutrons are effectively constants, and the form factor for neutrons is constant as a function of scattering angle. This results in diffraction at large scattering angles providing important data. It is customary to use b_j to represent the scattering length of neutrons, and f_j as scattering length of X-rays. The b_j values exhibit a few differences from f_j values. Isotopes of the same element generally have differing b_j values, b_j values can be negative indicating a 180 ° phase shift on scattering, and there is no regular progression of b_j with Z.

A monochromatic neutron beam for a powder diffraction experiment forms a simple Gaussian line-shape, suitable for profile fitting techniques such as Rietveld analysis. Neutron diffraction is also less susceptible to aberrations such as extinction, micro-absorption, and preferred orientation.

As with synchrotron facilities, neutron facilities also have access programs for users. Similarly, a research group can fund an instrument in exchange for beam time. There are several neutron facilities available to Australian users and the one used in this study is outlined below. Additional to the reactor sources are neutron spallation sources. Despite their applicability to the analysis of complex materials such as cement, high demand of these sources such as at the ISIS facility (ISIS website) restrict their use in many cases.

The High-Flux Australian Reactor (HIFAR) at the Australian Science and Nuclear Technology Organisation (ANSTO) is the only nuclear reactor in Australia. The High Resolution Powder Diffractometer (HRPD) on the HIFAR is suited for the study of standard crystallographic problems (ANSTO website). It is capable of collecting powder diffraction patterns over the angular range 5-155°, at a variety of wavelengths. The features used in the investigations of this thesis are listed in table 3.1. Currently the instrument uses 24 ^{3}He detectors each separated by 5°. This allows a typical pattern to be collected in 12-24 hours, although for complex patterns longer times are sometimes required.

Table 3.1: Summary of the High Resolution Powder Diffractometer (ANSTO website).

Take off Angle	120^{o}	
Ge[hkl]	Wavelength (Å)	Relative Intensity
335	1.49	0.9
115	1.88	1.0
Pyrolytic Graphite Filter	Eliminates l /2 at 2.25 and 2.96 Å	
Be filter	Eliminates l < 4Å in 5.66 Å beam	
Beam Size	20 mm x 50 mm	
Flux at the sample	8×10^{4} n.cm^{-2}.s^{-1}	
Background (no sample)	0.1 Hz	
Gaussian Peak: U,V,W (º)	0.07, -0.15, 0.14	
P1750 Furnace	400-2000.K	

3.6 Rietveld Analysis

The Rietveld method of powder diffraction analysis was developed in the mid-1960s by H. M. Rietveld (Rietveld, 1967). The method was unique as it combined the steps of extracting the integrated intensities and then solving and/or refining the crystal structure by a single least squares process. This allowed dynamic interplay between the extraction of the overlapping reflection intensities and the structure refinement during each cycle of the least squares. This led to more accurate partitioning of the overlapping reflection groups during the next cycle of refinement.

A diffraction profile can be calculated as the sum of all the Gaussian peaks, and then fitted to the measured profile by non-linear least-squares refinement of the various parameters embedded in the Rietveld equation. The Rietveld method can be used with any powder diffractometer method, and in fixed wavelength or fixed angle mode. It can also be used in conjunction with Fourier techniques to assist in the ab-initio solution of crystal structures from powder diffraction data.

In the Rietveld method the least squares refinements are carried out until the best fit is obtained between the entire observed powder diffraction pattern, taken as a whole, and the entire calculated pattern. The fit is based on the simultaneously refined models for crystal structure(s), diffraction optics effects, instrumental factors, and specimen characteristics.

Rietveld (1967) first described a computer program for the implementation of the Rietveld method (Rietveld, 1969) and this program was written for the analysis of neutron diffraction data from fixed-wavelength diffractometers. Hewat (1973) further developed the program and Von Dreele *et al* (1982) extended the program to the refinement of patterns recorded with time of flight diffractometers. The first applications of Rietveld analysis to XRD data were reported by Malmros and Thomas (1977) and Khattak and Cox (1977). The program was modified to allow the refinement of crystal structures with sophisticated constraints by Pawley *et al* (1977) and Baerlocher (1993).

3.6.1 Core mathematics in Rietveld refinement

The basis of the Rietveld method is given in equation 3.37. Typically, multiple Bragg reflections contribute to the intensity observed at point i in the pattern. Equation 3.42 relates the net intensity calculated at i (y_{ic}) to the background intensity (y_{ib}), a normalised peak profile function (G_{ik}), and the intensity of the kth Bragg reflection (I_k) (Hunter and Howard, 2000).

$$y_{ic} = y_{ib} + \sum_{p} \sum_{k=k_1^p}^{k_2^p} G_{ik}^p I_k \tag{3.37}$$

In equation 3.37, $k_1 \ldots k_2$ are the reflections contributing intensity to the point i and the subscript p denotes possible phases present in the sample. I_k can be calculated, in equation 3.38, from the scale factor (S), the multiplicity (M_k), the Lorentz-polarisation factor (L_k), and the structure factor (F_k). Equation 3.38 incorporates the corrections A_k, the absorption factor that corrects for absorption, an extinction factor (E_k), and a preferred orientation factor (P_k) that corrects for powders affected by preferred orientation. For powders unaffected by preferred orientation $P_k = 1$.

$$I_k = SM_k L_k \left|F_k\right|^2 P_k A_k E_k \tag{3.38}$$

F_k can be calculated using equation 3.39 using the scattering factor of atom j and from the matrices $\mathbf{h}_k$, $\mathbf{r}_j$, and $\mathbf{B}_j$, that represent respectively the Miller indices, atomic coordinates, and anisotropic thermal vibration parameters. The scattering factor is represented as b_j for neutrons, f_j for X-rays. The superscipt t indicates matrix transposition.

$$F_k = \sum_{j=1}^{n} b_j \exp\left[2\pi i\left(\mathbf{h}_r^t \mathbf{r}_j - \mathbf{h}_k^t \mathbf{B}_j \mathbf{h}_k\right)\right] \tag{3.39}$$

The positions of the Bragg reflections from each phase are determined by their respective set of cell dimensions, in conjunction with a zero parameter and the wavelength or diffractometer constants provided. The wavelength or diffractometer

constant is refinable, with the condition that all of the cell dimensions are fixed to avoid divergences in the least squares procedure. If more than one wavelength is used in a histogram, such as $K\alpha^1$ and $K\alpha^2$, the second wavelength can be fixed to the first so that λ_1/λ_2 is constant. The ratio of the intensities for two possible wavelengths is absorbed into the calculation of $|F|^2$ so that only a single scale factor for each phase is required. This ratio is not a refinable parameter.

The least-squares procedure can use the Newton-Raphson algorithm to minimise the quantity, as in equation 3.40.

$$R = \sum_i w_i (y_{io} - y_{ic})^2 \tag{3.40}$$

In equation 3.40, y_{io} is the set of observed diffraction intensities collected at each step, y_{ic} is the set of corresponding calculated values, and w_i is the weight assigned to each observation. The minimisation of R is taken over all data points and the background. If x_m are adjustable parameters in the model, the elements of the normal equations matrix are given by equation 3.41.

$$M_{mn} = -\sum w_i \left[(y_{io} - y_{ic}) \frac{\partial^2 y_{ic}}{\partial x_m \partial x_n} - \frac{\partial y_{ic}}{\partial x_m} \frac{\partial y_{ic}}{\partial x_n} \right] \tag{3.41}$$

The shifts in the adjustable parameters, Δx_m, which best reduce the residual are given in equation 3.42.

$$\Delta x_m = -\frac{1}{2} \sum_n M_{mn}^{-1} \frac{\partial R}{\partial x_n} \tag{3.42}$$

The Marquardt algorithm can be used in addition to the least squares procedure algorithm to stabilise the model during the residual minimisation process. The algorithm adjusts the diagonal matrix elements of M to $M_{ii} = M_{ii} (1 + \varepsilon)$, where ε is the Marquardt parameter with a typical value in the range 1.0-0.0001. The estimated standard deviations of the parameters (σ_m) are calculated from the expression in equation 3.43.

$$\sigma_m = \left[M_{mm}^{-1} \frac{\sum_{i=1}^{N} w_i \left(y_{io} - y_{ic}\right)^2}{N - P} \right]^{1/2} \tag{3.43}$$

In equation 3.43, M_{mm}^{-1} is the diagonal element of the inverse matrix, N is the number of observations, and P is the number of adjustable parameters.

Figures Of Merit (FOM) are quoted once the analysis is complete, to give an indication of the closeness of the model to the sample. Three factors are typically used to assess agreement between the observations and the model. These factors are the R-pattern (R_p) given in equation 3.49, the goodness of fit (χ^2) given in equation 3.44, and the R-Bragg factor (R_B) given in equation 3.45 (Young, 1996).

$$R_p = \frac{\sum \left| y_{io} - y_{ic} \right|}{\sum y_{io}} \tag{3.44}$$

$$\chi^2 = \frac{\sum w_i \left(y_{io} - y_{ic}\right)^2}{N - P} \tag{3.45}$$

$$R_B = \frac{\sum \left| I_{ko} - I_{kc} \right|}{\sum I_{ko}} \tag{3.46}$$

In equation 3.45, χ^2 is related to the two other FOM factors, the expected R-factor (R_{exp}) and the weighted profile-factor (R_{wp}), by the expression $\chi^2 = [R_{wp}/R_{exp}]^2$. In equation 3.46, I_{ko} is the observed integrated intensity of reflection k, calculated at the end of refinement, after allocation of each y_{io} to contributing peaks and background according to the calculated intensities, I_{kc}.

Thermal atomic motion can be modelled in a Rietveld refinement. Thermal motion can be divided into isotropic thermal motion, where the thermal motion of the atom has spherical symmetry, and anisotropic thermal motion, usually representing motion with

non uniform vibrational distance (Giacovazzo *et al*, 2000). In Rietveld refinement models, the thermal motion of atom j can be described by the atomic temperature factor, B_j, which is effectively the Debye-Waller factor. B_j is given in equations 3.47 and 3.48 (Hunter and Howard, 2000).

$$B_j = \exp[-(\beta_{11}h^2 + \beta_{22}k^2 + \beta_{33}l^2 + 2\beta_{12}hk + 2\beta_{23}kl)] \quad (3.47)$$

$$B_j = \exp\left(-B_{iso}(\mathbf{Q}/4\pi)^2\right) \quad (3.48)$$

In equation 3.47, $\beta_{11}\ldots\beta_{23}$ are the anisotropic thermal parameters for atom j. Equation 3.48 gives the calculation using isotropic thermal parameters. Thermal displacements can also be calculated in terms of real space displacement, in Å^2. B_j is also described by equations 3.49 and 3.50, using u for anisotropic motion and U_{iso} for isotropic motion, respectively.

$$B_j = \exp[-2\pi^2(a^{*2}\langle u_{11}\rangle h^2 + b^{*2}\langle u_{22}\rangle k^2 + c^{*2}\langle u_{33}\rangle l^2 + a^*b^*\langle u_{12}\rangle hk + a^*c^*\langle u_{13}\rangle hl + b^*c^*\langle u_{23}\rangle kl)] \quad (3.49)$$

$$B_j = \exp\left(-\frac{1}{2}\langle U_{iso}\rangle \mathbf{Q}^2\right) \quad (3.50)$$

Comment [v1]:
Comment [v2]:
Comment [v3]:
Comment [v4]:
Comment [v5]:
Comment [v6]:

Quantitative phase analysis can be performed on multi-phase samples as described by Hill and Howard (1987). The scattering cross-section for Bragg scattering is proportional to N/V, where N is the number of unit cells contributing to the scattering and V is the unit cell volume. The scale factor, S, is proportional to N/V as shown in equation 3.51.

$$W_p = \frac{(SZMV)_p}{\sum_i (SZMV)_i} \quad (3.51)$$

In equation 3.51, the weight fraction of phase p, W_p, is related to N/V by the number of formula units per unit cell, *Z*, the molecular weight of the formula unit, M, and S. Hence, equation 3.51 provides relative concentrations for the identified phases.

Various peak shape functions are available depending on the Rietveld program being used. A variety of corrections, quantitative phase analysis calculations, and thermal parameter calculations are also available. For angle dispersive data, the dependence of the breadth, H, of the reflection profiles measured as the Full Width at Half Maximum (FWHM), has typically been modelled using equation 3.52 (Caglioti *et al,* 1958).

$$H^2 = U \tan^2 \theta + V \tan \theta + W \tag{3.52}$$

In equation 3.52, U, V and W are refinable parameters. More recently, analytical profile functions such as the pseudo-Voigt function have been available. The pseudo-Voigt function is given by the numerical convolution of a Lorentzian component, given in equation 3.53, and a Gaussian component, given in equation 3.54.

$$(C_1^{1/2} / H_k \pi) 1 / [1 + C_1(2\theta_i - 2\theta_{hkl})^2 / H_k^2] \tag{3.53}$$

$$(C_0^{1/2} / H_k \pi^{1/2}) \exp(-C_0(2\theta_i - 2\theta_k)^2 / H_k^2] \tag{3.54}$$

In equations 3.53 and 3.54, $C_0 = 4\ln 2$ and $C_1 = 4$. H_k is the FWHM of the k^{th} Bragg reflection. The peak shape, G_{ik}, is described as a pseudo-Voigt function in equation 3.55, commonly used to model XRD peak shapes.

$$G_{ik} = \gamma \frac{C_0^{1/2}}{H_k \pi} \left[1 + C_0 X_{ik}^2 \right]^{-1} + (1 + \gamma) \frac{C_1^{1/2}}{H_k \pi^{1/2}} \exp\left[- C_1 X_{ik}^2 \right] \tag{3.55}$$

In equation 3.55, $C_0 = 4$, $C_1 = 4\ln 2$, $X_{ik} = (2\theta_I - 2\theta_k)/H_k$, and γ is a refinable mixing parameter.

The Voigt function is a complex convolution of the Gaussian and Lorentzian peak shapes. Equation 3.56 represents G_{ik} as a Voigt function, commonly used to model neutron diffraction peak shapes.

$$G_{ik} = \frac{C_0^{1/2}}{H_{Gk} \pi^{1/2}} \mathrm{Re}\left[\omega \left(C_1^{1/2} X_{ik} + i C_3 \frac{H_{Lk}}{H_{Gk}} \right) \right] \tag{3.56}$$

In equation 3.56, $C_1 = 2\ln 2$, $C_3 = (\ln 2)^{1/2}$, H_{Gk} is the FWHM of the Gaussian component, H_{Lk} is the FWHM of the Lorentzian component, ω is the error function $\omega(z) = \exp(z^2)$, and Re denotes its real part.

In the cases of the pseudo-Voigt and Voigt profile functions, an asymmetry correction may also be applied in the form of a sum of five pseudo-Voigt or Voigt peaks. Howard (1982) demonstrated that this method is more physically appropriate for neutron fixed wavelength powder diffraction. Finger *et al* (1994) devised an asymmetry function that is useful for cases where instrumental asymmetry causes problems with the Howard (1982) recommended method. The Finger *et al* (1994) asymmetry is defined by the two parameters S/L and D/L, where S/L is the source size to sample-detector distance ratio and D/L is the detector size to sample-detector distance ratio.

The background, y_{ib}, can be modelled by refinement using a type I or II Chebyshev polynomial function (shifted or non-shifted), as in equation 3.57.

$$y_{ib} = \sum_{m=0}^{n} B_m T_m(2\theta) \qquad (3.57)$$

In equation 3.57, B_m are refinable parameters and T_m is the Chebychev function. This function is defined in equation 3.58.

$$T_{n+1}(x) - 2xT_n(x) + T_{n-1}(x) = 0 \qquad (3.58)$$

In equation 3.58, $T_0 = 1$ and $T_1 = x$ for a Chebychev type I non-shifted function. The number of background terms, n, used in the series calculations can be increased to accommodate complex backgrounds such as an amorphous background from a capillary tube.

Preferred orientation produces systematic distortions of the reflection intensities that corrections can be made for. The distortions can be modelled with the March-Dollase preferred orientation function (Dollase, 1986). Modelling of the preferred orientation effects can be incorporated by expanding the orientation distribution in spherical harmonics (Ahtee *et al,* 1989). The intensity I_k of the Bragg peaks can be modified

during refinement to allow for preferred orientation due to the presence of plate-like crystals, such as present in the β C_2S phase of cement clinker, using the March-Dollase function given in equation 3.59.

$$P_k = [P1^2\cos^2\alpha_k + P1^{-1}\sin^2\alpha_k]^{-3/2} \quad (3.59)$$

In equation 3.59, P1 is a refinable parameter, and α_k is the acute angle between the scattering vector and the normal to the crystallites, as calculated from the Miller index of the crystal platelet face. For symmetries lower than tetragonal P_k is not required. For higher symmetries P_k is calculated as a sum over all equivalent reflections, as the angle α_k can differ for each equivalent reflection.

As with any minimisation program, the Rietveld method is prone to false minima. Care must be taken to regularly check that refinement parameters are within acceptable and real limits. Additionally, large correlations can also develop between correlations. This is usually a symptom of a poor choice of adjustable parameters, where parameter changes may have similar effects on the calculated intensities. A correlation matrix is provided with the refinement output of most Rietveld programs, and this should be checked regularly for any unexpected or high correlations.

3.6.2 Combined X-ray and neutron Rietveld refinement

The complex nature of structure factors and the directional character of reciprocal space are lost in a powder diffraction experiment. The certainty of uniqueness of a result is thus smaller for the Rietveld refinement of a single powder pattern, than for the result of a single crystal refinement. A possible solution to this problem is suggested by the fact that X-rays and neutrons are scattered by different mechanisms.

Rietveld structure refinements done with X-ray and neutron data have complimentary relationships. The only significant difference arises in the scattering factors, obtained from using different sources. The scattering factor has the form of the Fourier transform (Guinier, 1963) of the distribution of scattering density, equal to the density of the scattering material times its scattering power. The Fourier transform of the more compact region of the scattering of neutrons does not fall off significantly over the

normal range of observation. Consequently, X-ray and neutron powder diffraction patterns are very different. The practical application of Rietveld method using neutron data is heavily reliant on the differences between the two scattering phenomena.

A crystal structure model that leads to calculated patterns matching both neutron and X-ray patterns is more likely to be unique and correct than that from a single pattern refinement (Young, 1996). Similarly, a structure model that matches all of the powder patterns from a multi-wavelength synchrotron X-ray experiment is more likely to be correct because the model has to match the wavelength-dependant differences in the scattering factors for the constituent atoms.

3.6.3 Rietveld refinement programs Rietica, GSAS, and JANA

There are many programs available for the Rietveld analysis of diffraction data. The three used in the investigations presented in this thesis are outlined.

Rietica (Hunter, 1999) is a Rietveld structure refinement program featuring a Windows front end to the program known as LHPM. LHPM is a computer program for Rietveld analysis of X-ray, neutron and synchrotron powder diffraction patterns. LHPM is a modified version of another Rietveld program for the analysis of X-ray or neutron diffraction patterns recorded with fixed-wavelength diffractometers (Wiles and Young, 1981). This earlier program allowed the structure refinement of two phases simultaneously, accommodated data recorded at one or two wavelengths, and offered a choice of four peak shape functions. The background could be prescribed or refined, and tables of X-ray scattering factors and neutron nuclear scattering lengths were included. Symmetry operators from standard space-group symbols were also calculated. The first version, DBW2.9 written in Fortran IV, was soon upgraded to version DBW3.2 and written in Fortran 77. LHPM5 was developed from DBW3.2.

Apart from the complete functionality of the LHPM program, the features of Rietica features include:

- Pattern plotting, monitoring of parameter changes and FOM at each refinement cycle.
- Manual editing of the input file with visual plotting and parameter monitoring.

- Macro language for complex batch processing and programming.
- Integrated Fourier plotting.
- Background and excluded region input via mouse control.
- Viewing of the bond distance and angle, bond valence, and summary output files.
- Simple database for storage and retrieval of instrumental parameters and structural data.

The General Structure Analysis System, GSAS, (Larson and Von Dreele, 2000) is a set of programs for the processing and analysis of both single crystal and powder diffraction data obtained with X-rays or neutrons. GSAS is written primarily in FORTRAN. The kit for each computing platform consists of a large compressed binary format file and some smaller files in uncompressed form. EXPGUI (Toby, 2001) is a Graphical User Interface (GUI) editor for GSAS experiment files and shell.

GSAS allows soft bond and angle constraints for structures, as well as rigid body constraints. In many structures, groups of atoms (molecules or coordination polyhedra) have an established structure and are not completely independent. Such groups can form relatively rigid units. Rigid bodies are valuable when the quality of the data is low, the ratio of observations to parameters is low, and/or the structure is very complicated. GSAS allows their incorporation into the analysis of powder diffraction data. Dinnebier (1999) illustrated the use of GSAS for rigid body constraints. It is often impossible to refine individual atomic positions if disorder occurs. By using rigid bodies it may be possible to model disorder in the case of powder data. The advantages which led to the introduction of rigid bodies in single crystal analysis are even more valid for powder data. Interestingly, very little has been done so far in this field and only a few Rietveld refinement programs offer a rigid body option.

JANA2000 (Petricek and Dusek, 2000) is a system for solving and refinement of regular, modulated, and composite structures from single crystal and powder diffraction data. JANA2000 was developed with the Lahey Fortran 95 compiler. JANA 2000 integrates all the usual tasks of the structure analysis except a plotting program and direct methods.

Features of JANA2000 include:

- Works with both single crystal and powder data, as well as X-ray and neutron data.
- Ordinary, modulated, and composite structures can be analysed.
- Reads output from many diffractometer types and can merge data sets from various sources.
- Works with various types of twinned crystals and overlapped reflections.
- Has support for the modelling of commensurate structures and anharmonic displacement parameters.
- Enables f' and f'' refinement. Enables special modulation functions.
- Calculates and plots x4 and t contour maps for modulated structures.
- Calculates and plots (joint) probability density functions.
- Calculates and plots various parameters like a function of t.

3.6.4 Pattern decomposition analysis

Pattern decomposition analysis, or the decomposition method, was first proposed by Pawley and is known as the Pawley extraction method (Pawley, 1981). The method aimed at the refinement of cell parameters from the whole pattern, however, the possibility to use the extracted intensities as the starting point for the application of direct methods was offered. In a similar way to the spread of the Rietveld method, the Pawley method was not recognised as a revolution for a long time. The Pawley method uses analytical profiles, whose widths are constrained to follow a Caglioti law. The main difference between the Pawley and Rietveld methods is that the intensities are considered as refinable parameters in the latter. Slack constraints were introduced in the Pawley method for stabilisation of the intensities of excessively overlapping reflections, allowing the reflection positions to be constrained by the cell knowledge. The cell parameters can also be refined during the process. The method can refine the unit cell parameters and decompose the whole powder pattern into individual reflections in one step. The method has a high potential for the analysis of powder data, in particular in the field of materials science. Unlike the Rietveld method, it requires no structural model in the least squares fitting.

There are two methods currently being widely used for estimating the integrated intensities. These are the Pawley method (Pawley, 1981) and the Le Bail method (Le Bail *et al,* 1988). In the original Rietveld work, the observed structure factors are estimated by partitioning among reflections contributing to each profile point of the pattern according to the calculated structure factors, and are thus biased. Iterating the Rietveld formula provides a simple method to extract the observed structure factors as accurately as possible, starting from initial structure factors, arbitrarily set to have the same value. The first study applying such an algorithm for structure determination purpose was that of Le Bail *et al* (1988). The algorithm has been implemented as an option in Rietveld programs, including Rietica, GSAS and JANA, although any Rietveld program can be modified to accommodate the algorithm. A definite advantage of the procedure is the very low number of parameters to be refined, allowing it to handle problems of any size.

The information the Pawley method has over the Le Bail method is the co-variance matrix, which describes the correlation of the extracted peak intensities with each other. These correlations can then be used in the structure solution program for reliable structure solution from extracted intensities. Most structure solution programs do not have the ability to use the co-variance matrix and are presently optimised for Le Bail extraction. Consequently, the estimated standard deviations are meaningless, and artificially set to a small value to prevent the software ignoring peaks.

3.7 Electron diffraction

Electron diffraction provides similar structural information to neutron diffraction. Electron diffraction is more useful than X-ray diffraction for determining proton positions. The strong interaction of electrons with matter results in a low penetration depth, hence, electron diffraction is usually used in a reflection geometry to study surfaces or thin films. Electron beams are easy to manipulate, detect, and focus to small spots to provide high spatial resolution.

Most electron diffraction is performed with high-energy electrons whose wavelengths are orders of magnitude smaller than the interplanar spacings in most crystals. For

example, for 100 keV electrons $l < 3.7 \times 10^{-12}$ m. Typical lattice parameters for crystals are around 0.3 nm.

There exist important features of diffraction using high-energy electrons. Since the wavelength of the electrons (λ) is very small, Bragg angles are also small. Consequently, the Bragg law can be simplified, as in equation 3.60.

$$\lambda = 2d\theta \tag{3.60}$$

In equation 3.60, θ is the angle of the incident electrons on the crystal and d is the distance between the atomic planes in the crystal. The small λ results in a large radius Ewald sphere for high-energy electrons. Therefore, it samples a virtually plane section of the reciprocal lattice, often the zero order Laue zone. Electron diffraction patterns can be equated with reciprocal lattice patterns. Lenses are able to focus the diffraction pattern and to change the camera length, which is equivalent to moving the film in an X-ray experiment.

Transmission electron diffraction is usually carried out in a transmission electron microscope, and the technique is known as Transmission Electron Microscopy (TEM). In TEM, it is possible to perform backscattered electron diffraction from particle surfaces to try to define the surface crystallographically.

3.8 X-ray fluorescence

X-ray Fluorescence (XRF) is a simple, accurate and economical method for the determination of the chemical composition of many types of materials. It is non-destructive and reliable, requires very little sample preparation, and is suitable for solid, liquid, and powdered samples. It provides detection limits at the ppm level; it can also precisely measure concentrations of up to 100 %.

Analysis using XRF is called X-ray Fluorescence Spectroscopy. The XRF method is widely used to measure the elemental composition of materials. Since this method is fast and non-destructive to the sample, it is the method of choice for field applications and industrial production for control of materials, such as cement clinker production.

When a primary X-ray excitation or radioactive source strikes a sample, the X-ray can either be absorbed by the atom or scattered through the material. The photoelectric effect is the process in which an X-ray is absorbed by an atom by transferring its energy to an innermost electron. During this process, if the primary X-ray has sufficient energy, electrons are ejected from the inner shells creating vacancies. These vacancies present an unstable condition for the atom. As the atom returns to its stable condition, electrons from the outer shells are transferred to the inner shells. In this process, the atom emits a characteristic X-ray, whose energy is the difference between the two binding energies of the corresponding shells. During this transition a photon may be emitted from the atom. This fluorescent light is called the characteristic X-ray of the element.

Due to the fact that the energy difference between two specific orbital shells in a given element is characteristic for that particular element, the photon emitted when an electron moves between these two levels will always have the same energy. Therefore, by determining the energy (wavelength) of the X-ray light (photons) emitted by a particular element, it is possible to determine the identity of that element.

For a particular wavelength of fluorescent light emitted by an element, the number of photons per unit time (peak intensity or count rate) is related to the concentration of element in the sample.

Counting rates for all detectable elements within a sample are usually calculated by counting for a set time the number of photons that are detected for the characteristic X-ray energy lines. By determining the energy of the X-ray peaks in spectrum and calculating the count rate of the various elemental peaks, it is possible to quantitatively establish the elemental composition of the sample.

Sometimes, as the atom returns to its stable condition, it transfers the excitation energy directly to one of the outer electrons causing it to be ejected from the atom. The ejected electron is called an Auger electron. This process is a competing process to XRF. Auger electrons are more probable in the low Z elements than in the high Z elements.

3.9 Differential thermal analysis

Differential Thermal Analysis (DTA) is a method that detects the heat released or absorbed as a result of chemical and physical changes that occur when materials are heated or cooled. This knowledge is valuable in understanding thermal properties of materials. Points where changes occur can be used to predict what occurred. The relative magnitude of the change and the shape of the curve can indicate how much of the change occurred.

DTA involves heating or cooling a sample and an inert reference, under identical conditions, and observing any temperature difference between the sample and reference. Differences in temperature are plotted with respect to either time or heating temperature. Sample changes that lead to the absorption or evolution of heat can be detected relative to the inert reference.

As differential temperatures can arise between two inert samples when their response to the applied heat treatment is not identical, this method can be used to study thermal properties and phase changes that do not lead to a change in enthalpy. The baseline of the DTA curve should exhibit discontinuities at the transition temperatures and the slope of the curve at any point will depend on the microstructural constitution at that temperature.

A DTA curve can be used as a finger print for identification purposes, such as in the study of tricalcium silicate polymorphs, where the structural similarity of the polymorphic modifications can make diffraction experiments difficult to interpret.

The key features of a differential thermal analysis instrument are as follows:

- Sample holder consisting of thermocouples, sample containers, and a ceramic or metallic block.
- Furnace.
- Temperature programmer.
- Recording system.

The furnace should provide a stable and sufficiently large enough hot-zone, and be sensitive enough to respond rapidly to the temperature programmer. A temperature programmer is essential in order to obtain constant heating rates. The recording system must have a low inertia in order to reproduce variations in the experimental set-up.

The sample holder assembly, with a thermocouple each for the sample and reference, should be surrounded by a block to ensure an even heat distribution. The sample should be contained in a crucible made of various materials such as silica, nickel, or platinum, depending on the temperature and nature of the investigation. High thermal conductivity of some metallic blocks may lead to smaller DTA peaks. The sample assembly should be isolated against electrical interference from the furnace wiring with an earthed sheath.

During experiments at temperatures in the range 200-500 ºC, problems may be encountered in transferring heat uniformly away from the specimen. These may be mitigated by using thermocouples in the form of discs to ensure optimum thermal contact with the sample container. To ensure reproducibility, it is necessary to ensure that the thermocouple and container are consistently located with respect to each other.

Care is necessary in selecting the experimental parameters. Experiments performed on powders produce results that may not be representative of bulk samples, where transformations may be controlled by the build up of strain energy. The packing state of any powder sample also becomes important in decomposition reactions and can lead to large variations between apparently identical samples.

In some circumstances, the rate of heat evolution may be high enough to saturate the response capability of the measuring system; it is better then to dilute the test sample with inert material. For the measurement of phase transformation temperatures, it is necessary to ensure that the peak temperature does not vary with sample size.

The shape of a DTA peak is dependent on sample weight and the heating rate used. Lowering the heating rate is approximately equivalent to reducing the sample weight; both lead to sharper peaks with improved resolution, although this is only useful if the signal to noise ratio is not compromised.

There are difficulties with the measurement of transition temperatures using DTA curves. The onset of the DTA peak in principle gives the start temperature, however, there may be temperature lags depending on the location of the thermocouple with respect to the reference and test samples, or the DTA block.

It is wise to calibrate the apparatus with materials of precisely known melting points. The peak area (A), which is related to enthalpy changes in the test sample, is that enclosed between the peak and the interpolated baseline. When the differential thermocouples are in thermal, but not physical, contact with the test and reference materials, it can be shown that A is given by equation 3.61.

$$A = mq/gK \tag{3.61}$$

In equation 3.61, m is the sample mass, q is the enthalpy change per unit mass, g is a measured shape factor, and K is the thermal conductivity of sample.

CHAPTER 4

QUANTITATIVE PHASE DETERMINATION OF CEMENT CLINKER USING THE RIETVELD METHOD

4.1 Introduction

This chapter summarises investigations on the QPA of cement clinker using the Rietveld method. Two clinkers, one standard cement clinker and one industrial clinker, were analysed using laboratory X-ray, synchrotron, neutron, and combined synchrotron and neutron powder diffraction data. The results were presented in the published papers "Rietveld refinement of neutron, synchrotron and combined powder diffraction data of cement clinker" (Peterson *et al,* 2002a) and in "Quantitative phase analysis of cement clinker using Rietveld analysis: comparison of results from various sources" (Peterson *et al,* 2002b), which is currently under review. Both publications are reproduced in this chapter.

The production of a standard clinker series by the National Institute of Standards and Technology, NIST, (Stutzman and Leigh, 1989) has allowed the comparison of phase quantification results through both round robin inter-laboratory testing, and within individual testing institutes. This has enabled the reproducibility of methods for the QPA of cement to be evaluated and compared to other methods. Results of such investigations in the literature indicate the Rietveld method as one of the better methods for this purpose. Despite this, accurate and precise QPA of cement clinker is difficult and has yet to be achieved.

A major advantage of the Rietveld method is that it is the only method to incorporate crystallographic modifications of components, such as polymorphs, into the QPA results. Given the advantages of the method, there has recently been an increase in the number of publications on the Rietveld analysis of cement and its components (Pritula and Smrčok, 2003) (Courtial *et al*, 2003) (de Noirfontaine *et al*, 2003) (Suherman *et al,* 2002) (Singh *et al,* 2002) (de la Torre *et al,* 2002) (Füllmann *et al*, 2001) (Jupe *et al*,

2001) (Scarlett *et al*, 2001) (Pritula, 2001) (Prodjosantoso *et al,* 2000) (Taylor *et al,* 2000) (Feret and Feret, 1999).

Despite the number of publications comparing the Rietveld method to other methods for QPA of cement, such as MPC, there appears to be a gap in investigations that compare the QPA results using Rietveld analysis obtained with different sources. There also appears no reported work in the literature on the comparison of polymorphic quantities obtained using the Rietveld method, particularly in relation to quantitative determination of the C_3S polymorphs.

In industry laboratory X-ray powder diffraction sources and lower-resolution neutron sources have been used in the on-line QPA of cement clinker (Scarlett *et al*, 2001). Laboratory X-ray, synchrotron, and neutron powder techniques have all been applied in the research analysis of clinker. The diffraction data used in industrial analysis of cement is of lower quality than the data available for the research analysis of clinker. The difference between results obtained from Rietveld analysis using various diffraction sources, in terms of both the quality of the data and diffraction mechanism (type of data), is therefore of interest. No work has been published that makes this comparison. The work in this chapter highlights the deficiencies of the Rietveld method for the QPA of clinker in industry, which is particularly important for on-line processing techniques. A comparison of results for the QPA of cement obtained using Rietveld analysis of various diffraction data is presented.

This chapter focuses on comparing the QPA results of clinker, including those of the C_3S polymorphs, obtained using the Rietveld method and various powder diffraction sources. Inconsistencies and errors in the method are identified.

4.2 Comparison of different sources

QPA of the NIST standard clinker 8488 and the Aalborg brand Danish cement clinker was performed using Rietveld analysis. Laboratory X-ray, synchrotron, neutron, and combined synchrotron and neutron data sets were collected and analysed. Comparisons between the QPA results for different data sets were made. Results for the NIST 8488 clinker were also compared to other published results obtained using both Rietveld

analysis and other methods. These investigations were presented in Peterson *et al* (2002a) and Peterson *et al* (2002b). These publications follow, reproduced in published or submitted format, where appropriate.

Peterson *et al,* 2002a

"Rietveld refinement of neutron, synchrotron and combined powder diffraction data of cement clinker"

V. Peterson, B. Hunter, A. Ray, and L.P. Aldridge

Appl. Phys. **A 74 [Suppl.]**, S1409 -S1411 (2002).

Reproduced as published

Appl. Phys. A 74 [Suppl.], S1409–S1411 (2002) / Digital Object Identifier (DOI) 10.1007/s003390201430

Applied Physics A
Materials
Science & Processing

Rietveld refinement of neutron, synchrotron and combined powder diffraction data of cement clinker

V. Peterson[1,*], B. Hunter[2], A. Ray[1], L.P. Aldridge[2]

[1] Department of Chemistry, Materials and Forensic Science, University of Technology, Sydney, P.O. Box 123, Broadway, NSW, 2007 Australia
[2] Australian Nuclear Science and Technology Organisation, P.M.B. 1, Menai, NSW, 2234 Australia

Received: 22 July 2001/Accepted: 8 January 2002 – © Springer-Verlag 2002

Abstract. Ordinary Portland-cement clinkers were characterised using neutron and synchrotron powder diffraction. Rietveld analysis was performed using individual as well as combined data. Comparisons were made between phase quantifications made using these different data sets, and with published results from other methods. Neutron results showed difficulty in distinguishing between tri- and dicalcium silicate phases, whilst synchrotron results compared well to other methods. Refinements were performed with and without refinement of the atomic positions of some atoms in the two main phases of a sample, and the results compared. Less than 1% adjustment in the atomic positions was found to decrease Bragg *R*-factors by about 20%.

PACS: 83.85.Hf; 61.12.Ld; 61.18.-j

Portland cement clinkers are mostly composed of a mixture of crystalline phases formed from heating clay and lime in a process known as clinkering. Typically the major crystalline phases present in clinker are tricalcium silicate (Ca_3SiO_5), dicalcium silicate (Ca_2SiO_4), tricalcium aluminate ($Ca_3Al_2O_6$), tetracalcium aluminoferrite ($Ca_i(Al_2O_3)_x(Fe_2O_3)_{1-x}$), and alkali metal oxides present as impurities from the reaction materials. Clinker composition is complicated by the presence of polymorphic modifications of these phases. Polymorphs present at high temperatures during the clinkering process are stabilised during cooling by the presence of other ions, such as found in the impurity compounds. The solid solution of tricalcium silicate in cement is called alite. At least seven polymorphs of tricalcium silicate, and five dicalcium silicate polymorphs exist. Theoretically all polymorphs can be present in a clinker, although a smaller range of tricalcium silicate polymorphs, and only one dicalcium silicate type have been found to be present in cement clinkers [1]. Tricalcium aluminate has three polymorphs and all have been found in cement clinkers, whilst tetracalcium aluminoferrite can appear with a varying Al : Fe ratio.

Phase quantification of the crystalline phases of cement is difficult due to the complexity of phases. Methods of cement analysis include calculation from chemical (oxide)analysis, such as the Bogue calculation, and microscopy methods, such as Microscope Point Counting (MPC), as discussed by Taylor [1]. Both these methods deal with total component concentrations and do not include polymorphic assay. The Bogue method has been found to give incorrect results, especially for alite, and MPC is labour intensive. Powder diffraction methods using Rietveld refinement have been used and allow some polymorphic assay, however results from X-ray analysis can vary [2], and it is important that a full crystallographic study be included [3].

1 Experiment

In this paper, an Aalborg brand Danish industry cement clinker and NIST reference material 8488 cement clinker were investigated using full-profile Rietveld analysis with a modified version of the program LHPM [4]. Structures used

Table 1. Refinement structures

Component	Space group	Crystal system	Ref.
Tricalcium silicate	*P* 1bar	Triclinic	[5]
Tricalcium silicate	*C* 1 *m* 1	Monoclinic (Superlattice)	[6]
Tricalcium silicate	*C* 1 *m* 1	Monoclinic (Sublattice)	[7]
Tricalcium silicate	*R* 3 *m*	Trigonal (hex.)	[8]
Dicalcium silicate	*P* 1 21/*n* 1	Monoclinic	[9]
Tricalcium aluminate	*P a* 3bar	Cubic	[10]
Tricalcium aluminate	*P* 1 1 21/*a*	Monoclinic	[11]
Tetracalcium aluminoferrite	*I b m* 2	Orthorhombic	[12]
Calcium oxide	*F m* 3bar *m*	Cubic	[13]

*Corresponding author.
(Fax: +61-2/9717-3606, E-mail: vkp@ansto.gov.au)
Supported by Australian PhD and AINSE awards.

Table 2. Phase quantification and Bragg *R*-factors for Aalborg clinker

	Synchrotron		Neutron		Combined		
	wt. %	R_B	wt. %	R_B	wt. %	R_B Synchrotron	R_B Neutron
Total alite	69.8(6)	–	66.8(8)	–	64.6(7)	–	–
Tricalcium silicate Triclinic	65.7(5)	4.6	53.7(7)	2.4	58.1(5)	2.3	5.1
Tricalcium silicate Monoclinic Sup.	1.3(2)	4.5	10.3(3)	2.6	1.2(1)	2.3	5.6
Tricalcium silicate Rhombohedral	2.7(3)	4.9	2.8(3)	2.3	5.3(4)	1.8	5.1
Dicalcium silicate	26.1(3)	3.9	30.1(4)	2.6	31.4(3)	2.4	4.8
Tricalcium aluminate Cubic	3.3(1)	3.0	1.4(2)	2.4	3.6(1)	2.3	5.4
Calcium oxide	0.80(4)	2.3	1.7(1)	3.0	0.40(4)	2.1	11.0

Table 3. Phase quantification and Bragg *R*-factors for NIST 8488 clinker

	Synchrotron		Neutron		Combined		
	wt. %	R_B	wt. %	R_B	wt. %	R_B Synchrotron	R_B Neutron
Total alite	65.6(3)	–	72.4(5)	–	61.2(4)	–	–
Tricalcium silicate Triclinic	7.6(1)	2.3	63.3(5)	2.1	11.2(2)	2.8	7.5
Tricalcium silicate Monoclinic Sub.	58.1(3)	1.7	9.1(2)	2.7	50.1(4)	2.4	7.3
Dicalcium silicate	16.0(2)	1.4	12.2(2)	1.9	18.3(4)	1.5	6.6
Tricalcium aluminate Monoclinic	4.1(1)	3.0	2.6(2)	2.5	6.2(2)	4.5	6.7
Tetracalcium aluminoferrite	13.1(1)	2.0	12.7(2)	1.5	13.2(2)	1.5	4.9
Calcium oxide	1.2(1)	0.6	–	–	1.1(1)	0.86	8.6

for refinement are shown in Table 1; the phases that best fitted each data set were used. Synchrotron data was collected on BL20B, a Debye-Scherrer powder diffractometer at KEK, Japan. Neutron data was collected on the high resolution powder diffractometer at HIFAR, Australia.

2 Results and discussion

Figures 1a and b show refinements for NIST 8488 clinker using neutron and synchrotron sources respectively. Phase quantification and Bragg R-factors of Aalborg clinker and NIST 8488 clinker are presented in Tables 2 and 3. Table 4 compares the phase quantifications of NIST 8488 clinker obtained using each data set, with results of X-ray diffraction and MPC by Taylor et al. [3].

As shown in Tables 2 and 3, the refinements of different datasets gave varying wt. %'s of tricalcium silicate polymorphs. In the case of the neutron diffraction data, the excessive peak overlap makes distinguishing the various polymorphs difficult. Polymorphic determination of tricalcium silicate from synchrotron data was considered to be more accurate due to the higher resolution of the data.

Table 4 shows that synchrotron data for NIST 8488 clinker gave excellent comparison with MPC results, slightly better than literature laboratory X-ray results. Neutron data showed poor agreement for alite and dicalcium silicate, and it is thought that there was insufficient resolution to distinguish the phases. For the synchrotron refinement, the dicalcium silicate showed the largest difference to the MPC results. For the neutron refinement, significant differences to the MPC results occur for both the alite and dicalcium silicate phases. Previous neutron analysis of NIST 8488 clinker using only a monoclinic tricalcium silicate polymorph, also gave a poor result for the dicalcium silicate phase [14]. Despite the individual neutron and synchrotron wt. %'s for dicalcium silicate being less than the MPC result, a result surprisingly similar to MPC was obtained from the combined data set. This

Table 4. Standard deviations (difference in the two determinations divided by the combined estimated errors) from MPC results of Taylor et al. [3] of NIST 8488 clinker

	Neutron	Sync.	Combined	X-ray [3]
Alite	9.5	0.92	5.2	2.1
Dicalcium silicate	9.3	3.9	0.24	4.7
Tricalcium aluminate	1.2	0.14	1.4	0
Tetracalcium aluminoferrite	0.42	0.65	0.70	1.2

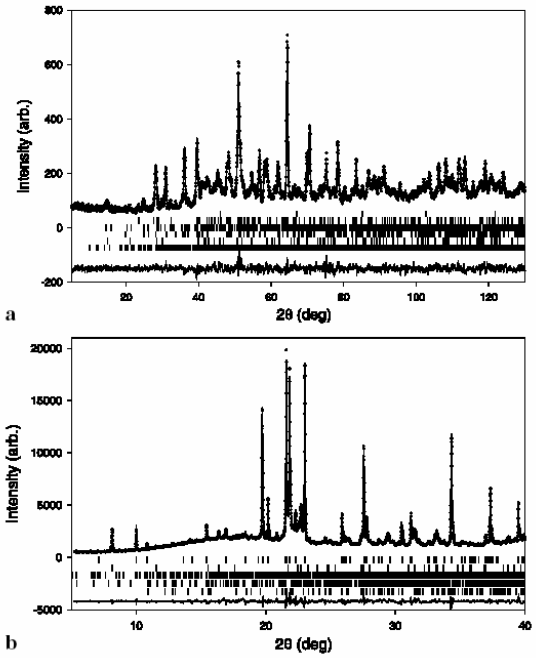

Fig. 1. Neutron and synchrotron diffraction data and Rietveld fit of NIST 8488 clinker

study noticed that in the work of Taylor et al. [3] there existed significant variation in the amount of dicalcium silicate in NIST 8488 clinker found by Rietveld analysis of laboratory X-ray data upon variation of the tricalcium silicate polymorphs used in the refinement. Quantification by laboratory X-ray diffraction methods of tricalcium and dicalcium silicates in mixtures is difficult due to the wide range of overlapping reflections [15]. This problem was also noticed in neutron results of this study, although the combination of neutron and synchrotron data allowed better discrimination between alite and dicalcium silicate phases.

The Ca and Si atomic positions in triclinic tricalcium silicate and dicalcium silicate structures were refined using synchrotron data of NIST 8488 clinker. Less than 1% average alteration to bond distances in the refinement resulted in a 20% and 24.5%, improvement in the fits of the dicalcium silicate and triclinic tricalcium silicate clinker phases respectively. As synchrotron data was used, the oxygen atoms, which are the bulk of the cell, were not moved. Refinement of the neutron and combined data incorporating the effect of atomic position adjustments are in progress.

3 Conclusions

In this study it was found that synchrotron refinements gave results consistent with literature phase quantifications, while the neutron refinements did not for tricalcium and dicalcium silicates. Upon refinement of the atomic positions of triclinic tricalcium and dicalcium silicates, relatively minor adjustments to the structures resulted in significant improvement in the fit of the phases. This suggests that the published structures are not identical to those found in clinker materials.

References

1. H.F.W. Taylor: *Cement Chemistry* (Thomas Telford, London 1997)
2. L.P. Aldridge: Cem. Concr. Res. **12**, 381 (1982)
3. J.C. Taylor, I. Hinczak, C.E. Matulis: Powder. Diffr. **15**, 7 (2000)
4. R.J. Hill, C.J. Howard: Report No. AAEC/M112 (1986)
5. N.I. Golovastikov, R.G. Mateeva, N.V. Belov: Sov. Phys. Crystallogr. **20**, 441 (1975)
6. F. Nishi, Y. Takeuchi: Zeitschrift Kristallographie **172**, 297 (1985)
7. W.G. Mumme: Neues Jahrb. Mineral., Montash **1995**, 145 (1995)
8. A.M. Ilinets, Y. Malinovskii, N.N. Nevskii: Dokl. Akad. Nauk SSSR **281**, 332 (1985)
9. W.G. Mumme, R.J. Hill, G. Bushnell-Wye, E.R. Segnit: Neues Jahrb. Mineral., Abh. **169**, 35 (1995)
10. P. Mondal, J.W. Jeffery: Acta. Cryst. **B31**, 689 (1975)
11. Y. Takeuchi, F. Nishi: Zeitschrift Kristallographie **152**, 259 (1980)
12. A.A. Colville, S. Geller: Acta. Cryst. **B31**, 1169 (1974)
13. I. Oftedal: Z. Phys. Chem. **128**, 135 (1927)
14. R. Berliner, C. Ball, P.B. West: Mat. Res. Soc. Proc. **376**, 487 (1995)
15. J. Neubauer, R. Sieber: Materials Science Forum **228–231**, 807 (1996)

Peterson *et al,* 2002b

"Quantitative phase analysis of cement clinker using Rietveld analysis: comparison of results from various sources"

V. K. Peterson, B. Hunter, and A. Ray

Journal of the American Ceramics Society, (2002).
Under review

Reproduced as submitted

Rietveld phase quantification of cement clinker using powder diffraction data*

Vanessa K. Peterson[a], Abhi Ray[a] and Brett A. Hunter[b]

[a]*Department of Chemistry, Materials and Forensic Science, University of Technology Sydney.*
Broadway. NSW. 2007. Australia.
[b]*Australian Nuclear Science and Technology Organisation.*
Menai. NSW. 2234. Australia.

Abstract

Rietveld refinement of neutron, x-ray and synchrotron powder diffraction data of NIST SRM clinker 8488 was performed. Quantitative phase analysis (QPA) results were compared with other studies, and cell lattice results are discussed. QPA results for the main phases in the clinker were in found to be agreement between the different sources used in this and other studies, although QPA of the tricalcium silicate polymorphs was shown to be inconsistent. Quantification and refined lattice constants of the tricalcium aluminate phase varied between sources, and the neutron source was unable to distinguish this phase.

Introduction

Major phases present in clinker are tricalcium silicate (C_3S), dicalcium silicate (C_2S), tricalcium aluminate (C_3A), and tetracalcium aluminoferrite (C_4AF), along with impurities. Clinker composition is complicated by the crystal modification of these phases, and it is well documented that polymorphs present during the high-temperature clinkering processes can be stabilised during cooling by the presence of impurity ions [1]. Table I summarises information on the four main clinker components, their possible crystal modifications, those modifications likely to be present in cement clinker, and the modifications that have structural information available for use in Rietveld models. The solid solution of C_3S in cement is called alite. At least seven polymorphs of C_3S exist, three triclinic (T_1, T_2, T_3), three monoclinic (M_1, M_2, M_3) and one rhombohedral

* Based in part on the thesis to be submitted by V. K. Peterson for the degree of PhD in Science, University of Technology, Sydney. Supported by an Australian Post-Graduate Award, and a Postgraduate Research Award provided by the Australian Institute of Nuclear Science and Engineering.

modification (R). All can exist in cement, although it has been shown that the polymorphs likely to be present are M_3, M_2, occasionally T_2, and rarely R [1]. Only one of the five C_2S polymorphs has been shown likely to be present in cement clinkers, the monoclinic ß-type [1]. Pure C_3A does not have polymorphs, although through ion substitution monoclinic (M), orthorhombic (O), and cubic (C_I, C_{II}) modifications exist. The cubic and orthorhombic modifications of this phase are likely to be present in clinker. C_4AF appears in one form, with a varying Al:Fe ratio [1, 2].

There has been an increase in the use of Rietveld refinement of powder diffraction data for the QPA of cement and analysis of cement components in recent years [2-6]. The complex nature of cement clinker components, structural modifications of each phase and overlapping phase peaks from the multiphase system in diffraction patterns make QPA by Rietveld analysis difficult. For cement clinker analysis, only three polymorphs of the C_3S system have fully determined structures for use with Rietveld models. They are the T_1, M_3 and R types, although the T_1 and T_2 powder diffraction patterns have been shown to be similar [1]. Structures for other typical components of cement clinker have been determined, although recently the model for the C_4AF phase was re-investigated [2].

Quantification of the polymorphs of C_3S has the potential to be extremely useful to industrial applications. Harada *et al* [7] showed that each polymorph of C_3S has a different rate of hydration, which was reflected in their resultant strength properties. Mascolo *et al* [8], noted that the compressive strength of the polymorphs appeared to be related to the type of stabilising ion entering the lattice. Taylor *et al* [3] recently investigated the importance of including tricalcium silicate polymorphs in the Rietveld model for the phase quantification of cement clinker components, and stated that quantitative analysis of these polymorphs can be obtained using powder diffraction and Rietveld analysis.

The Microscope Point Counting (MPC) technique has been used by the National Institute of Standards and Technology (NIST) [9] and in the study of Taylor *et al* [3], to characterise Standard Reference Material (SRM) clinker 8488. Although results for phase quantification of C_3S and C_2S in cement clinkers are very precise, it does not give

polymorphic identification, and is very tedious [1]. Rietveld analysis of laboratory x-ray diffraction data of cement clinkers has been shown to be in agreement with MPC result for the QPA of the C_3S and C_2S phases [3]. MPC has, however, been shown to have difficulty in distinguishing the C_3A and C_4AF phases in clinkers [1], and Rietveld analysis methods are better than MPC methods for the identification of these phases.

The presence of multiple phases in a diffraction pattern inevitably leads to an increase in diffraction peak density. Hill and Howard [10] showed that in binary mixtures the derived crystal structure parameters were statistically independent of abundance down to at least 10 wt. %. It is plausible to assume that QPA of clinker phases of less than a few weight percent is difficult with Rietveld techniques. A serious problem with QPA of cement clinker using the Rietveld method is the existence of phases other than the modelled major components, each of weight fraction less than the detectable few percent. The problem occurs when these smaller weight fraction phases combine to form a significant proportion of the sample, and can result in significant missing information from the Rietveld model. In an already complicated model, with many overlapping peaks, the best mathematical fit of an incomplete model to the data may appear surprisingly good, although the result may be incorrect. This problem also occurs when one or more tricalcium silicate polymorphs are missing from the Rietveld model. Bulk chemical analysis of cement clinker may not reveal phases not included in a Rietveld model, as some are present as polymorphs, or are composed of the same atoms, with varying stoichiometry.

The problem caused by multiple, small, and unknown weight fraction phases, manifests itself further in the calculated fit of a Rietveld model. Recent investigations [3,4] have reported very small (<1 wt.%) phase fractions of components in cement clinkers. This is common with some approaches used for routine analysis of cements [5,11]. The inclusion of additional phases into the Rietveld model causes an increase in the number of parameters being modelled. This can result in a statistically better fit of the model to the data, although the amounts found may be unrealistic. A good indication of the fit of a model in Rietveld analysis can be obtained upon visual inspection of the modelled and experimental data. The absence of Rietveld plots in the literature allows for comparisons using only the numerical results, which may be misleading.

Neutrons and x-rays give different information about clinker composition, and it is therefore possible that simultaneous Rietveld analysis of these data types will give a more reliable refinement result. The directional character of reciprocal space as well as the complex nature of structure factors and both reduced in a powder diffraction experiment. Results from refinement of single crystal data are more certain than the results from a refinement of a single powder pattern. The fact that x-rays and neutrons are scattered by different mechanisms means that the crystal structure model that has calculated patterns that match both neutron and x-ray patterns is more likely to be correct than that from a single pattern refinement. Initial investigations on the phase quantification of cement clinker revealed that although total alite quantification was similar for different data types, polymorphic quantification was highly variable [12]. This result may have been related to resolution of the different instruments, or as a result of the relatively small two-theta range used in synchrotron data collection. It is believed that the collection of data to a higher two-theta value may give a different result.

This paper presents the results of a Rietveld full profile analysis of constant wavelength neutron, x-ray and synchrotron diffraction patterns, as well as Rietveld refinement of the combined neutron and synchrotron data-sets obtained on the NIST SRM clinker 8488. Differences in phase quantification results for the four main components, as well as the C_3S polymorphs were investigated, and comparisons between each set of data collected, and to other studies, were made.

Experimental Procedure

A laboratory x-ray powder diffraction pattern was collected using Cu Kα radiation (Scintag X1, Scintag Instruments, USA). Clinker was loaded onto a flat-plate sample holder, using a side-loading technique designed to reduce preferred orientation effects. Data were collected over the range $2\theta = 2.00 – 90.00°$ with a stepping of 0.02°. A corundum standard from NIST was used to determine the zero point of the instrument for use in Rietveld refinements.

Neutron diffraction data were obtained from the High Resolution Powder Diffractometer (HRPD) at the High Flux Australian Reactor (HIFAR). Clinker was

loaded into a vanadium can which was rotated during data acquisition. Data over the range 2θ = 0.0 - 153.0° was obtained using steps of 0.05°. The wavelength of the neutrons was determined as 1.8823(1) Å using a corundum standard from NIST.

Synchrotron diffraction data were collected at the Australian National Beamline Facility (ANBF), on beam line 20B, at the Photon Factory, Tsukuba, Japan. A wavelength of 1.04461(1) Å was determined using the same corundum standard from NIST as was used for XRD zero point and neutron wavelength determination. Clinker was sealed in glass capillary tube of 0.3 mm diameter which was rotated during data collection. Image plate detectors were used over the ranges 2θ = 2.00 – 40.00° on the first plate, and 2θ = 45.00 – 70.00° on the second, using increments of 0.010044°.

A fit to the data was modelled and refined using the Rietveld refinement program *Rietica* [13]. The modelled clinker component structures were chosen from the literature [3-5, 9, 12]. Approximate phase quantification for the crystalline phases from each data-set was calculated relative to each data set, from the Rietveld model, using the method described by Hill and Howard [10]. All polymorphs of each component were tested for the best fit to the data, and multiple alite polymorphs were eventually chosen as the best fit combination. Fits were assessed visually, and using the factors R_p, R_{wp} and Goodness Of Fit (GOF). Individual phase fits were evaluated using their Bragg R-factors (R_B). The structural models with their references are listed in Table II.

A Newton-Raphson refinement strategy was used for all data sets. A Chebychev type I polynomial was used for background modelling, with the minimum number of points necessary being used, to a maximum of eleven for the laboratory x-ray model. All peak shapes were modelled using the Pseudo-Voigt peak shape function, except for neutron data which was modelled using the Voigt function. The mixing parameter (γ) remained between 0.1 and 0.9 throughout the refinements. Atomic displacement (isotropic thermal) parameters were refined, as some published structures were found to have unreasonably high values. Phases present in quantities less than 5 wt. % did not have their atomic displacement parameters refined, but fixed to a value of 1.0 for oxygen atoms, and 0.6 for other atoms. All atomic displacement parameters that were refined were constrained to the same value for each atom type within the same phase. For all

refinements these values remained in the acceptable range of 0.2 to 2.0. As the C_4AF phase exists over a varying Al/Fe ratio, the site occupancies of the Al and Fe atoms that shared positions were refined in the modelling of this phase, for all data sets.

Results and Discussion

Whole pattern figures of merit and refinement plots

Rietveld refinements for the clinker were performed successfully with x-ray, synchrotron and neutron data sets, the corresponding refinement patterns of which are shown in Figures 1-3 respectively. Refinement of combined synchrotron and neutron data sets was also performed successfully. R_p, R_{wp} and GOF values for each refinement are shown in Table III.

Intensities of the peaks collected in synchrotron patterns using image plates are relative, and were all scaled as outlined by Cookson [20]. A better comparison of fits between the patterns can be gained from comparison of R_p values than from GOF values.

The poorest figures of merit were obtained for the laboratory x-ray data set, and visual inspection of the Rietveld residual plot indicates a poor fit relative to those of other data sets. The C_2S phase is affected by preferred orientation due to its lamellar particle shape [1], and any preferred orientation could have been significant in the laboratory x-ray data, which was collected using a flat-plate system. Although a side loaded flat plate designed to minimise preferred orientation was used, some may have been experienced. The sample was spinning during neutron and synchrotron data collection so preferred orientation of this phase would have been minimised in these data sets. The March model was used in the laboratory x-ray refinement to examine reflections thought to have been affected, however no significant deviation of the refinable parameter from 1.0 was found. One possible explanation is that any preferred orientation of the dicalcium silicate phase may have blended into the heavily overlapping alite peaks surrounding this phase. Hence, preferred orientation may not have been visible in the residual plot of the refinement as the effects of this may have been absorbed into the models of other phases, such as the C_3S structures. This could explain why no preferred orientation was identified, and the fit was not optimal.

A visual inspection of the fits in Figures 1-3 was made, and any poorly fitting peaks were listed. Overall the fits were excellent. Two imperfections were however consistent throughout the fits to the three data types. At approximate d-spacings of 1.98 Å and 1.76 Å, there appeared to be too much, and too little intensity, respectively. Small, missing peaks, usually with broad peak shapes, as well as missing intensities, appeared throughout all refinements. A possible explanation could be the existence of very small phase fraction impurities. CaO [21] was initially included in the models using the three data types. Weight fractions found in neutron and laboratory x-ray data were 0.06(3) and 0.09(3) respectively. These were not thought to have been significant enough to report as final weight fractions, especially as the synchrotron source refinement failed to yield any CaO.

Phase quantification of clinker components

Phase quantification and individual phase fits (Bragg R-factors) for NIST SRM clinker 8488 are shown in Table IV. Phase quantification as measured by various sources are compared in Figure 4.

QPA for the total alite in the clinker of the four refinements were found to be similar. In particular, the synchrotron and laboratory x-ray results were in agreement. QPA from the four refinements for C_2S phase were also similar.

Phase quantification for the C_3S polymorphs varied between refinements, although all refinements consistently found lower amounts of the rhombohedral polymorph, than other polymorphs.

None of the refinement results for the C_3A phase were in agreement. This was thought to have been due to the highly superimposed alite and dicalcium silicate phases at the position of the most intense peak of the C_3A phase. In neutron data, the phase is barely distinguishable from other phases. Figure 5 shows the contribution of the background and C_3A phase to the model. Although this peak is clearly visible in the corresponding synchrotron (and x-ray) patterns, as shown in Figure 6, its intensity is governed by the background of other peaks in the surrounding area.

The refinement results for the QPA of the C_4AF phase appear similar in Figure 4. The small standard errors associated with the quantification values means that some refinement results are many standard deviations from each other.

Figures of merit for clinker components within refinements

C_3S phases had the highest Bragg R-factors for all refinements when compared to other components, particularly for synchrotron, laboratory x-ray and the combined data refinements of the rhombohedral modification. Poor fits of the tricalcium silicate phases may be caused by slight crystallographic alterations to the structures as present in the clinker, such as the presence of other polymorphs that do not yet have published structures. Differences in the C_3S polymorph structures of the same space group are believed to involve shifts of some atomic positions, without changes to the symmetry or space group, and as atomic positions were not refined in this study, these would not have been accounted for. The poor fits of the rhombohedral modification may also be explained in this way, as this phase may have been altered in the refinement model to compensate for missing phases of other polymorphs.

The C_2S phase had reasonably low Bragg R-factors from all refinements. The best fit was recorded by the neutron refinement, which was contrary to results from two other studies, which both recorded a poor fit of the C_2S model to neutron data of this clinker [4, 12].

Comparison of phase quantification of clinker components to other studies

Comparison of the phase quantification results for SRM clinker 8488 of this study, see Table IV, were made with those for other studies as listed in Table V. Differences between the structures used in the Rietveld model existed between this and other studies. In Table V, the orthorhombic modification of C_3A, as used in this study, was not used by Taylor *et al* [3] in their model. Berliner *et al* [4] used only the super-lattice monoclinic modification of C_3S of Nishi *et al* [15] in their neutron model. Comparison to these results was therefore limited.

The QPA by MPC results of NIST for the SRM 8488 clinker are an average of a range of weight fractions of multiple MPC results [9]. The NIST MPC investigation for the

total alite produced results that varied from 64.20 to 65.50 wt. %, and the C_2S result ranged from 17.94 to 19.31 wt. %. Similarly, the C_3A phase ranged from 3.08 to 6.24 wt. %, and the C_4AF phase from 10.25 to 13.46 wt. %. The relatively large result range for the C_3A and C_4AF phases illustrate the difficulty in identification of these phases by MPC. The MPC results are considered precise only for the C_3S and C_2S phases.

Less alite was found in the clinker from all refinements of this study than was found in the studies of Table V. A study by Suherman *et al* found a similar amount of alite in this clinker by XRD, despite only using the monoclinic modification of C_3S of Nishi *et al* [15] in their refinement. It seems likely that Rietveld methods are consistent in finding less alite in this clinker. As Rietveld analysis by mathematical definition is quantitative only for crystalline phases, a possible explanation for the difference in QPA of alite from MPC and Rietveld methods is that the MPC result includes phases that are of less crystalline form than those found in Rietveld analysis. Suherman *et al* suggests that the findings of MPC results are incorrect. The author of this study believes that although both results are precise, the additional material found by MPC may be less crystalline alite forms, in which case the MPC is closer to the true value, or other non-crystalline material, in which case the Rietveld method is closer to the true value.

Taylor *et al* [3] investigated the polymorphic QPA of alite using Rietveld analysis of laboratory x-ray diffraction data. Although their results were not in agreement with those of this study, both studies have found rhombohedral C_3S to be present in the least amount.

The laboratory x-ray refinement result for the QPA of C_2S was within 1 standard deviation of all results from the studies in Table V. Other refinement results from this study indicated that more C_2S was present than was determined in the studies of Table V. QPA results for this phase were no more than 4 standard deviations greater than the MPC value of NIST. Interestingly, these refinement results compliment the results for the QPA of the total alite, as the total calcium silicate found in the system remains approximately constant for all refinements.

The QPA MPC results of NIST for the C_3A phase were highly varied. Despite this, quantification results for the C_3A phase of the studies listed in Table V were in close agreement with the mean reported by NIST. This study found significant variation in the quantification of this phase depending on the source used; the synchrotron and combined data refinements gave results that were within the range of quantities found by the MPC investigation of NIST.

The amount of C_4AF found by all refinements was within the MPC result range of NIST. Due to the problems associated with the MPC determination of aluminate and ferrite phases [1], the standard error in the NIST calculation was very large. Hence, all results for the quantification of the C_4AF phase in this study were in agreement within 1 standard deviation of the NIST MPC results. Laboratory x-ray and combined data refinement results of this study were in agreement within 1 standard deviation the laboratory study of Taylor *et al* [3]. Both neutron results of this study and that of Berliner *et al* [4] found the least amount of C_4AF out of all the sources used in Tables IV and V.

Deviations in lattice parameters of structures after refinement

Lattice parameter refinement results are shown in Table VI. Laboratory x-ray data gave slightly larger lattice parameters than most of the refinements of other data. This trend was likely due to instrument error.

There was variation in the lattice parameters between the refined structures using the different data sources and the literature values. This was the case for all components in the model. A significant variation in lattice parameters occurred on refinement of the C_3ST (T_1) model. Similar results were obtained by Taylor *et al* [3], listed in Table VII. It is generally accepted that the T_2 triclinic C_3S polymorph is the likely triclinic modification to be present in alite [1]. The deviation of refined results from the T_1 structure used suggests that the model of this phase was adjusted to accommodate missing C_3S polymorph structures not present in the model. Similar, less marked differences were observed with the monoclinic model. The neutron study of Berliner *et al* [4], see Table VIII, used the monoclinic super-lattice of Nishi *et al* [15], as was used in this study. This was however, their only alite model used. Taylor *et al* [3] used the

sub-lattice structure of Mumme [22] as a model for the monoclinic C_3S, so comparison was not possible. As expected, the C_3SR model showed negligible variation in lattice parameters from the literature structure upon refinement.

A slightly smaller β angle of the C_2S phase was observed upon refinement of all data when compared to the literature structure. This was consistent with results of other studies, listed in Tables VII and VIII.

Neutron data found different C_3A lattice parameters to the synchrotron and laboratory x-ray sources in this study. Other studies used different polymorphs of this phase so comparison could not be made. The laboratory x-ray study of Taylor *et al* [3] in Table VII only used the monoclinic and cubic C_3A polymorphs. An orthorhombic modification of C_3A [18] was used in this study, while Berliner *et al* [4] found predominantly cubic modification. Not greater than 1 wt. % cubic C_3A was found in this study using any diffraction data.

The lattice parameters of the C_4AF phase refined to smaller values than the literature structure. This result was expected due to the variable ratio of Al : Fe of this compound causing distortions in the cell parameters of the crystal. This result compared well to other studies, with close agreement between the lattice parameters determined in the neutron study of Berliner *et al* [4] and this study, and also between the x-ray results of Taylor *et al* [3] and this study.

Other refinable parameters

Refinement of the atomic displacement (thermal) parameters gave results that were all within acceptable ranges. The C_3A phase exhibited the largest atomic displacement parameters, and were relatively unstable compared to those of atoms in other phases.

Peak shapes for the C_3A phase were very broad, relative to other phases within each refinement. The U peak shape parameter in the Pseudo-Voigt function for the synchrotron data of this phase refined to a very large value of around 2.2, and was set at a fixed value of 0.8. Similarly for the neutron data, the size parameter in the Voigt function of this phase refined to a negative value and was fixed to 0.10.

Site occupancy factors of the Fe and Al sites in the C_4AF phase were refined. These results were compared to the results from a recent structural investigation of a typical C_4AF by Jupe *et al* [2]. Deviation in occupancy from the sample of Jupe *et al* [2] implies different substitutions in the sample. Site occupancies for all refinements of this study for the octahedrally and tetrahedrally coordinated Fe sites refined to negative values, and were fixed to 0. These results differed significantly to the results of Jupe *et al* [2], who obtained values of 2.92(3) and 4-Fe(oct.) for the Fe(oct.) and Fe(tet.) sites respectively. Results of this study therefore suggested that no Fe was substituted into this structure in this clinker.

Summary

Rietveld quantification for the NIST SRM clinker 8488 of the C_3S, C_2S and C_4AF phases compared well between diffraction data sources of this and other studies. The QPA results for C_3A varied significantly between sources, and appeared that the neutron data used in this study was unable to quantify the phase. The polymorphs of C_3S were difficult to quantify using this method, although it was clear that the rhombohedral modification of this phase was present in the least amount. In a complicated Rietveld model such as that required for cement clinkers, a good mathematical fit based on ample refinable parameters does not necessarily demonstrate the best fit, or that the correct structures or phases have been selected for the model. The Rietveld model can incorporate missing phases and incorrect structures to give an approximation the best fit.

Acknowledgments

The authors wish to thank the Australian Nuclear Science and Technology Organisation and the Australian National Beamline Facility for additional support. Thanks to Professor Brian O'Connor for reviewing the manuscript.

References

1. H. F. W. Taylor, *Cement Chemistry.* Thomas Telford, London, 1997.

2. A. C. Jupe, J. K Cockroft, P. Barnes, S. L. Colston, G. Sankar and C. Hall, "The site occupancy of Mg in the brownmillerite structure and its effect on hydration properties: an X-ray/neutron diffraction and EXAFS study," *J. App. Cryst.,* 34 55-61 (2001).

3. J. C. Taylor, I. Hinczak, C. E. Matulis, "Rietveld full-profile quantification of Portland cement clinker: The importance of including a full crystallography of the major phase polymorphs," *Powder. Diffr.,* 15 7-18 (2000).

4. R. Berliner, C. Ball and P. B. West, "Neutron powder diffraction studies of Portland cement and cement compounds,"; pp.487-492 in Neutron Scattering in Materials Science II, proceedings of the Materials Research Society Symposium (Boston, Massachusetts, November 1994) volume 376. Edited by D. A. Neumann, T. P. Russell and B. J. Wuensch. Materials Research Society, Pennsylvania, 1995.

5. B. Feret and C. F. Feret, "C^{em}QUANT® software mathematical modeling in quantitative phase analysis of Portland cement," *Cement and Concrete Research,* 29 1627-1633 (1999).

6. P. M. Suherman, A. Riessen, B. O'Connor, L Deyu, D. Bolton and H. Fairhurst "Determination of amorphous phase levels in Portland cement clinker," *Powder Diffraction,* 17 *in press* (2002).

7. T. Harada, M. Ohta and S. Takagi, "Effect of polymorphism of tricalcium silicate on structure and strength characteristics of hardened cement paste," Japan. Rev. Gen. Meet., Tech. Sess. - Cem. Assoc. Jpn. 31 31-33 (1977).

8. G. Mascolo, B. Marchese, G. Frigione and R. Sersale, " Influence of polymorphism and stabilizing ions on the strength of alite," *Journal of The American Ceramic Society*, 56 [4] 222-223 (1977).

9. NIST (1989). National Institute of Standards and Technology, Report of Investigations, Reference Materials 8486, 8487, 8488, Portland Cement Clinker, S.D. Rasberry, Chief, Office of Standard reference Materials, May 22nd, Gaithersburg, MD.

10. R.J Hill and C.J. Howard, "Quantitative phase analysis from neutron powder diffraction data using the Rietveld method," *J. Appl. Cryst.,* 20 467-474 (1987).

11. T. Füllmann, G. Walenta, H. Pöllmann, M. Gimenez, C. Lauzon, S. Hagopian-Babikian, T. Dalrymple and P. Noon. "Quantitative Rietveld analysis of Portland cement clinkers and Portland cements using the TOPAS software – applications as a method of automated quality and process control in industrial production – part 1," *International Cement Research*, 1 41-43 (2001).

12. V. K. Peterson, B. Hunter, A. Ray and L. P. Aldridge, "Rietveld refinement of neutron, synchrotron and combined powder diffraction data of cement clinker," *Applied Physics A (ICNS 2001 Proceedings),* In publication.

13. B. Hunter, "Rietica – A visual Rietveld program," *Powder Diffraction Newsletter,* 20, 21 (1999).

14. N. I. Golovastikov, R. G. Matveera, N. V. Belov, "Crystal structure of the tricalcium silicate $3CaO.SiO_2 = C_3S$," *Sov. Phys. Crystallogr.* 20 721-729 (1975).

15. F. Nishi, Y. Takéuchi and I. Maki "Tricalcium silicate $Ca_3O[SiO_4]$: The monoclinic superstructure," *Zeitschrift fur Krystallographie,* 172 297-314 (1985).

16. A. M. Ilinets, Y. Malinovskii and N. N. Nevskii, "Crystal structure of the rhombohedral modification of tricalcium silicate Ca_3SiO_5," *Dokl. Akad. Nauk SSSR,* 281 191-193 (1985).

17. W. G. Mumme, R. J. Hill, G. Bushnell-Wye and E. R. Segnit, "Rietveld crystal structure refinements, crystal chemistry and calculated powder diffraction data for the polymorphs of dicalcium silicate," *Neues Jahrb. Mineral., Abh.,* 169 35-68 (1995).

18. F. Nishi and Y. Takéuchi, "The Al_6O_{18} rings of tetrahedra in the structure of $Ca_{8.5}NaAl_6O_{18}$," *Acta Cryst.,* B31 1169-1173 (1975).

19. A. A. Colville and S. Geller, "Crystal structures of $Ca_2Fe_{1.43}Al_{0.57}O_5$ and $Ca_2Fe_{1.28}Al_{0.72}O_5$," *Acta Cryst.,* B28 3196-3200. (1972).

20. D. J. Cookson, "Calculation of Absolute Intensities from X-ray Imaging Plates", *J. Synchrotron Rad.,* 5 1375-1382. (1998).

21. I. Oftedal, "Die Gitterkonstanten von CaO, CaS, CaSe, CaTe," *Zeitschrift fuer Physikalische Chemie,* 128 135-158 (1927).

22. W. G. Mumme, "Crystal structure of tricalcium silicate from a Portland Cement clinker and its application to quantitative XRD analysis," *Nues Jahrb. Mineral., Monatsh,* 4 145-160, (1995).

Table I. Summary of clinker component information

Clinker Component	Crystal Modifications	Modifications in Clinker	Known Crystal Structures
Tricalcium silicate Ca_3SiO_5	T_1, T_2, T_3, M_1, M_2, M_3, R (polymorphs)	M_3, M_1,T_2, R	T_1, M_3, R
Dicalcium silicate Ca_2SiO_4	γ, β, α'_L, α'_H, α (polymorphs)	β	γ, β, α'_L, α'_H, α
Tricalcium aluminate $Ca_3Al_2O_6$	C_I, C_{II}, O, M (ion stabilised)	C_I, C_{II}, O	C_I, C_{II}, O, M
Tetracalcium aluminoferrite $Ca_2(Al_2O_3)_x(Fe_2O_3)_{1-x}$	Orthorhombic (Fe/Al range)	Orthorhombic	Orthorhombic

Table II. Structures used in pattern refinements of NIST SRM clinker 8488

Component	Nomenclature	Space group	Crystal system	Reference
Tricalcium silicate	C_3ST	P $\bar{1}$	Triclinic	Golovastikov *et al* [14]
	C_3SM	C 1 m 1	Monoclinic	Nishi *et al* [15]
	C_3SR	R 3 m	Trigonal (hexagonal)	Ilinets *et al* [16]
Dicalcium silicate	C_2S	P 1 21/n 1	Monoclinic	Mumme *et al* [17]
Tricalcium aluminate	C_3A	P b c a	Orthorhombic	Nishi and Takéuchi [18]
Tetracalcium aluminoferrite	C_4AF	I b m 2	Orthorhombic	Colville and Geller [19]

Table III. Figures of merit for Rietveld analysis for NIST SRM clinker 8488

Data source	R_p	R_{wp}	GOF (χ^2)
Laboratory x-ray	7.12	9.14	3.39
Synchrotron combined histograms	3.55	4.53	6.08
Synchrotron histogram 1	3.74	4.95	4.24
Synchrotron histogram 2	2.90	3.76	1.84
Neutron	3.46	4.39	5.32
Combined refinement: combined synchrotron/neutron histograms	3.68	4.71	13.04
Combined refinement: Synchrotron histogram 1	3.89	5.12	4.65
Combined refinement: Synchrotron histogram 2	2.87	3.66	1.85
Combined refinement: Neutron histogram	3.74	4.83	6.54

Table IV. QPA and component fits of NIST SRM clinker 8488 by different data sources.

Data	Sync.	Neutron	Lab. x-ray	Combined sync. and neutron	Sync. *	Neutron	Lab. x-ray	Combined sync. and neutron *
	Wt. %	Wt. %	Wt. %	Wt. %	R_B	R_B	R_B	R_B
Alite	61.0(4)	57(1)	61(2)	62(1)	-	-	-	-
C_3ST	26.5(3)	21.9(7)	17(1)	27.4(7)	H1: 2.75 H2: 1.22	2.57	5.45	H1:2.47 H2:1.50 H3:3.16
C_3SM	22.3(3)	32.5(6)	35(1)	27.7(7)	H1:2.98 H2:1.62	2.72	4.74	H1:2.57 H2:1.71 H3:3.11
C_3SR	12.1(2)	2.8(2)	8.9(7)	7.4(4)	H1: 3.57 H2:1.87	2.34	5.31	H1:3.27 H2:2.07 H3:3.29
C_2S	20.4(2)	22.7(4)	18.0(6)	20.5(4)	H1:2.17 H2:0.77	2.10	3.38	H1:2.12 H2:0.78 H3:2.47
C_3A	5.44(9)	9.6(3)	8.4(4)	4.8(1)	H1:2.58 H2:0.66	2.92	2.23	H1:1.96 H2:0.49 H3:2.35
C_4AF	13.2(1)	10.0(2)	12.5(4)	12.2(2)	H1:1.51 H2:0.92	2.01	3.96	H1:1.65 H2:1.12 H3:2.09

*Histograms were as follows: H1 = Lower 2θ synchrotron, H2 = Higher 2θ synchrotron, H3 = neutron

Table V. Comparison of QPA of NIST SRM clinker 8488 to other studies

Phase	Taylor *et al* [3] Lab. x-ray wt. %	NIST (MPC) [9] wt. %	Berliner *et al* [4] Neutron wt. %
Total alite	66(1)	65.0(6)	67.5(7)
C_3ST	40(1)	-	-
C_3SM	21(1)	-	67.5(7)
C_3SR	5.3(7)	-	-
C_2S	17.4(6)	18.5(6)	18.5(5)
C_3A total	4.3(3) (C_3A cubic and monoclinic)	4(1)	4(1) (C_3A cubic and orthorhombic)
C_4AF	12.1(4)	12(2)	7.2(1)

Table VI. Refined and original lattice parameters of components in NIST SRM clinker 8488.

Data Source	Phase	a	b	c	α	β	γ
Nishi *et al* [15]	C_3SM	33.083(8)	7.027(2)	18.499(4)	90	94.12(2)	90
XRD		33.133(5)	7.073(1)	18.599(2)	90	94.174(8)	90
Sync.		33.065(1)	7.057(2)	18.5569(5)	90	94.174(2)	90
Neutron		33.039(3)	7.0686(6)	18.570(1)	90	94.265(8)	90
Combined		33.061(1)	7.0565(4)	18.555(7)	90	94.191(3)	90
Golovastikov *et al* [14]	C_3ST	11.67	14.24	13.72	105.50	94.33	90
XRD		11.691(1)	14.096(1)	13.629(2)	105.106(6)	94.950(8)	89.96(1)
Sync.		11.6663(5)	14.0701(5)	13.6072(9)	105.076(4)	95.028(4)	89.99(1)
Neutron		11.637(2)	14.126(3)	13.635(4)	104.637(2)	94.80(2)	89.92(3)
Combined		11.6646(6)	14.0706(5)	13.6078(9)	105.062(5)	94.989(4)	90.045(6)
Ilinets *et al* [16]	C_3SR	7.0567	7.0567	24.974	90	90	120
XRD		7.0696(4)	7.0696(4)	25.074(2)	90	90	120
Sync.		7.05605(9)	7.05605(9)	25.0017(5)	90	90	120
Neutron		7.045(2)	7.045(2)	25.04(1)	90	90	120
Combined		7.0530(2)	7.0530(2)	25.003(1)	90	90	120
Mumme *et al* [17]	C_2S	5.5121	6.7575	9.3138	90	94.581	90
XRD		5.515(2)	6.775(2)	9.348(3)	90	94.16(2)	90
Sync.		5.4974(7)	6.7484(7)	9.314(1)	90	94.101(9)	90
Neutron		5.491(1)	6.754(2)	9.334(2)	90	94.22(2)	90
Combined		5.4951(7)	6.7498(8)	9.321(1)	90	94.16(1)	90
Nishi and Takéuchi[18]	C_3A	10.875(3)	10.859(3)	15.11(1)	90	90	90
XRD		11.00(1)	10.81(1)	15.140(1)	90	90	90
Sync.		10.8467(2)	10.814(2)	15.106(2)	90	90	90
Neutron		10.637(3)	10.834(3)	15.293(4)	90	90	90
Combined		10.831(2)	10.793(3)	15.110(3)	90	90	90
Colville and Geller [19]	C_4AF	5.588(5)	14.61(2)	5.380(5)	90	90	90
XRD		5.5338(2)	14.586(2)	5.345(1)	90	90	90
Sync.		5.5298(6)	14.5508(8)	5.3319(4)	90	90	90
Neutron		5.524(1)	14.568(2)	5.3352(9)	90	90	90
Combined		5.5288(6)	14.5512(9)	5.3302(4)	90	90	90

Table VII. Comparison of lattice parameters to the lab. X-ray study of Taylor *et al* [3]

Data Source x-rays	Phase	a	b	c	α	β	γ
Taylor *et al*	C_3ST	11.6499(6)	14.149(1)	13.654(1)	105.064(7)	94.835(4)	90.080(6)
This study		11.691(1)	14.096(1)	13.629(2)	105.106(6)	94.950(8)	89.96(1)
Taylor *et al*	C_3SR	7.069(1)	7.069(1)	25.045(3)	-	-	-
This study		7.0696(4)	7.0696(4)	25.074(2)	-	-	-
Taylor *et al*	C_2S	5.490(3)	6.733(4)	9.367(5)	-	93.54(5)	-
This study		5.515(2)	6.775(2)	9.348(3)	-	94.16(2)	-
Taylor *et al*	C_4AF	5.539(2)	14.576(2)	5.344(2)	-	-	-
This study		5.5338(2)	14.586(2)	5.345(1)	-	-	-

Table VIII. Comparison of lattice parameters to neutron study of Berliner *et al* [4]

Data Source neutrons	Phase	a	b	c	β
Berliner *et al*	C_3SM	33.12(1)	7.067(2)	18.565(5)	94.24(3)
This study		33.01(5)	7.0554(9)	18.541(2)	94.28(1)
Berliner *et al*	C_2S	5.499(2)	6.765(2)	9.353(3)	94.21(3)
This study		5.486(1)	6.746(1)	9.326(2)	94.23(2)
Berliner *et al*	C_4AF	5.542(2)	14.592(3)	5.331(2)	-
This study		5.520(1)	14.549(2)	5.3237(9)	-

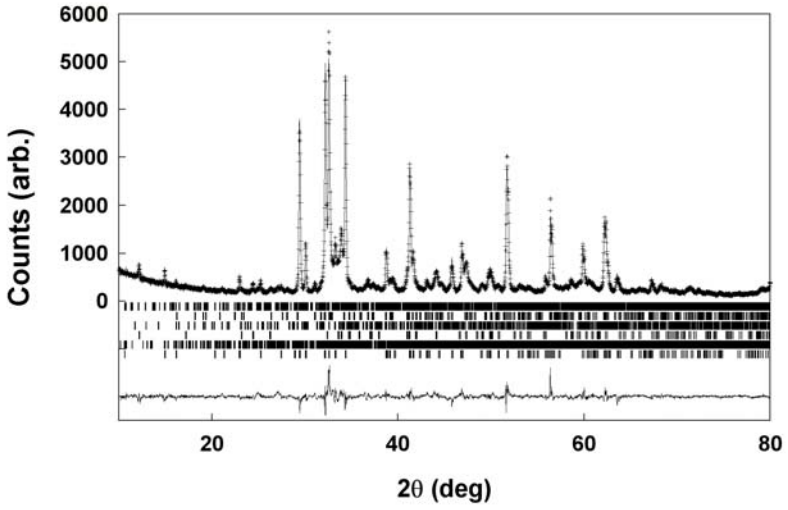

Figure 1: Rietveld refinement of NIST SRM clinker 8488 using laboratory x-ray data. The crosses are the observed data, and the solid line through the observed data is the result of the Rietveld fit. The short vertical bars mark the positions of the Bragg reflections of each phase. From top to bottom they represent the phases C_3SM, C_2S, C_3A, C_4AF, C_3ST, C_3SR. The line below the markers represents the residual or difference line.

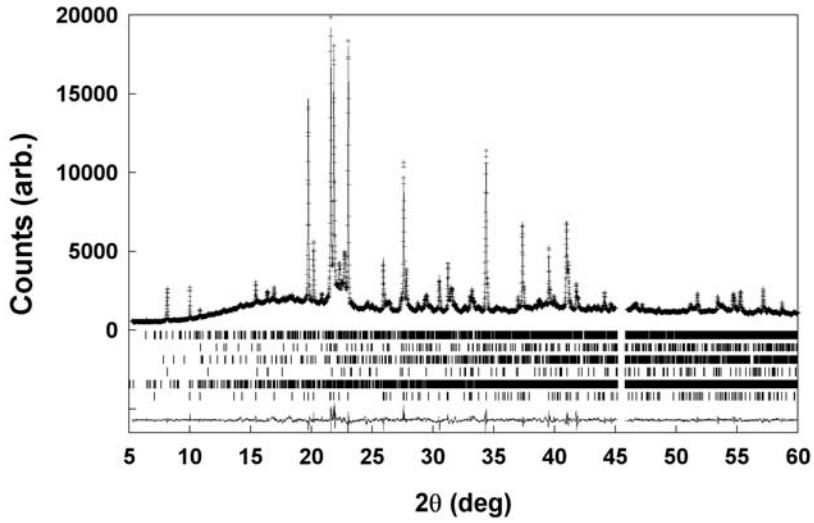

Figure 2: Rietveld refinement of NIST SRM clinker 8488 using synchrotron data. The crosses are the observed data, and the solid line through the observed data is the result of the Rietveld fit. The short vertical bars mark the positions of the Bragg reflections of each phase. From top to bottom they represent the phases C_3SM, C_2S, C_3A, C_4AF, C_3ST, C_3SR. The line below the markers represents the residual or difference line.

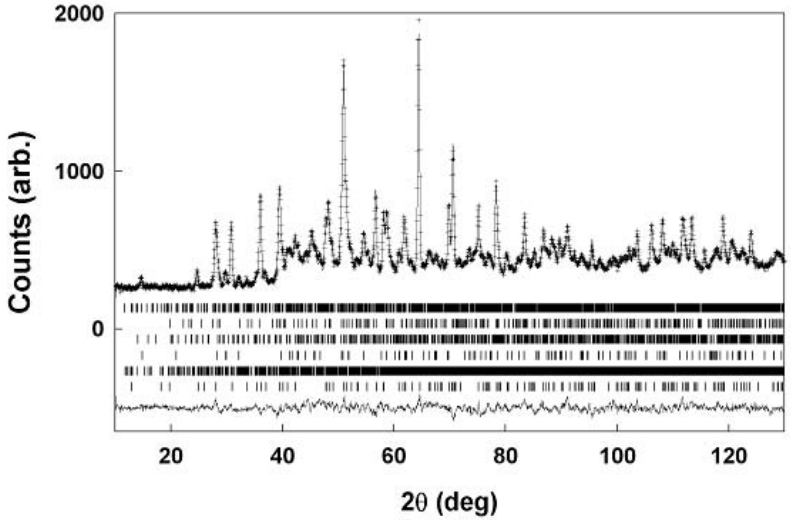

Figure 3: Rietveld refinement of NIST SRM clinker 8488 using neutron data. The crosses are the observed data, and the solid line through the observed data is the result of the Rietveld fit. The short vertical bars mark the positions of the Bragg reflections of each phase. From top to bottom they represent the phases C_3SM, C_2S, C_3A, C_4AF, C_3ST, C_3SR. The line below the markers represents the residual or difference line.

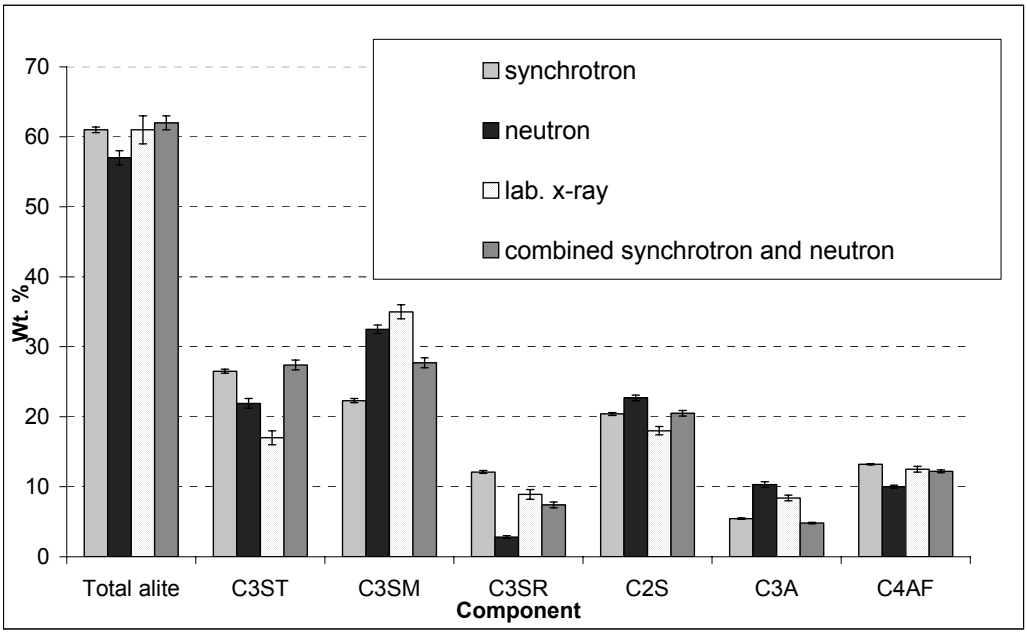

Figure 4: Comparison of quantitative phase analysis of NIST SRM clinker 8488 by different data sources.

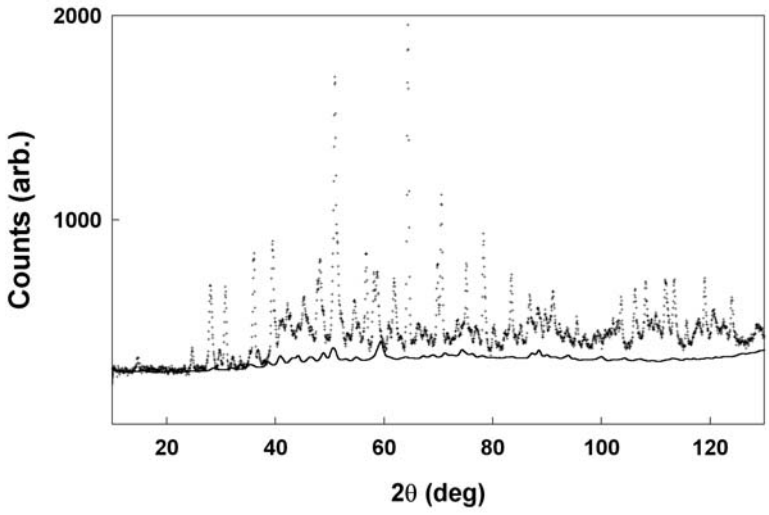

Figure 5: Model of the C_3A phase with background in relation to the neutron powder data of NIST SRM clinker 8488.

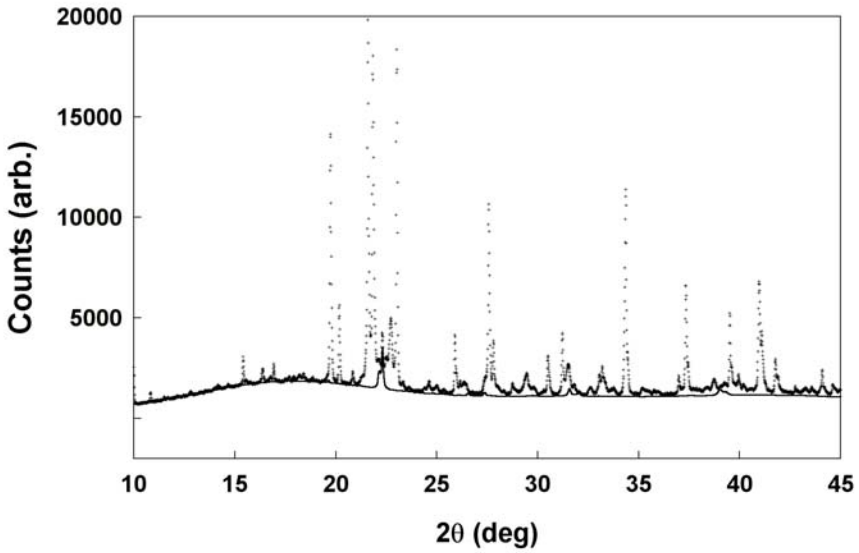

Figure 6: Model of the C_3A phase with background in relation to the synchrotron powder data of NIST SRM clinker 8488

4.3 Summary

The QPA for the main phases in the clinkers showed good agreement between different diffraction sources, and to published results including other methods.

A few deficiencies of the Rietveld method for the QPA of clinker were identified. The first was that a good mathematical fit of a refinement did not always demonstrate the best fit, or that the structural models have been chosen to adequately describe the phases. It was also found that the Rietveld model was able to incorporate missing phases and incorrect structures to give an approximation of the best fit.

Other deficiencies were identified that could be investigated further. These fell into two broad categories.

1. Quantitative results for the polymorphs of C_3S were inconsistent between diffraction sources.
   - C_3S polymorph results were found to correlate with, and affect, the QPA results for other phases. This was particularly evident with the C_2S phase.
   - Published structures for triclinic C_3S may not adequately describe the triclinic form in the clinker. This was also the case, to a lesser extent, with the monoclinic form.
   - An inadequate structural description of the alite phase may potentially cause problems with the QPA results for the other phases.
   - The less complex model for rhombohedral C_3S appeared to have the most consistent QPA results, compared to other C_3S forms. The rhombohedral C_3S form was consistently present in the least amount.

2. Reliability of the Rietveld method for QPA of clinker was thought to be linked to counting statistics and instrument resolution.
   - QPA of clinker was found difficult and results found sometimes to be unreliable when lower resolution data, such as that obtained from the lower resolution neutron and laboratory X-ray sources, was used.
   - Higher resolution data was considered to give more reliable results, however, also found to reveal C_3S superstructure reflections. This resulted in the C_3S

models used in the Rietveld analysis of higher resolution data being inadequate for the description of the modulated (non rhombohedral) types of C_3S.

- Refinement of the combined synchrotron and neutron data set was considered to give the most reliable result. This was primarily believed to be caused by the conservative error estimation resulting from the additional information.
- Results using the combined data set gave the best discrimination between the overlapping reflections of C_3S and C_2S.
- Synchrotron data was considered to give the most reliable result for a single pattern refinement.
- The neutron source used was unable to distinguish the C_3A phase.

CHAPTER 5

COMPLICATIONS OF CEMENT CLINKER ANALYSIS USING THE RIETVELD METHOD

5.1 Introduction

This chapter provides a summary of investigations based on the complex problems associated with the QPA of clinker using the Rietveld method. These include the effect of low count statistics on the validity of the Rietveld result, and an investigation into the structural deviations of the C_3S forms in the sample from the forms being modelled. The results from this work were presented in the publications "Importance of minor phase inclusion in the Rietveld analysis of cement clinkers" (Peterson *et al,* 2003a) and "Neutron diffraction investigation of structural deviations in cement clinker" (Peterson *et al,* 2002c). Both papers are reproduced in this chapter.

The results from the work presented in chapter 4 indicated there were two main causes for the inconsistencies in QPA results obtained from Rietveld analysis. The first was that data obtained from lower resolution sources or low count data, may produce different results from those obtained from higher resolution sources or data with higher counts. The second appeared as the result of a significant deviation of the C_3S form found in clinker from the form being modelled, where poorer than expected fits of C_3S phases to the data were noted. This is evidenced from the fact that the triclinic C_3S polymorph that may be present in clinker samples does not have it's structure determined, and can therefore not be modelled. As diffraction patterns for unknown polymorphs are expected to be similar to those already known, it is possible in a Rietveld model for a polymorph to compensate for those that are present, but unable to be modelled. The ability of the Rietveld model to compensate for missing phases or incorrect structures to give an approximately good fit was also revealed as a result of chapter 4.

This chapter focuses on identifying sources of error within the Rietveld method, and creating an awareness of the problems and complications that may produce results not reflective of the true composition, or quantities, of phases in clinker.

5.2 Modelling of minor phases into the Rietveld analysis of cement

The effect of variation in counting statistics on phase quantification results by the Rietveld method was investigated in this section. In order to produce a diffraction pattern in which the exact composition was known, a data set with known weight fractions was artificially simulated by a calculation from the *Z*MV relationship, shown in equation 3.48 of chapter 3. This type of investigation using simulated data had not been previously published for the investigation of Rietveld analysis of cements.

This investigation is presented in Peterson *et al* (2003a), which follows.

Peterson *et al,* 2003a

"Importance of minor phase inclusion in the Rietveld analysis of cement clinkers"

V.K. Peterson, A. Ray, and B. Hunter

Proceedings of the 11th International Congress on the Chemistry of Cement (Durban 2003), 146-150, Cement and Concrete Institute, Durban (2003).

Reproduced as published

IMPORTANCE OF MINOR PHASE INCLUSION IN THE RIETVELD ANALYSIS OF CEMENT CLINKER

V. K. Peterson[1], A. Ray[1] and B. A. Hunter[2]

[1]Department of Chemistry, Materials and Forensic Science, University of Technology, Sydney, Australia. E-mail: vkp@ansto.gov.au
[2]Neutron Scattering, Australian Nuclear Science and Technology Organisation, Menai, Australia. E-mail: bah@ansto.gov.au

ABSTRACT

The effect of minor phases on the quantitative phase analysis of cement clinker by the Rietveld method was investigated. Simulated laboratory x-ray data-sets were constructed from set quantities of cement clinker components that approximated a known clinker, with differing counting statistics. These simulated data-sets were then refined with and without prior knowledge of the phases present. In half of the refinements the smallest weight percentage phase, the rhombohedral tricalcium silicate phase, was not included in the refinement. Comparison of the phase quantification results obtained from these different strategies showed that in the refinements from the high count data-set, the phase quantities were not significantly disturbed by not including the minor phase, whereas the refinements using the low count data-set showed a large variation in phase quantification results. This has implications for the interpretation of quantitative phase analysis results from low count data such as obtained from on-line cement analysis.

1. INTRODUCTION

There has been an increase in the use of Rietveld refinement of powder diffraction data for the quantitative phase analysis of cement and analysis of cement components in recent years [1]. The complex nature of cement clinker components and structural modifications of each phase makes phase quantification of cement clinker difficult. Although Rietveld provides the most consistent results for even the interstitial phases, overlapping phase peaks from the multiphase system in diffraction patterns further complicated phase analysis by this method.

Major phases present in clinker are tricalcium silicate (Ca_3SiO_5), dicalcium silicate (Ca_2SiO_4), tricalcium aluminate ($Ca_3Al_2O_3$), and tetracalcium aluminoferrite ($Ca_2(Al_2O_3)_x(Fe_2O_3)_{1-x}$). Clinker composition is complicated by the crystal modification of some of these phases. The solid solution of tricalcium silicate in cement is called alite. Three structural models are commonly used in the Rietveld analysis of cement clinkers, including a triclinic, a monoclinic and a rhombohedral model. Only one of the dicalcium silicate polymorphs has been shown likely to be present in cement clinkers, the monoclinic ß-type. Tricalcium aluminate exists in three modifications, a monoclinic, an orthorhombic, and a cubic type, through ion substitution. The cubic and orthorhombic modifications of this phase are likely to be present in clinker. Tetracalcium aluminoferrite appears in one form, with a varying Al:Fe ratio.

Rietveld analysis techniques are currently applied to on-line powder diffraction data from cement clinker directly from the kiln. A common practise is to refine until a good figure of merit is achieved. One of the problems with the Rietveld analysis of cement clinkers is the existence of

Proceedings of the 11th International Congress on the Chemistry of Cement (ICCC)
'Cement's Contribution to the Development in the 21st Century'
Hosted by: The Cement and Concrete Institute of South Africa
CD-ROM produced by: Document Transformation Technologies
11 - 16 May 2003, Durban, South Africa
ISBN Number: 0-9584085-8-0
Editors: Dr G. Grieve and G. Owens
Congress Organised by: Event Dynamics

multiple small weight percentage phases. Often these smaller phases can exist below the detectable limit for Rietveld methods, which is dependent on the size and complexity of the unit cell being modelled. The compounded effect of multiple missing phases in the Rietveld model means that if the fit of the model to the data is still good despite multiple missing phases, then the model is compensating for these missing phases which could generate incorrect results. If the Rietveld analysis model is being used for phase quantification purposes, the effect of missing phases could result in incorrect quantitative phase analysis of the clinker material.

2. EXPERIMENTAL

Simulated data was used as a tool for investigating the effect of minor phases on Rietveld analysis of data with differing counting statistics. Cement clinker powder diffraction data-sets were simulated using the Rietveld program Rietica [2]. Typical counting intensities were modelled from real data collected using Cu Kα radiation on the Scintag x-ray diffractometer at the Australian Nuclear Science and Technology Organisation (Scintag X1, Scintag Instruments, U.S.A.). Data were simulated over the range $2\theta = 2.00 - 90.00°$ with a stepping of 0.02°. A single-term 5^{th} order polynomial function was used to model the background, and peak shape parameters were based on real cement clinker sample data taken from the instrument that was simulated. Rietveld scale factors were calculated from weight percentages based on real clinker compositions using the ZMV relationship [3], where Z is the number of formula units per unit cell, M is the mass of the formula unit and V is the unit cell volume. Instrumental noise was simulated using a random number generator with a normal distribution. Two data-sets were generated, one known as the high count data-set, where counting statistics resulted in the most intense peak from the pattern having an intensity of around 3000 counts, the other known as the low count data-set, where this peak had an intensity of around 600 counts. The background term used in the low count data-set was $1/5^{th}$ of that used in the high count data-set. Modelled phase compositions were based on a real ordinary Portland cement clinker composition. The model constitution is outlined in Table 1.

Table 1. Component structures and composition used in data simulation

Phase	Structural reference	Wt. % from ZMV
Alite	-	61.14
Tricalcium silicate triclinic	T_1 [4]	19.84
Tricalcium silicate monoclinic	M_3 [5]	38.86
Tricalcium silicate rhombohedral	R [6]	2.44
Dicalcium silicate	β [7]	17.07
Tricalcium aluminate	Orthorhombic [8]	9.21
Tetracalcium aluminoferrite	Orthorhombic [9]	12.58

Each data-set was at first refined with a new refinement data file, and approached with prior knowledge of all phases present, but without knowledge of peak shapes, scale factors, or any refinable parameters. This was known as refinement strategy number 1. The next refinement was performed in the same manner as the first, but approached as a blind data-set refinement, without prior knowledge of the phases present. This was known as refinement strategy number 2. Refinements were deemed finished when no further significant improvement in fit could be made.

3. RESULTS AND DISCUSSION

Table 2 shows the ZMV calculated or "ideal" phase quantities, as well as the phase quantification results for the two refinements made for each data-set. The Rietveld figures of merit R_p and Goodness Of Fit (GOF) are listed in Table 3. In the first column of Table 3, the figures of merit are based on fits of the ideal input to the simulated data without refinement of any parameter. In the case of refinement strategy 2 of both data-sets, the fits of the model to the data were deemed good

enough to not to continue searching for any further phases. The approach to Rietveld refinement of a cement clinker data-set often involves the search for one polymorph of tricalcium silicate at a time. As the rhombohedral modification of tricalcium silicate is usually present in much lower quantities than all other polymorphs, if at all, it is usual to include this as a final step of phase identification. Hence refinements using strategy number 2 did not include the search for this phase. Inspection of the difference line did not yield visual clues to the possibility of a missing phase. The intensity of the largest reflection from this phase was observed as approximately 135 counts in the low count data-set, and 675 counts in the high count data-set.

In Figures 1-4, crosses represent the observed data, and the solid line through the observed data is the result of the Rietveld fit. The line below the markers represents the residual or difference line.

Figures 1 and 2 represent refinements of the high count data-set, and Figures 3 and 4 represent refinements of the low count data-set. The short vertical bars mark the positions of the Bragg reflections of each phase. Figures 1 and 3 represent refinements with all phases present, and peak markers from top to bottom represent the phases triclinic tricalcium silicate, rhombohedral tricalcium silicate, dicalcium silicate, monoclinic tricalcium silicate, tricalcium aluminate and tetracalcium aluminoferrite respectively. Figures 2 and 4 represent refinements without the rhombohedral tricalcium silicate phase present, and peak markers from top to bottom represent the phases triclinic tricalcium silicate, dicalcium silicate, monoclinic tricalcium silicate, tricalcium aluminate and tetracalcium aluminoferrite respectively.

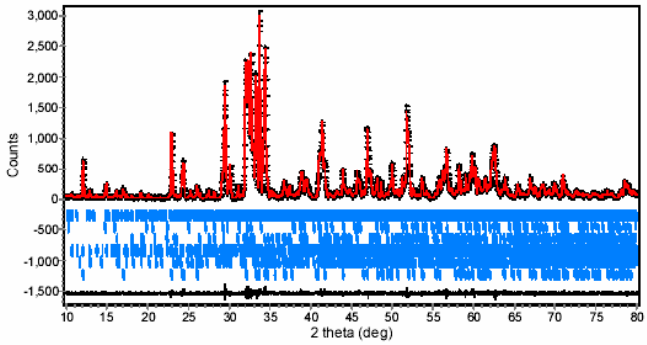

Figure 1. High count data-set refinement with all phases.

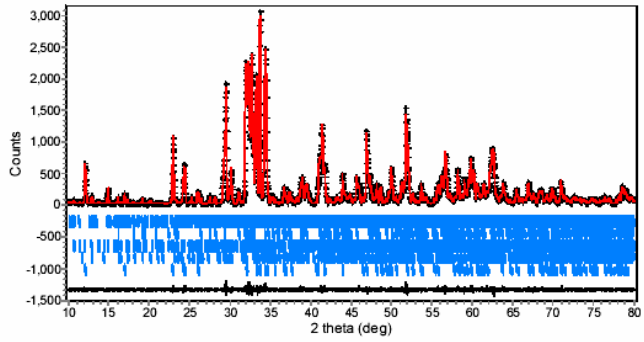

Figure 2. High count data-set refinement not including rhombohedral tricalcium silicate

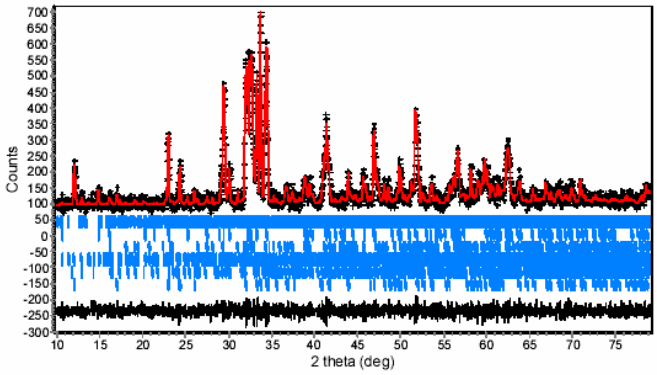

Figure 3. Low count data-set refinement with all phases

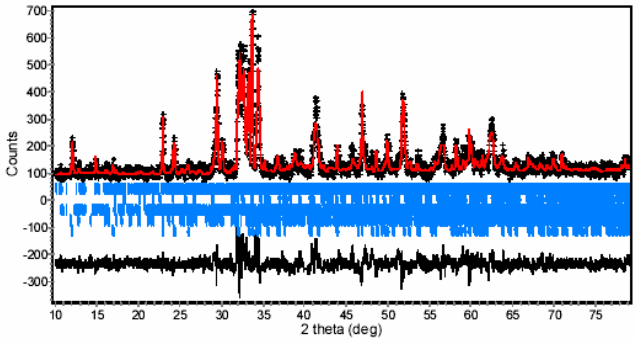

Figure 4. Low count data-set refinement not including rhombohedral tricalcium silicate

Table 2. Phase quantification results from refinements of the low and high count data-sets

	Wt. % "Ideal"	Wt. % 6 phases	Wt. % 5 phases	Wt. % 6 phases	Wt. % 5 phases
Phase/Refinement		1 (High count)	2 (High count)	1 (Low count)	2 (Low count)
Alite	61.1	61.4(5)	61.5(3)	62.4(9)	72.1(7)
Ca_3SiO_5 T_1	19.8	20.0(3)	20.1(2)	20.0(6)	69(1)
Ca_3SiO_5 M_3	38.9	39.1(5)	41.9(3)	41(1)	2.8(4)
Ca_3SiO_5 R	2.4	2.4(3)	Not inc.	1.71(6)	Not inc.
Ca_2SiO_4	17.1	16.8(2)	16.9(2)	16.0(5)	4.9(5)
$Ca_3Al_2O_3$	9.2	9.2(1)	9.1(1)	9.0(3)	9.8(4)
Ca_2FeAlO_5	12.58	12.63(9)	12.56(7)	12.6(2)	13.3(2)

Table 3. Figures of merit for refinements of the low and high count data-sets

Figures of merit/Refinement	"Ideal"	Refinement 1 6 phases	Refinement 2 5 phases
GOF (High count)	1.031	1.030	1.051
Rp (High count)	3.002	2.993	3.027
GOF (Low count)	1.036	1.022	2.266
Rp (Low count)	6.653	6.662	9.913

As expected, Rietveld figures of merit were generally better for the refinements of the high count data-set than for those of the low count data-set, although refinement strategy number 1 of the low count data-set resulted in an unusually good GOF, even when compared to the "ideal" GOF. This result was not reflected in the R_p value. In both data-sets, refinement with all phases (refinement

strategy number 1) resulted in better Rietveld figures of merit than were obtained from using refinement strategy number 2, where a phase was missing from each model.

Refinement using strategy number 1 of both data-sets, where all phases were used, yielded phase quantification results near to the "ideal" amounts. Refinement strategy number 2, where the rhombohedral modification of tricalcium silicate was not modelled, yielded similar results to the "ideal" amounts from the high count data-set, but the low count data-set exhibited some large phase quantification variations. The most significant differences in results between the two data-sets using the refinement strategy number 2 was the weight percentages of tricalcium silicate and dicalcium silicate phases. Using refinement strategy number 2 and the high count data-set, an amount of dicalcium silicate and tricalcium silicate polymorphs (both the triclinic and monoclinic forms) similar to the ideal quantity was found. The corresponding refinement of the low count data-set however, resulted in approximately 71wt. % less dicalcium silicate, 245 wt. % more triclinic tricalcium silicate, 93 wt. % less monoclinic tricalcium silicate, and 18 wt. % more total alite than was found using refinement strategy number 1. This result is alarming, as the incorrect result is not reflected in the figure of merit, which is still reasonably good. The amounts of tricalcium aluminate and tetracalcium aluminoferrite phases found using refinement strategies 1 and 2 were not notably different.

Rietveld packages specifically designed to give phase quantification results of cement clinker are being increasingly used in industry, and although they represent the best routine analysis methods available, they are limited by the statistics available from the data count rates. The tricalcium and dicalcium silicate phase in cement powder diffraction patterns are heavily overlapped and the effect of this can be detrimental to phase quantification results from Rietveld analysis, especially at lower count rates when resolution becomes an issue. As the powder patterns for the polymorphs of tricalcium silicate are similar, it is difficult to locate which polymorphs are present in clinker, although it is important that care be taken to look for all polymorphs. Low count data appears to be more prone to false refinement minima during Rietveld analysis that the high count data.

ACKNOWLEDGEMENTS

This work forms part of a PhD thesis to be submitted by V. Peterson. The research project is funded by an Australian PhD and an Australian Institute of Nuclear Science and Engineering post-graduate award.

REFERENCES

[1] Peterson, V.K., Ray, A. and Hunter, B.A. Rietveld phase quantification of cement clinker using powder diffraction data, Journal of the American Ceramics Society, submitted for publication.
[2] Hunter, B. Rietica – A visual Rietveld program, Powder Diffraction Newsletter, vol.20, 1999, pp. 21.
[3] Hill, R.J. and Howard, C.J. Quantitative phase analysis from neutron powder diffraction data using the Rietveld method, Journal of Applied Crystallography, vol.20, 1987, pp. 467-474.
[4] Golovastikov, N.I., Matveera, R.G. and Belov, N.V. Crystal structure of the tricalcium silicate 3CaO.SiO2 = C3S, Sov. Phys. Crystallogr. Vol.20, 1975, pp. 721-729.
[5] Nishi, F., Takèuchi, Y. and Maki, I. Tricalcium silicate Ca3O[SiO4]: The monoclinic superstructure, Zeitschrift fur Krystallographie, vol.72 1985, pp. 297-314.
[6] Ilinets, A.M., Malinovskii, Y. and Nevskii, N.N. Crystal structure of the rhombohedral modification of tricalcium silicate Ca3SiO5, Dokl. Akad. Nauk SSSR, vol. 281, 1985, pp. 191-193.
[7] Mumme, W.G., Hill, R.J., Bushnell-Wye G. and Segnit, E.R. Rietveld crystal structure refinements, crystal chemistry and calculated powder diffraction data for the polymorphs of dicalcium silicate, Neues Jahrb. Mineral., Abh., vol. 169, 1995, pp. 35-68.
[8] Nishi, F. and Takèuchi, Y. The Al6O18 rings of tetrahedra in the structure of Ca8.5NaAl6O18, Acta Cryst., vol. B31, 1975, pp. 1169-1173.
[9] Colville, A.A. and Geller, S. Crystal structures of Ca2Fe1.43Al0.57O5 and Ca2Fe1.28Al0.72O5, Acta Cryst., vol. B28, 1972, pp. 3196-3200.

5.3 Structural deviations of tricalcium silicate in clinker

This investigation concentrated on the differences between C_3S polymorphs present in the clinker and those used in the Rietveld model. The effects of atomic shifts between the refinement and original structural model of the C_3S phases in clinker were investigated. This was done via a comparison of the Bragg-R factors, R_B, (fit) of phases to the data before and after atomic position refinement.

Differences in C_3S forms are believed to involve the orientation of the SiO_4 tetrahedra. A neutron source was therefore chosen for locating the O atoms of C_3S in the Ca/Si rich environment, as the atomic positions of the oxygen atoms were to be refined in the Rietveld model.

From previous experiments on the NIST clinker 8488 (chapter 4) it is known that both triclinic and monoclinic types of C_3S are present. The monoclinic phase in clinker has been shown to be primarily M_3, whilst the triclinic phase in clinker, if present, is usually the T_2 form (Taylor, 1997). The C_3S structural model that exists for the monoclinic type is the M_3 form, however, the triclinic model represents the T_1 modification. It was therefore expected that the monoclinic phase would deviate less than the triclinic phase, after refinement of the Rietveld model to fit the data from this clinker.

This investigation was presented in Peterson *et al,* (2002c), which follows.

Peterson *et al,* 2002c

"Neutron diffraction investigation of structural deviations in cement clinker"

V.K. Peterson, B. Hunter, and A. Ray

Proceedings of the Australian Institute of Physics 15th Biennial Congress (Sydney 2002), 1-3, AIP, Sydney (2002)

Presented as published.

Australian Institute of Physics
15th Biennial Congress

8 - 11 July 2002
Sydney

NEUTRON DIFFRACTION INVESTIGATION OF STRUCTURAL DEVIATIONS IN CEMENT CLINKER

Vanessa K. PETERSON[1], Brett A. HUNTER[2] and Abhi RAY[1]

1. University of Technology Sydney
PO Box 123, Broadway, NSW, 2007.
vkp@ansto.gov.au
2. Australian Nuclear Science and Technology Organisation, PMB 1, Menai, NSW, 2234.

Abstract

This paper reports the changes in quantitative phase analysis (QPA) and figures of merit from Rietveld refinement of neutron powder diffraction data of cement clinker when atomic positions of the main phases are refined. A previous study reported that less than a 1% (average) alteration to bond distances resulted in an approximately 25% improvement in the fits of a tricalcium silicate phase [1]. As a synchrotron source was used, the atomic positions of the oxygen atoms were not refined. The phases in cement all have more than 50 % oxygen atoms, and neutron data was expected to be better for this investigation. In this neutron study, relatively minor adjustments to the structures also resulted in decreased R-Bragg factors (R_B) of tricalcium silicate phases with very little changes to the average Ca-O bond distances.

Phases typically present in clinker are tricalcium silicate (Ca_3SiO_5 or C3S), dicalcium silicate (Ca_2SiO_4 or C2S), tricalcium aluminate ($Ca_3Al_2O_6$ or C3A), and tetracalcium aluminoferrite ($Ca_2(Al_2O_3)_x(Fe_2O_3)_{1-x}$ or C4AF). Rietveld analysis of clinker is complicated by the crystal modification of many of these phases. At least seven C3S polymorphs exist and only three have fully determined structures. These are the triclinic T_1, the monoclinic M_3, and rhombohedral R. Differences in polymorphs of the same space group are believed to involve shifts of some atomic positions, without changes to the symmetry. For C2S, one type has been shown likely to be present in clinker. C3A has three modifications, all found, whilst C4AF appears with a varying Al:Fe ratio.

The polymorphic identification of C3S types in cement has the potential to be extremely useful for industrial applications. Polymorphs have been shown to possess different strength properties, based on varying rates of hydration [2]. Rietveld methods have the ability to define the C3S form. It is usual to include a polymorph of one of each of the three crystal systems encountered when beginning a refinement, and then exclude the crystal system(s) not found.

Experimental

Neutron diffraction data were obtained from the High Resolution Powder Diffractometer at the High Flux Australian Reactor. NIST SRM clinker 8488 was loaded into a vanadium can which was rotated during data acquisition. Data over the range 2θ = 0.0 - 153.0° was obtained using steps of 0.05°. The wavelength of the neutrons was determined as 1.8823(1) Å, using the NIST 674 standard. Rietveld refinement was performed using Rietica [3]. Refinement results with and without atomic position refinement of the C3S phases were compared. Identical structures to [1]

ISBN 0-9598064-4-X

were used in refinements of this study. Subsequent calculations involving the Ca-O bond lengths were performed with bond lengths up to 3.000 Å.

Results and Discussion

Refinement of the atomic positions of the C3S R phase induced instability in the model. This was thought to be caused by the relatively small weight fraction of this phase. In subsequent refinements atomic positions of this phase were unrefined.
Refinement results are presented in Tables 1 and 2. Figure 1 shows a typical residual plot.

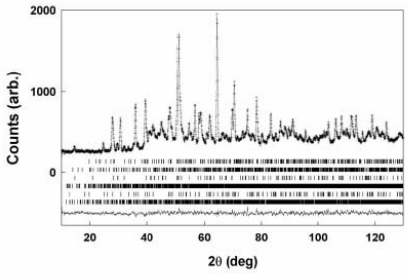

Figure 1: Residual plot with atomic position refinement of both C3SM and T phases

The figures of merit R_p, χ^2 and R_B generally improved with atomic position refinement of the C3S phases. The most significant improvement was noticed upon refinement of the T_1 C3S model. Poorer fits of the C3S phases where atomic positions were not refined may have been caused by crystallographic differences between the modelled and real structures, as present in the clinker. These structural deviations may have been absorbed into the model by other phases, as evidenced by the improved R_B values for all phases after atomic position refinement of only the C3S T model. It is generally accepted that T_2 is the triclinic C3S modification likely to be present in clinker [4]. The T_1 model of Golovastikov *et al* [5] is the only triclinic form that has fully known structural details. The deviation of the refinement results of the T_1 model in the clinker from the original T_1 structure suggests that this phase in the clinker could possibly be T_2 and not T_1. Marginal improvements in the R_p and χ^2 whole pattern figures of merit were noted after refinement of the C3S M phase, and some R_B values actually increased. This could have been caused by the C3S M model absorbing problems associated with the C3S T model, as the best figures of merit were achieved after atomic position refinement in both of these phases.
Changes in the QPA of the C3SM and T phases were noted upon refinement of their atomic positions. The total C3S (alite) remained approximately the same, with only a small increase in the amount found. The C3S R and C2S phases also remained approximately the same. The C3A phase showed significant deviation in the QPA result, however other studies [6] have noted difficulty in identification of this phase using neutron data due to the heavily overlapping peaks in the fingerprint region of this phase. The QPA of the C3A was therefore thought not to be accurate.

ISBN 0-9598064-4-X

Table 1: Whole pattern figures of merits and bond distances.

Phase of atomic refinement	Unrefined	C3SM (537 atomic position parameters) (2277 reflections)	C3ST (237 atomic position parameters) (4046 reflections)	C3S T and C3SM
R_p	3.39	3.19	2.83	2.56
χ^2	4.91	4.34	3.33	2.80
Ca-O average length (Å)	2.431 (T_1) 2.422 (M_3)	2.421	2.443	2.428 (T_1) 2.421 (M_3)

Table 2: Individual phase quantifications and figures of merit

	Unrefined	C3SM	C3ST	C3ST and C3S M	Unrefined	C3SM	C3ST	C3ST and C3SM
Phase	Wt. %	Wt. %	Wt. %	Wt. %	R_B	R_B	R_B	R_B
Alite	57(1)	58.0(9)	58.4(6)	61.5(7)	-	-	-	-
C3SM	32.5(6)	35.0(6)	31.7(4)	34.7(5)	2.58	2.94	1.85	1.57
C3ST	21.9(7)	20.2(1)	23.2(5)	24.2(5)	2.40	2.36	1.61	1.33
C3SR	2.8(2)	2.8(2)	2.8(2)	2.6(1)	2.27	2.66	1.74	1.53
C2S	22.7(4)	21.4(4)	21.7(3)	20.4(3)	1.99	1.61	1.29	1.00
C3A	10.3(4)	9.6(3)	9.4(3)	8.6(3)	1.92	1.45	1.29	0.84
C4AF	10.0(2)	13.2(1)	11.2(2)	11.0(1)	2.02	1.58	1.57	0.98

Conclusion

Refinement of the atomic positions of the main phase of cement clinker from neutron data resulted in better figures of merit. This was thought to have been caused by crystallographic alterations to the pure structures caused by the presence of tricalcium silicate polymorphs. In particular, the greatest deviation in structure occurred in the T_1 modification of tricalcium silicate.

References

1. Peterson, V. K., Hunter, B., Ray, A. and Aldridge, L. P. Rietveld refinement of neutron, synchrotron and combined powder diffraction data of cement clinker, In press, *Applied Physics A (ICNS 2001 Proceedings).*
2. Harada, T., Ohta, M. and Takagi, S. 1977. Effect of polymorphism of tricalcium silicate on structure and strength characteristics of hardened cement paste, *Japan. Rev. Gen. Meet., Tech. Sess. - Cem. Assoc. Jpn.* 31:31-33..
3. Hunter, B. 1999. Rietica – A visual Rietveld program, *Powder Diffraction Newsletter,* 20: 21.
4. Taylor, H. F. W. 1997. Cement Chemistry. *Thomas Telford, London.*
5. Golovastikov, N. I., Matveeva, R. G. and Belov, N. V. 1975. Crystal structure of the tricalcium silicate $3CaO.SiO_2 = C_3S$, *Sov. Phys. Crystallogr.* 20: 721-729
6. Peterson, V. K., Hunter, B. and Ray, A. Rietveld phase quantification of cement clinker using diffraction data. Submitted for publication.

ISBN 0-9598064-4-X © 2002 AIP

5.4 Summary

Two deficiencies of the Rietveld method for the QPA of clinker were investigated.

The first was the link between the quality of data used in the Rietveld refinement to the reliability of the results. Results obtained using a low intensity source, where data collection time would be unreasonably high to produce significant counts, were investigated in terms of counting statistics and instrument resolution.

The second was the identification/quantification of C_3S polymorphs in clinker, and the ability of the structural models to describe C_3S forms in the clinker.

Numerous problems associated with refinements using lower quality data were identified:

- Rietveld models of low-count clinker data were more prone to false minimum than high-count data.
- Data with less information was found to artificially reduce the GOF factors from the Rietveld refinement. This data was found to hide errors, resulting in incorrect QPA results.
- QPA results were more reliable when all clinker phases, including multiple C_3S polymorphs, were present in the Rietveld models. The inclusion of all phases present into the Rietveld model was believed to be a necessity for a meaningful result in the case of low-count data.
- Heavily overlapping C_3S and C_2S diffraction patterns were found to be detrimental to the QPA results from Rietveld analysis for all phases, particularly for low-count data where resolution may become an issue.

Determination of the polymorphic type(s) present in the clinker was difficult. The main reasons for this were identified and included:

- The similarity between diffraction patterns for C_3S polymorphs.
- The structural models for C_3S were shown to be poor crystallographic representations of the polymorphs in clinker, particularly for the triclinic (T_1) model.

- Inadequate structural models for the triclinic forms of C_3S resulted in the structural deviation (compensation) of other C_3S polymorph models to better describe the entire alite phase.

CHAPTER 6

STRUCTURAL INVESTIGATION OF TRICALCIUM SILICATE

6.1 Introduction

The work reported in this chapter involved a study of the crystallographic structure of triclinic C_3S. Investigations based on solving new structures for unknown triclinic C_3S polymorphs, and yielding information concerning the mechanisms of transitions between polymorphs, were performed. The results of this work are presented in "Tricalcium silicate T_1 and T_2 polymorphic investigations: Rietveld refinement at various temperatures using synchrotron powder diffraction" (Peterson *et al,* 2003b), which is currently under review and is reproduced in this chapter. The structure of the T_1 modulated C_3S form was also investigated. This investigation is presented at the end of the chapter.

C_3S is the principle hydraulic phase of clinker, having the decisive impact on the strength of OPC. In solid solutions, the various polymorphs of C_3S occur in stabilised form, and hence they can be studied at room temperature. Since alite is a C_3S solid solution and the main constituent of cement clinker, these investigations are of practical importance in understanding the nature of the alite phase in cement clinker.

Of the seven known C_3S polymorphs, the T_2, T_3, and M_1 modifications do not have their structures determined. Of the triclinic polymorphs, the T_2 form is the triclinic form most likely to be present in clinker (Taylor, 1997). The only structural model currently available to describe the triclinic forms of C_3S (Golovastikov *et al,* 1975) was shown, in the previous chapter (Peterson *et al,* 2002c), to be inadequate for the description of the triclinic form found in clinker.

In addition to the missing structural information concerning C_3S forms, there exist unexplained phenomena in the DTA curves of C_3S. One such phenomenon is a small broad peak at approximately 675 °C found by Miyabe and Roy (1964) in the DTA of pure C_3S. The feature was attributed to the β C_2S-α' C_2S transition, despite the fact that a pure C_3S sample was used in the experiment. Another poorly understood feature of the

DTA curve of C_3S is the large transformation enthalpy of the T_3-T_2 transition. Bigaré *et al* (1967) suggested the energy anomaly was possibly caused by the existence of a superstructure that exists in T_1 and T_2, but not in T_3, accompanied by a doubling of the a and b axis in the superstructures.

There has been a recent surge in publications involving the investigation of missing polymorphs from the C_3S series (de Noirfontaine *et al,* 2003) (Urabe *et al,* 2002) (De La Torre *et al*, 2002) (Morita *et al,* 2002) (Urabe *et al*, 2000) (Shirakami *et al,* 1999) (Viani *et al*, 1998). Despite these investigations, no new structural models for any polymorphs of C_3S, further information on the mechanism of the transitions, or structural behaviour during the transitions has been published. The differences between triclinic C_3S forms and the phenomena of the high-energy requirement of the transition between triclinic forms of C_3S remains unexplained.

There are several benefits to be gained from the structural solution of all C_3S polymorphs. These can be separated into the following categories:

1. Accurate QPA of the C_3S polymorphs using Rietveld analysis would be possible for the first time.

2. Knowledge of transition mechanics between polymorphs would be gained.
   The clarification of the alite form in clinker would improve the reliability of QPA results for all phases in clinker.

3. There exists the possibility for the incorporation of a reliable alite description into the Rietveld analysis of on-line diffraction data, from clinker as it emerges from the kiln.
   The implication of this ability for industry is the automatic adjustment of kiln feed materials and process optimisation, for the production of hydraulically favourable polymorphs and phase combinations.

This chapter focuses on investigations into the crystallographic structures of triclinic C_3S polymorphs and the differences between the forms.

6.2 Polymorphic investigations

This investigation involved analysis of the T_1 and T_2 type C_3S polymorphic components of cement clinker in their pure form. Identifying the polymorphs is difficult using conventional diffraction equipment. Observing a change in the structure, or difference between structures, can give a clearer indication of which polymorph is present. By using high-resolution Synchrotron X-ray Powder Diffraction (SXRPD) during in-situ heating of the sample, crystallographic changes can be observed and a structural solution attempted using Rietveld analysis. Important new information concerning the T_2 polymorph structure and the mechanism of T_1-T_2 transition was expected.

Four attempts were made, one successful, to collect reliable data containing useful information on the triclinic C_3S forms. These are outlined in sections 6.2.1-6.2.3. The C_3S sample analysed in each case was the same sample obtained from Construction Technology Laboratories (CTL) Inc., Illinois, USA. The sample was analysed using X-ray Fluorescence, DTA, and powder diffraction, as described in the following sections and in Peterson *et al* (2003b).

6.2.1 Neutron investigation of polymorphism

Neutron diffraction was thought appropriate for the determination of oxygen atomic positions, in different polymorphs, as it was successfully applied to the study of the previous chapter, concerning structural deviations in C_3S. A phase pure C_3S type T_1 sample was loaded into a stainless steel can and neutron powder diffraction data was collected using the HRPD at HIFAR. The sample was rotated, during heating in a P1700 furnace, and data was collected for 24 hours per pattern. The neutron wavelength was determined to be 1.8823 Å using the NIST Al_2O_3 674 standard. Rietveld refinement was performed using Rietica (Hunter, 1999). C_3S was modelled using the Golovastikov *et al* (1975) structure and the Nishi *et al* (1985) structure. The iron can was modelled using the structure of Basinski *et al* (1955). Data is represented in the Rietveld refinement plots shown in Figures 4.0-4.7. In Figures 4.0-4.7, the short blue vertical bars are reflection markers for the phases. The data points are shown in black, the calculation from the model is shown in red, and the residual plot in green.

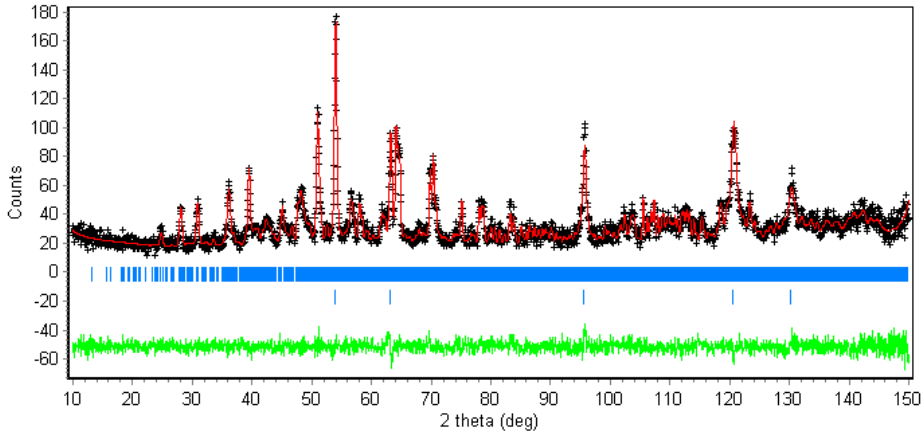

Figure 6.1: Refinement plot of neutron data of C_3S at ambient temperature.

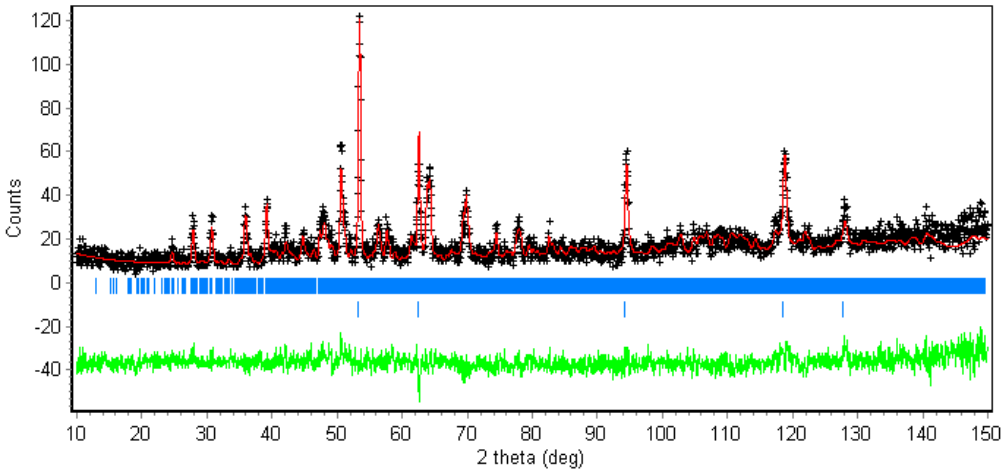

Figure 6.2: Refinement plot of neutron data of C_3S at approximately 570 °C.

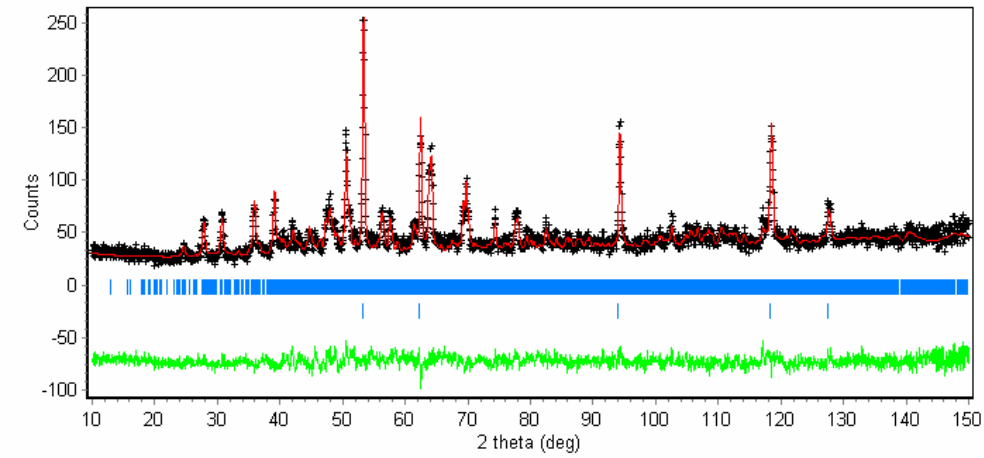

Figure 6.3: Refinement plot of neutron data of C_3S at approximately 670 °C.

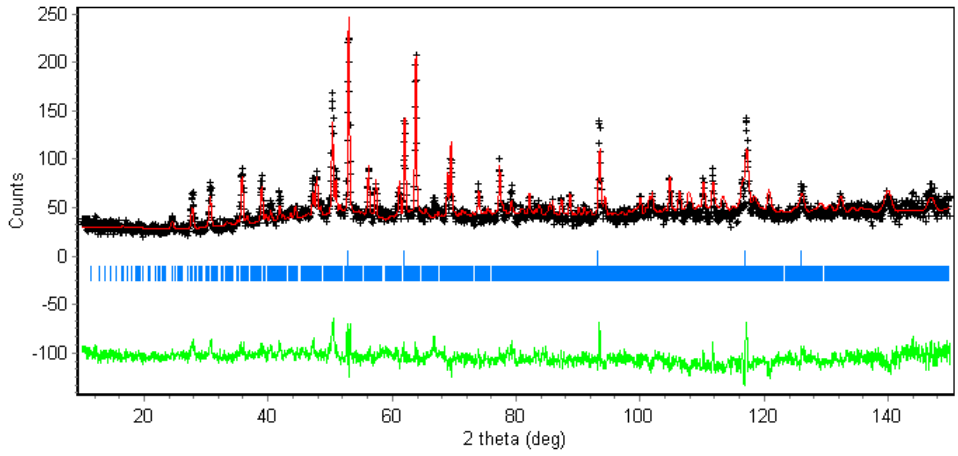

Figure 6.4: Refinement plot of neutron data of C_3S at approximately 950 °C.

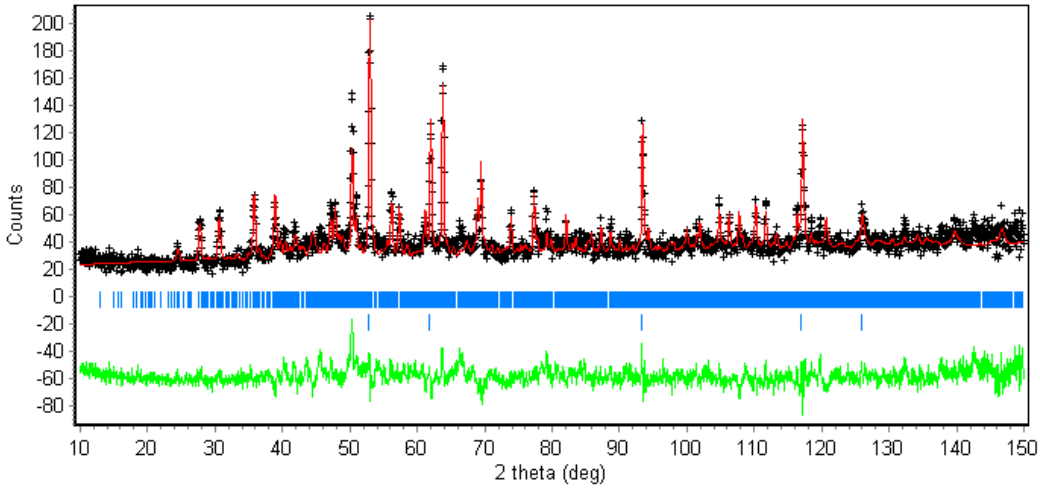

Figure 6.5: Refinement plot of neutron data of C_3S at approximately 980 °C.

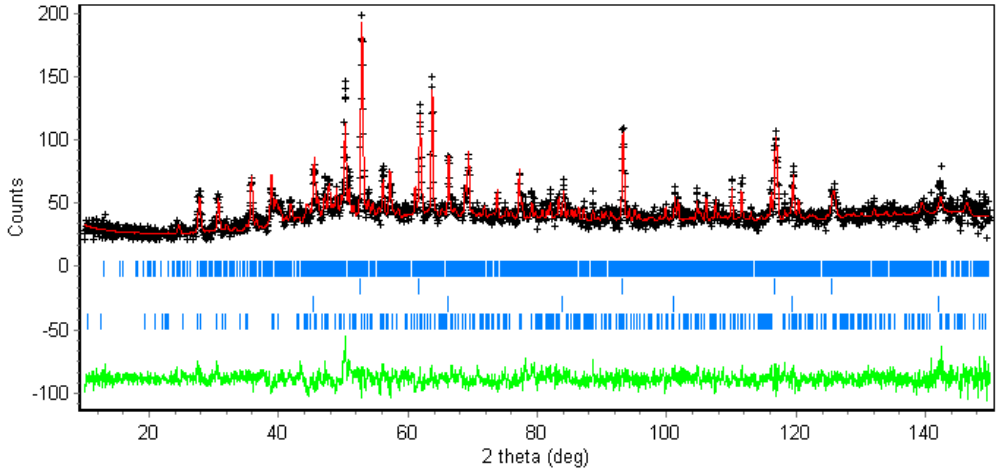

Figure 6.6: Refinement plot of neutron data of C_3S at approximately 1035 °C

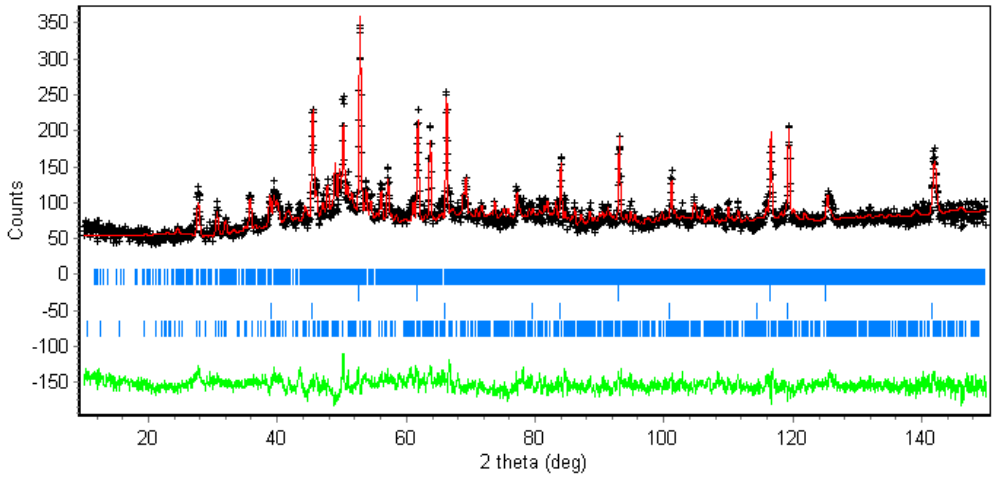

Figure 6.7: Refinement plot of neutron data of C_3S at approximately 1120 °C.

Figures 6.1-6.7 exhibit a range of fits of the model to the data. In most cases, the refinement was performed with data of lower statistics than expected. Diffraction of the complex sample using this source resulted in a poorer resolution of the pattern reflections than was expected. This resulted in a significant problem concerning overlapping reflections of the complex tricalcium silicate phase, and it was difficult to determine if the phase was monoclinic or triclinic. Consequently, Rietveld refinement was difficult, and any structural solutions of the polymorphs were unable to be extracted from this data. The long data acquisition times from this neutron source meant that the collection of further data from this source, suitable for C_3S structural solution, was not feasible.

In addition to the above problem, figures 6.6 and 6.7 represent patterns in which sample degradation was evident. It is possible that patterns as early in the heating as figure 6.2 reflect this. Degradation products of C_3S in these cases were identified as crystalline α'_L C_2S and amorphous CaO. The α'_L C_2S phase was included in the refinement using the structural model of Udagawa *et al* (1979). These products were consistent with those noted in the literature (Taylor, 1997). The degradation of C_3S is known to be accelerated by the presence of its degradation products (Carlson, 1931). Consistent with this, further degradation was observed at higher temperatures.

6.2.2 Synchrotron investigation of polymorphism at the High Energy Accelerator Research Organisation, Japan.

To increase counts and resolution, synchrotron radiation was used next for the investigation of C_3S polymorphism. Experiments were performed using the high-resolution powder diffractometer at the Australian National Beamline Facility (ANBF) on beam line 20B at the High Energy Accelerator Research Organisation (KEK), Japan.

Synchrotron diffraction data were collected at the ANBF at the KEK, Japan. A wavelength of 1.04461(1) Å was determined using the NIST standard Al_2O_3 674. Clinker was sealed in glass capillary tube of approximately 0.3 mm diameter, which was rotated during data collection. Image plate detectors were used over the 2θ range 2.00-40.00 ° on the first plate and 45.00-70.00 ° on the second, with a step of 0.010 °.

The advantage of synchrotron radiation over lower resolution sources for the investigation of the tricalcium silicate form is illustrated below. The illustration is made simple by the use of the same data type, in this case synchrotron X-ray and laboratory X-ray radiation. Figures 6.8 and 6.9 show the same set of reflections from the same C_3S sample obtained from CTL at room temperature, using laboratory X-rays and high-energy X-rays (from synchrotron radiation at the ANBF) respectively. Laboratory X-ray powder data was collected primarily using Cu Kα radiation (Scintag X1, Scintag Instruments, USA). Clinker was loaded onto a flat-plate sample holder. Data were collected over the 2θ range 2.00-90.00 ° with a step of 0.02 °.

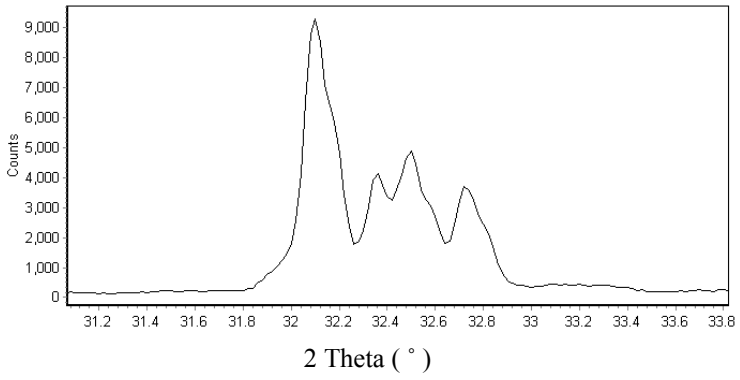

Figure 6.8: Laboratory X-ray data showing reflections of C_3S at ambient temperature.

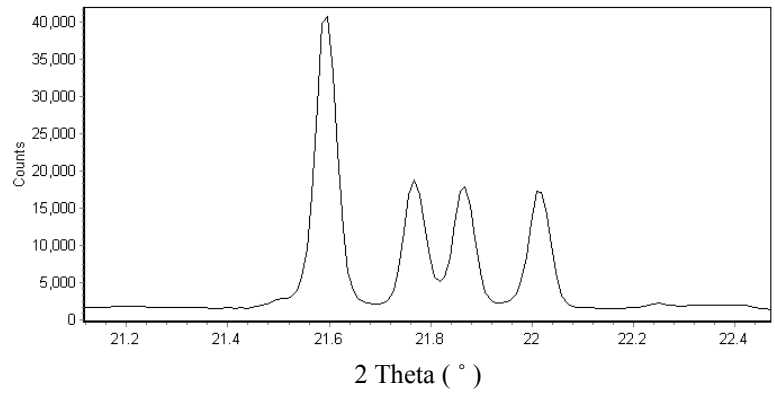

Figure 6.9: Synchrotron data showing reflections of C_3S at ambient temperature.

The lower resolution X-ray source is observed, in figure 6.8, to interfere with the reflection independence. This resulted in obscured information and complex peak shapes for the Rietveld model. Figure 6.9 shows clear resolution of individual reflections.

For the investigation of polymorphism, a furnace with capabilities to approximately 1000 ° C was devised by Dr Cliff Ball of ANSTO and modified by the author for use with the diffractometer. Data was collected for 10 minutes per pattern. Figure 6.10 shows the sample in the furnace during heating.

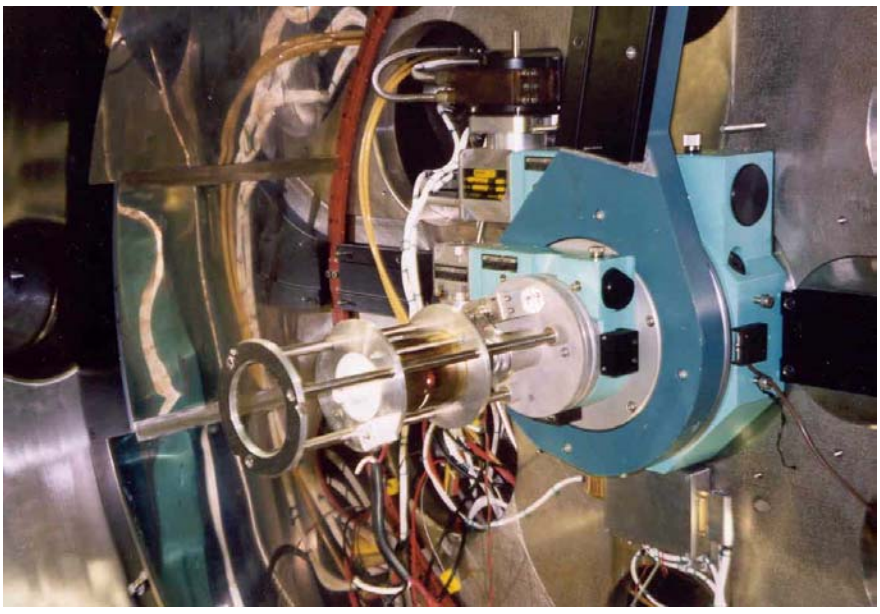

Figure 6.10: Experimental set-up showing in-situ furnace on beam line 20B at the KEK synchrotron, Japan.

Figure 6.11 shows off-set synchrotron data plots of intensity versus 2θ.

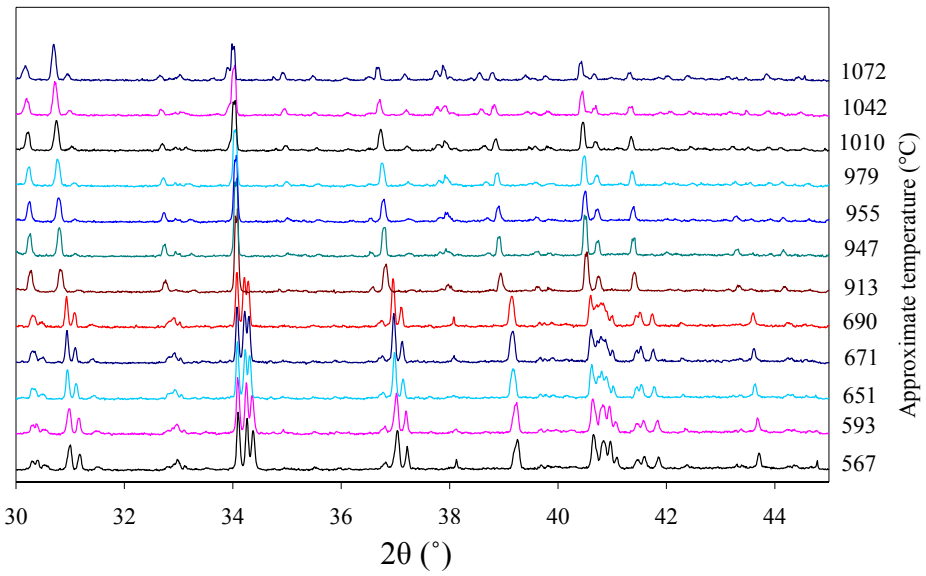

Figure 6.11: Synchrotron data of C_3S at various temperatures taken on beam line 20B, KEK, Japan.

At temperatures above 1000 °C, other phases appeared in the diffraction pattern. These were identified in the higher temperature data as the decomposition products α'_L C_2S and poorly crystalline CaO. These were recognised as the same products that were identified in the neutron powder diffraction experiment of section 6.2.1. An intense reflection also appeared to emerge from the amorphous lump characteristic of the sample capillary. A quartz phase was thought to be responsible for the emergent reflection, caused by crystallisation of the amorphous glass sample tube. This hypothesis was evidenced by the fact that upon cooling, the tube became fragile and crumbled. The exact crystalline quartz phase was unable to be identified, although many quartz structures had strong reflections in this region.

The contamination of the already congested diffraction pattern with additional reflections, contributed from the two decomposition products and the quartz phase, made Rietveld analysis of the data difficult. The subtle differences between the powder diffraction patterns of triclinic C_3S forms were swamped by additional reflections, particularly from the α'_L C_2S phase, which heavily overlapped the C_3S reflections. Hence, structural solutions for any of the C_3S polymorphs in the patterns were unable to be obtained.

6.2.3 Synchrotron investigation of polymorphism at the National Synchrotron Light Source, USA

The necessary evacuation of the sample chamber for use with the image plate detector system, used in the previous synchrotron experiment (section 6.2.2), was thought to have contributed to the degradation of the C_3S. An alternative to the image plate system is the Position Sensitive Detector (PSD), which allow experiments to be carried out in an air atmosphere. Beam line X7A at the National Synchrotron Light Source (NSLS) at Brookhaven National Laboratories (BNL), USA, has a PSD available for use with their powder diffractometer. An experiment similar to the one in section 6.2.2 was devised. Figure 6.12 shows the experimental set-up with the sample, furnace, and Kr PSD.

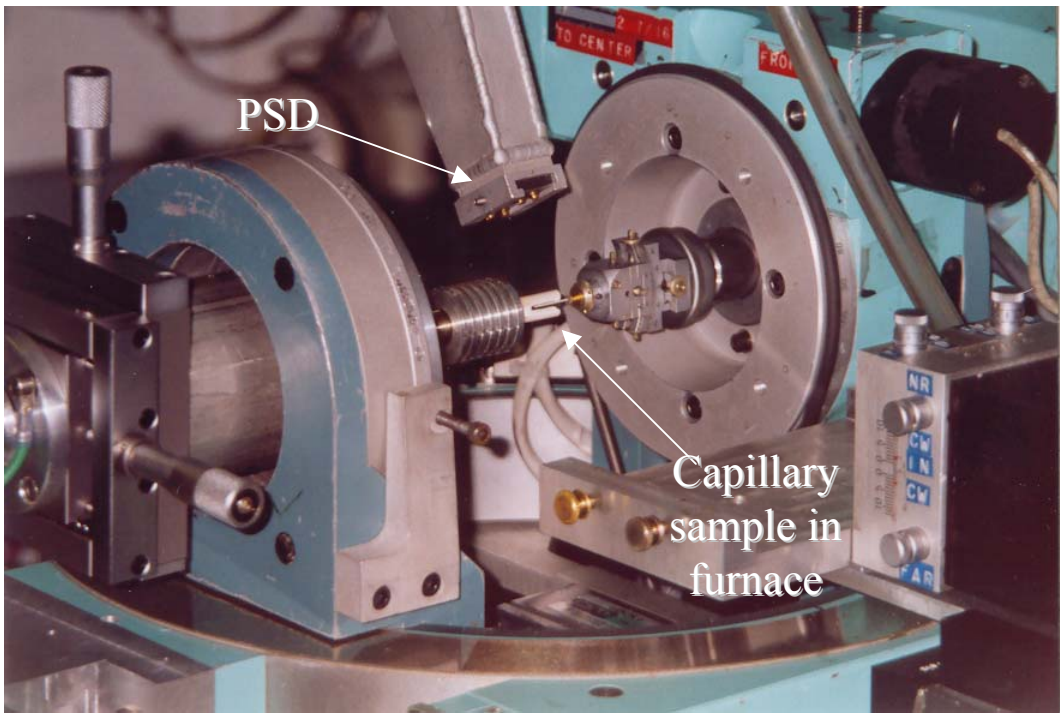

Figure: 6.12: Experimental set-up on beam line X7A at the NSLS, BNL, USA

The details and results of this successful investigation were presented in Peterson *et al* (2003b), which follows and is currently under review.

Peterson *et al,* 2003b

"Tricalcium silicate T_1 and T_2 polymorphic investigations: Rietveld refinement at various temperatures using synchrotron powder diffraction"

V.K. Peterson, B. Hunter, and A. Ray

Journal of the American Ceramics Society, (2003).
Under Review

Reproduced as submitted

Tricalcium silicate T_1 and T_2 polymorphic investigations: Rietveld refinement at various temperatures using synchrotron powder diffraction*.

Vanessa K. Peterson[a], Brett A. Hunter[b] and Abhi Ray[a]

[a]*Department of Chemistry, Materials and Forensic Science, University of Technology Sydney.*
Broadway. NSW. 2007. Australia.
[b]*Australian Nuclear Science and Technology Organisation.*
Menai. NSW. 2234. Australia.

Abstract

The lattice parameters, cell volume, and structure of a sample of phase pure triclinic tricalcium silicate were determined using in-situ high temperature synchrotron powder diffraction and full profile Rietveld refinement. The temperature range covered was from ambient to 740 °C. Evidence of superstructure was found. The T_2 type structure with disordered SiO_4 tetrahedra was observed, and an average structure for the sub-cell ($P\bar{1}$, a = 11.7416(2) Å, b = 14.2785(2) Å, c = 13.7732(2) Å, α = 105.129(1) º, β = 94.415(1) º, γ = 89.889(1) º), is presented. Differential thermal analysis and x-ray fluorescence was also performed.

Introduction

Solid solutions of tricalcium silicate are the major constituent of Portland cement clinker. Currently there are seven known modifications of pure tricalcium silicate: three triclinic, three monoclinic, and a rhombohedral form. These modifications are reported to appear via successive, reversible, phase transitions when heated, occurring in the following sequence [1]:

$$T_1 \overset{620\,^\circ C}{\longleftrightarrow} T_2 \overset{920\,^\circ C}{\longleftrightarrow} T_3 \overset{980\,^\circ C}{\longleftrightarrow} M_1 \overset{990\,^\circ C}{\longleftrightarrow} M_2 \overset{1060\,^\circ C}{\longleftrightarrow} M_3 \overset{1070\,^\circ C}{\longleftrightarrow} R$$

Transition temperatures have been previously investigated by diffraction, microscopy and thermal methods, and a summary of these investigations was presented by Bigaré *et*

* Based in part on the thesis to be submitted by V. K. Peterson for the degree of Ph.D. in Science, University of Technology, Sydney. Supported by an Australian Post-Graduate Award, and a Post-

al [2]. In the triclinic series, the T_1-T_2 transition is invisible to microscopy methods, while the T_2-T_3 transition is thought to be invisible to diffraction methods. Thermal analysis methods such as Differential Thermal Analysis (DTA) have shown the T_1-T_2 transition as a broad, reversible peak with an extremely small transformation enthalpy, and strong hysteresis. Strangely, the T_2-T_3 transition has the largest transformation enthalpy of all the transitions. The T_1-T_2 and T_2-T_3 transitions have so far been characterised as discontinuous [2].

The only forms to have fully determined structures are the T_1 [3], M_3 [4, 5] and R [6, 7] modifications, although the forms likely to be present in clinker are the M_3, M_1 and T_2 modifications [1]. Recently there has been a surge in interest in the structural analysis of unknown tricalcium silicate polymorphs [8-14].

Structural differences within the same space group are believed to involve shifts in some of the atomic positions, in particular the oxygen atoms of the SiO_4 tetrahedra. Two possible calcium sites have been established in the monoclinic system, and the Ca location is thought to be dependent on the orientations of the nearby SiO_4 tetrahedra [4]. Rietveld analysis is being used increasingly for the phase quantification of components in cement clinker, however, the original tricalcium silicate structures deviate significantly after refinement [15]. This implies that the tricalcium silicate structures being modelled do not adequately describe those found in clinker. As a result, the quantification of the total amount of tricalcium silicate is consistent, but the amount of each polymorph found varies. It is possible that the polymorphs of tricalcium silicate being modelled will compensate for phases not being modelled, leading to errors, potentially for all phases concerned. Quantification of the polymorphs of tricalcium silicate has the potential to be extremely useful to industrial applications. Harada *et al* [16] showed that each polymorph has a different rate of hydration, which was reflected in their resultant strength properties. Mascolo *et al* [17], noted that the compressive strength of the polymorphs appeared related to the type of stabilising ion entering the lattice. Recently, a link between tricalcium silicate polymorphism and strength of cement was demonstrated by Staněk and Sulovský [18], (although no reference to the earlier works of Harada *et al* [15] or Mascolo *et al* [17] was made). Taylor *et al* [19] and Peterson *et al* [20] recently highlighted the importance of including tricalcium

Graduate Research Award provided by the Australian Institute of Nuclear Science and Engineering.

silicate polymorphs in the Rietveld model for the phase quantification of cement clinker, and noted that quantitative analysis of these polymorphs can be obtained using powder diffraction and Rietveld analysis.

Structurally solving tricalcium silicate polymorphs would allow a better understanding of the relationship between polymorphs and analogous crystal systems. In addition, the applications to cement would be the identification and quantification of polymorphs in clinker. These benefits would allow better quantification of other phases through the improvement of the entire Rietveld model. In addition, the incorporation of tricalcium silicate polymorphic analysis into on-line systems would mean process optimisation and the possibility for the production of hydraulically favourable polymorphs.

This investigation aimed at yielding a structural solution for the T_2 tricalcium silicate polymorph, and exposing information on the T_1-T_2 transition.

Experimental

Synchrotron X-Ray Powder Diffraction (SXRPD) was performed using the powder diffractometer on beamline X7A at the National Synchrotron Light Source (NSLS) at Brookhaven National Laboratories (BNL) in Upton, U.S.A. Tricalcium silicate powder sample was inserted into a 0.2 mm "quartz" type capillary, and the end sealed. The sample was rotated in the furnace during data acquisition. The wavelength used was determined as 0.70321(3) Å using the NIST CeO_2 674 standard. Data acquisition lasted approximately 1 hour per pattern. The x-ray beam incident to the sample was 2 mm wide by 0.8 mm high. The furnace temperature was calibrated separately to the experimental run using the known thermal expansion of NaCl. A Kr position sensitive detector meant that the sample capillary could be heated without a vacuum during data collection from 2-50 ° with a step size of 0.01. Heating tricalcium silicate in a vacuum was thought to be the cause of sample degradation in previous experiments [21]. This caused the presence of other phases in the data and resulted in multiphase Rietveld analysis.

Initially, a sample was heated in approximately 100 °C steps to 770 °C, however, upon inspection of the pattern acquired at the top temperature, crystalline quartz peaks could be seen emerging from the amorphous background, visible as a broad bump in the low

two-theta range. The capillary shattered upon cooling of this sample, also indicating that crystallisation of the tube had occurred. The process was repeated, but heating only to 760 °C, and then cooling to 470 °C, where no crystallisation of the capillary occurred. Patterns were taken in approximately 20 °C increments during lattice expansion/contraction and at intervals approximately every 10 °C around anticipated transition temperatures.

Rietveld refinements were performed using the programs Rietica [22] and GSAS [23]. A pseudo-Voigt peak shape [24] with FCJ asymmetry function [25] was employed. A 24- term Chebyshev type I background function was used for modelling in Rietica, whilst a 36-term Chebyshev function was used in GSAS.

X-Ray Fluorescence (XRF) analysis was performed on a PW 2400 XRF instrument (Philips) at the Australian Nuclear Science and Technology Organisation (ANSTO). Two samples of approximate mass 7372 mg and 2670 mg were analysed as loose powder samples under He, using Uni Quant V 5.03 (Omega data systems bv, Netherlands). Four standards were analysed and subtracted from the background: F, Si, Al and $CaPO_4$.

DTA was performed at the University of Technology, Sydney using a SDT 2960 (TA Instruments, U.S.A.). The software used was Thermal Solution OS2 Warp V 3.0 (IBM, U.S.A.). Sample size was approximately 14.23 mg, and was measured using a heating rate of 10 °C / min for four cycles of heating to 1200 °C then cooling to 400 °C. The DTA data was transformed into its first-derivative form using Origin (Origin V 7.03, OriginLab Corporation, U.S.A.), and represented as derivative DTA data to enhance the features.

Results and discussion

XRF analysis

Both samples contained minimal amounts of MgO, Al_2O_3, and Fe_2O_3. Analysis showed 0.17(2) wt. % and 0.19(1) wt. % MgO, 0.10(1) and 0.09(1) wt. % Al_2O_3 and 0.053(3) and 0.045(2) wt. % Fe_2O_3 in the first and second analyses respectively. All other impurities were present at a concentration of less than 100 mg/kg. From these results it

was assumed that no impurities were present at a level contributing to any significant stabilisation of high temperature polymorphs or effects on the crystal chemistry.

Differential Thermal Analysis

DTA results are shown in figure 1. The DTA curve was not unusual for a T_1 type tricalcium silicate, with three main features present in the DTA curve. Temperature features of the derivative DTA curve are listed in table I. The first feature is a broad, reversible peak exhibiting strong hysteresis. This feature was attributed to the T_1-T_2 transformation [2]. This assignment was not unreasonably different from the SXRD determined transition point of approximately 590 °C for the heating cycle, discussed later. As no transition was observed upon cooling to 500 °C, this would be consistent with a hysteretic transition temperature. The differences between these transition temperatures could be explained by lag in the DTA determined temperature, the different heating rates used, as well as experimental error. This transition temperature appeared consistent between heating cycles with a range of 681 – 685 °C, however during cooling the transition temperature was variable, with a range of 549 – 589 °C recorded. This made the hysteresis of this transition between 92 and 136 °C between heating and cooling cycles, consistent with a first order type.

The second feature is the largest peak on the DTA curve, and has in the literature been assigned to the T_2-T_3 transition [2]. It is thought that at this point the triclinic superstructure 2a, 2b, c becomes a, b, c [2]. This peak was consistent in location within both the heating and cooling cycles, appearing in the ranges 913-916 °C and 885-887 °C respectively. A less marked hysteresis of this peak, 28-31 °C was observed, which has previously been commented upon [2]. The third feature is a peak not exhibiting notable hysteresis (9-12 °C), and that has in the literature been assigned to the T_3 – M_1 transition. This was located at 961-964 °C during heating, and at 952 °C during cooling.

Analysis of diffraction data

Powder diffraction data collected during heating are shown in figure 2. After Rietveld refinement of each pattern using Rietica, the cell parameters, and the calculated cell

volume were extracted. In these refinements, the internal T_1 structure was fixed to that of Golovastikov *et al* [3].

Figure 3 shows a calculated pattern of the Golovastikov *et al* [3] T_1 structure using instrumental parameters identical to collection SXRPD conditions on the instrument used. Figure 4-6 show refinement plots of data at ambient, and at the two higher temperature points, I and II. Figures 3-7 feature insets of the fingerprint regions unique to different polymorphs. Bigaré *et al* [2], and more recently, Urabe *et al* [12], presented laboratory x-ray powder diffraction studies on the tricalcium silicate type T_1. Both studies found characteristic reflections in the fingerprint regions that resembled T_1 of this study (shown inset in figures 4 and 5), and not of the Golovastikov *et al* [2] structure (shown inset in figure 3). This suggests that the Golovastikov *et al* [2] structure may not be appropriate model, particularly for powder diffraction.

Variation of cell volume with temperature is shown in figure 1, and variation of cell parameters a, b, c and α, β, γ with temperature are reported in figures 8a and 8b respectively. Figures 1, 8a, and 8b also show the corresponding section of DTA heating and cooling traces (for the first cycle). Figure 1 shows no appreciable change in the rate of change of cell volume, that is, no discontinuities. Lattice parameters in figures 8a and 8b show broad changes consistent with the literature T_1-T_2 transition temperature [1]. Interestingly, lattice parameter γ exhibited a unique angular contraction just prior to the transition. Figure 11 from the publication of Bigaré *et al* [1], shows a similar trend of the γ lattice parameter, although the number of data points in the figure were few and it was not commented upon in the publication. This figure was apparently taken from work by Regourd [26], although no such figure was located in the latter. Point I was designated as high temperature T_1 as it exists just previous to the transition, and point II was designated as T_2 as it exists just after the transition.

At the T_1-T_2 transition point a sudden increase in the instrumental zero error parameter in the refinement model occurred. Before the transition, all data converged to give an instrumental zero error of –0.009(1) º, and after the transition, beginning with the first data-set of the transition, refinements converged to give identical values of an amount 0.015 º greater than the previous values. If refinements are fixed to –0.009(1) º, there is

a sudden decrease in the volume of the calculated cell at the transition point. Similarly, a sudden discontinuity in cell parameters a, b and c was also observed upon fixing the zero of the data-set refinements after the T_1-T_2 transition point. Upon examination of the correlation matrix for the refinements, the zero parameter is observed to strongly correlate (approximately 80 %) with the cell parameters a, b, and c. The zero parameter was however, not observed to strongly correlate to the parameters α, β and γ. Parameters α, β and γ exhibited a broad transition T_1 –T_2, over the approximate temperature range 565(21)-685(28) º C (including 20 º C data-steps), irrespective of the instrumental zero, that is, in both cases with and without zero refinement. The parameters a, b and c closely resembled this broad transition if the zero parameter was refined. The figures of merit for Rietveld refinement of the data after the transition also were also reduced by a factor of approximately 2 if the zero was refined. For these reasons, the zero was refined in all data-sets. Why there was a small increase in the instrumental zero of 0.015 º at exactly the transition point T_1-T_2 is unknown.

Identification of superstructure

Table II presents the figures of merit for Rietveld refinements using Rietica, of the T_1 and T_2 structural data using the Golovastikov *et al* [3] structure as a starting model only. The χ^2 values seemed abnormally high for both the T_1 and T_2 polymorphs. Upon close inspection of the powder diffraction patterns, more reflections were clearly visible in the T_1 (ambient and high temperature) than were in the T_2 structure. These are highlighted in figure 9. A significant portion of the literature seems to indicate the existence of a triclinic superstructure. This was first proposed by Bigaré *et al* [2] to explain the large peak in the DTA curve of tricalcium silicate, representing a transition within the same space-group (T_2 – T_3). This feature could be explained by the collapse of a superstructure that exists in T_1 and T_2, but not in T_3. The concept of a possible second doubling of the a and b axis in the T_1 structure was also proposed by Bigaré *et al* [2]. Any super-lattice reflections would be evident at lower two-theta range, and would reduce with temperature. Previous results from lower resolution neutron and laboratory x-ray sources have shown excellent agreement with the Golovastikov *et al* [3] structure of T_1 [21], although the synchrotron results of this study did not. Table II shows a very high χ^2 factor for the sub-cell refinement of the T_1 (ambient) tricalcium silicate data. The χ^2 factor appeared to decrease consistently with temperature. The poor fit revealed by the high χ^2 was though to have been caused by the exposure of additional sample

information by the higher resolution data source not accounted for in the Golovastikov *et al* model. Upon casual inspection of the residual Rietveld plots in figures 4-7, the fits appear excellent, but upon closer inspection of the smaller reflections, the model does not appear to fit the data. The model appears to fit the data better at higher temperatures. This would be consistent with the reduction of superlattice reflections with heating. The $T_{2\text{-}3}$ transition data listed in table II, and was determined as being part of the T_2-T_3 transition from the decrease in "superstructure" seen by the sharp decrease in the fit of the sub-cell model to this data. The Rietveld refinement plot for this data is shown in figure 7.

Upon inspection of the T_2 average structure obtained using Rietica, it was found that the SiO_4 tetrahedra were highly distorted. The Si-O bond lengths varied from as low as 1.16 Å as high as 2.11 Å. The O-Si-O bond angles also showed significant deviation from the tetrahedral angle. Considering the evidence for existence of a superstructure in this system, the tetrahedral distortion observed could represent an average structure of a larger super-cell in which repeating SiO_4 tetrahedral units have various orientations.

Lattice parameter information for the refined T_1 and T_2 structures using Rietica are listed in table III. The calcium – oxygen average coordination was calculated for the structures, with exclusion to bonds greater than 3.0 Å. These are listed in table IV. There appears to be a steady decrease in the Ca-O coordination number with temperature, until the $T_{2\text{-}3}$ dataset.

Modelling of the sub-cell distortion and average structure in T_2

The average T_2 structure was re-investigated using GSAS, by the refinement of data at point II, with the addition of soft constraints on Si-O bond lengths and O-Si-O bond angles. The T_1 model of Golovastikov *et al* [3] was used as a starting model for the refinements. When Si-O bond lengths were restricted to 1.64(6) Å, using a weighting factor of F = 500, the Si-O bonds were able to be maintained within a single standard deviation of the prescribed restriction with only very minor effect on the χ^2. When the O-Si-O bond angles were constrained to 109(5) °, the minimum achievable χ^2 was 1107. These results further supported the theory that the SiO_4 tetrahedral distortion was due a disordered structure, possibly due to an apparent superstructure. Figure 10 shows

a Rietveld refinement plot of the GSAS refinement. In this refinement, a χ^2 of 7.115 and R_p of 0.0293 % were achieved, for 289 variables. The number of observations was 16286, and 36 Si-O bond restraints were applied. The Ca-O average coordination, excluding bonds greater than 3 Å, was 6.148. The average structure for the T_2 sub-cell is presented in tables V and VI, where all atoms are fully occupied. Tetrahedral bond lengths and angles are reported in tables VII and VIII respectively. Figure 11 shows atomic representation of the T_2 average structure, produced using the program Atoms [27]. The hexagonal basal plane that exists in the rhombohedral polymorph in the <001> plane and is common to all other polymorphs with differing degrees of deformation was located and highlighted within the structure using a yellow outline. In this figure, silicon - oxygen tetrahedra with central silicon atoms are shown as filled tetrahedra. Polyligand oxygen atoms that form SiO_4 tetrahedra are shown with small radii, whilst those that form part of Ca-O bonds are larger in radius. Calcium atoms are the remaining dark, larger atoms. The unit cell is highlighted by a black box. In the average structure, the most distortion was evident in the Si4 tetrahedra.

Summary

The T_1-T_2 structural transition of tricalcium silicate was investigated using high-temperature SXRD with Rietveld refinement of the sub-cell lattice parameters. The T_1-T_2, T_2-T_3 and T_3-M_1 transitions were observed using DTA. The T_1 and T_2 phases were shown to exhibit superstructure. The T_2 structure was investigated using an average sub-cell structure. The average sub-cell was determined to be $P\bar{1}$, with lattice parameters a = 11.7416(2) Å, b = 14.2785(2) Å, c = 13.7732(2) Å, α = 105.129(1) º, β = 94.415(1) º, and γ = 89.889(1) º. The new T_2 average sub-cell structure exhibited distorted SiO_4 tetrahedral angles.

Acknowledgments

The authors wish to thank Australia's Access to Major Research Facilities Program for additional support. Thanks to Drs Yoongjae Lee and Tom Vogt from BNL. XRF thanks to Ned Blagojevic from ANSTO for assistance gathering XRF data, and to Jean-Pierre Guerbois from UTS for assistance gathering DTA data.

References

1. H. F. W. Taylor, *Cement Chemistry.* Thomas Telford, London, 1997.

2. M. Bigaré, A. Guinier, C. Mazières, M. Regourd, N. Yannaquis, W. Eysel, T. Hahn and E. Woermann, "Polymorphism of tricalcium silicate and its solid solutions" *J. Am. Ceram. Soc.* 50 609-619 (1967).

3. N. I. Golovastikov, R. G. Matveera, N. V. Belov, "Crystal structure of the tricalcium silicate $3CaO.SiO_2 = C_3S$," *Sov. Phys. Crystallogr.* 20 721-729 (1975).

4. W. G. Mumme, "Crystal structure of tricalcium silicate from a Portland Cement clinker and its application to quantitative XRD analysis," *Nues Jahrb. Mineral., Monatsh,* 4 145-160, (1995).

5. F. Nishi, Y. Takèuchi and I. Maki "Tricalcium silicate $Ca_3O[SiO_4]$: The monoclinic superstructure," *Zeitschrift fur Krystallographie,* 172 297-314 (1985).

6. A. M. Ilinets, Y. Malinovskii and N. N. Nevskii, "Crystal structure of the rhombohedral modification of tricalcium silicate Ca_3SiO_5," *Dokl. Akad. Nauk SSSR,* 281 191-193 (1985).

7. F. Nishi and Y. Takéuchi, "The rhombohedral structure of tricalcium silicate at 1200 ºC", *Zeit. Krist.* **168,** 197-212 (1984).

8. M. –N. de Noirfontaine, F. Dunstetter, M. Courtial, G. Gasecki, and M. Signes-Frehel, "Tricalcium silicate Ca_3SiO_5, the major component of anhydrous Portland cement: on the conservation of distances and directions and their relationship to the structural elements" *Zeit. Krist.* **218,** 8-11 (2003).

9. H. Morita, H. Nakano, T. Shirakami, and K. Urabe, "Super structure of tricalcium silicate doped with ZnO" *Key Engineering Materials,* **206-213,** 747-750, (2002).

10. Á. G. De La Torre, S. Bruque, J. Campo and M. A. G. Aranda, "The superstructure of C_3S from synchrotron and neutron powder diffraction and its role in quantitative phase analysis" *Cem. Concr. Res.* **32,** 1347-1356, (2002).

11. K. Urabe, H. Nakano, and H. Morita, "Structural modulations in monoclinic tricalcium silicate solid solutions doped with zinc oxide, M1, M11 and M111" *J. Am. Ceram. Soc.* **85** [2], 423-429. (2002).

12. K. Urabe, T. Shirakami, and M. Iwashima, "Superstructure in a triclinic phase of tricalcium silicate" *J. Am. Ceram. Soc.* **83**, 1253-1258, (2000).

13. A. Viani, G. Artlioli, and M. Bellotto, in Materials Science Forum **278-281** Pt 1 May 25-28 1997, Trans Tech Publ Ltd. 1998 p.p.384-389.

14. M. Courtial, M. –N. de Norifontaine, F. Dunstetter, G. Gasecki and M. Signes-Frehel, "Polymorphism of tricalcium silicate in Portland cement: A fast visual identification of structure and superstructure" *Powder Diffraction* **18** [1], 7-15 (2003).

15. V.K. Peterson, B. Hunter and A. Ray, "Neutron diffraction investigation of structural deviations in cement clinker", AIPC 2002 proceedings CDROM Australian Institute of Physics 15th Biennial Congress, 8 - 11 July 2002, Sydney, 2002.

16. T. Harada, M. Ohta and S. Takagi, "Effect of polymorphism of tricalcium silicate on structure and strength characteristics of hardened cement paste," Japan. Rev. Gen. Meet., Tech. Sess. - Cem. Assoc. Jpn. 31 31-33 (1977).

17. G. Mascolo, B. Marchese, G. Frigione and R. Sersale, " Influence of polymorphism and stabilizing ions on the strength of alite," *Journal of The American Ceramic Society*, 56 [4] 222-223 (1977).

18. T. Staněk and P. Sulovský, "The influence of the alite polymorphism on the strength of the Portland Cement" *Cem. Concr. Res.*, **32,** 1169-1175, (2002).

19. J. C. Taylor, I. Hinczak, C. E. Matulis, "Rietveld full-profile quantification of Portland cement clinker: The importance of including a full crystallography of the major phase polymorphs," *Powder Diffraction,* 15 7-18 (2000).

20. V. K. Peterson, B. Hunter and A. Ray "Rietveld phase quantification of cement clinker using powder diffraction data" *submitted to the Journal of the American Ceramics Society*.

21. V. K. Peterson "Powder diffraction investigations of cement and its major component, tricalcium silicate" Ph.D Thesis, *to be submitted to the University of Technology, Sydney*.

22. B. Hunter, "Rietica – A visual Rietveld program," *Powder Diffraction Newsletter,* 20, 21 (1999).

23. A. C. Larson and R. B. Von Dreele, General Structure Analysis System (GSAS), *Los Alamos National Laboratory Report LAUR*, 2000, 86-748.

24. P. Thompson, D. E. Cox and J. B. Hasting, "Rietveld refinement of Debye-Scherrer synchrotron X-ray data from Al_2O_3", *J. Appl. Crystallog.* **27,** 79-83 (1994).

25. L. W. Finger, D. E. Cox and A. P. Jephcoat, "A correction for powder diffraction peak asymmetry due to diaxial divergence" *J. Appl. Crystallogr.* **27,** 892-900 (1994).

26. M. M. Regourd, "Détermination des réseaux de cristaux microscopiques. Application aux différentes formes du silicate tricalcique" *Bull. Soc. Minér. Crist. Franç,* **87**, 241-272 (1964).

27. ATOMS for Windows V5.06, Eric Dowty, 1999.

Table I: Derivative DTA curve features for pure tricalcium silicate

	First feature	Second feature	Third feature
Transition	T_1-T_2	T_2-T_3	T_3-M_1
1st heating	685 °C	916 °C	964 °C
1st cooling	563 °C	887 °C	952 °C
2nd heating	681 °C	913 °C	961 °C
2nd cooling	549 °C	886 °C	952 °C
3rd heating	684 °C	913 °C	961 °C
3rd cooling	589 °C	886 °C	952 °C
4th heating	681 °C	913 °C	961 °C
4th cooling	580 °C	885 °C	952 °C

Table II: Figures of merit for refinements of SXRPD data after refinement of the Golovastikov *et al* [2] T_1 sub-cell model.

Polymorph/model/temperature	χ^2	R_p	R-Bragg factor
T_1 sub-cell ambient	22.81	3.52	1.66
T_1 sub-cell 549(21) º C	7.47	3.29	1.52
T_2 sub-cell 682(28) º C	6.96	2.99	1.24
T_{2-3} sub-cell 740(31) º C	5.55	3.01	1.26

Table III: Lattice Parameters for triclinic tricalcium silicate polymorphs after refinement of the T_1 sub-cell

Polymorph temperature	a	b	c	α	β	γ
T_1 [3] Calculated	11.67	14.24	13.72	105.5	94.33	90.00
T_1 ambient	11.6320(1)	14.2100(2)	13.6836(2)	105.3098(6)	94.5593(6)	89.8516(7)
T_1 549(21) º C	11.7017(2)	14.2772(2)	13.7628(2)	105.2900(6)	94.3691(6)	89.8580(7)
T_2 682(28) º C	11.7406(1)	14.2768(2)	13.7719(2)	105.1281(7)	94.4168(6)	89.8884(7)
T_{2-3} 740(31) º C	11.7558(1)	14.2807(2)	13.7821(2)	105.0953(8)	94.4123(6)	89.9028(9)

Table IV: Ca-O coordination (bonds up to 0.300 nm) for tricalcium silicate polymorphs after refinement of the sub-cell

Polymorph/temperature	Average coordination
T_1 [1] calculated	6.21
T_1 ambient	6.15
T_1 549(21) º C	6.07
T_2 682(28) º C	5.93
T_{2-3} 740(31) º C	5.96
Monoclinic M_3 [1] calculated	6.15
Rhombohedral R [1] calculated	5.66

Table V: Crystal constants for the average sub-cell structure of T_2 tricalcium silicate at 682(28) ºC

Space group	$P\bar{1}$
Z	18
a (Å)	11.7416(2)
b (Å)	14.2785(2)
c (Å)	13.7732(2)
α (°)	105.129(1)
β (°)	94.415(1)
γ (°)	89.889(1)
Cell Volume ($Å^3$)	2222.02(8)

Table VI: Atomic positional and displacement parameters for the average sub-cell structure of T_2 tricalcium silicate at 682(28) ºC

Atom	x	y	z	U_{iso}
Ca1	0.709(2)	0.005(2)	0.971(2)	0.0268(6)
Ca2	0.336(2)	0.158(2)	0.668(2)	0.0268(6)
Ca3	0.669(2)	0.331(2)	0.327(2)	0.0268(6)
Ca4	0.847(2)	0.172(2)	0.164(2)	0.0268(6)
Ca5	0.186(2)	0.318(1)	0.822(2)	0.0268(6)
Ca6	0.325(2)	0.406(2)	0.667(2)	0.0268(6)
Ca7	0.640(2)	0.086(2)	0.329(2)	0.0268(6)
Ca8	0.037(2)	0.167(2)	0.626(2)	0.0268(6)
Ca9	0.622(2)	0.180(2)	0.712(2)	0.0268(6)
Ca10	0.384(2)	0.334(2)	0.311(2)	0.0268(6)
Ca11	0.963(2)	0.331(2)	0.362(2)	0.0268(6)
Ca12	0.034(2)	0.401(2)	0.630(2)	0.0268(6)
Ca13	0.372(2)	0.069(2)	0.287(2)	0.0268(6)
Ca14	0.624(2)	0.436(2)	0.705(2)	0.0268(6)
Ca15	0.970(2)	0.099(2)	0.373(2)	0.0268(6)
Ca16	0.456(2)	0.095(2)	0.861(2)	0.0268(6)
Ca17	0.192(2)	0.244(2)	0.474(2)	0.0268(6)
Ca18	0.787(2)	0.261(2)	0.514(2)	0.0268(6)
Ca19	0.523(2)	0.419(2)	0.137(2)	0.0268(6)
Ca20	0.723(2)	0.492(2)	0.954(2)	0.0268(6)
Ca21	0.707(2)	0.233(2)	0.963(2)	0.0268(6)
Ca22	0.302(2)	0.269(2)	0.032(2)	0.0268(6)
Ca23	0.873(2)	0.077(2)	0.810(2)	0.0268(6)
Ca24	0.133(2)	0.430(2)	0.187(2)	0.0268(6)
Ca25	0.016(2)	0.245(2)	0.995(2)	0.0268(6)
Ca26	0.000	0.000	0.000	0.0268(6)
Ca27	0.000	0.500	0.000	0.0268(6)
Ca28	0.500	0.000	0.500	0.0268(6)
Ca29	0.500	0.500	0.500	0.0268(6)
Si1	0.827(2)	0.420(2)	0.168(2)	0.021(1)
Si2	0.481(2)	0.352(2)	0.889(2)	0.021(1)
Si3	0.167(2)	0.083(2)	0.831(2)	0.021(1)
Si4	0.805(2)	0.010(2)	0.547(2)	0.021(1)
Si5	0.187(2)	0.490(2)	0.445(2)	0.021(1)
Si6	0.511(2)	0.160(2)	0.127(2)	0.021(1)
Si7	0.129(2)	0.189(2)	0.214(2)	0.021(1)
Si8	0.872(2)	0.320(2)	0.787(2)	0.021(1)
Si9	0.504(2)	0.244(2)	0.503(2)	0.021(1)
O1	0.012(3)	0.214(4)	0.274(4)	0.021(2)
O2	0.511(4)	0.276(2)	0.182(4)	0.021(2)
O3	0.635(3)	0.144(4)	0.077(4)	0.021(2)
O4	0.153(4)	0.089(3)	0.128(3)	0.021(2)
O5	0.224(4)	0.284(4)	0.641(4)	0.021(2)
O6	0.491(4)	0.062(4)	0.687(4)	0.021(2)

O7	0.433(4)	0.129(4)	0.020(3)	0.021(2)
O8	0.217(3)	0.202(4)	0.315(3)	0.021(2)
O9	0.688(4)	0.082(4)	0.827(4)	0.021(2)
O10	-0.011(4)	0.256(4)	0.491(4)	0.021(2)
O11	0.464(4)	0.063(3)	0.157(4)	0.021(2)
O12	0.176(4)	0.253(4)	0.142(4)	0.021(2)
O13	0.783(4)	0.404(3)	0.474(4)	0.021(2)
O14	0.319(3)	0.484(4)	0.414(4)	0.021(2)
O15	0.187(4)	0.425(4)	0.527(4)	0.021(2)
O16	0.319(4)	0.428(4)	0.174(4)	0.021(2)
O17	0.126(4)	0.390(4)	0.999(4)	0.021(2)
O18	0.064(3)	0.473(4)	0.375(3)	0.021(2)
O19	0.284(3)	0.057(4)	0.772(3)	0.021(2)
O20	0.916(4)	0.375(4)	0.082(3)	0.021(2)
O21	0.189(4)	0.188(3)	0.916(3)	0.021(2)
O22	0.161(4)	0.003(3)	0.891(4)	0.021(2)
O23	0.806(4)	0.204(4)	0.334(4)	0.021(2)
O24	0.871(4)	0.146(4)	1.005(4)	0.021(2)
O25	0.554(4)	0.455(4)	0.332(4)	0.021(2)
O26	0.077(3)	0.047(4)	0.731(3)	0.021(2)
O27	0.544(4)	0.303(3)	0.423(3)	0.021(2)
O28	0.764(4)	0.056(4)	0.660(2)	0.021(2)
O29	0.386(3)	0.391(4)	0.972(3)	0.021(2)
O30	0.605(3)	0.326(3)	0.843(3)	0.021(2)
O31	1.003(3)	0.297(4)	0.755(4)	0.021(2)
O32	0.720(3)	0.069(3)	0.484(3)	0.021(2)
O33	0.792(4)	0.230(3)	0.799(4)	0.021(2)
O34	0.710(3)	0.417(4)	0.093(3)	0.021(2)
O35	0.775(4)	0.314(4)	0.694(3)	0.021(2)
O36	0.834(5)	0.087(3)	0.482(4)	0.021(2)
O37	0.868(5)	0.433(2)	0.854(4)	0.021(2)
O38	0.404(3)	0.159(3)	0.478(3)	0.021(2)
O39	0.180(5)	0.101(3)	0.525(4)	0.021(2)
O40	0.792(4)	0.425(4)	0.282(3)	0.021(2)
O41	0.415(4)	0.254(3)	0.817(3)	0.021(2)
O42	0.508(4)	0.260(3)	0.626(2)	0.021(2)
O43	0.381(3)	0.295(3)	0.486(3)	0.021(2)
O44	0.168(4)	0.465(2)	0.770(4)	0.021(2)
O45	0.474(4)	0.417(4)	0.807(3)	0.021(2)

Table VII: Si-O bond lengths for the average sub-cell structure of T_2 tricalcium silicate at 682(28) ºC

Atom 1	Atom 2	Length (Å)
Si1		
	O20	1.643(7)
	O34	1.643(7)
	O40	1.643(7)
	O44	1.646(7)
Si2		
	O29	1.641(7)
	O30	1.645(7)
	O41	1.645(7)
	O45	1.640(7)
Si3		
	O19	1.645(7)
	O21	1.646(7)
	O22	1.645(7)
	O26	1.640(7)
Si4		
	O28	1.640(7)
	O32	1.642(7)
	O36	1.643(7)
	O39	1.643(7)
Si5		
	O13	1.646(7)
	O14	1.641(7)
	O15	1.645(7)
	O18	1.641(7)
Si6		
	O2	1.640(7)
	O3	1.641(7)
	O7	1.640(7)
	O11	1.641(7)
Si7		
	O1	1.636(7)
	O4	1.642(7)
	O8	1.640(7)
	O12	1.639(7)
Si8		
	O31	1.639(7)
	O33	1.642(7)
	O35	1.637(7)
	O37	1.645(7)
Si9		
	O27	1.645(7)
	O38	1.643(7)
	O42	1.641(7)
	O43	1.646(7)

Table VIII: O-Si-O bond angles for the average sub-cell structure of T_2 tricalcium silicate at 682(28) ºC

Central Atom	Leg 1	Leg 2	Angle (º)
Si1			
	O20	O34	98.9(27)
	O20	O40	145.3(28)
	O20	O44	121.5(30)
	O34	O40	109.4(29)
	O34	O44	100.7(29)
	O40	O44	73.2(27)
Si2			
	O29	O30	159.6(28)
	O29	O41	101.0(28)
	O29	O45	109.2(29)
	O30	O41	95.2(25)
	O30	O45	80.4(27)
	O41	O45	97.8(31)
Si3			
	O19	O21	107.6(29)
	O19	O22	101.9(29)
	O19	O26	96.3(26)
	O21	O22	108.6(29)
	O21	O26	133.0(28)
	O22	O26	105.0(30)
Si4			
	O28	O32	99.1(28)
	O28	O36	116.7(33)
	O28	O39	134.9(33)
	O32	O36	49.4(22)
	O32	O39	108.5(30)
	O36	O39	108.3(31)
Si5			
	O13	O14	89.3(29)
	O13	O15	97.3(33)
	O13	O18	121.0(32)
	O14	O15	102.5(31)
	O14	O18	131.4(29)
	O15	O18	109.2(31)
Si6			
	O2	O3	103.8(31)
	O2	O7	113.0(31)
	O2	O11	133.5(29)
	O3	O7	95.6(28)
	O3	O11	113.6(32)
	O7	O11	90.4(29)
Si7			
	O1	O4	127.0(31)
	O1	O8	96.6(30)

	O1	O12	123.4(33)
	O4	O8	111.2(32)
	O4	O12	89.9(29)
	O8	O12	108.7(31)
Si8			
	O31	O33	119.0(31)
	O31	O35	115.4(30)
	O31	O37	108.4(31)
	O33	O35	80.2(26)
	O33	O37	125.5(33)
	O35	O37	103.2(30)
Si9			
	O27	O38	125.3(32)
	O27	O42	138.0(35)
	O27	O43	82.9(26)
	O38	O42	94.5(27)
	O38	O43	72.3(23)
	O42	O43	99.2(26)

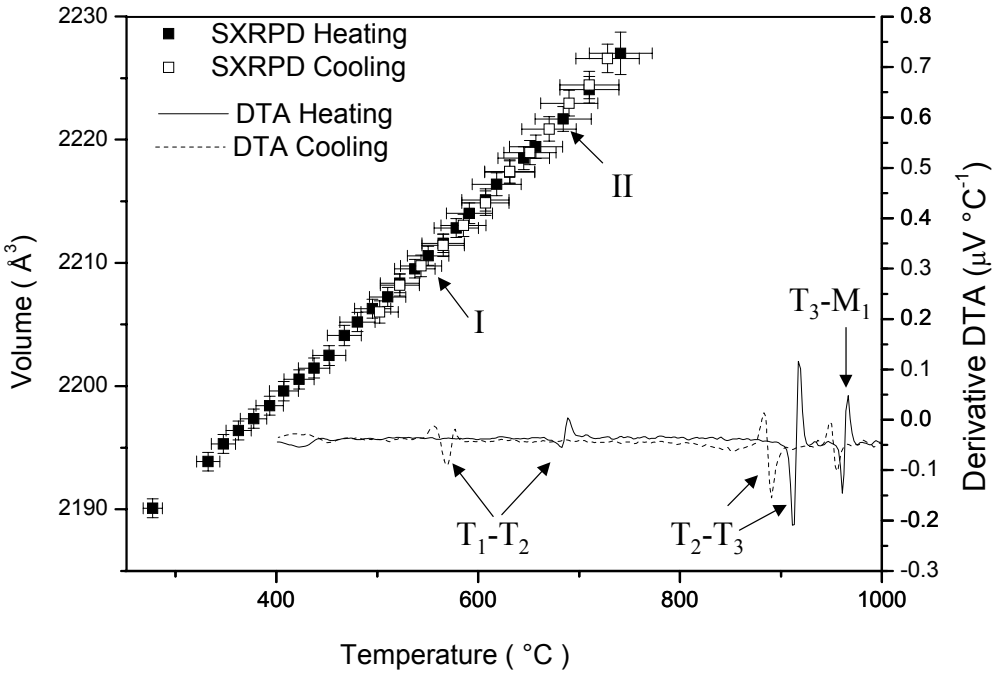

Figure 1: Cell volume from SXRPD and DTA during heating and cooling of tricalcium silicate, where points I and II show patterns of T_1 and T_2 polymorphs respectively, and transitions recognised by DTA are also marked.

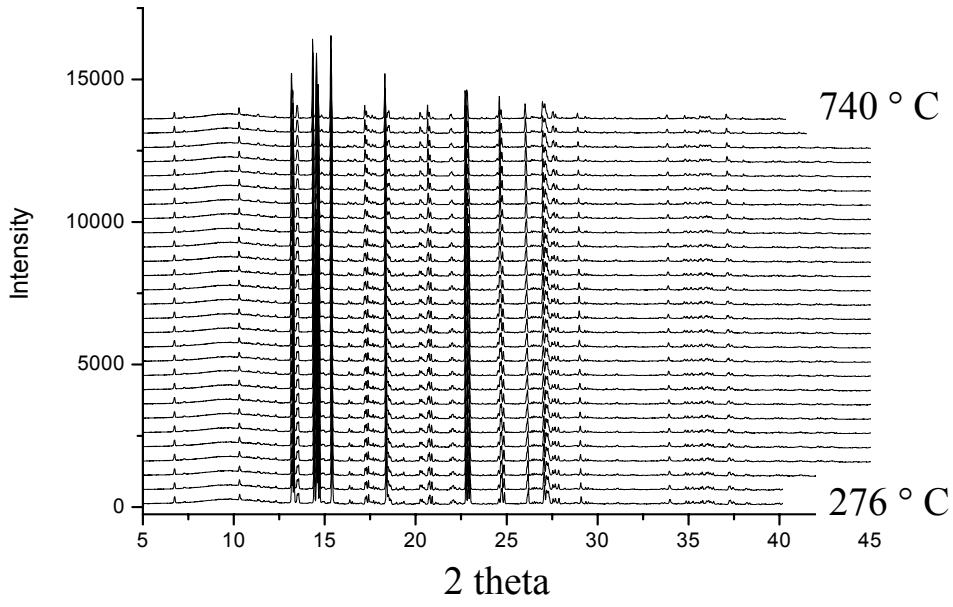

Figure 2: Offset powder diffraction patterns of tricalcium silicate during heating

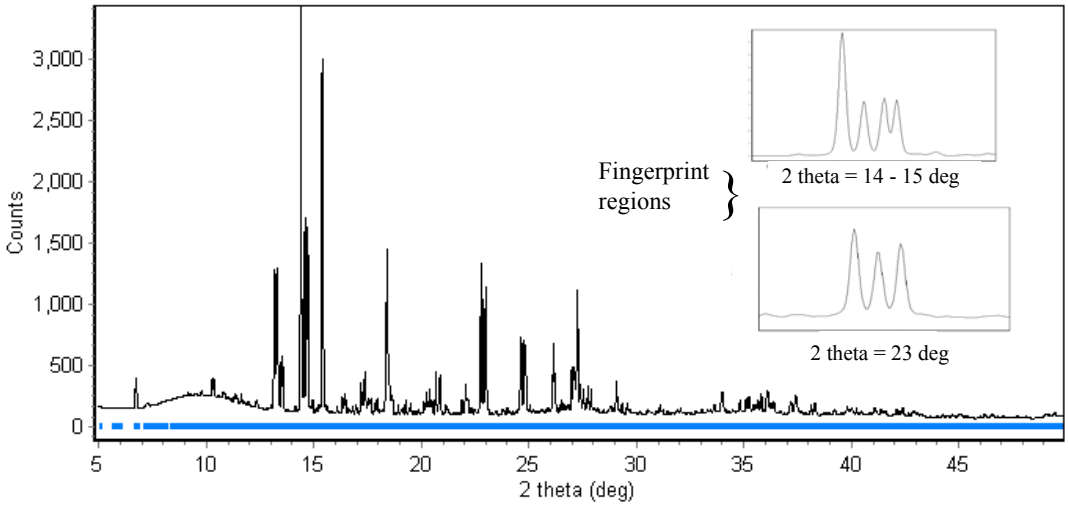

Figure 3: Golovastikov *et al* [2] T_1 tricalcium silicate calculated SXRPD pattern for the X7A beamline at BNL using a background representative of the capillary tube inserted from another data-set.

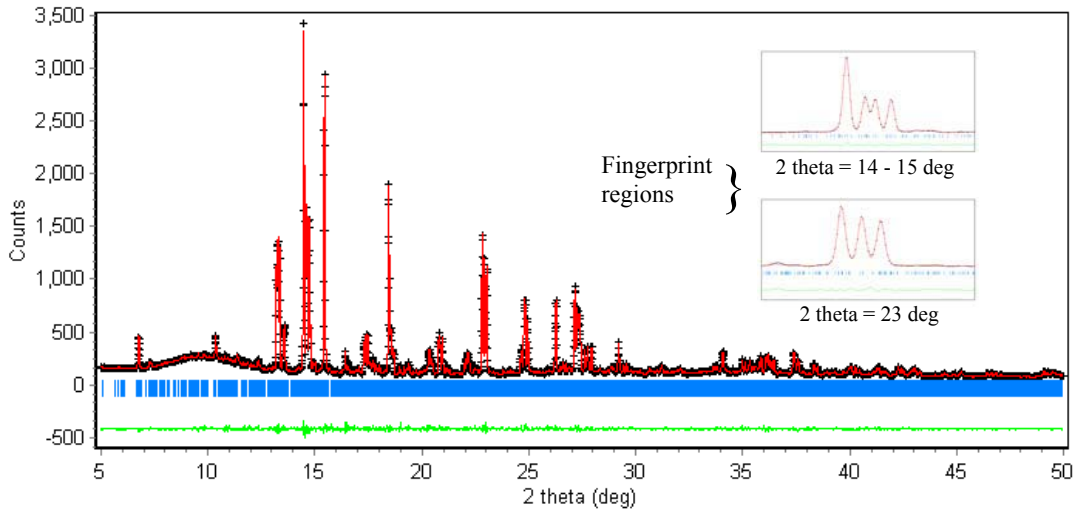

Figure 4: Refinement plot for T_1 tricalcium silicate SXRPD data at ambient temperature.

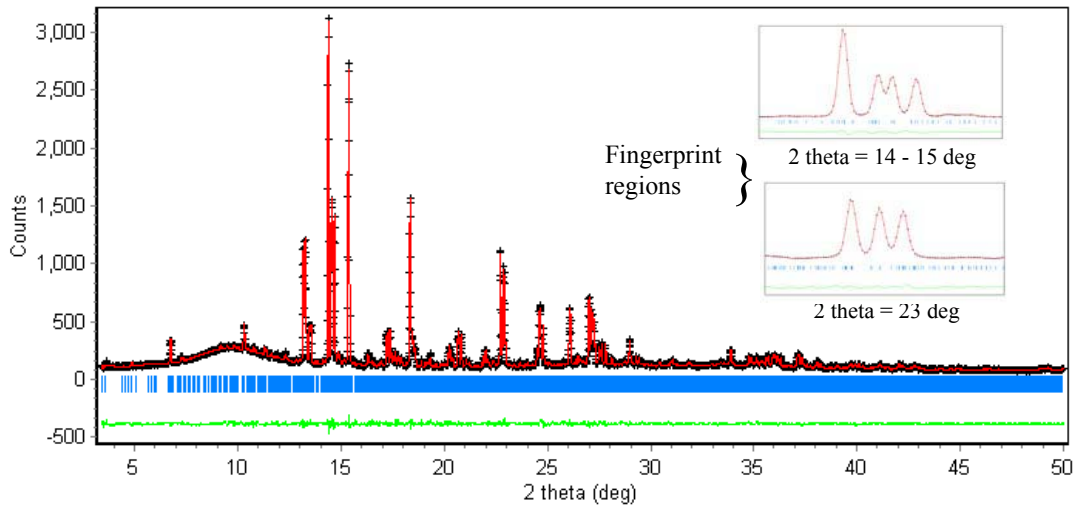

Figure 5: Refinement plot for T_1 tricalcium silicate SXRPD data at 549(21) ° C (point I).

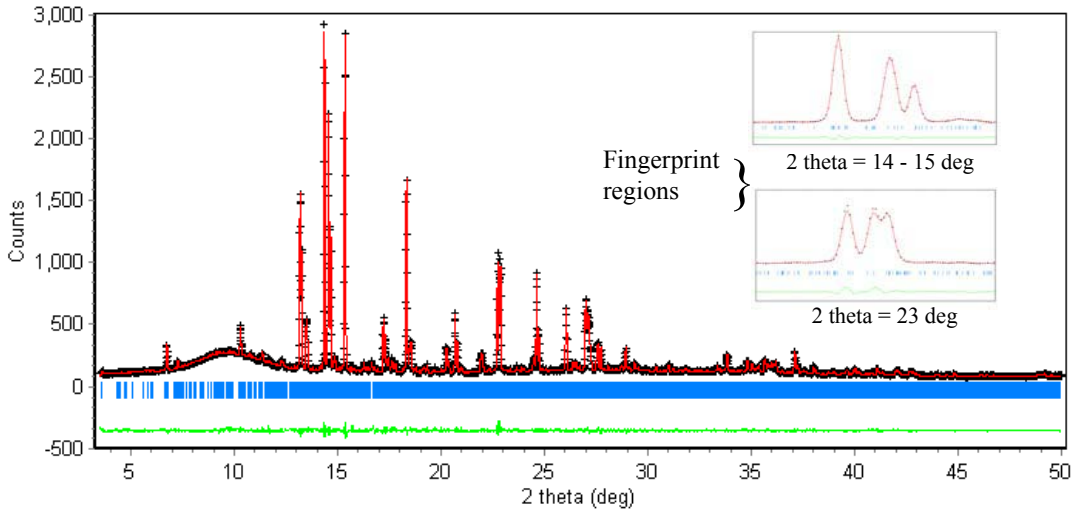

Figure 6: Refinement plot for T_2 tricalcium silicate SXRPD data at 682(28) º C (point II).

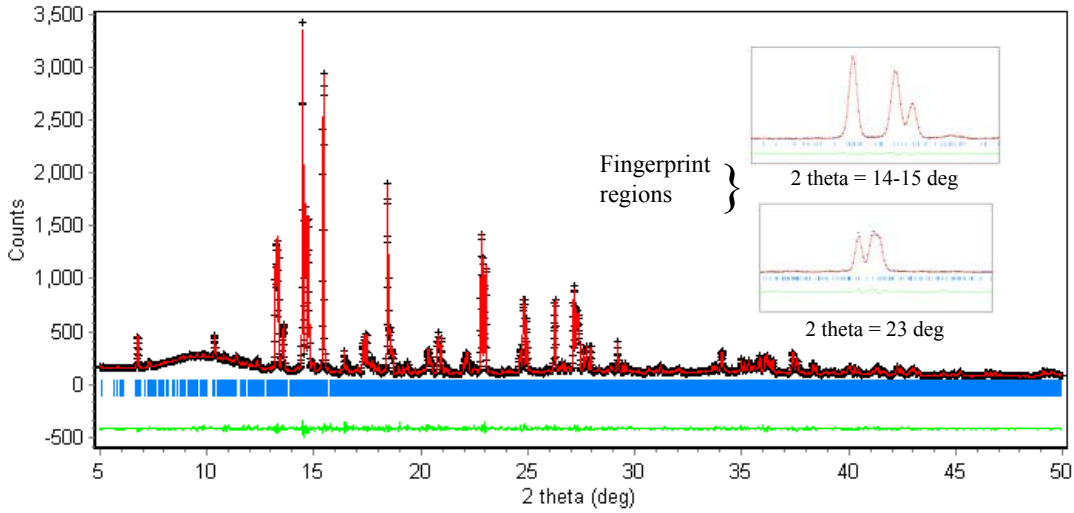

Figure 7: Refinement plot for $T_{2\text{-}3}$ tricalcium silicate SXRPD data at 740(31) º C.

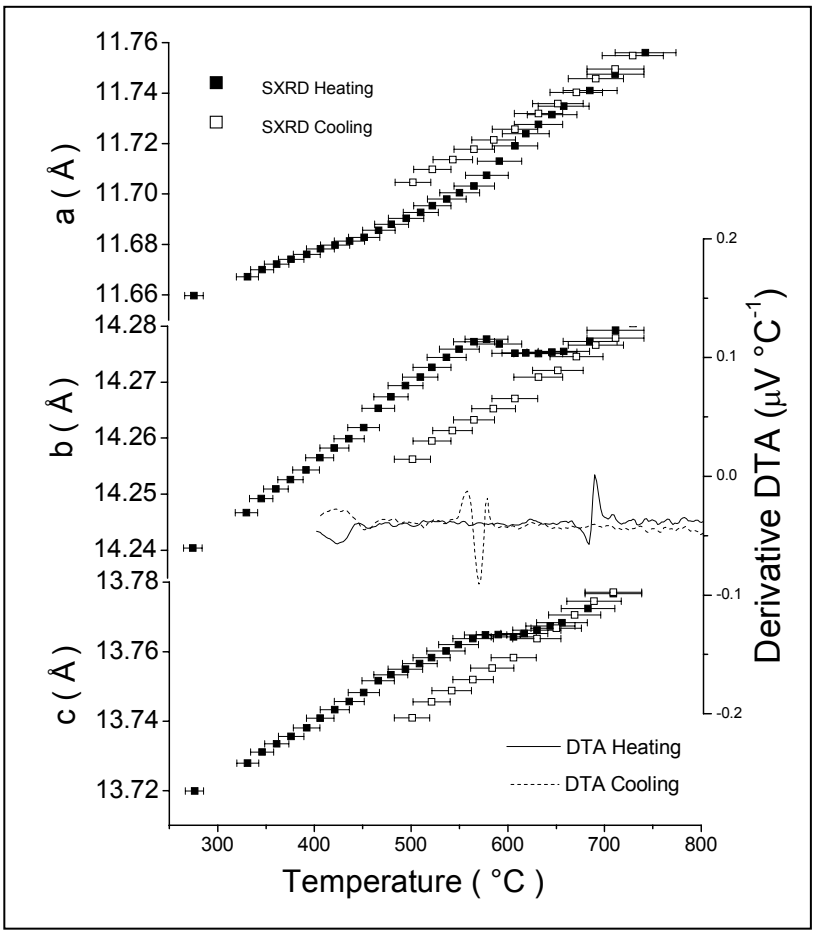

Figure 8a: Cell parameters a, c and c from SXRPD during heating and cooling of tricalcium silicate, and derivative DTA of T_1-T_2 transition.

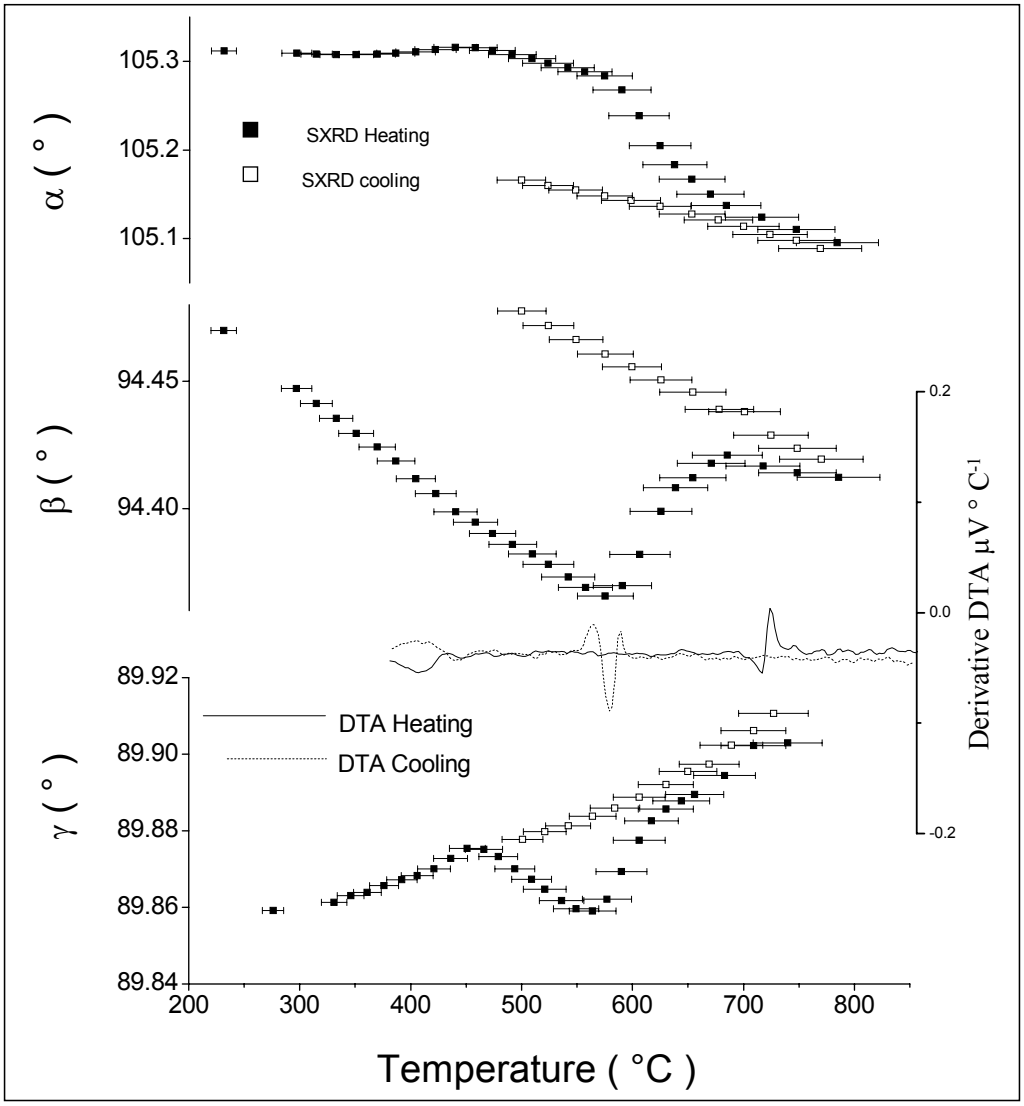

Figure 8b: Cell parameters α, β and γ from SXRPD during heating and cooling of tricalcium silicate and derivative DTA of T_1-T_2 transition.

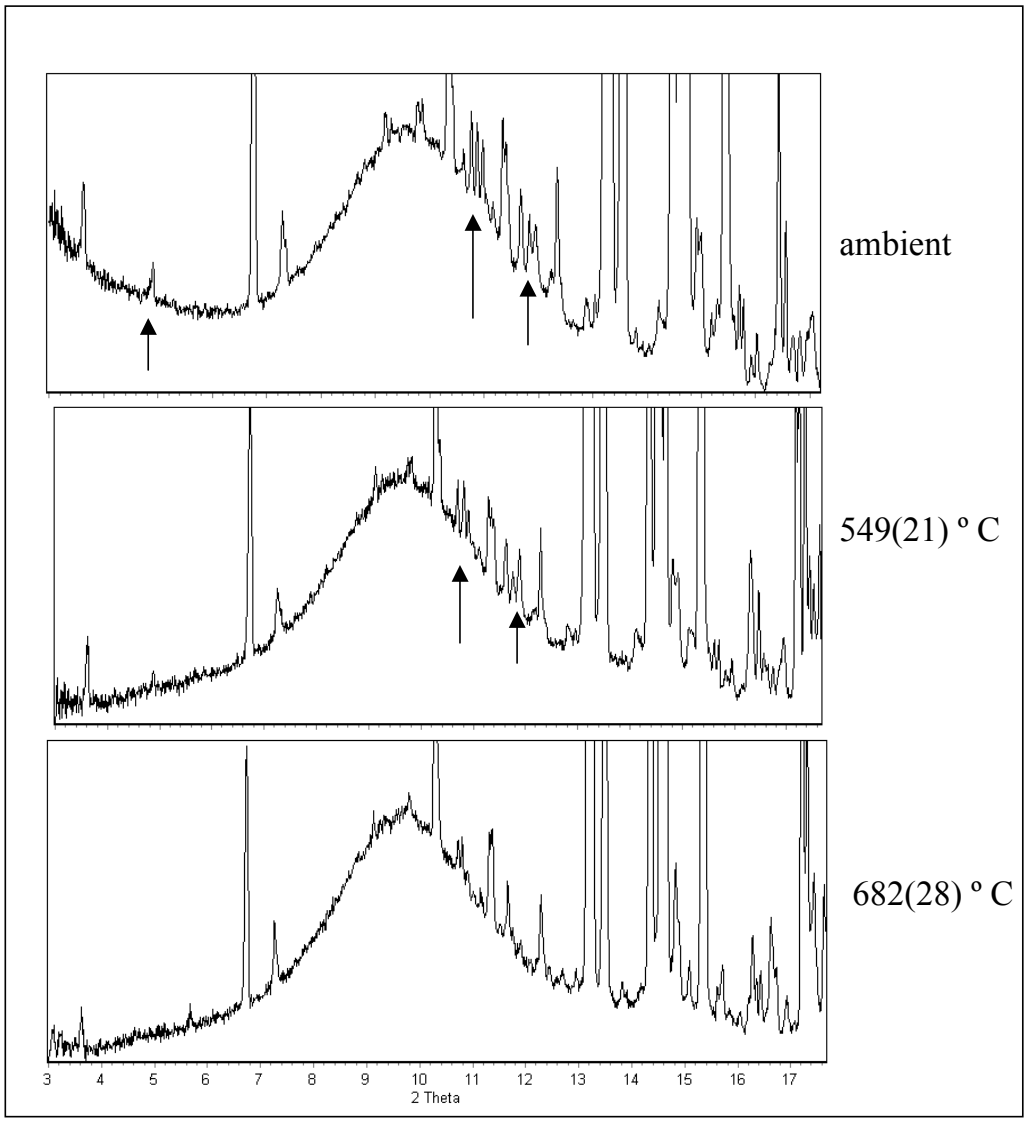

Figure 9: SXRPD data at low two theta for T_1 at ambient and 549(21) º C, and T_2 at 682(28) º C, highlighting additional reflections present at lower temperature.

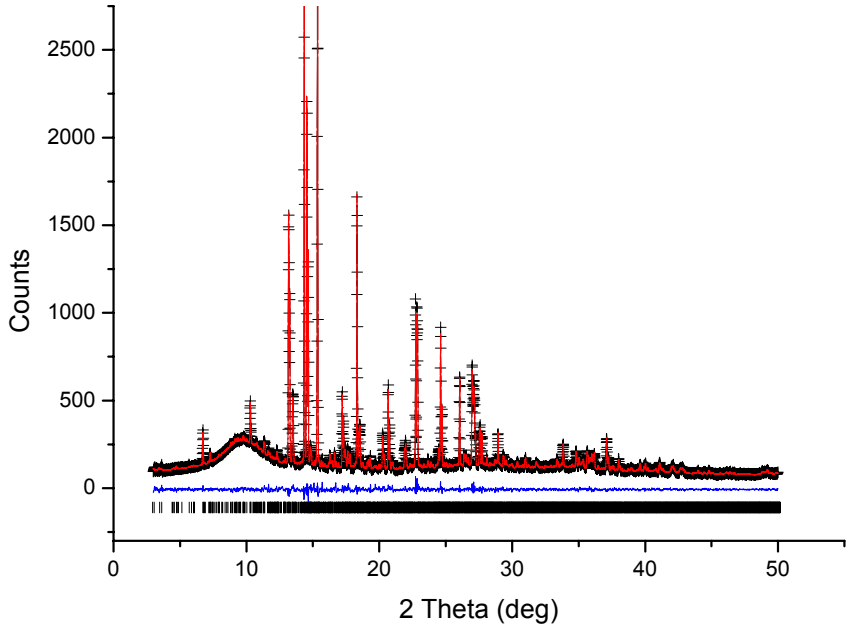

Figure 10: GSAS refinement plot for T_2 tricalcium silicate SXRPD data at 682(28) º C (point II).

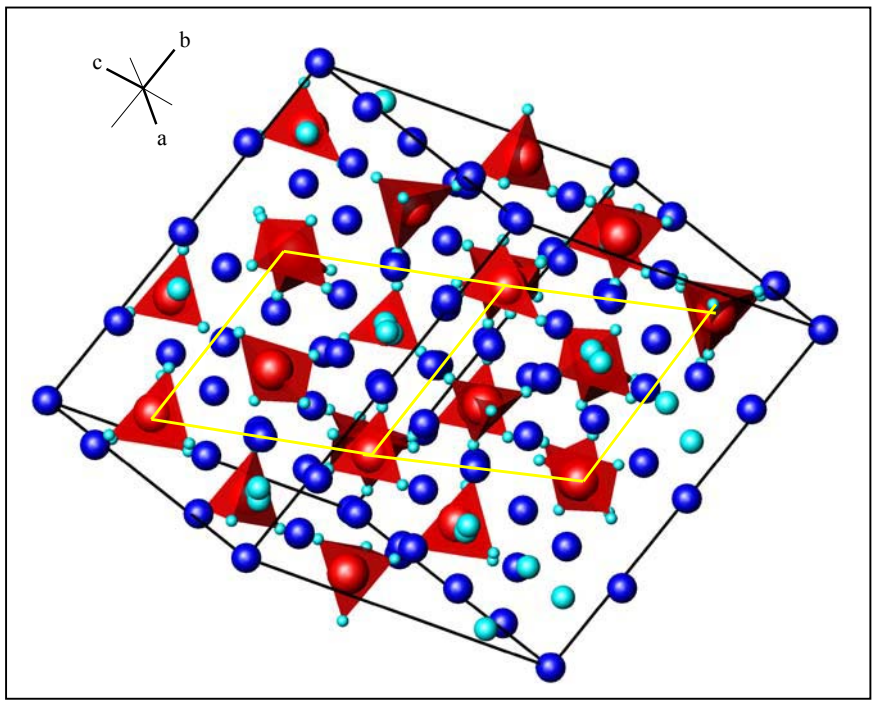

Figure 11: Unit cell representation with transformation showing common hexagonal plane of structure in triclinic C_3S type T_2 at 682(28) º C from this study. Inset shows crystal axes arrangement.

6.3 Structural modulation in tricalcium silicate

Bigaré *et al* (1967) suggested the existence of a superstructure that exists in T_1 and T_2, but not in T_3. In their work it was speculated that there was a doubling, and then a second doubling, of the a, b, and d lattice constants of the basal plane of the pseudohexagonal cell of the pseudotrigonal structure, shown in figure 2.3 of Chapter 2. If this hypothesis were true, the T_1 and T_2 structures would have lattice parameters 4a, 4b, and c with respect to the a, b, and c lattice parameters of the R form, in the trigonal-hexagonal setting. Correspondingly, the T_3 form would have lattice parameters 2a, 2b, and c. Structural modulation in the T_2 and T_3 C_3S forms remains speculative.

Based on the work of Urabe and Yamamoto (1996), Urabe *et al* (2000) investigated the superstructure in the T_1 form of C_3S, using HRTEM. In their work, the direction of the structural modulation present in the T_1 type was investigated, although no information on the atomic co-ordinates of the sub-structure, or modelling of the modulation, was published. Shirakami *et al* (1999) investigated the structural modulation present in a monoclinic form using electron diffraction. Using this work, Morita *et al* (2002) and Urabe *et al* (2002) further investigated the structural modulation present in the monoclinic system. The M_1, M_2, and M_3 C_3S forms were shown to possess structural modulation.

The presence of superstructure in T_1, T_2, M_1, M_2, and M_3 C_3S forms has exposed the current crystallographic models as approximations, or sub-structure averages, of the true structures. The possibility that the T_3 form is modulated also exists, although has not been observed. Only the unmodulated R C_3S form has its structure correctly and simply described.

The identification of a "parent" structure and the direction of structural modulation (modulation wave-vector) in the T_1 and monoclinic C_3S forms (Urabe *et al,* 2000) (Urabe *et al,* 2002), allows for the first time the potential to model the structural modulation. The Rietveld method can be applied, using higher dimension crystallography, for structural solution of the modulated structures. Once the direction of the modulation has been identified with respect to the sub-structure, a superspace group can be used to describe the superstructure symmetry. In this manner, diffraction

data shown to contain modulation information (superstructure reflections) suitable for Rietveld refinement can be used to solve the modulated sub-structure. This technique has the potential to be applied to all structurally modulated polymorphs.

This investigation concentrated on the T_1 modulated C_3S form. A suitable sub-structure model suitable for 4-dimensional Rietveld refinement was investigated, using the work of Urabe *et al* (2000). The corresponding modulation wave-vector for this sub-structure and the space group were also determined.

6.3.1 Formulation of the parent sub-structure

It is thought that C_3S polymorphs differ in their sub-structure and their modulation. In this case, it is likely that polymorphs possessing different symmetry have different sub-structures, represented by a deformation in the basal hexagonal plane. The exact relationship between the structural transitions between C_3S forms of the same space group and their modulations, is unknown. Urabe *et al* (2002) hypothesised that the differences in the deformation of the basal plane of the pseudotrigonal sub-cells (in the hexagonal setting) of the monoclinic forms, were attributable to differences in the ordering of the orientations of the apices of the silicate tetrahedra occurring along the direction of the modulation. In their work, both the modulation and sub-structure appear to differ between monoclinic C_3S forms. No information on such a relationship has been published for the triclinic forms.

The high-temperature form is the unmodulated rhombohedral form. The common link between polymorphs appears to be a deformation of the basal hexagonal plane of this trigonal form, in the rhombohedral setting. Urabe and Yamamoto (1996) and Urabe *et al* (2000) identified this pseudohexagonal sub-cell, as a pseudotrigonal cell in the hexagonal setting, as a parent structure, able to be modulated to represent the superstructures in T_1 C_3S.

The HRTEM figures in the publication of Urabe *et al* (2000) exhibit characteristic extinction features in the reflections observed for the pseudotrigonal sub-cell, in the hexagonal setting. These arise from the Bravais lattice centrings of the hexagonal setting. If the sub-structure is triclinic, then the symmetry of the sub-lattice and

superstructure do not allow for these extinction conditions. In order to further investigate the triclinic T_1 superstructure, in terms of the modulation of this sub-structure, these characteristic extinction conditions must be removed. Transformation from the hexagonal setting of the trigonal parent sub-structure, determined by Jeffery (1952), into the rhombohedral setting of the trigonal sub-structure, with primitive cell (P), was therefore necessary. Tables 6.1 and 6.2 show the cell coordinates and atomic positions as transformed from the hexagonal setting of space group 160 to the rhombohedral (primitive cell) setting.

Table 6.1: Crystal constants for the rhombohedral sub-structure of C_3S.

Space group	*R*3*m*(R)
Z	3
a (Å)	9.261
α (°)	44.4115
Cell Volume (Å^3)	353.59

Table 6.2: Atomic positions for the rhombohedral sub-structure of C_3S.

	Multiplicity Wyckoff	x	y	z	SOF
Si1	1a	1	1	1	1/6
Si2	1a	0.774	0.774	0.774	1/6
Si3	1a	0.217	0.217	0.217	1/6
Ca1	3b	0.492	0.492	0.007	1/2
Ca2	3b	0.723	0.723	0.218	1/2
Ca3	3b	0.281	0.281	0.766	1/2
O1	1a	0.936	0.936	0.936	1/6
O2	1a	0.71	0.71	0.71	1/6
O3	1a	0.153	0.153	0.153	1/6
O4	1a	0.602	0.602	0.602	1/6
O5	1a	0.494	0.494	0.494	1/6
O6	1a	0.386	0.386	0.386	1/6
O7	3b	0.144	0.144	0.772	1/2
O8	3b	0.67	0.67	0.042	1/2
O9	3b	0.361	0.361	0.989	1/2

Figures 6.13 and 6.14 are atomic representations of the Jeffery (1952) structure in the rhombohedral (primitive cell) setting using program Atoms (Dowty, 1999). Silicon-oxygen tetrahedra with central silicon atoms are shown in red, calcium atoms are dark

blue, and oxygen atoms are shown in turquoise. The unit cell is outlined with black. Crystal axes representation is shown inset.

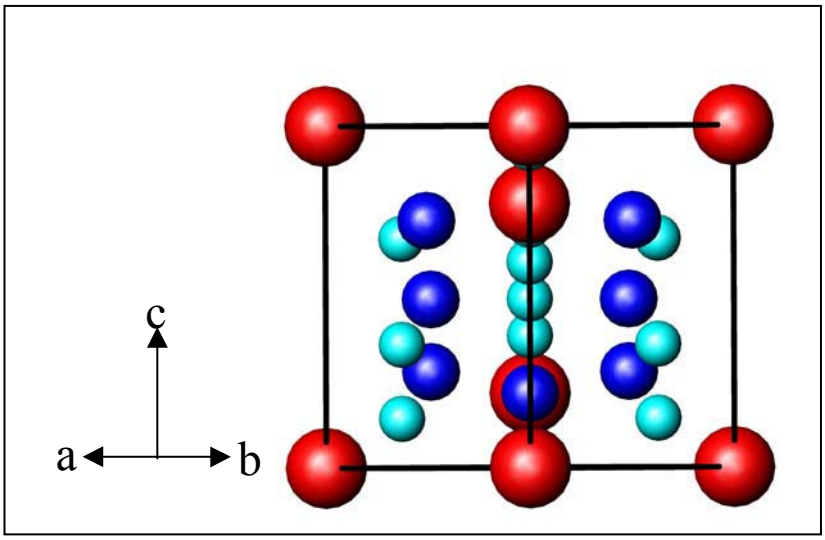

Figure 6.13: First unit cell representation of structure in C_3S type R in the rhombohedral setting (Jeffery, 1952).

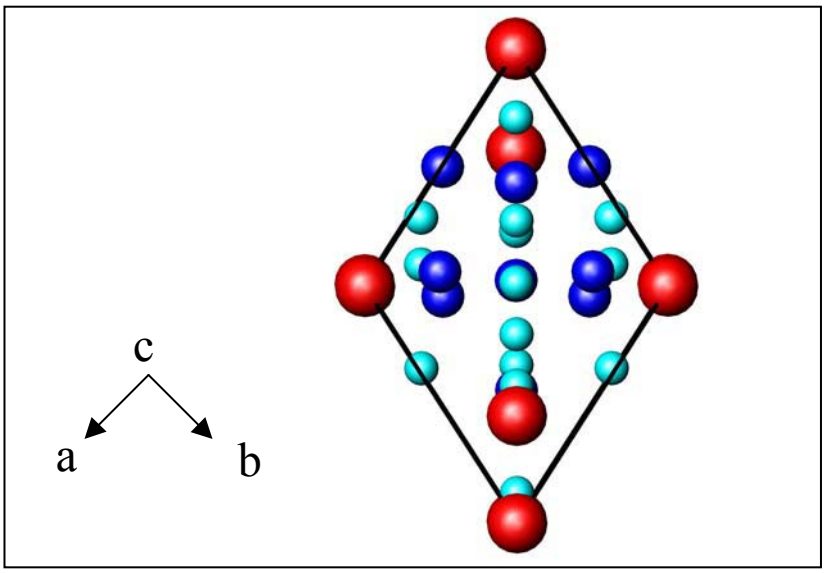

Figure 6.14: Second unit cell representation of structure in C_3S type R in the rhombohedral setting (Jeffery, 1952).

Assuming that the investigations of Urabe *et al* (2000) into the structural modulation in C_3S T_1 are correct, the primary modulation wave-vector **q** runs along 1/6[122]* in the hexagonal setting of the pseudotrigonal parent (*R*3*m*) sub-structure, where * denotes

operation in reciprocal space. As **q** is not along any symmetry direction of this parent sub-structure, the metric symmetry of the trigonal sub-structure, in the rhombohedral setting, reflects the triclinic symmetry.

For a description of the triclinic superstructure, a transformation of the lattice parameters from the hexagonal setting of the pseudotrigonal parent sub-structure used by Urabe *et al* (2000) into the rhombohedral (primitive cell) setting was performed. The lattice parameter transformations used are shown in equations 6.01-6.03, where the subscripted R represents rhombohedral setting and the subscripted H represents hexagonal setting.

$$a_R = 1/3(- a_H - 2b_H + c_H) \quad (6.01)$$

$$b_R = 1/3(2a_H + b_H + c_H) \quad (6.02)$$

$$c_R=1/3(-a_H + b_H + c_H) \quad (6.03)$$

In the rhombohedral setting of this space group, q = 1/6[-1, 2, 1]R*. The corresponding superspace group then becomes *P*1(-1/6, 1/3, 1/6), No.1.1 in Table 9.8.3.5 of Janssen *et al* (Int. Tables Vol.C) The new T_1 pseudotrigonal sub-structure in the rhombohedral setting, transformed from the pseudotrigonal form in the hexagonal setting of Urabe *et al* (2000), is shown in tables 6.3 and 6.4.

Table 6.3: Crystal constants for unrefined sub-structure of C_3S T_1.

Space group	*P*1 (-1/6, 1/3, 1/6)
Z	3
a (Å)	9.3623
b (Å)	9.3341
c (Å)	9.3551
α (°)	44.5288
β (°)	44.2069
γ (°)	44.7805
Cell Volume (Å^3)	365.214

Table 6.4: Atomic positions for unrefined sub-structure of C_3S T_1.

Atom	x	y	z
Si1	0	0	0
Si2	0.774	0.774	0.774
Si3	0.217	0.217	0.217
Ca1	0.492	0.492	0.007
Ca2	0.723	0.723	0.218
Ca3	0.281	0.281	0.766
Ca4	0.007	0.492	0.492
Ca5	0.492	0.007	0.492
Ca6	0.218	0.723	0.723
Ca7	0.723	0.218	0.723
Ca8	0.766	0.281	0.281
Ca9	0.281	0.766	0.281
O1	0.936	0.936	0.936
O2	0.71	0.71	0.71
O3	0.153	0.153	0.153
O4	0.602	0.602	0.602
O5	0.494	0.494	0.494
O6	0.386	0.386	0.386
O7	0.144	0.144	0.772
O8	0.67	0.67	0.042
O9	0.361	0.361	0.989
O10	0.772	0.144	0.144
O11	0.144	0.772	0.144
O12	0.042	0.67	0.67
O13	0.67	0.042	0.67
O14	0.989	0.361	0.361
O15	0.361	0.989	0.361

The triclinic metric symmetry is maintained in the sub-structure shown in tables 6.3 and 6.4. In these tables all atomic positions are fully occupied.

The pseudotrigonal structure in the rhombohedral setting shown in tables 6.3 and 6.4 has 27 atoms in the unit cell, compared to the 4.5 per unit of the trigonal structure in the rhombohedral setting, shown in tables 6.1 and 6.2. Golovastikov *et al* (1975) determined the average structure of type T_1 to have 29 Ca, 9 Si, and 45 O atoms in its asymmetric unit.

The identification of the parent sub-structure in a form suitable for Rietveld refinement, the modulation wave-vector, and the superspace group for the T_1 superstructure from this thesis has for the first time allowed the possibility for refinement of the modulated

structure. Refinement of the modulated structure was beyond the scope of this thesis, although it is expected that a structural solution for the T_1 sub-structure using Rietveld analysis of the modulated structure, will arise as a direct result of these investigations. It is hoped that the demonstration of sub-structure solutions through refinement of the modulated T_1 form will lead to solutions for the other triclinic C_3S forms.

It is hypothesised that there exists a common link in the structural modulation between the modulated C_3S forms. It is thought that the application of the Rietveld method for the refinement of the modulated structures will expose this link.

6.4 Summary

This chapter investigated the exact crystallographic structures of the triclinic form of C_3S.

The T_1-T_2, T_2-T_3, and T_3-M_1 structural transitions were observed using DTA, and a comparison made to the results reported in the literature. For the first time:

- The T_1-T_2 structural transition of tricalcium silicate was investigated using high-temperature SXRPD with Rietveld refinement of the average sub-cell lattice parameters.
- The lattice parameters of the $P\bar{1}$ average sub-cell were followed in depth during the T_1-T_2 transition.

The T_2 average structure was investigated using an average structure. For the first time:

- The average T_2 structure was determined to be $P\bar{1}$, with lattice parameters a = 11.7416(2) Å, b = 14.2785(2) Å, c = 13.7732(2) Å, α = 105.129(1) º, β = 94.415(1) º, and γ = 89.889(1) º.

The triclinic superstructures were also investigated.

- The superstructure reflections from the T_1 and T_2 forms were observed for the first time using SXRPD.
- The new T_2 average structure exhibited distorted SiO_4 tetrahedral angles, which further evidenced the structural modulation present.

The parent sub-cell of the T_1 C_3S form that is modulated in results of Urabe *et al* (2000), was re-investigated.

- A parent sub-structure for the T_1 modulated form was presented, in a form useful for the refinement of the modulated structure, for the first time. Lattice parameters were extracted by transformation of the pseudotrigonal cell in the hexagonal setting of Urabe *et al* (2000), to the rhombohedral (primitive) cell setting. Atomic positions for the sub-structure were reported based on the symmetry of the new cell, although refinement of these positions was not performed.

- The T_1 pseudotrigonal sub-structure in the rhombohedral setting was described, with lattice parameters a = 9.3623 Å, b = 9.3341 Å, c = 9.3551 Å, α = 44.5288 º, β = 44.2069 º, and γ = 44.7805 º.
- The modulation wave-vector of the pseudotrigonal sub-structure in the rhombohedral sub-structure was determined to be q = 1/6[-1,2,1]R*.
- The superspace group of the T_1 superstructure was determined to be *P*1(-1/6, 1/3, 1/6).

CONCLUSIONS AND FUTURE RESEARCH

In this work, the Rietveld method has been critically investigated as a tool for the identification and quantification of phases of cement clinker. Data from various diffraction sources including laboratory X-ray, synchrotron X-ray, neutron, and combined data were used in the investigations. The Rietveld method is identified as a powerful tool for the determination of the exact quantified crystallographic composition of cement. It was shown that the reliability of this method is directly linked to the quality of data in terms of counting statistics and resolution, and the ability of the structural models used to correctly describe the phases present in the sample.

The only currently published triclinic (T_1) C_3S structure is shown inadequate for the description of the form likely to be found in cement (T_2). For the first time the T_1-T_2 triclinic C_3S transformation was observed using SXRPD and superstructure reflections from the T_1 and T_2 forms were observed. A new model of the average T_2 structure was determined. The parent sub-structure for the T_1 modulated form was presented, in a form useful for the refinement of the modulated structure, for the first time. The corresponding modulation wave-vector of this sub-structure and superspace group of the superstructure, were also determined. The results from this thesis will enable the first Rietveld analysis of a modulated C_3S form to be performed. Application of the Rietveld method for the refinement of other modulated C_3S forms has the potential to solve the phase transition mechanisms between all forms of C_3S, with the possible exposition of new forms.

APPENDIX A

CRYSTAL STRUCTURE OF CLINKER COMPONENTS

Where listed, Z is the number of formulae units per unit cell, and a, b, c, α, β and γ are the lattice constants of the cell. SOF is the site occupancy factor of an atom. If the SOF is not present, this designates that all atoms are fully occupied. B is the atomic displacement parameter of an atom.

A1 Crystal structures for tricalcium silicate

Structural information for the C_3S modifications are listed in the following tables.

A1.1 T_1 C_3S structure $Ca_3(SiO_4)O$ determined by Golovastikov *et al* (1975).

Table A1.1: Crystal constants for T_1 C_3S (Golovastikov *et al,* 1975).

Space group	$P\bar{1}$
Z	18
a (Å)	11.670
b (Å)	14.240
c (Å)	13.720
α (°)	105.5
β (°)	94.3
γ (°)	90.0
Cell Volume (Å^3)	2190

Table A1.2: Atomic positional and displacement parameters for T_1 C_3S (Golovastikov *et al,* 1975).

Atom	x	y	z	B (Å^2)
Ca1	0.7102	0.0039	0.975	0.4
Ca2	0.3541	0.1525	0.6527	0.45
Ca3	0.6751	0.3207	0.3351	0.51
Ca4	0.8454	0.1667	0.1697	0.4
Ca5	0.1908	0.3284	0.8152	0.4
Ca6	0.3328	0.4107	0.6483	0.45

Ca7	0.6476	0.0817	0.334	0.25
Ca8	0.0536	0.1663	0.6176	0.33
Ca9	0.6438	0.1808	0.7226	0.43
Ca10	0.383	0.3474	0.3033	0.33
Ca11	0.965	0.3339	0.3678	0.32
Ca12	0.0498	0.3977	0.6244	0.33
Ca13	0.3604	0.0547	0.2888	0.3
Ca14	0.622	0.4145	0.7117	0.51
Ca15	0.9682	0.1048	0.3762	0.37
Ca16	0.4651	0.0913	0.8506	0.37
Ca17	0.2141	0.2419	0.4658	0.32
Ca18	0.804	0.2472	0.5175	0.33
Ca19	0.5363	0.4148	0.1508	0.27
Ca20	0.7012	0.488	0.9589	0.28
Ca21	0.7241	0.2378	0.97	0.31
Ca22	0.3039	0.2766	0.0251	0.54
Ca23	0.8729	0.0824	0.8173	0.3
Ca24	0.1371	0.4262	0.1848	0.34
Ca25	0.0205	0.2604	0.9897	0.5
Ca26	0	0	0	0.41
Ca27	0	0.5	0	0.3
Ca28	0.5	0	0.5	0.13
Ca29	0.5	0.5	0.5	0.12
Si1	0.8322	0.4165	0.1646	0.2
Si2	0.4748	0.344	0.871	0.21
Si3	0.1616	0.08	0.8192	0.04
Si4	0.8002	0.0183	0.5467	0.23
Si5	0.1922	0.4972	0.4486	0.25
Si6	0.5221	0.1553	0.1222	0.15
Si7	0.1492	0.1806	0.2057	0.17
Si8	0.8709	0.3207	0.7842	0.17
Si9	0.4977	0.2486	0.5043	0.23
O1	0.0339	0.1943	0.2619	0.41
O2	0.5127	0.2655	0.1925	0.67
O3	0.6528	0.1486	0.0807	0.62
O4	0.1584	0.0685	0.1427	0.59
O5	0.2204	0.2685	0.6427	0.34
O6	0.5037	0.0541	0.6743	0.31
O7	0.4211	0.1297	0.0254	0.6
O8	0.2625	0.206	0.2903	0.54

O9	0.6673	0.0923	0.8532	0.57
O10	0.0105	0.2584	0.4944	0.38
O11	0.5133	0.0806	0.191	0.45
O12	0.1592	0.2553	0.1291	0.55
O13	0.8279	0.395	0.4729	0.48
O14	0.3124	0.4978	0.4018	0.37
O15	0.1825	0.4137	0.5105	0.59
O16	0.3379	0.4353	0.1771	0.5
O17	0.161	0.3931	0.986	0.28
O18	0.088	0.4729	0.356	0.53
O19	0.2777	0.0582	0.7617	0.52
O20	0.9492	0.4026	0.107	0.59
O21	0.161	0.1919	0.8857	0.39
O22	0.1468	0.0064	0.8928	0.42
O23	0.8031	0.1819	0.3337	0.33
O24	0.8955	0.1402	0.9995	0.37
O25	0.5583	0.4518	0.338	0.46
O26	0.0487	0.0587	0.7321	0.4
O27	0.6123	0.2397	0.446	0.36
O28	0.7683	0.0509	0.6645	0.48
O29	0.4446	0.3903	0.9879	0.39
O30	0.6109	0.3254	0.863	0.57
O31	0.9981	0.3075	0.7361	0.49
O32	0.6869	0.0169	0.4682	0.83
O33	0.8604	0.2449	0.8521	0.52
O34	0.7189	0.3952	0.086	0.36
O35	0.7741	0.3028	0.6875	0.56
O36	0.8915	0.0963	0.5267	0.52
O37	0.8639	0.4292	0.8575	0.35
O38	0.4144	0.1476	0.4653	0.59
O39	0.1459	0.0887	0.4737	0.65
O40	0.827	0.3351	0.2302	0.43
O41	0.3964	0.244	0.8327	0.56
O42	0.5193	0.2654	0.6264	0.46
O43	0.4178	0.3379	0.484	0.42
O44	0.182	0.4733	0.7596	0.36
O45	0.44	0.4192	0.8047	0.41

A1.2 M_3 C_3S structure $Ca_{2.89}Mg_{0.11}(SiO_4)O$ determined by Nishi *et al* (1985).

Table A1.3: Crystal constants for M_3 C_3S (Nishi *et al,* 1985).

Space group	*C*1*m*1
Z	36
a (Å)	33.083
b (Å)	7.027
c (Å)	18.499
β (°)	94.1
Cell Volume (Å^3)	4289

Table A1.4: Atomic positional and displacement parameters for M_3 C_3S (Nishi *et al,* 1985).

Atom	x	y	z	SOF	B (Å^2)
Ca1	0.0075	0	0.009	0.5	4
Ca2	0.0024	0	0.0056	0.5	4
Ca3	0.6672	0	0.1751	0.5	0.1
Ca4	0.6673	0	0.1741	0.5	0.1
Ca5	0.324	0	0.333	0.5	1
Ca6	0.3193	0	0.3307	0.5	1
Ca7	0.002	0	0.5044	0.5	0.4
Ca8	0.0133	0	0.4971	0.5	0.4
Ca9	0.664	0	0.6714	0.5	0.6
Ca10	0.6632	0	0.6697	0.5	0.6
Ca11	0.3428	0	0.8352	0.5	1.6
Ca12	0.3301	0	0.8217	0.5	1.6
Ca13	0.5973	0	-0.0611	0.5	0.2
Ca14	0.5911	0	-0.0691	0.5	0.2
Ca15	0.2611	0	0.0952	0.5	2.5
Ca16	0.2568	0	0.0864	0.5	2.5
Ca17	0.0801	0	0.2667	0.5	1.3
Ca18	0.081	0	0.2644	0.5	1.3
Ca19	0.5874	0	0.439	0.5	0.9
Ca20	0.5856	0	0.4369	0.5	0.9
Ca21	0.2575	0	0.5989	0.5	0.2
Ca22	0.2561	0	0.5976	0.5	0.2
Ca23	0.0742	0	0.7698	0.5	0.6

Ca24	0.0743	0	0.7689	0.5	0.6
Ca25	0.7356	0	-0.1037	0.5	0.3
Ca26	0.7413	0	-0.0957	0.5	0.3
Ca27	0.4	0	0.0792	0.5	3.9
Ca28	0.3982	0	0.0706	0.5	3.9
Ca29	0.0651	0	0.2486	0.5	0.9
Ca30	0.0628	0	0.2445	0.5	0.9
Ca31	0.7286	0	0.401	0.5	1.8
Ca32	0.7272	0	0.4042	0.5	1.8
Ca33	0.4004	0	0.5711	0.5	1.4
Ca34	0.3984	0	0.5675	0.5	1.4
Ca35	0.0694	0	0.7491	0.5	1.5
Ca36	0.0647	0	0.7349	0.5	1.5
Ca37	0.0846	0.2988	-0.0926	0.5	1
Ca38	0.0793	0.2677	-0.0789	0.5	1
Ca39	0.5799	0.3018	0.0844	0.5	1.6
Ca40	0.585	0.2058	0.1013	0.5	1.6
Ca41	0.2411	0.2447	0.247	0.5	0.2
Ca42	0.2459	0.2559	0.2501	0.5	0.2
Ca43	0.0941	0.2566	0.413	0.5	0.2
Ca44	0.0885	0.255	0.4273	0.5	0.2
Ca45	0.5744	0.2726	0.5851	0.5	0.8
Ca46	0.5784	0.2399	0.5943	0.5	0.8
Ca47	0.2435	0.2491	0.7443	0.5	0.5
Ca48	0.2468	0.2347	0.7554	0.5	0.5
Ca49	0.0052	0.2343	-0.1598	0.5	0.1
Ca50	0.0051	0.2338	-0.1501	0.5	0.1
Ca51	0.6704	0.2318	0.0073	0.5	0.2
Ca52	0.6771	0.2306	0.0144	0.5	0.2
Ca53	0.3354	0.2257	0.1731	0.5	0.3
Ca54	0.3365	0.2385	0.1853	0.5	0.3
Ca55	0.0047	0.2281	0.3417	0.5	0.2
Ca56	0.0018	0.254	0.349	0.5	0.2
Ca57	0.663	0.2288	0.5097	0.5	0.9
Ca58	0.6688	0.2292	0.5147	0.5	0.9
Ca59	0.335	0.2592	0.675	0.5	0.7
Ca60	0.336	0.2165	0.6827	0.5	0.7
Ca61	0.8294	0.2577	-0.0192	0.5	1.2

Ca62	0.8306	0.2893	-0.0026	0.5	1.2
Ca63	0.484	0.2722	0.1583	0.5	1.8
Ca64	0.4905	0.2303	0.1584	0.5	1.8
Ca65	0.1468	0.2503	0.3304	0.5	1.4
Ca66	0.1562	0.29	0.332	0.5	1.4
Ca67	0.8167	0.2762	0.4875	0.5	0.6
Ca68	0.8224	0.252	0.4918	0.5	0.6
Ca69	0.4941	0.2854	0.6505	0.5	0.9
Ca70	0.4893	0.2759	0.6649	0.5	0.9
Ca71	0.1569	0.2749	0.8198	0.5	0.1
Ca72	0.1643	0.2675	0.8283	0.5	0.1
Si1	0.0833	0	0.4288	1	2.1
Si2	0.2384	0	-0.0838	1	0.3
Si3	0.4292	0	0.746	1	1.5
Si4	0.5699	0	0.7506	1	0.2
Si5	0.0943	0	0.0741	1	0.1
Si6	0.1015	0	0.5918	1	1.5
Si7	0.0966	0	-0.0851	1	0.5
Si8	0.1637	0	0.1591	1	1
Si9	0.1628	0	0.6629	1	0.3
Si10	0.234	0	0.4118	1	3.8
Si11	0.4214	0	0.2509	1	1.5
Si12	0.5008	0	0.0039	1	0.7
Si13	0.4975	0	0.5004	1	2.5
Si14	0.5682	0	0.2442	1	0.3
Si15	0.76	0	0.0882	1	0.2
Si16	0.7563	0	0.5803	1	0.2
Si17	0.1748	0	0.3338	1	0.4
Si18	0.1693	0	-0.1575	1	0.2
O1	0.99	0	0.245	0.5	4.2
O2	0.988	0	0.245	0.5	4.2
O3	0.038	0	0.119	0.5	3.8
O4	0.052	0	0.124	0.5	3.8
O5	0.03	0	0.599	0.5	2.8
O6	0.038	0	0.61	0.5	2.8
O7	0.004	0	0.753	0.5	1
O8	0.005	0	0.754	0.5	1
O9	0.372	0	-0.077	0.5	2.8

O10	0.373	0	-0.047	0.5	2.8
O11	0.329	0	0.075	0.5	4.1
O12	0.331	0	0.077	0.5	4.1
O13	0.289	0	0.211	0.5	2.7
O14	0.289	0	0.223	0.5	2.7
O15	0.362	0	0.441	0.5	0.8
O16	0.362	0	0.442	0.5	0.8
O17	0.325	0	0.583	0.5	0.1
O18	0.334	0	0.595	0.5	0.1
O19	0.282	0	0.724	0.5	1.4
O20	0.293	0	0.732	0.5	1.4
O21	0.666	0	-0.093	0.5	0.5
O22	0.675	0	-0.081	0.5	0.5
O23	0.627	0	0.049	0.5	1.5
O24	0.634	0	0.067	0.5	1.5
O25	0.706	0	0.285	0.5	2.6
O26	0.704	0	0.29	0.5	2.6
O27	0.648	0	0.421	0.5	2.1
O28	0.655	0	0.414	0.5	2.1
O29	0.608	0	0.554	0.5	1.5
O30	0.622	0	0.567	0.5	1.5
O31	0.705	0	0.763	0.5	1.4
O32	0.709	0	0.771	0.5	1.4
O33	0.949	0	0.376	0.5	1.5
O34	0.957	0	0.401	0.5	1.5
O35	0.96	0	0.897	0.5	0.8
O36	0.965	0	0.907	0.5	0.8
O37	0.111	0	0.357	1	8.1
O38	0.035	0	0.408	1	4.2
O39	0.096	0.187	0.474	1	3.2
O40	0.215	0	-0.011	1	0.5
O41	0.286	0	-0.063	1	2.9
O42	0.226	0.184	-0.133	1	2.1
O43	0.45	0	0.668	1	1.7
O44	0.379	0	0.73	1	2.3
O45	0.443	0.183	0.791	1	1.6
O46	0.549	0	0.83	1	2.1
O47	0.616	0	0.767	1	1.5

O48	0.555	0.188	0.704	1	2
O49	0.118	0	0.149	1	1.5
O50	0.044	0	0.093	1	1.2
O51	0.107	0.187	0.027	1	2.7
O52	0.123	0	0.669	1	4.7
O53	0.054	0	0.608	1	3.8
O54	0.117	0.186	0.542	1	2.3
O55	0.119	0	-0.161	0.68	0.7
O56	0.048	0	-0.103	0.68	1.6
O57	0.11	0.189	-0.038	0.68	3.9
O58	0.074	0	-0.009	0.32	4
O59	0.055	0	-0.138	0.32	2
O60	0.125	0.189	-0.073	0.32	1.9
O61	0.141	0.05	0.08	0.5	3.5
O62	0.134	-0.123	0.208	0.5	3.5
O63	0.205	-0.123	0.151	0.5	3.5
O64	0.176	0.197	0.202	0.5	3.5
O65	0.185	0	0.587	0.59	1.3
O66	0.114	0	0.645	0.59	1.3
O67	0.176	0.189	0.71	0.59	1.3
O68	0.14	0	0.739	0.32	1.3
O69	0.212	0	0.681	0.32	1.3
O70	0.141	0.189	0.627	0.32	1.3
O71	0.14	0.05	0.584	0.045	1.3
O72	0.133	-0.123	0.712	0.045	1.3
O73	0.204	-0.123	0.655	0.045	1.3
O74	0.175	0.197	0.706	0.045	1.3
O75	0.255	0	0.335	0.59	11
O76	0.268	0	0.48	0.59	2.7
O77	0.206	0.189	0.415	0.59	2
O78	0.212	0	0.487	0.41	6
O79	0.283	0	0.43	0.41	2
O80	0.221	0.189	0.365	0.41	3
O81	0.444	0	0.175	0.57	5
O82	0.372	0	0.233	0.57	3
O83	0.435	0.189	0.298	0.57	3
O84	0.399	0	0.327	0.43	5
O85	0.382	0	0.193	0.43	5

O86	0.45	0.189	0.257	0.43	2.3
O87	0.478	0	0.08	0.43	6
O88	0.55	0	0.022	0.43	6
O89	0.487	0.189	-0.043	0.43	6
O90	0.478	0.05	-0.075	0.285	6
O91	0.466	-0.123	0.04	0.285	6
O92	0.542	-0.123	-0.004	0.285	6
O93	0.513	0.197	0.047	0.285	6
O94	0.52	0	0.425	0.37	3.4
O95	0.448	0	0.483	0.37	3.4
O96	0.511	0.189	0.547	0.37	3.4
O97	0.52	0.05	0.58	0.315	3.4
O98	0.526	-0.128	0.451	0.315	3.4
O99	0.456	-0.123	0.508	0.315	3.4
O100	0.481	0.197	0.463	0.315	3.4
O101	0.591	0	0.169	0.37	16
O102	0.602	0	0.312	0.37	12
O103	0.54	0.189	0.248	0.37	2.4
O104	0.546	0	0.32	0.63	12
O105	0.617	0	0.262	0.63	6
O106	0.555	0.189	0.197	0.63	16
O107	0.782	0	0.169	0.22	11
O108	0.711	0	0.312	0.22	4
O109	0.773	0.189	0.248	0.22	2
O110	0.738	0	0.164	0.78	6
O111	0.726	0	0.02	0.78	2.4
O112	0.788	0.189	0.085	0.78	3.3
O113	0.778	0	0.505	0.93	0.4
O114	0.707	0	0.565	0.93	0.5
O115	0.769	0.191	0.626	0.93	1.4
O116	0.734	0	0.656	0.07	0.8
O117	0.717	0	0.522	0.07	0.8
O118	0.787	0.18	0.594	0.07	0.8
O119	0.197	0	0.409	0.07	4.6
O120	0.126	0	0.352	0.07	4.6
O121	0.188	0.189	0.287	0.07	4.6
O122	0.197	0.05	0.255	0.2325	4.6
O123	0.204	-0.123	0.383	0.2325	4.6

O124	0.134	-0.123	0.326	0.2325	4.6
O125	0.163	0.197	0.377	0.2325	4.6
O126	0.152	0.05	0.413	0.2325	4.6
O127	0.145	-0.123	0.285	0.2325	4.6
O128	0.216	-0.123	0.342	0.2325	4.6
O129	0.187	0.197	0.291	0.2325	4.6
O130	0.192	0	-0.082	0.78	2
O131	0.12	0	-0.14	0.78	2
O132	0.183	0.189	-0.204	0.78	2
O133	0.192	0.05	-0.237	0.11	2
O134	0.199	-0.123	-0.108	0.11	2
O135	0.128	-0.123	-0.165	0.11	2
O136	0.158	0.21	-0.125	0.11	2

A1.3 M_3 C_3S structure $Ca_{2.99}Na_{0.01}(Si_{0.90}Al_{0.04}Fe_{0.02}P_{0.03}Mg_{0.05})O_5$ determined by Mumme (1995).

Table A1.5: Crystal constants for M_3 C_3S (Mumme, 1995).

Space group	*C*1*m*1
Z	6
a (Å)	12.235
b (Å)	7.073
c (Å)	9.298
β (°)	116.3
Cell Volume (Å^3)	721.3

Table A1.6: Atomic positional and displacement parameters for M_3 C_3S (Mumme, 1995).

Atom	x	y	z	B (Å^2)
Ca1	0.0199	0.2664	0.3207	2.03
Ca2	0.9799	0.7335	0.6687	1.66
Ca3	0.2491	0.2522	0.9984	2.36
Ca4	0.2111	0.5	0.6666	1.69
Ca5	0.7836	0.5	0.3168	1.91
Ca6	0.0002	0.5	0.9995	2.28
Si1	0.0028	0	0.0007	1.01
Si2	0.2174	0	0.6523	0.48

Si3	0.7858	0	0.3573	1.11
O1	0.3501	0.5	0.5507	1.22
O2	0.0015	0.5	0.5031	2.38
O3	0.18	0.1766	0.7143	7.77
O4	0.3576	0	0.7172	5.54
O5	0.0635	0	0.197	2.75
O6	0.1599	0	0.4566	8.88
O7	0.1166	0.5	0.8554	6.74
O8	0.3776	0	0.1259	3.16
O9	0.0435	0.8144	0.9467	4.23
O10	0.1356	0.5	0.2855	2.02
O11	0.3622	0.5	0.943	4.02
O12	0.3231	0.6929	0.2881	1.54

A1.4 R C_3S structure $Ca_3(SiO_4)O$ determined by Il'inets *et al* (1985).

Table A1.7: Crystal constants for R C_3S (Il'inets *et al,* 1985).

Space group	*R*3*m*
Z	9
a (Å)	7.057
c (Å)	24.974
Cell Volume ($Å^3$)	1077

Table A1.8: Atomic positional and displacement parameters for R C_3S (Il'inets *et al,* 1985).

Atom	x	y	z	B ($Å^2$)
Ca1	-0.1764	0.1764	0.667	0.57
Ca2	-0.155	0.155	0.2174	0.67
Ca3	-0.1674	0.1674	0.4415	0.73
Si1	0	0	0.9885	0.52
Si2	0	0	0.557	0.96
Si3	0	0	0.7737	0.60
O1	0	0	0.8373	1.0
O2	0	0	0.3957	0.9
O3	0	0	0.1511	1.1
O4	0	0	0.9248	0.8
O5	0	0	0.2717	1.2

O6	0	0	0.6218	2.1
O7	0.115	-0.115	0.7427	3.6
O8	-0.118	0.118	0.5295	2.2
O9	0.1259	-0.1259	0.0092	0.9

A1.5 R C_3S structure $Ca_{2.98}Si_{0.98}Al_{0.04}O_5$ determined by Nishi *et al* (1985).

Table A1.9: Crystal constants for R C_3S (Nishi *et al,* 1985).

Space group	*R*3*m*
Z	9
a (Å)	7.135
c (Å)	25.586
Cell Volume ($Å^3$)	1128

Table A1.10: Atomic positional and displacement parameters for R C_3S (Nishi *et al,* 1985).

Atom	x	y	z	SOF	B ($Å^2$)
Ca1	0.488	-0.488	0.001	1	0
Ca2	0.826	-0.826	-0.111	1	0
Ca3	0.509	-0.509	-0.225	1	0
Si1	0	0	0	1	0
Si2	0	0	-0.213	1	0
Si3	0	0	-0.784	1	0
O1	0	0	-0.385	1	3
O2	0	0	-0.504	1	13
O3	0	0	-0.627	1	1
O4	0.057	-0.057	-0.057	0.3333	36
O5	-0.13	0.13	-0.007	0.3333	11
O6	0.223	0.148	0.032	0.3333	11
O7	0.016	-0.016	-0.276	0.10	1
O8	-0.128	0.128	-0.199	0.10	1
O9	0.241	0.13	-0.188	0.10	1
O10	0.032	-0.032	-0.152	0.23	1
O11	-0.131	0.131	-0.219	0.23	1
O12	0.234	0.137	-0.241	0.23	1
O13	-0.032	0.032	-0.845	0.3333	5
O14	0.131	-0.131	-0.778	0.3333	22
O15	0.137	0.234	-0.756	0.3333	22

A1.6 R C_3S structure $Ca_3(SiO_4)O$ determined by Jeffery (1952).

Table A1.11: Crystal constants for R C_3S (Jeffery, 1952).

Space group	*R*3*m*
Z	9
a (Å)	7
c (Å)	25
Cell Volume ($Å^3$)	1060.88

Table A1.12: Atomic positional and displacement parameters for R C_3S (Jeffery, 1952).

Atom	x	y	z
Ca1	0.495	0.505	-0.003
Ca2	0.835	0.165	-0.112
Ca3	0.505	0.495	-0.224
Si1	0	0	1
Si2	0	0	-0.226
Si3	0	0	-0.783
O1	0	0	-0.064
O2	0	0	-0.290
O3	0	0	-0.847
O4	0	0	-0.398
O5	0	0	-0.506
O6	0	0	-0.614
O7	0.124	0.876	-0.980
O8	0.876	0.124	-0.206
O9	0.124	0.876	-0.763

A2 Crystal structures for dicalcium silicate

Structural information for the C_2S monoclinic β polymorph is listed in the following tables.

A2.1 β C_2S structure Ca_2SiO_4 determined by Mumme *et al* (1995).

Table A2.1: Crystal constants for β C_2S (Mumme *et al,* 1995).

Space group	*C*1*m*1
Z	4
a (Å)	5.512
b (Å)	6.758
c (Å)	9.314
β (°)	94.6
Cell Volume ($Å^3$)	345.8

Table A2.2: Atomic positional and displacement parameters for β C_2S (Mumme *et al,* 1995).

Atom	x	x	y	B ($Å^2$)
Ca1	0.2276	0.3435	0.4304	0.52
Ca2	0.2203	0.9979	0.7018	0.45
Si1	0.268	0.7806	0.4193	0.67
O1	0.2195	0.0077	0.4424	0.59
O2	0.4753	0.7496	0.3083	0.49
O3	0.0158	0.6728	0.3619	0.44
O4	0.3431	0.6757	0.5718	0.70

A3 Crystal structures for tricalcium aluminate

Structural information for C_3A modifications is listed in the following tables.

A3.1 Cubic C_3A $Ca_9(Al_6O_{18})$ structure determined by Mondal and Jeffery (1975).

Table A3.1: Crystal constants for cubic C_3A (Mondal and Jeffery, 1975).

Space group	$Pa\overline{3}$
Z	8
a (Å)	15.263
Cell Volume ($Å^3$)	3555.66

Table A3.2: Atomic positional and displacement parameters for cubic C_3A (Mondal and Jeffery, 1975).

Atom	Atom type	x	y	z
Ca1	Ca	0	0	0
Ca2	Ca	0.5	0	0
Ca3	Ca	0.2561	0.2561	0.2561
Ca4	Ca	0.3750	0.3750	0.3750
Ca5	Ca	0.1386	0.3763	0.1272
Ca6	Ca	0.3800	0.3838	0.1209
Al1	Al	0.2526	0.0133	0.0197
Al2	Al	0.2444	0.2335	0.0046
O1	O	0.2777	0.1241	0.0103
O2	O	0.4835	0.1315	0.2536
O3	O	0.2664	0.2841	0.1049
O4	O	0.2350	0.4047	0.2921
O5	O	0.3491	-0.0385	-0.0174
O6	O	0.1509	-0.0104	-0.0242

A3.2 Cubic C_3A $Ca_{8.688}Na_{0.625}(Al_6O_{18})$ structure determined by Takéuchi *et al* (1980).

Table A3.3: Crystal constants for cubic C_3A (Takéuchi *et al*,1980).

Space group	$P2_13$
Z	8
a (Å)	15.248
Cell Volume ($Å^3$)	3545.18

Table A3.4: Atomic positional and displacement parameters for cubic C_3A (Takéuchi *et al,* 1980).

Atom	x	y	z	SOF	B ($Å^2$)
Ca1	0.0000	0.0000	0.0000	1	0.98
Ca2	0.5018	0.5018	0.5018	1	0.59
Ca3	0.2630	0.2630	0.2630	0.91	0.74
Na1	0.2630	0.2630	0.2630	0.09	0.74
Ca4	-0.2562	-0.2562	-0.2562	0.73	0.69
Na2	-0.2562	-0.2562	-0.2562	0.27	0.69
Ca5	0.3814	0.3814	0.3814	0.97	1.13
Na3	0.3814	0.3814	0.3814	0.03	1.13
Ca6	-0.3763	-0.3763	-0.3763	0.76	0.89
Na4	-0.3763	-0.3763	-0.3763	0.24	0.89
Ca7	0.3720	0.1400	0.1361	0.5	2.17
Ca8	0.3678	0.1262	0.1345	0.5	0.77
Ca9	0.6232	0.1376	0.1180	0.5	0.78
Ca10	0.6431	0.1363	0.1287	0.5	0.99
Ca11	0.3821	0.3863	0.1213	1	0.76
Ca12	-0.3800	-0.3881	-0.1201	1	0.62
Na5	0.121	0.121	0.121	0.31	1.89
Na6	0.875	0.875	0.875	0.31	7.56
Al1	0.2539	0.0134	0.0167	1	0.46
Al2	-0.2534	-0.0129	-0.0232	1	0.46
Al3	0.2434	0.2371	0.0053	1	0.54
Al4	-0.2445	-0.2377	-0.0063	1	0.43
O1	0.2630	0.1264	0.0029	1	1.86
O2	-0.2658	-0.1258	-0.0230	1	2.91
O3	0.4759	0.1327	0.2475	1	0.89

O4	-0.4952	-0.1310	-0.2368	1	1.54
O5	0.2729	0.2765	0.1082	1	1.38
O6	-0.2629	-0.2906	-0.1058	1	1.48
O7	0.2406	0.4114	0.3040	1	1.26
O8	-0.2281	-0.4062	-0.2878	1	1.23
O9	0.3502	-0.0321	-0.0274	1	1.09
O10	-0.3505	0.0233	0.0234	1	1.57
O11	0.1497	-0.0173	-0.0171	1	1.02
O12	-0.1515	0.0150	0.0163	1	0.59

A3.3 Orthorhombic C_3A $Ca_{8.5}NaAl_6O_{18}$ structure determined by Nishi and Takéuchi (1975).

Table A3.5: Crystal constants for orthorhombic C_3A (Nishi and Takéuchi, 1975).

Space group	*Pbca*
Z	4
a (Å)	10.859
b (Å)	10.875
c (Å)	15.105
α (°)	89.999
γ (°)	90
Cell Volume ($Å^3$)	1783.774

Table A3.6: Atomic positional and displacement parameters for orthorhombic C_3A (Nishi and Takéuchi, 1975).

Atom	x	y	z	SOF
Ca1	0.00268	0.00196	0.51825	0.25
Ca2	-0.00394	0.01771	0.23927	1
Ca3	0.00928	0.26744	0.13313	1
Ca4	0.25648	0.2706	0.25278	1
Ca5	0.26267	0.24622	0.49832	1
Na1	0	0	0	1
Al1	-0.00482	-0.21407	0.11603	1
Al2	0.23755	-0.00327	0.11292	1
Al3	0.24208	0.00543	-0.10861	1

O1	-0.14416	-0.13388	0.10911	1
O2	0.11066	-0.10125	0.12634	1
O3	0.28698	-0.02208	0.00229	1
O4	-0.00730	-0.28562	0.21778	1
O5	0.01956	-0.29335	0.01724	1
O6	0.35529	-0.07220	0.17361	1
O7	0.18863	0.14794	0.13240	1
O8	0.16233	-0.12774	-0.14188	1
O9	0.37170	0.06610	-0.15970	1

A3.4 Orthorhombic C_3A $Ca_{8.393}Na_{0.875}(Al_{5.175}Fe_{0.45}Si_{0.375}O_{18})$ structure determined by Takéuchi *et al* (1980).

Table A3.7: Crystal constants for orthorhombic C_3A (Takéuchi *et al*, 1980).

Space group	*Pbca*
Z	4
a (Å)	10.845
b (Å)	10.879
c (Å)	15.106
α (°)	89.999
γ (°)	90
Cell Volume (Å^3)	1782.247

Table A3.8: Atomic positional and displacement parameters for orthorhombic C_3A (Takéuchi *et al*, 1980).

Atom	x	y	z	SOF	B (Å^2)
Ca1	0.0026	0.0023	0.51866	0.5	1.09
Ca2	-0.003	0.01681	0.24207	1	0.84
Ca3	0.00873	0.26471	0.13216	1	0.84
Ca4	0.25522	0.27092	0.25253	1	1.12
Ca5	0.26315	0.24684	0.49821	0.696	1.03
Na1	0.26315	0.24684	0.49821	0.304	1.03
Na2	0.0026	-0.0156	-0.0073	0.125	2.82
Al1	-0.0043	-0.21416	0.11621	0.888	0.55
Fe1	-0.0043	-0.21416	0.11621	0.061	0.55
Si1	-0.0043	-0.21416	0.11621	0.051	0.55
Al2	0.23742	-0.0042	0.1125	0.868	0.57
Fe2	0.23742	-0.0042	0.1125	0.072	0.57

Si2	0.23742	-0.0042	0.1125	0.06	0.57
Al3	0.24056	0.0042	-0.10879	0.831	0.63
Fe3	0.24056	0.0042	-0.10879	0.092	0.63
Si3	0.24056	0.0042	-0.10879	0.077	0.63
O1	-0.1447	-0.1352	0.1101	1	1.61
O2	0.1142	-0.1052	0.1313	1	1.81
O3	0.2857	-0.0258	0.0017	1	1.23
O4	-0.0125	-0.2866	0.2178	1	1.83
O5	0.0215	-0.2942	0.0180	1	1.42
O6	0.3571	-0.0715	0.1716	1	1.33
O7	0.1904	0.1477	0.1314	1	1.39
O8	0.1638	-0.1281	-0.1444	1	1.20
O9	0.3722	0.0672	-0.1580	1	1.27

A3.5: Monoclinic C_3A $Ca_{8.25}Na_{1.5}(Al_6O_{18})$ structure determined by Takéuchi *et al* (1980).

Table A3.9: Crystal constants for monoclinic C_3A (Takéuchi *et al,* 1980).

Space group	$P112_1/a$
Z	4
a (Å)	10.887
b (Å)	10.854
c (Å)	15.135
γ (°)	90.1
Cell Volume ($Å^3$)	1786.82

Table A3.10: Atomic positional and displacement parameters for monoclinic C_3A (Takéuchi *et al,* 1980).

Atom	x	y	z	SOF	B ($Å^2$)
Ca1	0.0009	0.0021	0.5196	0.5	1.17
Ca2	0.00079	0.01849	0.23822	1	0.78
Ca3	0.0119	0.26769	0.13253	1	0.76
Ca4	0.26248	0.27015	0.2523	1	1.07
Ca5	0.2610	0.2460	0.49889	0.803	0.84
Na1	0.2610	0.2460	0.49889	0.197	0.84
Ca6	0.5024	0.4979	0.4838	0.5	0.95
Ca7	0.49159	0.48333	-0.24018	1	0.76

Ca8	0.50547	0.23286	-0.13408	1	0.79
Ca9	0.74938	0.22972	-0.25329	1	1.07
Ca10	0.7629	0.2524	-0.4986	0.447	1.23
Na2	0.7629	0.2524	-0.4986	0.553	1.23
Na3	0.001	-0.015	-0.0099	0.375	2.56
Na4	0.5023	0.5184	0.0110	0.375	2.72
Al1	-0.0027	-0.2155	0.11637	1	0.50
Al2	0.2403	-0.0041	0.11432	1	0.60
Al3	0.2395	0.0058	-0.10741	1	0.56
Al4	0.4944	0.7137	-0.1161	1	0.53
Al5	0.7351	0.5030	-0.11134	1	0.53
Al6	0.7442	0.4950	0.10988	1	0.55
O1	-0.1380	-0.1309	0.1070	1	1.88
O2	0.1172	-0.1079	0.1287	1	1.81
O3	0.2864	-0.0223	0.0026	1	1.12
O4	-0.0150	-0.2877	0.2174	1	1.55
O5	0.0235	-0.2941	0.0174	1	1.08
O6	0.3611	-0.0703	0.1727	1	1.29
O7	0.1849	0.1433	0.1367	1	1.54
O8	0.1617	-0.1295	-0.1379	1	1.25
O9	0.3680	0.0677	-0.1604	1	1.15
O10	0.3522	0.6365	-0.1118	1	1.42
O11	0.6053	0.5968	-0.1242	1	1.73
O12	0.7853	0.5221	-0.0013	1	1.26
O13	0.4990	0.7844	-0.2184	1	1.75
O14	0.5142	0.7929	-0.0173	1	1.59
O15	0.8508	0.5733	-0.1727	1	1.14
O16	0.6888	0.3503	-0.1297	1	1.26
O17	0.6638	0.6255	0.1450	1	1.06
O18	0.8760	0.4337	0.1591	1	1.14

A4 Crystal structures for tetracalcium aluminoferrite

Structural information for orthorhombic C_4AF is listed in the following tables.

A4.1 Orthorhombic C_4AF $Ca_2(Fe_{1.28}Al_{6.72})O_5$ structure determined by Colville and Geller (1971).

Table A4.1: Crystal constants for orthorhombic C_4AF (Colville and Geller, 1971).

Space group	*Ibm*2
Z	4
a (Å)	5.374
b (Å)	5.584
c (Å)	8.264
α (°)	109.744
β (°)	108.972
γ (°)	89.999
Cell Volume ($Å^3$)	219.061

Table A4.2: Atomic positional and displacement parameters for orthorhombic C_4AF (Colville and Geller, 1971).

Atom	x	y	z	SOF
Ca	0.0273	0.1087	0.4920	1
Fe1	0	0	0	0.76
Fe2	0.9283	0.25	0.9533	0.24
Al1	0	0	0	0.24
Al2	0.9283	0.25	0.9533	0.76
O1	0.2523	0.9861	0.2491	1
O2	0.0680	0.1493	0.0246	1
O3	0.8607	0.25	0.6193	1

APPENDIX B

MATERIALS AND EXPERIMENTAL

B1 Characterisation of tricalcium silicate from Construction Technology Laboratories (CTL).

The main sample of C_3S was obtained from CTL, Illinois, USA. A phase pure triclinic sample of Ca_3SiO_5 was requested, that would be of type T_1. The composition of the obtained sample was determined using XRF, DTA, and Rietveld refinement of synchrotron data from BNL, as outlined in Chapter 6 and in Peterson *et al* (2003b).

B1.1 XRF analysis of tricalcium silicate from CTL.

Sample composition was provided by CTL. Additional XRF data was obtained by a XRF bead method service provided from the University of New South Wales in Sydney. XRF analysis was also performed at the ANSTO on a PW 2400 XRF instrument (Philips). Two samples of approximate mass 7372 mg and 2670 mg were analysed at the ANSTO, as loose powder samples under He, using Uni Quant V 5.03 (Omega data systems bv, Netherlands). Four standards were analysed and subtracted from the background. These standards were F, Si, Al, and $CaPO_4$. Results for these analyses are presented below.

Table B1.1: Composition of triclinic C_3S from CTL provided by CTL.

Compound	Value (%)
CaO	72.27
SiO_2	25.38
Al_2O_3	1.88
MgO	0.46

Table B1.2: XRF composition of triclinic C_3S from CTL by the bead method provided by University of New South Wales.

Compound	Value (%)
Na_2O	0.35
MgO	0.57
Al_2O_3	-0.83
SiO_2	26.55
P_2O_5	0.040
SO_3	0.189
K_2O	-0.026
CaO	74.02
TiO_2	0.009
V_2O_5	0.005
Cr_2O_3	0.047
MnO	0.020
Fe_2O_3	0.72
NiO	-0.010
CuO	0.010
ZnO	0.005
As_2O_3	0.003
Rb_2O	-0.015
SrO	0.015
Y_2O_3	0.005
ZrO_2	0.011
BaO	-0.039
CeO_2	0.015
PbO	-0.001
ThO_2	0.098
U_3O_8	0.013
Total	101.7

Table B1.3: XRF composition of triclinic C_3S from CTL performed at ANSTO on a larger powder sample.

Compounds with < 100 mg/kg detected	Value (%)
MgO	0.19(1)
Al_2O_3	0.09(1)
SiO_2	29.0(3)
CaO	70.6(2)
Sc_2O_3	0.015(2)
Fe_2O_3	0.045(2)
SrO	0.020(1)

Table B1.4: XRF composition of triclinic C_3S from CTL performed on a smaller powder sample at ANSTO.

Compounds with < 100 mg/kg detected	Value (%)
MgO	0.17(2)
Al_2O_3	0.10(1)
SiO_2	30.8(3)
Ar	0.23(1)
CaO	68.5(2)
Sc_2O_3	0.030(4)
TiO_2	0.011(3)
Fe_2O_3	0.053(3)
SrO	0.013(1)

B1.2 Rietveld analysis of tricalcium silicate obtained from CTL.

Rietica was used refine the crystallographic structure of CTL, without the application of any bond length or angle constraints. The FOM for the refinement for data collected at ambient temperature were: $\chi^2 = 22.81$, $R_p = 3.52$, and $R_B = 1.66$. FOM for data collected at 549(21) º C were: $\chi^2 = 7.47$, $R_p = 3.29$, and $R_B = 1.52$. FOM for data collected at 682(28) º C were: $\chi^2 = 6.96$, $R_p = 2.99$, and $R_B = 1.24$. These results are supplementary to those presented in Peterson *et al* (2003b).

Table B1.5: Atomic positional and displacement parameters for the average sub-cell structure of T_1 triclinic C_3S T_1 from CTL at ambient temperature after refinement of synchrotron data from BNL.

Atom	x	y	z	B
Ca1	0.717(1)	-0.003(1)	0.970(1)	0.56(3)
Ca2	0.356(1)	0.161(1)	0.653(1)	0.56(3)
Ca3	0.660(1)	0.337(1)	0.339(1)	0.56(3)
Ca4	0.827(1)	0.175(1)	0.170(1)	0.56(3)
Ca5	0.181(1)	0.331(1)	0.826(1)	0.56(3)
Ca6	0.336(1)	0.410(1)	0.670(1)	0.56(3)
Ca7	0.672(1)	0.099(1)	0.320(1)	0.56(3)
Ca8	0.037(1)	0.160(1)	0.618(1)	0.56(3)
Ca9	0.631(1)	0.178(1)	0.713(1)	0.56(3)

Ca10	0.373(1)	0.336(1)	0.302(1)	0.56(3)
Ca11	0.974(1)	0.332(1)	0.375(1)	0.56(3)
Ca12	0.050(1)	0.401(1)	0.627(1)	0.56(3)
Ca13	0.361(1)	0.066(1)	0.286(1)	0.56(3)
Ca14	0.624(1)	0.431(1)	0.708(1)	0.56(3)
Ca15	0.952(1)	0.105(1)	0.373(1)	0.56(3)
Ca16	0.464(1)	0.092(1)	0.851(1)	0.56(3)
Ca17	0.209(1)	0.242(1)	0.462(1)	0.56(3)
Ca18	0.803(1)	0.255(1)	0.518(1)	0.56(3)
Ca19	0.546(1)	0.405(1)	0.148(1)	0.56(3)
Ca20	0.710(1)	0.510(1)	0.970(1)	0.56(3)
Ca21	0.703(1)	0.237(1)	0.971(1)	0.56(3)
Ca22	0.291(1)	0.266(1)	0.030(1)	0.56(3)
Ca23	0.863(1)	0.078(1)	0.813(1)	0.56(3)
Ca24	0.138(1)	0.419(1)	0.181(1)	0.56(3)
Ca25	0.015(1)	0.255(1)	1.000(1)	0.56(3)
Ca26	0	0	0	2.3(1)
Ca27	0	0.5	0	2.3(1)
Ca28	0.5	0	0.5	2.3(1)
Ca29	0.5	0.5	0.5	2.3(1)
Si1	0.827(2)	0.422(2)	0.174(2)	-0.08(8)
Si2	0.459(2)	0.352(1)	0.885(1)	-0.08(8)
Si3	0.166(2)	0.079(2)	0.824(2)	-0.08(8)
Si4	0.819(2)	0.006(1)	0.544(1)	-0.08(8)
Si5	0.187(2)	0.495(1)	0.449(2)	-0.08(8)
Si6	0.525(2)	0.166(1)	0.131(2)	-0.08(8)
Si7	0.147(2)	0.187(1)	0.210(1)	-0.08(8)
Si8	0.882(2)	0.313(2)	0.786(1)	-0.08(8)
Si9	0.477(1)	0.248(1)	0.504(1)	-0.08(8)
O1	0.041(3)	0.201(3)	0.252(3)	0.16(8)
O2	0.509(3)	0.254(3)	0.181(3)	0.16(8)
O3	0.653(3)	0.140(3)	0.067(3)	0.16(8)
O4	0.143(3)	0.067(3)	0.162(3)	0.16(8)
O5	0.224(3)	0.275(3)	0.643(2)	0.3(2)
O6	0.500(3)	0.038(3)	0.660(2)	0.3(2)
O7	0.422(3)	0.139(3)	0.040(2)	0.16(8)
O8	0.246(3)	0.223(2)	0.328(2)	0.16(8)
O9	0.697(3)	0.085(3)	0.845(3)	0.3(2)
O10	0.022(3)	0.248(3)	0.498(3)	0.3(2)
O11	0.484(3)	0.082(3)	0.164(3)	0.16(8)
O12	0.161(3)	0.252(3)	0.146(2)	0.16(8)
O13	0.826(3)	0.403(3)	0.480(3)	0.16(8)
O14	0.318(3)	0.469(3)	0.412(3)	0.16(8)
O15	0.202(3)	0.418(2)	0.551(3)	0.16(8)
O16	0.354(3)	0.432(3)	0.152(3)	0.3(2)
O17	0.155(3)	0.356(3)	0.987(3)	0.3(2)
O18	0.080(3)	0.449(2)	0.360(2)	0.16(8)
O19	0.285(3)	0.065(3)	0.775(3)	0.16(8)

O20	0.933(3)	0.399(3)	0.103(3)	0.16(8)
O21	0.170(3)	0.165(2)	0.901(2)	0.16(8)
O22	0.107(3)	-0.009(2)	0.887(2)	0.16(8)
O23	0.802(3)	0.234(2)	0.339(2)	0.3(2)
O24	0.887(3)	0.139(3)	1.015(2)	0.3(2)
O25	0.548(3)	0.460(3)	0.318(3)	0.3(2)
O26	0.055(3)	0.041(2)	0.716(2)	0.16(8)
O27	0.625(3)	0.242(3)	0.440(3)	0.16(8)
O28	0.760(3)	0.038(3)	0.670(2)	0.16(8)
O29	0.463(3)	0.374(3)	0.985(3)	0.16(8)
O30	0.628(3)	0.359(2)	0.891(2)	0.16(8)
O31	0.987(2)	0.306(2)	0.746(2)	0.16(8)
O32	0.683(2)	0.012(3)	0.477(2)	0.16(8)
O33	0.843(3)	0.241(2)	0.862(2)	0.16(8)
O34	0.727(3)	0.411(2)	0.091(2)	0.16(8)
O35	0.774(3)	0.321(2)	0.705(2)	0.16(8)
O36	0.821(3)	0.081(2)	0.486(2)	0.16(8)
O37	0.854(3)	0.432(2)	0.876(2)	0.16(8)
O38	0.450(2)	0.157(2)	0.468(2)	0.16(8)
O39	0.099(3)	0.095(2)	0.462(2)	0.16(8)
O40	0.828(3)	0.354(2)	0.229(2)	0.16(8)
O41	0.425(3)	0.240(2)	0.804(2)	0.16(8)
O42	0.520(3)	0.282(2)	0.635(2)	0.16(8)
O43	0.423(3)	0.343(2)	0.487(2)	0.16(8)
O44	0.169(3)	0.457(2)	0.757(2)	0.16(8)
O45	0.441(3)	0.426(2)	0.813(2)	0.16(8)

Table B1.6: Si-O bond lengths of triclinic C_3S T_1 from CTL at ambient temperature after refinement of synchrotron data from BNL.

Atom 1	Atom 2	Length (Å)	Std. Error
Si1			
	O20	1.60	0.03
	O34	1.53	0.03
	O40	1.37	0.03
	O44	1.73	0.03
Si2			
	O29	1.31	0.03
	O30	1.96	0.03
	O41	1.71	0.03
	O45	1.63	0.03
Si3			
	O19	1.58	0.02
	O21	1.38	0.03
	O22	1.86	0.03
	O26	1.85	0.03
Si4			
	O28	1.85	0.02

	O32	1.78	0.03
	O36	1.49	0.02
	O39	1.71	0.03
Si5			
	O13	1.52	0.02
	O14	1.65	0.02
	O15	2.00	0.02
	O18	1.67	0.02
Si6			
	O2	1.27	0.02
	O3	1.79	0.02
	O7	1.63	0.02
	O11	1.48	0.02
Si7			
	O1	1.40	0.02
	O4	1.67	0.02
	O8	1.86	0.02
	O12	1.43	0.02
Si8			
	O31	1.37	0.03
	O33	1.73	0.03
	O35	1.63	0.03
	O37	1.85	0.03
Si9			
	O27	1.98	0.03
	O38	1.30	0.03
	O42	1.76	0.03
	O43	1.55	0.03

Table B1.7: O-Si-O bond angles of triclinic C_3S T_1 from CTL at ambient temperature after refinement of synchrotron data from BNL .

Atom	Leg 1	Leg 2	Angle (º)	Std. Error
Si1				
	O20	O34	99.38	0.92
	O20	O40	107.86	1.31
	O20	O44	110.53	1.02
	O34	O40	115.21	1.41
	O34	O44	106.14	1.07
	O40	O44	116.41	1.62
Si2				
	O29	O30	90.45	0.92
	O29	O41	126.26	1.03
	O29	O45	127.58	1.05
	O30	O41	103.42	0.98
	O30	O45	94.03	1.04
	O41	O45	103.27	1.55
Si3				

	O19	O21	109.19	1.32
	O19	O22	122.45	0.98
	O19	O26	105.31	0.97
	O21	O22	101.69	0.78
	O21	O26	127.82	1.23
	O22	O26	91.09	1.22
Si4				
	O28	O32	93.74	1.21
	O28	O36	119.39	1.02
	O28	O39	106.99	0.97
	O32	O36	68.98	0.89
	O32	O39	126.95	1.03
	O36	O39	130.31	0.96
Si5				
	O13	O14	115.65	0.78
	O13	O15	99.24	0.99
	O13	O18	119.27	0.81
	O14	O15	93.57	1.02
	O14	O18	114.17	1.20
	O15	O18	110.06	1.10
Si6				
	O2	O3	118.13	1.21
	O2	O7	106.8	1.02
	O2	O11	122.43	0.98
	O3	O7	103.82	0.97
	O3	O11	111.48	1.22
	O7	O11	87.05	1.42
Si7				
	O1	O4	99.82	0.97
	O1	O8	99.87	0.98
	O1	O12	110.94	0.89
	O4	O8	110.44	1.23
	O4	O12	121.46	1.06
	O8	O12	111.55	1.02
Si8				
	O31	O33	122.14	1.12
	O31	O35	113.92	1.10
	O31	O37	115.4	0.92
	O33	O35	110.19	0.98
	O33	O37	96.38	0.92
	O35	O37	94.06	0.98
Si9				
	O27	O38	95.56	1.21
	O27	O42	103.66	0.94
	O27	O43	103.52	1.08
	O38	O42	113.58	1.77
	O38	O43	133.28	1.97
	O42	O43	102.8	1.63

Table B1.8: Atomic positional and displacement parameters for the average sub-cell structure of T_1 triclinic C_3S T_1 from CTL at 549(21) ° C after refinement of synchrotron data from BNL.

Atom	x	y	z	B
Ca1	0.703(1)	0.006(1)	0.969(1)	1.63(5)
Ca2	0.353(1)	0.161(1)	0.657(1)	1.63(5)
Ca3	0.661(1)	0.326(1)	0.337(1)	1.63(5)
Ca4	0.835(1)	0.177(1)	0.177(1)	1.63(5)
Ca5	0.187(1)	0.328(1)	0.824(1)	1.63(5)
Ca6	0.334(1)	0.408(1)	0.666(1)	1.63(5)
Ca7	0.673(1)	0.088(1)	0.325(1)	1.63(5)
Ca8	0.043(1)	0.163(1)	0.621(1)	1.63(5)
Ca9	0.634(1)	0.181(1)	0.715(1)	1.63(5)
Ca10	0.382(1)	0.330(1)	0.298(1)	1.63(5)
Ca11	0.967(2)	0.338(1)	0.367(1)	1.63(5)
Ca12	0.045(1)	0.401(1)	0.622(1)	1.63(5)
Ca13	0.368(1)	0.067(1)	0.298(1)	1.63(5)
Ca14	0.626(1)	0.433(1)	0.709(1)	1.63(5)
Ca15	0.964(1)	0.096(1)	0.370(1)	1.63(5)
Ca16	0.466(1)	0.091(1)	0.851(1)	1.63(5)
Ca17	0.214(1)	0.227(1)	0.468(1)	1.63(5)
Ca18	0.790(1)	0.259(1)	0.518(1)	1.63(5)
Ca19	0.550(1)	0.415(1)	0.148(1)	1.63(5)
Ca20	0.693(1)	0.502(1)	0.961(1)	1.63(5)
Ca21	0.702(1)	0.233(1)	0.967(1)	1.63(5)
Ca22	0.282(1)	0.268(1)	0.031(1)	1.63(5)
Ca23	0.872(1)	0.081(1)	0.818(1)	1.63(5)
Ca24	0.146(1)	0.428(1)	0.188(1)	1.63(5)
Ca25	0.011(1)	0.253(1)	0.995(1)	1.63(5)
Ca26	0	0	0	2.6(3)
Ca27	0	0.5	0	2.6(3)
Ca28	0.5	0	0.5	2.6(3)
Ca29	0.5	0.5	0.5	2.6(3)
Si1	0.838(2)	0.420(2)	0.166(2)	0.68(9)
Si2	0.461(2)	0.346(2)	0.890(1)	0.68(9)
Si3	0.152(2)	0.077(2)	0.821(2)	0.68(9)
Si4	0.804(2)	0.013(2)	0.544(2)	0.68(9)
Si5	0.204(2)	0.481(2)	0.457(2)	0.68(9)
Si6	0.501(2)	0.155(2)	0.125(2)	0.68(9)
Si7	0.168(2)	0.159(1)	0.201(2)	0.68(9)
Si8	0.863(2)	0.318(2)	0.781(2)	0.68(9)
Si9	0.503(2)	0.245(2)	0.488(2)	0.68(9)
O1	0.043(3)	0.218(3)	0.258(3)	1.6(1)
O2	0.487(3)	0.281(3)	0.185(3)	1.6(1)
O3	0.629(3)	0.144(3)	0.08(3)	1.6(1)

O4	0.144(3)	0.060(3)	0.145(3)	1.6(1)
O5	0.198(2)	0.280(2)	0.642(2)	-0.3(2)
O6	0.516(3)	0.071(2)	0.634(2)	-0.3(2)
O7	0.427(3)	0.139(3)	0.035(3)	1.6(1)
O8	0.248(3)	0.202(3)	0.288(3)	1.6(1)
O9	0.657(3)	0.098(3)	0.827(3)	-0.3(2)
O10	0.011(3)	0.248(3)	0.481(3)	-0.3(2)
O11	0.506(3)	0.076(3)	0.189(3)	1.6(1)
O12	0.137(3)	0.240(3)	0.130(3)	1.6(1)
O13	0.823(3)	0.409(3)	0.477(3)	1.6(1)
O14	0.321(3)	0.473(3)	0.408(3)	1.6(1)
O15	0.176(3)	0.414(3)	0.518(3)	1.6(1)
O16	0.351(3)	0.401(2)	0.149(3)	-0.3(2)
O17	0.141(3)	0.402(2)	1.017(2)	-0.3(2)
O18	0.115(3)	0.457(3)	0.353(3)	1.6(1)
O19	0.294(3)	0.044(3)	0.754(2)	1.6(1)
O20	0.914(3)	0.418(3)	0.132(2)	1.6(1)
O21	0.154(3)	0.172(3)	0.882(3)	1.6(1)
O22	0.118(3)	-0.002(3)	0.869(3)	1.6(1)
O23	0.826(3)	0.193(2)	0.329(2)	-0.3(2)
O24	0.881(2)	0.123(3)	1.003(2)	-0.3(2)
O25	0.566(2)	0.485(2)	0.348(2)	-0.3(2)
O26	0.089(3)	0.092(3)	0.756(3)	1.6(1)
O27	0.614(3)	0.241(3)	0.441(3)	1.6(1)
O28	0.764(3)	0.045(3)	0.656(3)	1.6(1)
O29	0.456(3)	0.350(3)	0.984(3)	1.6(1)
O30	0.610(3)	0.319(3)	0.848(3)	1.6(1)
O31	1.007(3)	0.300(3)	0.751(3)	1.6(1)
O32	0.665(3)	-0.007(3)	0.46(3)	1.6(1)
O33	0.866(3)	0.258(3)	0.862(3)	1.6(1)
O34	0.719(3)	0.377(3)	0.056(3)	1.6(1)
O35	0.743(3)	0.313(3)	0.694(3)	1.6(1)
O36	0.874(3)	0.093(3)	0.508(3)	1.6(1)
O37	0.863(3)	0.412(3)	0.859(3)	1.6(1)
O38	0.435(3)	0.156(3)	0.460(3)	1.6(1)
O39	0.146(3)	0.072(3)	0.464(3)	1.6(1)
O40	0.777(3)	0.367(3)	0.234(3)	1.6(1)
O41	0.422(3)	0.225(3)	0.810(3)	1.6(1)
O42	0.492(3)	0.282(3)	0.635(3)	1.6(1)
O43	0.423(3)	0.336(3)	0.471(3)	1.6(1)
O44	0.181(3)	0.461(3)	0.766(3)	1.6(1)
O45	0.444(3)	0.428(3)	0.805(3)	1.6(1)

Table B1.9: Si-O bond lengths of triclinic C_3S T_1 from CTL at 549(21) º C after refinement of synchrotron data from BNL.

Atom 1	Atom 2	Length (Å)	Std. Error
Si1			
	O20	1.04	0.03
	O34	1.95	0.02
	O40	1.56	0.03
	O44	1.74	0.03
Si2			
	O29	1.29	0.03
	O30	1.89	0.02
	O41	1.82	0.02
	O45	1.86	0.02
Si3			
	O19	1.95	0.02
	O21	1.39	0.02
	O22	1.52	0.03
	O26	1.18	0.03
Si4			
	O28	1.59	0.02
	O32	1.86	0.02
	O36	1.60	0.02
	O39	1.33	0.03
Si5			
	O13	1.63	0.03
	O14	1.57	0.02
	O15	1.48	0.03
	O18	1.67	0.03
Si6			
	O2	1.79	0.03
	O3	1.65	0.02
	O7	1.42	0.03
	O11	1.59	0.03
Si7			
	O1	1.81	0.02
	O4	1.44	0.02
	O8	1.45	0.02
	O12	1.73	0.02
Si8			
	O31	1.77	0.03
	O33	1.57	0.02
	O35	1.77	0.03
	O37	1.48	0.03
Si9			
	O27	1.48	0.03
	O38	1.46	0.03
	O42	1.96	0.02
	O43	1.66	0.03

Table B1.10: O-Si-O bond angles of triclinic C_3S T_1 from CTL at 549(21) º C after refinement of synchrotron data from BNL.

Atom	Leg 1	Leg 2	Angle (º)	Std. Error
Si1				
	O20	O34	105.37	0.98
	O20	O40	140.3	1.23
	O20	O44	107.56	1.01
	O34	O40	91.67	1.32
	O34	O44	111.33	1.04
	O40	O44	98.64	0.98
Si2				
	O29	O30	111.70	0.97
	O29	O41	111.18	1.02
	O29	O45	138.85	1.01
	O30	O41	85.89	0.97
	O30	O45	88.33	1.02
	O41	O45	105.6	1.53
Si3				
	O19	O21	112.85	0.98
	O19	O22	110.83	0.89
	O19	O26	102.53	1.20
	O21	O22	116.56	1.12
	O21	O26	95.79	1.13
	O22	O26	116.78	0.98
Si4				
	O28	O32	102.96	0.97
	O28	O36	116.22	1.02
	O28	O39	105.15	0.88
	O32	O36	106.17	0.87
	O32	O39	109.40	1.01
	O36	O39	116.08	0.91
Si5				
	O13	O14	113.75	0.99
	O13	O15	107.25	0.91
	O13	O18	107.29	1.08
	O14	O15	120.32	1.02
	O14	O18	98.99	1.12
	O15	O18	108.18	0.96
Si6				
	O2	O3	105.14	0.98
	O2	O7	103.71	1.10
	O2	O11	121.4	1.02
	O3	O7	101.95	1.20
	O3	O11	101.34	1.14
	O7	O11	120.49	1.15
Si7				
	O1	O4	111.95	0.97

	O1	O8	95.15	0.79
	O1	O12	78.23	1.08
	O4	O8	132.42	1.17
	O4	O12	112.04	1.10
	O8	O12	111.31	0.95
Si8				
	O31	O33	97.18	1.01
	O31	O35	126.07	1.21
	O31	O37	105.32	0.82
	O33	O35	121.47	0.88
	O33	O37	92.25	0.79
	O35	O37	108.74	0.97
Si9				
	O27	O38	115.57	1.11
	O27	O42	123.02	0.92
	O27	O43	112.53	1.03
	O38	O42	100.17	1.88
	O38	O43	109.47	1.79
	O42	O43	93.42	1.62

Table B1.11: Si-O bond lengths of triclinic C_3S T_1 from CTL at 682(28) º C after refinement of synchrotron data from BNL.

Atom 1	Atom 2	Length (Å)	Std. Error
Si1			
	O20	1.16	0.01
	O34	1.88	0.02
	O40	1.78	0.02
	O44	1.82	0.02
Si2			
	O29	1.68	0.02
	O30	1.83	0.03
	O41	1.65	0.02
	O45	1.47	0.03
Si3			
	O19	1.79	0.02
	O21	2.11	0.02
	O22	1.22	0.03
	O26	1.41	0.02
Si4			
	O28	1.51	0.02
	O32	1.81	0.02
	O36	2.10	0.01
	O39	1.52	0.02
Si5			
	O13	1.87	0.03
	O14	1.99	0.02
	O15	1.44	0.02

	O18	1.51	0.02
Si6			
	O2	1.43	0.02
	O3	1.48	0.02
	O7	1.76	0.02
	O11	1.88	0.02
Si7			
	O1	1.76	0.02
	O4	1.33	0.02
	O8	1.64	0.03
	O12	1.59	0.02
Si8			
	O31	1.20	0.01
	O33	1.90	0.02
	O35	1.82	0.03
	O37	1.59	0.02
Si9			
	O27	1.69	0.02
	O38	1.79	0.02
	O42	1.71	0.02
	O43	1.65	0.02

Table B1.12: O-Si-O bond angles of triclinic C_3S T_1 at 682(28) º C from CTL after refinement of synchrotron data from BNL.

Atom	Leg 1	Leg 2	Angle (º)	Std. Error
Si1				
	O20	O34	132.23	0.27
	O20	O40	108.08	0.28
	O20	O44	119.32	0.21
	O34	O40	104.51	0.20
	O34	O44	101.18	0.20
	O40	O44	77.20	0.27
Si2				
	O29	O30	140.43	0.22
	O29	O41	113.35	0.32
	O29	O45	100.11	0.21
	O30	O41	78.50	0.23
	O30	O45	111.85	0.21
	O41	O45	108.66	0.21
Si3				
	O19	O21	124.0	0.32
	O19	O22	85.73	0.31
	O19	O26	130.70	0.43
	O21	O22	112.22	0.21
	O21	O26	96.60	0.27
	O22	O26	105.08	0.19
Si4				

	O28	O32	123.33	0.31
	O28	O36	77.87	0.44
	O28	O39	86.33	0.43
	O32	O36	46.62	0.59
	O32	O39	109.59	0.23
	O36	O39	99.22	0.19
Si5				
	O13	O14	83.36	0.28
	O13	O15	117.94	0.41
	O13	O18	121.35	0.23
	O14	O15	99.11	0.29
	O14	O18	117.01	0.21
	O15	O18	112.22	0.33
Si6				
	O2	O3	137.79	0.21
	O2	O7	95.83	0.39
	O2	O11	98.87	0.21
	O3	O7	114.41	0.21
	O3	O11	104.83	0.27
	O7	O11	98.07	0.29
Si7				
	O1	O4	103.14	0.19
	O1	O8	100.74	0.29
	O1	O12	99.35	0.22
	O4	O8	141.25	0.21
	O4	O12	106.91	0.24
	O8	O12	98.71	0.22
Si8				
	O31	O33	103.70	0.18
	O31	O35	110.01	0.33
	O31	O37	114.06	0.15
	O33	O35	99.97	0.19
	O33	O37	110.48	0.22
	O35	O37	116.90	0.21
Si9				
	O27	O38	101.48	0.22
	O27	O42	133.56	0.27
	O27	O43	105.63	0.32
	O38	O42	88.77	0.19
	O38	O43	101.21	0.19
	O42	O43	116.67	0.18

B1.3 DTA analysis of tricalcium silicate obtained from CTL.

DTA was performed at the University of Technology, Sydney using a SDT 2960 (TA Instruments, USA). The software used was Thermal Solution OS2 Warp V 3.0 (IBM, USA). Sample size was approximately 14.23 mg. Measurements were taken using a heating rate of 10 °C per minute. Four cycles of heating to 1200 °C then cooling to 400 °C, were performed. The DTA data was transformed into its first-derivative form, using Origin (Origin V 7.03, OriginLab Corporation, USA), and represented as derivative DTA data to enhance the features.

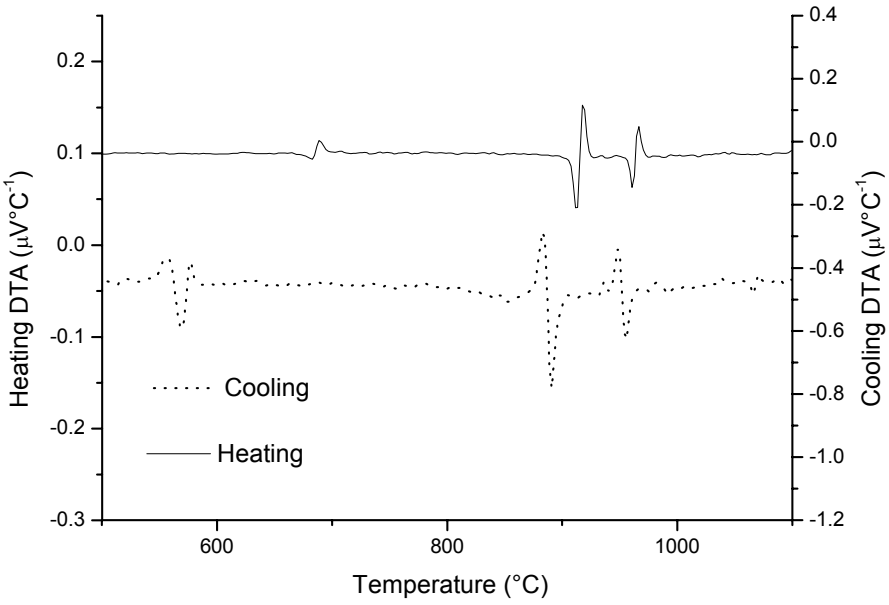

Figure B1.1: Derivative-DTA data for the first heating and cooling cycle of triclinic C_3S from CTL.

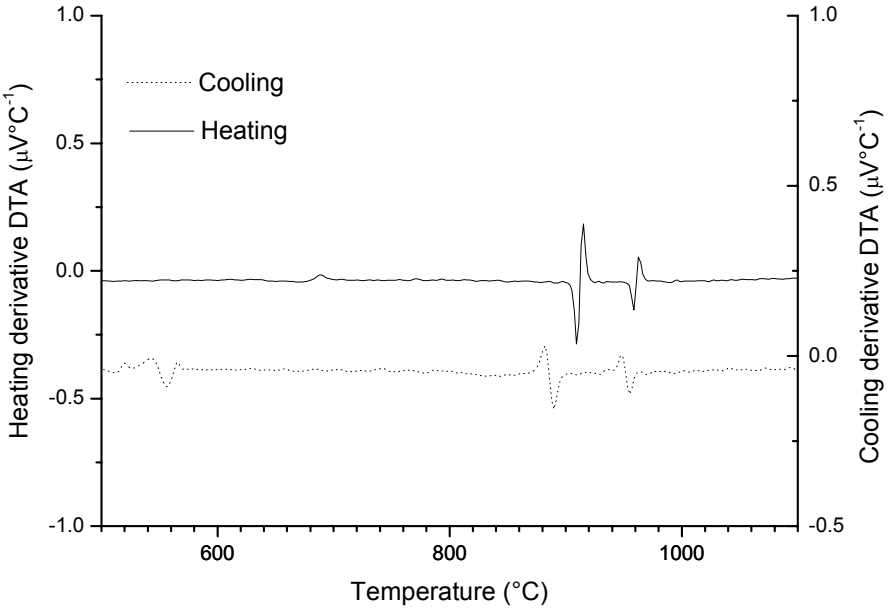

Figure B1.2: Derivative-DTA data for the second heating and cooling cycle of triclinic C_3S from CTL.

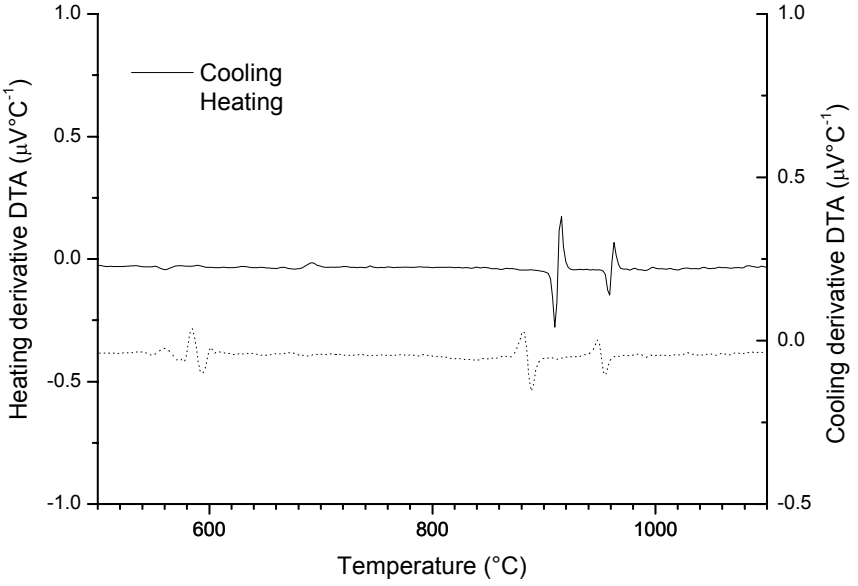

Figure B1.3: Derivative-DTA data for the third heating and cooling cycle of triclinic C_3S from CTL.

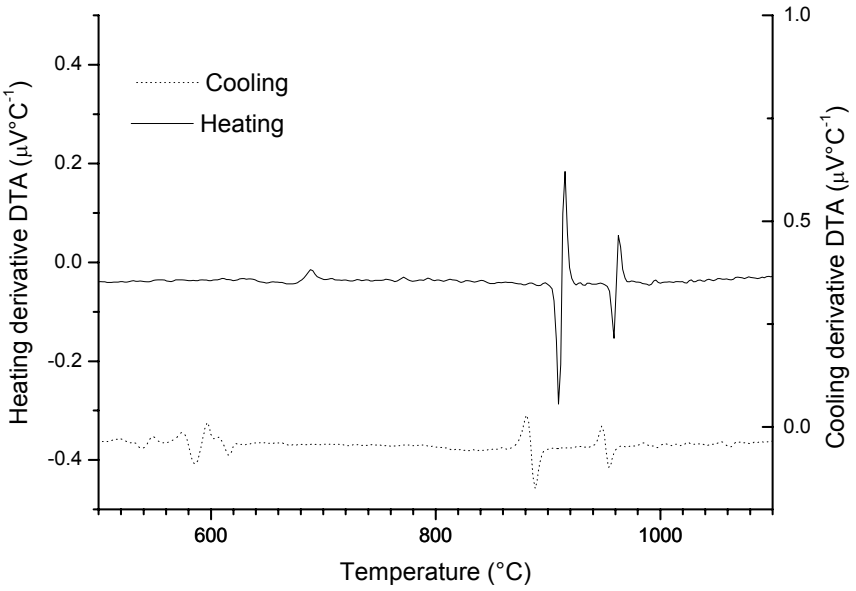

Figure B1.4: Derivative-DTA data for the fourth heating and cooling cycle of triclinic C_3S from CTL.

B2 Characterisation of tricalcium silicate synthesised at ANSTO

A sample of C_3S was synthesised at the ANSTO. The composition of the sample was determined using XRF. Rietveld refinement of data collected at the KEK (as outlined in Chapter 6, section 6.2.2) and DTA (as outlined in Peterson *et al*, 2003b), were also performed.

Most batches made were of the T_1 type, expected from this method. An interesting abnormal batch was, however, also produced. The XRF/Rietveld results for this batch are presented below. These results suggested that Mg-stabilisation of another form occurred.

B2.1 Method of tricalcium silicate synthesis

Composition:

15.00 g of "AEROSIL® 150" hydrophilic fumed SiO_2 (specific surface area = $150m^2/g$ from Degussa, Germany) and 74.96 g $CaCO_3$ (98.5-100.5 % from Bacto Laboratories, Australia), were combined. Mettler Toledo scales, 5-3100 g PB3002, Switzerland, calibrated by Cyrullas' Instruments, Australia, were used to weigh the reactants.

Method:

The mixture was ground, by hand, using a mortar and pestle for 20 minutes. The mixture was then palletised at 5000 PSI (Archer hydraulics, Australia) using a stainless steel die, and then let sit for 30 s before being palletised again, and then removed from the die. The mixture was fired (1700 ° C HT 04/17 furnace with Eurotherm 2404 controller, Labec laboratory equipment, Australia) using the following firing schedule:

1. 5 °C / min to 900 °C, with a dwell time of 5 minutes
2. 5 °C / min to 1500 °C, with a dwell time of 2 hours
3. 5 °C / min to 30 °C.

This process was repeated 4 times, or until no free CaO was visible in XRD analysis. XRD was performed using Cu Kα radiation (Scintag X1, Scintag Instruments, U.S.A.). Clinker was loaded onto a flat-plate sample holder, using a side-loading technique designed to reduce preferred orientation effects. Data were collected over the 2θ range 2.00-90.00°, with a stepping of 0.02°. A corundum standard (alumina powder std. 676 NIST, USA) was used to determine the zero point of the instrument for use in Rietveld refinements.

B2.2 XRF analysis of tricalcium silicate synthesised at ANSTO.

XRF analysis was performed at the ANSTO on a PW 2400 XRF instrument (Philips). One sample of approximate mass 2670 mg was analysed as a loose powder under He, using Uni Quant V 5.03 (Omega data systems bv, Netherlands). Four standards were analysed and subtracted from the background. These were F, Si, Al, and $CaPO_4$.

Table B2.1: XRF composition of triclinic C_3S of Mg-stabilised triclinic type synthesised at ANSTO.

Compounds with < 100 mg/kg detected	Value (%)
MgO	0.59(3)
Al_2O_3	0.09(1)
SiO_2	30.5(3)
Ar	0.24(1)
CaO	68.5(2)
Sc_2O_3	0.018(4)
Fe_2O_3	0.031(3)
SrO	0.035(2)

B2.3 Rietveld analysis of tricalcium silicate synthesised at ANSTO.

Rietica was used to refine the structure of the C_3S, without the application of any bond length or angle constraints. Synchrotron power diffraction data was gathered using the ADHOC system at KEK, Japan. In this way, data was obtained in a similar manner to that outlined in section 6.2.2 of Chapter 6. FOM for the first histogram (2θ = 10-40 °) refinement were: $\chi^2 = 4.15$, $R_p = 3.57$, and $R_B = 1.31$. FOM for the second histogram (2θ = 50-70 °) refinement were: $\chi^2 = 1.66$, $R_p = 3.02$, and $R_B = 1.64$. Atomic displacement parameters were constrained between atom types. Oxygen atoms associated and not associated with SiO_4 groups were also constrained within these groups. Additionally, calcium atoms on special and general positions were constrained within these groups.

Figures B2.3 and B2.4 show atomic representation of the Mg-stabilised triclinic average structure, produced using the program Atoms (1999). Silicon-oxygen tetrahedra with central silicon atoms are shown in red, calcium atoms are dark blue, and oxygen atoms are shown in turquoise. The unit cell is outlined with black. Polyligand oxygen atoms that form SiO_4 tetrahedra are shown with small radii, whilst those that form part of Ca-O bonds are larger in radius. The unit cell is highlighted by a black box. In figure, 2.3, the hexagonal basal plane that exists in the pseudo-trigonal

cell in the rhombohedral setting was located and highlighted within the structure using a yellow outline.

In table B2.3, all atoms are fully occupied (SOF = 1).

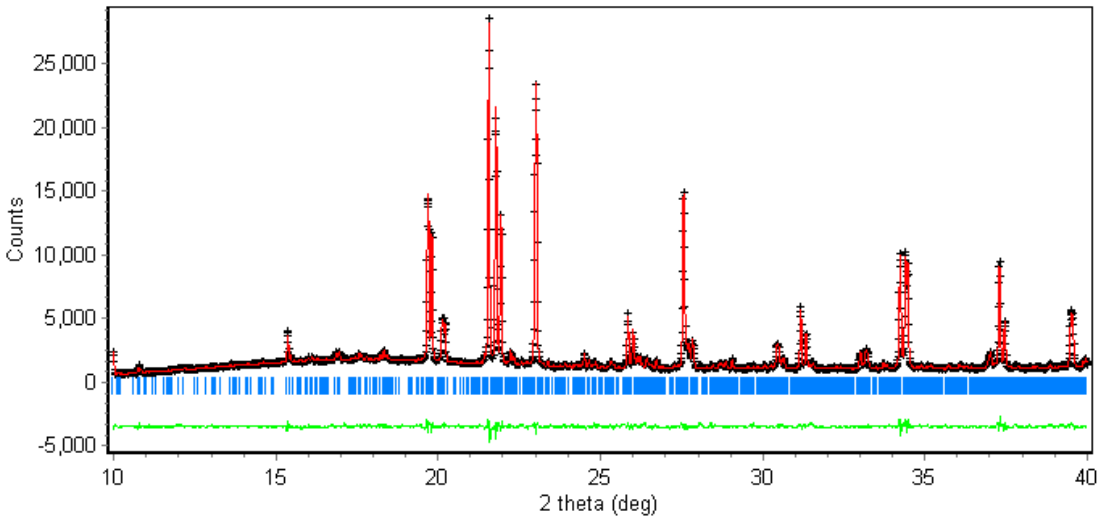

Figure B2.1: First histogram refinement plot of Mg-stabilised triclinic C_3S using Rietica.

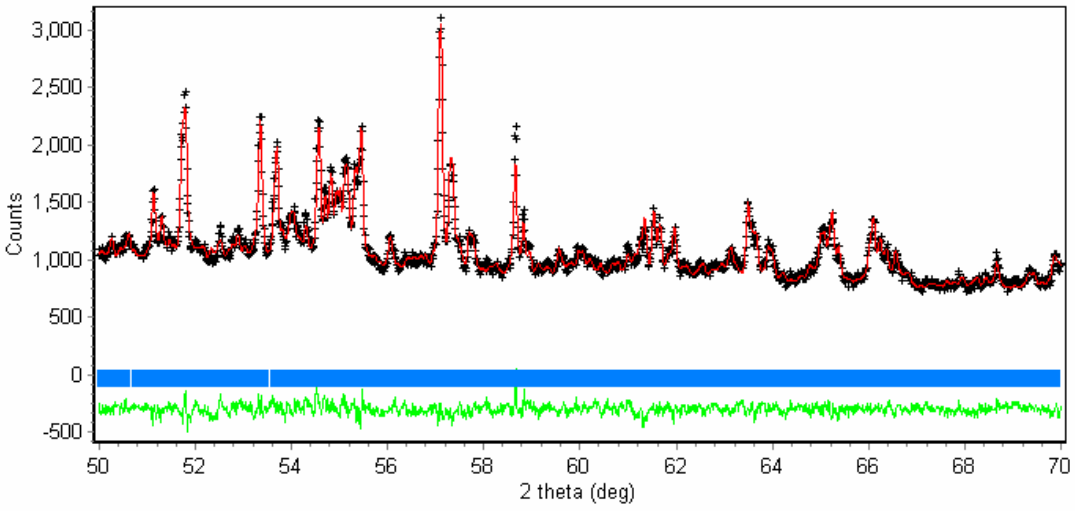

Figure B2.2: Second histogram refinement plot of Mg-stabilised triclinic C_3S using Rietica.

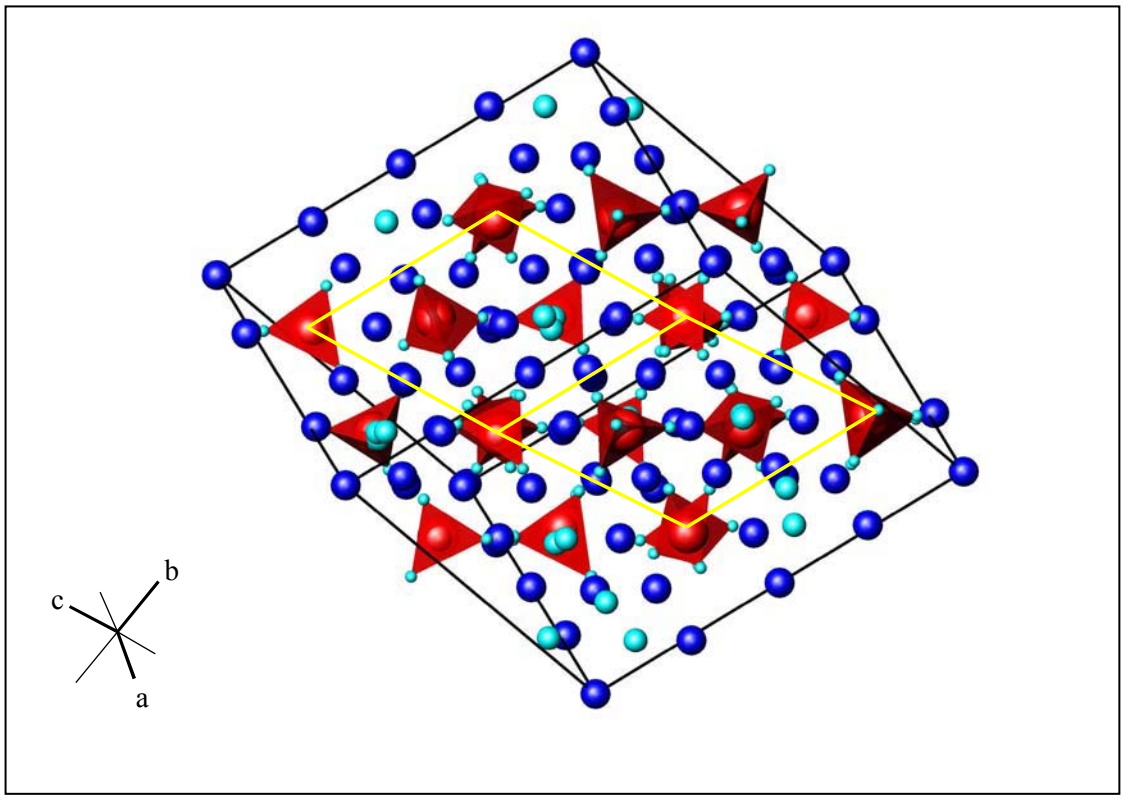

Figure B2.3: Unit cell representation with transformation showing common hexagonal plane of structure in Mg-stabilised triclinic C_3S, with crystal axes arrangement shown.

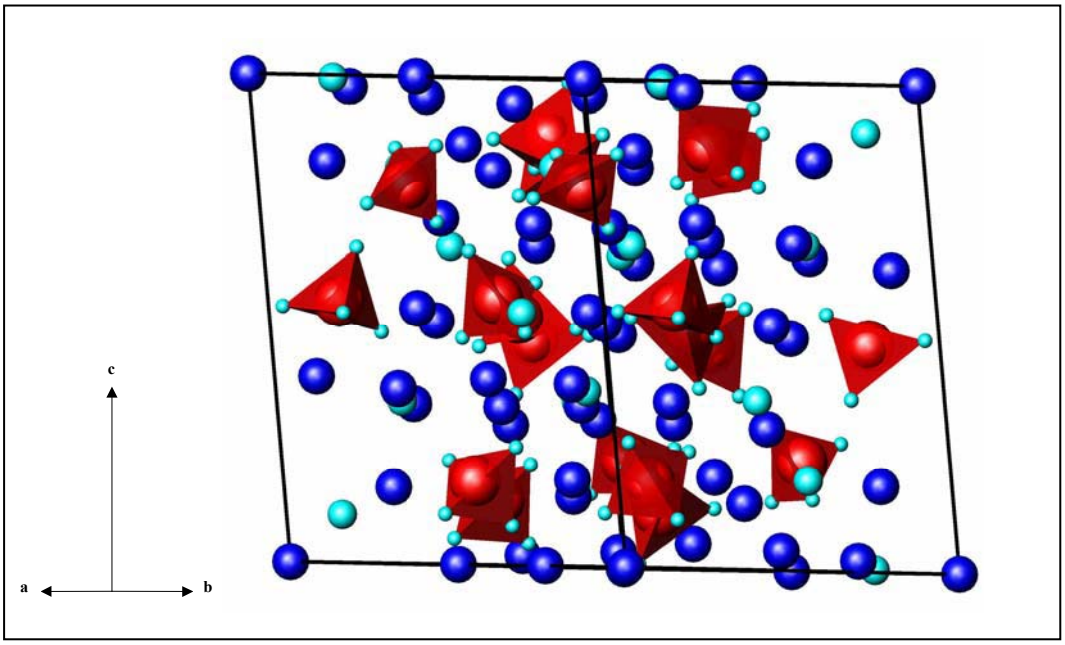

Figure B2.4: Unit cell representation of structure in Mg-stabilised triclinic C_3S, with crystal axes arrangement shown.

Table B2.2: Crystal constants for Mg-stabilised triclinic C_3S.

Space group	$P\bar{1}$
Z	18
a (Å)	11.6362(1)
b (Å)	14.1893(1)
c (Å)	13.6501(2)
α (°)	104.9868(9)
β (°)	94.6182(7)
γ (°)	90.105(1)
Cell Volume (Å^3)	2169.4(6)

Table B2.3: Atomic positional and displacement parameters for Mg-stabilised triclinic C_3S.

Atom	x	y	z	B (Å^2)
Ca1	0.707(1)	0.007(1)	0.978(1)	0.72(3)
Ca2	0.338(2)	0.159(1)	0.659(1)	0.72(3)
Ca3	0.668(2)	0.341(1)	0.325(2)	0.72(3)
Ca4	0.834(1)	0.163(2)	0.156(1)	0.72(3)
Ca5	0.188(1)	0.324(1)	0.823(1)	0.72(3)
Ca6	0.319(1)	0.407(1)	0.669(1)	0.72(3)
Ca7	0.668(1)	0.078(1)	0.328(1)	0.72(3)
Ca8	0.050(1)	0.164(1)	0.627(1)	0.72(3)
Ca9	0.640(1)	0.180(1)	0.711(1)	0.72(3)
Ca10	0.383(1)	0.341(1)	0.302(1)	0.72(3)
Ca11	0.959(1)	0.325(1)	0.358(1)	0.72(3)
Ca12	0.037(1)	0.400(1)	0.620(1)	0.72(3)
Ca13	0.364(1)	0.060(1)	0.289(1)	0.72(3)
Ca14	0.617(1)	0.433(1)	0.701(1)	0.72(3)
Ca15	0.969(1)	0.094(1)	0.380(1)	0.72(3)
Ca16	0.463(1)	0.091(1)	0.864(1)	0.72(3)
Ca17	0.196(1)	0.239(1)	0.478(1)	0.72(3)
Ca18	0.805(1)	0.250(1)	0.524(1)	0.72(3)
Ca19	0.535(1)	0.399(1)	0.144(1)	0.72(3)
Ca20	0.707(1)	0.497(1)	0.948(1)	0.72(3)
Ca21	0.711(1)	0.239(1)	0.960(1)	0.72(3)
Ca22	0.285(1)	0.271(1)	0.032(1)	0.72(3)

Ca23	0.868(1)	0.081(1)	0.824(1)	0.72(3)
Ca24	0.131(1)	0.425(1)	0.190(1)	0.72(3)
Ca25	0.015(1)	0.255(1)	1.000(1)	0.72(3)
Ca26	0	0	0	3.5(3)
Ca27	0	0.5	0	3.5(3)
Ca28	0.5	0	0.5	3.5(3)
Ca29	0.5	0.5	0.5	3.5(3)
Si1	0.847(2)	0.420(2)	0.172(2)	-0.12(8)
Si2	0.466(2)	0.352(2)	0.884(2)	-0.12(8)
Si3	0.171(2)	0.077(2)	0.826(2)	-0.12(8)
Si4	0.795(2)	0.009(2)	0.537(2)	-0.12(8)
Si5	0.176(2)	0.489(2)	0.455(2)	-0.12(8)
Si6	0.525(2)	0.169(2)	0.136(2)	-0.12(8)
Si7	0.147(2)	0.181(2)	0.221(2)	-0.12(8)
Si8	0.868(2)	0.310(2)	0.777(2)	-0.12(8)
Si9	0.500(2)	0.246(2)	0.508(2)	-0.12(8)
O1	0.012(3)	0.192(3)	0.247(3)	1.3(1)
O2	0.520(3)	0.264(3)	0.207(3)	1.3(1)
O3	0.650(3)	0.148(3)	0.054(3)	1.3(1)
O4	0.157(3)	0.076(3)	0.152(3)	1.3(1)
O5	0.213(3)	0.284(3)	0.641(3)	-0.2(2)
O6	0.475(3)	0.038(3)	0.653(3)	-0.2(2)
O7	0.424(3)	0.143(3)	0.047(3)	1.3(1)
O8	0.254(3)	0.216(3)	0.305(3)	1.3(1)
O9	0.653(3)	0.083(3)	0.816(3)	-0.2(2)
O10	0.002(3)	0.247(3)	0.483(3)	-0.2(2)
O11	0.514(3)	0.076(3)	0.186(3)	1.3(1)
O12	0.156(3)	0.254(3)	0.154(3)	1.3(1)
O13	0.818(3)	0.390(3)	0.465(3)	1.3(1)
O14	0.301(3)	0.496(3)	0.419(3)	1.3(1)
O15	0.173(3)	0.412(3)	0.523(3)	1.3(1)
O16	0.335(3)	0.445(3)	0.180(3)	-0.2(2)
O17	0.164(3)	0.400(3)	0.995(3)	-0.2(2)
O18	0.089(3)	0.476(3)	0.357(3)	1.3(1)
O19	0.291(3)	0.072(3)	0.761(3)	1.3(1)
O20	0.912(3)	0.386(3)	0.103(3)	1.3(1)
O21	0.130(3)	0.177(3)	0.890(3)	1.3(1)
O22	0.168(3)	0.001(3)	0.901(3)	1.3(1)

O23	0.809(3)	0.185(3)	0.333(3)	-0.2(2)
O24	0.891(3)	0.143(3)	0.995(3)	-0.2(2)
O25	0.568(3)	0.465(3)	0.338(3)	-0.2(2)
O26	0.073(3)	0.032(3)	0.745(3)	1.3(1)
O27	0.594(3)	0.215(3)	0.448(3)	1.3(1)
O28	0.773(3)	0.052(3)	0.648(3)	1.3(1)
O29	0.435(3)	0.393(3)	0.993(3)	1.3(1)
O30	0.613(3)	0.331(3)	0.876(3)	1.3(1)
O31	0.987(3)	0.308(3)	0.738(3)	1.3(1)
O32	0.677(3)	0.009(3)	0.475(3)	1.3(1)
O33	0.839(3)	0.260(3)	0.854(3)	1.3(1)
O34	0.729(3)	0.403(3)	0.081(3)	1.3(1)
O35	0.779(3)	0.305(3)	0.702(3)	1.3(1)
O36	0.873(3)	0.096(3)	0.512(3)	1.3(1)
O37	0.878(3)	0.421(3)	0.859(3)	1.3(1)
O38	0.395(3)	0.157(3)	0.486(3)	1.3(1)
O39	0.140(3)	0.097(3)	0.476(3)	1.3(1)
O40	0.825(3)	0.326(3)	0.213(3)	1.3(1)
O41	0.407(3)	0.242(3)	0.818(3)	1.3(1)
O42	0.518(3)	0.250(3)	0.631(3)	1.3(1)
O43	0.405(3)	0.323(3)	0.488(3)	1.3(1)
O44	0.170(3)	0.466(3)	0.758(3)	1.3(1)
O45	0.455(3)	0.427(3)	0.800(3)	1.3(1)

Table B2.4: Si-O bond lengths of Mg-stabilised triclinic C_3S.

Atom 1	Atom 2	Length (Å)	Std. Error
Si1			
	O20	1.25	0.04
	O34	1.75	0.04
	O40	1.60	0.04
	O44	1.67	0.04
Si2			
	O29	1.53	0.04
	O30	1.75	0.03
	O41	1.69	0.04
	O45	1.76	0.03
Si3			
	O19	1.70	0.04
	O21	1.56	0.04
	O22	1.68	0.04
	O26	1.54	0.04

Si4			
	O28	1.53	0.04
	O32	1.56	0.03
	O36	1.66	0.04
	O39	1.65	0.04
Si5			
	O13	1.77	0.03
	O14	1.58	0.03
	O15	1.60	0.03
	O18	1.59	0.03
Si6			
	O2	1.45	0.03
	O3	1.89	0.03
	O7	1.59	0.03
	O11	1.64	0.03
Si7			
	O1	1.64	0.03
	O4	1.55	0.03
	O8	1.62	0.03
	O12	1.56	0.03
Si8			
	O31	1.52	0.03
	O33	1.47	0.04
	O35	1.38	0.03
	O37	1.67	0.04
Si9			
	O27	1.42	0.03
	O38	1.70	0.04
	O42	1.65	0.04
	O43	1.61	0.04

Table B2.5: O-Si-O bond angles of Mg-stabilised triclinic C_3S.

Atom	Leg 1	Leg 2	Angle (°)	Std. Error
Si1				
	O20	O34	89.71	1.3
	O20	O40	101.31	1.4
	O20	O44	131.74	1.38
	O34	O40	97.84	1.99
	O34	O44	102.6	1.93
	O40	O44	122.3	1.87
Si2				
	O29	O30	112.58	1.91
	O29	O41	118.09	1.99
	O29	O45	118.97	2.22
	O30	O41	101.87	1.85
	O30	O45	95.9	1.74
	O41	O45	105.99	1.97
Si3				
	O19	O21	120.45	2.21

	O19	O22	115.26	1.31
	O19	O26	104.79	1.45
	O21	O22	106.11	1.39
	O21	O26	107.84	1.33
	O22	O26	100.28	2.06
Si4				
	O28	O32	105.63	1.73
	O28	O36	102.06	2.25
	O28	O39	109.95	2.12
	O32	O36	105.44	1.87
	O32	O39	117.6	1.95
	O36	O39	114.7	1.62
Si5				
	O13	O14	94.41	2.12
	O13	O15	109.92	1.66
	O13	O18	112.82	2.01
	O14	O15	110.42	2.87
	O14	O18	106.4	2.20
	O15	O18	119.81	3.32
Si6				
	O2	O3	116.64	1.62
	O2	O7	115.79	2.13
	O2	O11	115.09	1.89
	O3	O7	97.51	2.01
	O3	O11	107.94	2.87
	O7	O11	101.56	1.23
Si7				
	O1	O4	106.66	2.11
	O1	O8	123.26	1.41
	O1	O12	101.02	1.45
	O4	O8	114.21	1.43
	O4	O12	108.59	1.13
	O8	O12	101.31	2.16
Si8				
	O31	O33	122.77	2.18
	O31	O35	113.18	2.22
	O31	O37	98.62	2.11
	O33	O35	112.97	2.19
	O33	O37	94.15	2.09
	O35	O37	111.62	2.02
Si9				
	O27	O38	111.46	2.04
	O27	O42	117.89	2.1
	O27	O43	125.18	2.16
	O38	O42	91.88	1.71
	O38	O43	89.7	2.01
	O42	O43	110.84	1.94

B2.4 DTA analysis of tricalcium silicate synthesised at ANSTO.

DTA was performed at the University of Technology, Sydney using a SDT 2960 (TA Instruments, USA). The software used was Thermal Solution OS2 Warp V 3.0 (IBM, USA). Sample size was approximately 14.23 mg. Measurements were taken using a heating rate of 10 °C per minute. Four cycles of heating to 1200 °C then cooling to 400 °C, were performed. The DTA data was transformed into its first-derivative form using Origin (Origin V 7.03, OriginLab Corporation, USA) and represented as derivative DTA data to enhance the features.

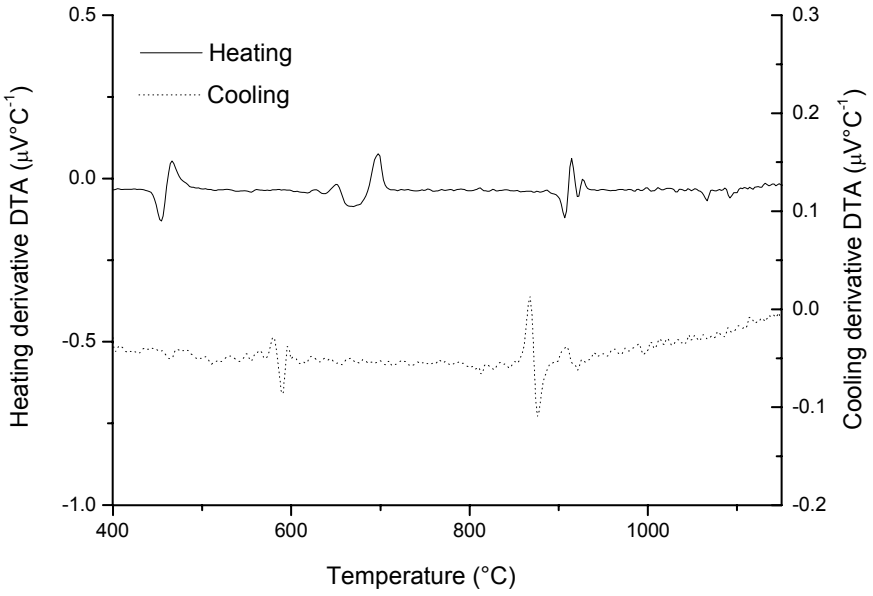

Figure B2.5: Derivative-DTA data for the first heating and cooling cycle of Mg-stabilised triclinic C_3S.

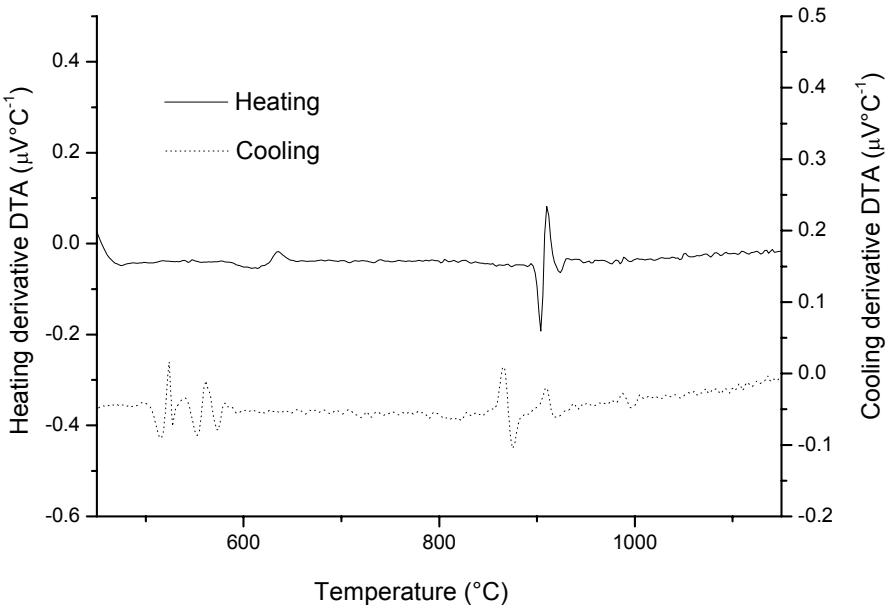

Figure B2.6: Derivative-DTA data for the second heating and cooling cycle of Mg-stabilised triclinic C_3S.

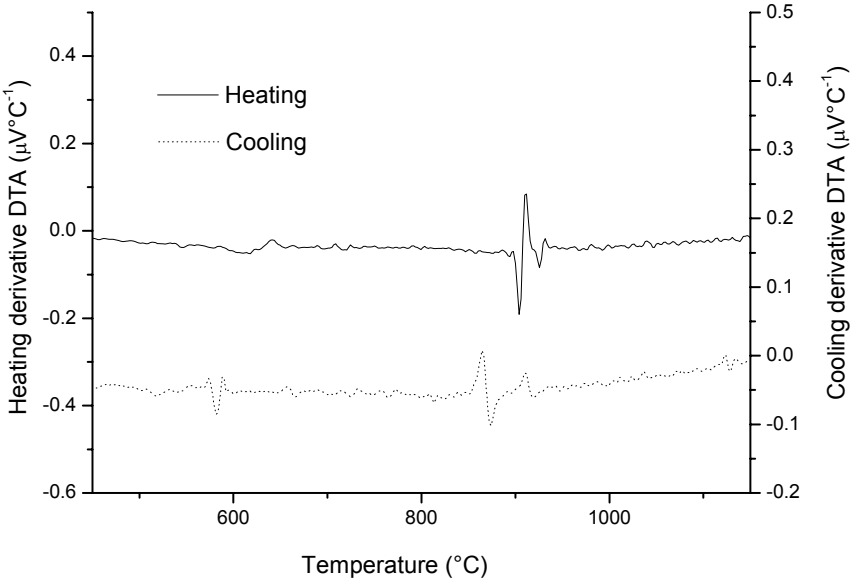

Figure B2.7: Derivative-DTA data for the third heating and cooling cycle of Mg-stabilised triclinic C_3S.

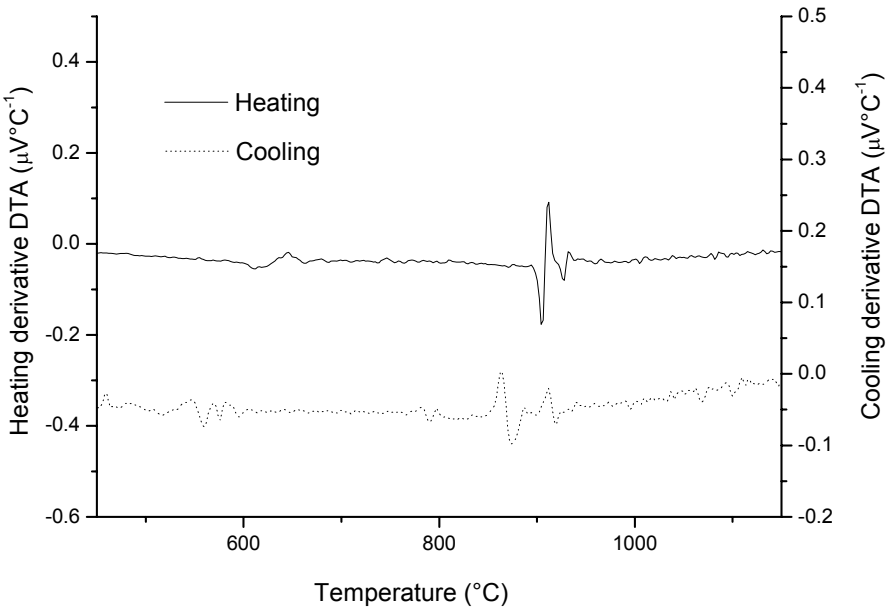

Figure B2.8: Derivative-DTA data for the fourth heating and cooling cycle of Mg-stabilised triclinic C_3S.

B3 Calibration of furnace at BNL from Chapter 6, section 6.2.3

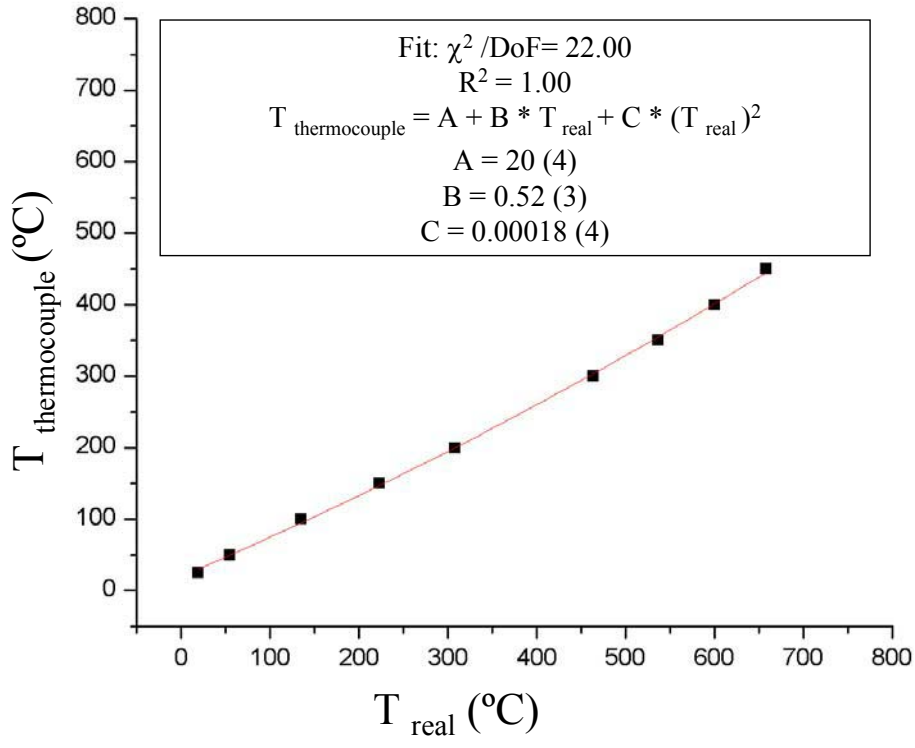

Figure B3.1: Calibration curve for furnace on beam-line X7A using NaCl.

REFERENCES

Ahtee, M., Nurmela, M., Suortii, P. and Jarvinen, M. (1989). *J. Appl. Crystallogr.* **22,** 261.

Aldridge, L.P. (1982). *Cem. Concr. Res.* **12**, 381.

Anderson, M.T., Vaughey, J.T. and Pöppelmeier, K.R. (1993). *Chem . Mater.* **5,** 151.

ANSTO website. http:www.ansto.gov.au/

ANBF website. http://www.ansto.gov.au/natfac/asrp1.

Ashcroft, N.W. and Mermin, N.D. *Solid State Physics,* Saunders College, Japan (1981).

Baerlocher, C. in *Proc. Int. Conf. On Zeolites,* Butterworths, London, Reno (1993).

Bacon, G.E. *Neutron Scattering in Chemistry,* Butterworths, London (1977).

Bellotto, M. and Signes-Frehel, M. (1998). *Materials Science Forum,* **278-281,** 846.

Bentur, A., Berger, R.L., Kung, J.H., Milestone, N.B. and Young, J.F. (1979). *J. Am. Ceram. Soc.* **62,** 362.

Bergstrom, T.B., Hall, C. and Scrivener, K. (1994). *Adv. Cement Res.* **4,** 141.

Berliner, R., Ball, C. and West, P.B. (1995). *Mat. Res. Soc. Symp. Proc.* **376** , 487.

Berliner, R., Ball, C. and West, P.B. (1997). *Cem. Concr. Res.* **27**, 551.

Berliner, R., Popovici, M., Herwig, K., Jennings, H.M. and Thomas, J. (1988). *Physica B (Amsterdam).* **241-243**, 1237.

Bertaut, E.F., Blum, P. and Sagnières, A. (1959). *Acta Crys.* **12,** 149.

Bigaré, M., Guinier, A., Mazières, C., Regourd, M., Yannaquis, N., Eysel, W., Hahn, T. and Woermann, E. (1967). *J. Am. Ceram. Soc.* **50,** 609.

Bogue, R.H. (1929). *Ind. Engnrg Chem. (Anal.)* **1,** 192.

Bragg, L. and Claringbull, G.F. *Crystal Structure of Minerals*, Cornwall Univ. Press, Ithaca (1965).

Caglioti, G., Paoletti, A, and Ricci, F.P. (1958) *Nucl. Instrum.* **3,** 223.

Carlson, E.T. (1931), *Rock Products,* **34[25],** 52.

Catti, M., Gazzoni, G. and Ivaldi, G. (1984) *Acta Crystallographica B,* **40,** 537.

Colville, A.A. and Geller, S. (1971). *Acta Cryst.* **B27,** 2311.

Colville, A.A. and Geller, S. (1972). *Acta Cryst.* **B28,** 3196.

Courtial, M., de Norifontaine, M. –N., Dunstetter, F., Gasecki, G. and Signes-Frehel, M. (2003), *Powder Diffraction* **18** [1], 7.

Cullity, B.D. *Elements of X-Ray Diffraction* (2nd Edn), Addison-Wesley, USA (1978).

Czaya, R. (1971). *Acta Crystallographica B,* **27,** 848.

Day, D.E. (1963). *Nature, Lond.* **200,** 649.

Dinnebier, R.E., (1999). *Powder Diffraction*, **14,** 84.

Dollase, W.A., (1986). *J. Appl. Crystallogr.* **19,** 267.

Dorner, B. *Coherent Inelastic Scattering in Lattice Dynamics.* Springer-Verlag, Berlin (1982).

Dowty, E. *ATOMS for Windows V5.06,* (1999).

Ewald, P.P, (1913), *Phys. Zeitschr*., **14**, 465.

Fayos, J., Glasser, F.P., Howie, R.A., Lachowski, E. and Perez-Mendez, M. (1985). *Acta Cryst.* **C41,** 814.

Feret, B. and Feret, C.F. (1999). *Cem. Concr. Res.* **29,** 1627.

Finger, L.W., Cox, D.E. and Jephcoat, A.P. (1994). *J. Appl. Crystallogr.* **27,** 892.

FitzGerald, S.A., Neumann, D.A., Rush, J.J., Bentz, D.P. and Livingston, R.A. (1998). *Chem. Mater.* **10**, 397.

Fujii, K. and Kondo, W. (1968). *J. Am. Ceram. Soc.* **57,** 492.

Füllmann, T., Walenta, G., Pöllmann, H., Gimenez, M., Lauzon, C., Hagopian-Babikian, S., Dalrymple, T. and Noon, P. (2001) *International Cement Research*, **1**, 41.

Garrett, R.F., Cookson, D.J., Foran, G.J., Sabine, T.M., Kennedy, B.J. and Wilkins, S.W. (1995). *Review of Scientific Instruments.* **66,** 1351.

Giacovazzo, C. in *Fundamentals of Crystallography*. p. 171, Oxford university press, USA (2000).

Giacovazzo, C., Monaco, H.L., Viterbo, D., Scordari, F., Gilli, G., Zanotti, G. and Catti, M. *Fundamentals of crystallography*, Oxford university press, USA (2000).

Gollop, R. and Taylor, H.F.W. (1994). *Cem. Concr. Res.* **24,** 1347.

Golovastikov, N.I., Matveeva, R.G. and Belov, N.V. (1975). *Kristallografiya.* **20,** 721.

Guinier, A. *X-ray Diffraction,* W. H. Freeman, San Francisco (1963).

Guinier, A. and Regourd, M., in *Proceedings of the 5th International Symposium on the Chemistry of Cement* (Tokyo 1968), Vol. 1, p. 1, Cement Association of Japan, Tokyo (1969).

Hahn, T., Eysel, W. and Woermann, E., in *Proceedings of the 5th International Symposium on the Chemistry of Cement* (Tokyo 1968), Vol. 1, p. 61, Cement Association of Japan, Tokyo (1969); summarised from E. Woermann, T. Hahn and W. Eysel, *Zem.-Kalik-Gips* **16,** 370 (1963); **20**, 385 (1967); **21,** 241 (1968); **22,** 235, 412 (1969).

Hansen, W.C., Brownmiller, L.T. and Bogue, R.H. (1928). *J. Am. Chem. Soc.* **50,** 396.

Harada, T., Ohta, M. and Takagi, S., in *Japan. Rev. Gen. Meet., Tech. Sess.* Vol. 31, p.31, Cement Association of Japan, Japan (1977).

Harrisson, A.M., Taylor, H.F.W. and Winter, N.B. (1985). *Cem. Concr. Res.* **15,** 775.

Haussler, F., Hempel M., Eichhorn, F., Hempel A. and Baumbach, H. (1995). *Physica Scripta.* **T57,** 184.

Haussler, F., Hempel, M. and Baumbach, H. (1997). *Advances in Cement Research*. **9**, 139.

Hawkins, K., in *Materials Characterisation Using Rietveld Analysis of Diffraction Data,* (Melbourne, 1995), p. 16, AXAA Inc. Victorian Branch, Australia (1995).

Hermann, H. and Ermrich, M. (1987) *Acta Cryst.* **A43,** 401.

Hewat, A.W. *UKAEA Research Group Report R7350*. Grenoble, France, (1973).

Hill, R.J. and Cranswick, L.M.D. (1994). *J. Appl. Cryst.* **27,** 802.

Hill, R.J. (1992). *J. Appl. Cryst,* **A35,** 248.

Hill, R.J. and Howard, C.J. Australian Atomic Energy Commission Report No. AAEC/M112, Lucas Heights Research Laboratories, Sydney, Australia (1986).

Hill, R.J. and Howard, C.J. (1987). *J. Appl. Cryst.* **20,** 467.

Howard, C.J. (1982). *J. Appl. Cryst.* **15,** 615.

Hudson, K.E. and Groves, G.W. (1982). *Cem. Concr. Res.,* **12,** 61.

Hunter, B.A. (1998). *Powder Diffraction Newsletter,* **20**, 21.

Hunter, B.A. and Howard, C.J. *LHPM A Computer Program for Rietveld Analysis of X-ray and Neutron Powder Diffraction Patterns,* Australian Nuclear Science and Technology Organisation, Australia (2000).

Il'inets, A.M., Malinovskii, Y. and Nevskii, N. N. (1985). *Dokl. Akad. Nauk SSSR.* **281,** 332.

Il'inets, A.M. and Bikbau, M.Ya. (1990). *Kristallografiya,* **35,** 91.

Il'inets, A.M. and Bikbau, M.Ya., in *Diffraction Methods in Materials Science* (ed. J. Hasek), p. 161, Nova Science Publishers, New York (1992).

International Tables for Crystallography. Vol. A, Ed. T Hahn, Kluwer Academic, Berlin, (1995).

International Tables for Crystallography. Vol. C, Ed. A. J. C. Wilson and E. Prince, Kluwer Academic, London, (1999).

ISIS website. http:www.isis.rl.ac.uk/

Isu, N., Ishida, H. and Mitsuda, T. (1995). *Cem. Concr. Res.* **25**, 243.

Jackman, J.M., Jones, R.C., Yost, R.S. and Babcock, C.J. (1997). *Soil. Sci. Soc. Am. J.* **61**, 618.

Janik, J.A., Kurdwski, W., Podsiadly, R. and Samseth, J. (1996). *Acta Physica Polonoca A.* **90**, 1179.

Jeffery, J.W. (1952). *Acta Cryst.* **5,** 26.

Jong, J.G.M. de, Stein, H.M. and Stevels, J.M. (1967). *J. App. Chem.* **17,** 246.

Jordan, B., O'Connor, B.H. and Li, D.Y. (1990). *Powder Diffraction,* **5,** 64.

Jost, K.H., Ziemer, B. and Seydel, R. (1977). *Acta Cryst.* **B33,** 1696.

Jupe, A.C., Cockroft, J.K., Barnes, P., Colston, S.L., Sankar, G. and Hall, C. (2001). *J. Appl. Cryst.* **34,** 55.

Khattak, C.P. and Cox, D.E. (1977). *J. Appl. Crystallogr.* **10,** 405.

Kisi, E.H. (1994). *Materials Forum,* **18,** 135.

Kisi, E.H., in *Materials Characterisation Using Rietveld Analysis of Diffraction Data,* (Melbourne, 1995), p. 30, AXAA Inc. Victorian Branch, Australia (1995).

Klug, H.P. and Alexander, L.E. *X-ray Diffraction Procedures for Polycrystalline and Amorphous Materials*. Wiley, New York (1974).

Larson, A.C. and Von Dreele, R.B. (2000). *Los Alamos National Laboratory Report LAUR*, 86.

La Torre, Á.G. de, Bruque, S., Campo, J and Aranda, M.A.G. (2002). *Cem. Concr. Res.* **32,** 1347.

Lea, F.M. *The Chemistry of Cement and Concrete* (3rd Ed.), Arnold, London (1988).

Lea, F.M. and Parker, T.W. (1934). *Phil. Trans. R. Soc.* **234,** 1.

Le Bail, A., Duroy, H. and Fourquet, J.L. (1988). *Math. Res. Bull.* **23**, 447.

Livingston, R.A., Neumann, D.A. and Rush, J.J. (1995). *Mater. Res. Soc. Symp. Proc.* **376,** 459.

Lovesey, S.W. *Theory of Neutron Scattering from Condensed Matter*. Oxford Science Publications, Oxford (1987).

Madsen, I.C., Scarlett, N.V.Y., Cranswick, L.M.D. and Lwin, T. (2001). *J. Appl. Cryst,* **34,** 409.

Maki, I. and Sugimura, T. (1970). *J. Ceram. Soc. Japan,* **78,** 129.

Maki, I. and Chromý, S. (1978). *Cemento,* **3,** 247.

Maki, I. and Kato, K. (1982). *Cem. Concr. Res.* **12,** 93.

Maki, I., in *Proceedings of the 8th International Congress on the Chemistry of Cement* (Rio de Janeiro 1986), Vol. 1, p. 34, Abla Gráfica e Editora Ltda, Rio de Janeiro (1986).

Maki, I., Fukuda, K., Oba, E., Yoshida, H., Mitsumatsu, M. and Ito, S. (1995). *Cem. Concr. Res.* **25,** 863.

Malmros, G. and Thomas, J.O. (1977). *J. Appl. Crystallogr.* **10,** 7.

Mascolo, G., Marchese, B., Frigione G. and Sersale, R. (1977). *J. Am. Ceram. Soc.* **56** [4], 222.

Matulis, C.E. and Taylor, J.C. (1992). *J. Appl. Cryst.* **26,** 351.

Matulis, C.E. and Taylor, J.C. (1992). *Powder Diffraction*. **7,** 89.

McKusker, L.B., Von Dreele, R.B., Cox, D.E., Louër, D. and Scardi, P. *J. Appl. Cryst.* (1999). **32**, 36.

Meyers, S.L. (1930). *Rock Prod*. **33**, 78.

Mindess, S. and Young, J.F. *Concrete,* Prentice Hall, USA (1981).

Miyabe, H. and Roy, D.M. (1964). *J. Am. Ceram. Soc.* **47**, 318.

Miyazaki, M, Yamazaki, S, Sasaki, K, Ishida, H and Toraya, H. (1998). *J. Am. Ceram. Soc.,* **81** [5] 1339.

Mondal, P. and Jeffery, J.W. (1975). *Acta Cryst.* **B31,** 689.

Moore , A.E. (1967). *Silicate Ind.* **32,** 87.

Morita, H., Nakano, H., Shirakami, T. and Urabe, K. (2002). *Key Engineering Materials,* **206-213,** 747.

Mumme, W.G. (1995). *N. Jb. Miner. Mh.* **1995,** 145.

Mumme, W.G., Hill, R.J., Bushnell-Wye, G. and Segnit, E.R. (1995). *N. Jb. Miner. Abh.* **169,** 35.

Mumme, W.G., Tsambourakis, G., Hill, R.J., and Madsen, I.C. in *Materials Characterisation Using Rietveld Analysis of Diffraction Data,* (Melbourne, 1995), p. 39, AXAA Inc. Victorian Branch, Australia (1995).

Mumme, W.G., Cranswick, L. and Chakoumakos, B. (1996). *N. Jb. Miner. Abh.* **170,** 171.

Neubauer, J. and Sieber, R. (1996). *Materials Science Forum*. **228**, 807.

Neubauer, J., Sieber, R., Kuzel, H.J. and Ecker, M. (1996). *Cem. Concr. Res.* **26,** 77.

Nishi, F. and Takéuchi, Y. (1975). *Acta Cryst.* **B31,** 1169.

Nishi, F. and Takéuchi, Y. (1984). *Zeit. Krist.* **168,** 197.

Nishi, F., Takéuchi, Y. and Maki, I. (1985). *Zeit. Krist.* **172**, 297.

Noirfontaine, M.-N. de Dunstetter, F., Courtial, M, Gasecki, G. and Signes-Frehel, M. (2003). *Zeit. Krist.* **218,** 8.

O'Connor, B.H. and Pratapa, S. (2002). *Advances in X-ray Analysis,* **45,** 158.

O'Connor, B.H., Li, D.Y., and Hunter, B.A. (2001). *Advances in X-ray Analysis,* **44,** 97.

O'Connor, B.H. and Li, D.Y. (2000). *Advances in X-ray Analysis,* **43,** 305.

O'Connor, B.H. and Li, D.Y. (2000). *Advances in X-ray Analysis,* **42,** 204.

O'Connor, B. in *Materials Characterisation Using Rietveld Analysis of Diffraction Data,* (Melbourne, 1995), p. 34, AXAA Inc. Victorian Branch, Australia (1995).

O'Connor, B.H., Li, D.Y., Jordan, B., Raven, M.D. and Fazey, P.G. (1990). *Advances in X-ray Analysis* **33,** 269.

Odler, I. (1973). *J. Appl. Chem. Biotechnol.* **23,** 661.

Oftedal, I. (1927). *Zeitschrift fuer Physikalische Chemie*. **128,** 135.

Pawley, G.S., Mackenzie, G.A., and Dietrich, O.W. (1977). *Act Crystallogr. A.* **33,** 142.

Pawley, G.S. (1981). *J. Appl. Cryst.* **14** 357.

Portland Cement Association website. http:www.portcement.org

Perez-Mendez, M., Howie, R.A. and Glasser, F.P. (1984). *Cem. Concr. Res.* **14**, 57.

Petricek, V. and Dusek, M. *Jana2000. The crystallographic computing system*. Institute of Physics, Praha, Czech Republic (2000).

Pritula, O. and Smrčok, L. (2003). *Powder Diffraction,* **18** [1], 16.

Pritula, O. (2001) *Materials Structure*, **8** [2], 88.

Prodjosantoso, A.K., Kennedy, B.J. and Hunter, B.A. (2000). *Aust. J. Chem.* 53, 195.

Pucharovsky, D. (1999) *Croatica Chemica Acta*, **72** [2-3], 135.

Rasberry, S.D. in *Report of Investigations, Reference Materials 8486, 8487, 8488, Portland Cement Clinker*, National Institute of Standards and Technology (NIST), Gaithersburg, MD (1989).

Raven, M.D., in *Materials Characterisation Using Rietveld Analysis of Diffraction Data,* (Melbourne, 1995), p. 20, AXAA Inc. Victorian Branch, Australia (1995).

Regourd, M., in *Proceedings of the 8th International Congress on the Chemistry of Cement* (Rio de Janeiro 1986)*,* Vol. 1, p. 199, Abla Gráfica e Editora Ltda, Rio de Janeiro (1986).

Regourd, M. (1986). *Chemica Scripta,* **26A,** 37.

Regourd, M (1964). *Bull. Soc. Minér. Crist. Franç,* **87**, 241.

Rietveld, H.M. (1967). *Acta Crystallogr*., **22**, 151.

Rietveld, H.M. (1969). *J. Appl. Cryst.* **2**, 65.

Sabine, T.M., Hunter, B.A., Sabine, W.R. and Ball, C.J. (1998). *J. Appl. Cryst.* **31**, 47.

Scarlett, N.V.Y., Madsen, I.C., Cranswick, L.M.D., Lwin, T., Groleau, E., Stephenson, G., Aylmore, M. and Agron-Olshina, N. (2002). *J. Appl. Cryst.* N. **35,** 383.

Scarlett, N.V., Madsen, I., Manias, C. and Retallack, D. (2001) *Powder Diffraction*. **16** [2], 71.

Shirakami, T., Iwashima, M., Shiraishi, A. and Urabe, K. (1999). *Cement Science and Concrete Technology,* **53,** 30.

Shpynova, L.G., Belov, N.V., Sanitski, M.A. and Chikh, V.I. (1968) *Dokl. Akad. Nauk SSSR*, **236,** 168.

Sinclair, W. and Groves, G.W. (1984) *J. Am. Ceram. Soc.* **67** [5], 325.

Singh, N.B. (1976). *J. Scient. Ind. Res.* **35,** 75.

Singh, N.B., Rai, S. and Singh, N. (2002). *J. Am. Ceram. Soc.* **85** [9], 2171.

Skalny, J. and Odler, I. (1972). *J. Colloid Interface Sci.* **40,** 199.

Skalny, J.P. and Young, J.F., in *Proceedings of the 8th International Congress on the Chemistry of Cement* (Paris 1980)*,* Vol. 1, p. II-1/3, Editions Septima, Paris (1980, 1981).

Smith, D.K. (1962). *Acta Crys.* **15,** 1146.

Squires, G.L. *Introduction to the theory of Thermal Neutron Scattering,* Cambridge University Press, Cambridge (1978).

Staněk, T. and Sulovský, P. (2002). *Cem. Concr. Res.*, **32,** 1169.

Stephan, D., Maleki, H., Knöfel, D., Eber, B. and Härdtl, R. (1999). *Cem. Concr. Res.,* **29,** 545.

Stutzman, P. and Leigh, S. *Phase Composition Analysis of the NIST Reference Clinkers by Optical Microscopy and X-ray Powder Diffraction,* National Institute of Standards and Technology, Gaithersburg, MD, 1989.

Suherman, P.M., van Riessen, A., O'Connor, B., Deyu, L., Bolton, D. and Fairhurst, H. (2002). *Powder Diffraction.* **17** [3], 178.

Takéuchi, Y., Nishi, F. and Maki, I. (1980). *Zeit. Krist.* **152,** 259.

Taylor, H.F.W. *Cement Chemistry,* Vol. 2, Academic Press, London (1997).

Taylor, J.C. (1986). *Z. Krist.* **176**, 183.

Taylor, J.C. (1987). *Z. Krist.* **181**, 151.

Taylor, J.C. (1991). *Powder Diffraction*. **6**, 2.

Taylor, J.C. and Matulis. C.E. (1991). *J. Appl. Cryst.*, **24**, 14.

Taylor, J.C. and Zhu, R. (1992). *Powder Diffraction.* **7**, 152.

Taylor, J.C. and Aldridge, L.P. (1993a). *Powder Diffraction.* **8**, 138.

Taylor, J.C. and Aldridge, L.P. (1993b). *Advances in X-Ray Analysis*. **36**, 309.

Taylor, J.C., Zhu, R. and Aldridge, L.P. (1993). *Materials Science Forum* **133-136,** 329.

Taylor, J.C. and Matulis C.E. (1994). *Powder Diffraction.* **9**, 119.

Taylor, J.C. and Matulis C.E., in *Materials Characterisation Using Rietveld Analysis of Diffraction Data,* (Melbourne, 1995), p. 6, AXAA Inc. Victorian Branch, Australia (1995).

Taylor, J.C. *Rietveld Made Easy.* J.C. Taylor, Sydney (1996).

Taylor, J.C., Hinczak, I. and Matulis, C.E. (2000). *Powder diffraction* **15,** 7.

Tilley, D.B, Barrows, T.T, Zimmerman, E.C. (1997). *Alcheringa*. **21**, 157.

Toby, B.H. (2001). *J. Appl. Cryst.* **34**, 210.

Udagawa, S., Urabe, K. and Yano, T. (1977). *Semento Hijutsu Nempo,* **31,** 26.

Udagawa, S., Urabe, K, Yano, T. and Natsume, M. (1979). *Semento Hijutsu Nempo,* **33,** 35.

Urabe, K. and Yamamoto, Y. (1996). *JCA Proc. Of Cem. Concr.* **50,** 14.

Urabe, K., Shirakami, T. and Iwashima, M. (2000). *J. Am. Ceram. Soc.* **83**, 1253.

Urabe, K., Nakano, H. and Morita, H. (2002). *J. Am. Ceram. Soc.* **85** [2], 423.

Viani, A., Artlioli, G. and Bellotto, M. (1998). *Materials Science Forum* **278-281** 384.

Von Dreele, R.B., Jorgensen, J.D., and Winsdor, C.G. (1982). *J. Appl. Cryst.* **15,** 581.

Ward, C.R., Taylor, J.C. and Cohen, D.R. (1999). *Journal of Sedimentary Research*, **69,** 1050.

Wiles, D.B. and Young, R.A. (1981). *J. Appl. Crystallogr.* **14,** 149.

Willis, B.T. (1969). *Acta Cryst.,* **A25**, 277.

Willis B.T.M. and Pryor, A.W. *Thermal Vibrations in Crystallography.* Cambridge University Press, Cambridge (1975).

Wolff, P.M. de (1961). *Acta Cryst.* **14,** 579.

Wolff, P.M. de (1974). *Acta Cryst.* **A30,** 777.

Wolff, P.M. de (1977). *Acta Cryst.* **A33,** 493.

Wolff, P.M. de, Janssen, T. and Janner, A. (1981). *Acta Cryst.* **A37,** 625.

Wolff. P.M. de, Belov, N.V., Bertaut, E.F., Buerger, M.J., Donnay, J.D.H., Fischer, W., Hahn, T., Kopstik, V.A., Mackay, A.L., Wondratschek, H., Wilson, A.J.C., and Abrahams, S.C. (1985). *Acta Cryst.* **A41,** 278.

X7A website. http://neutrons.phy.bnl.gov/~powder/

Yamamoto, A., Janssen, T., Janner, A. and de Wolff P.M. (1985). *Acta Cryst.* **A41,** 528.

Yannaquis, N and Guinier, A. (1959). *Bull. Soc. Franç. Minéral. Cryst.* **85,** 313.

Yang, R. (1996). *Cem. Concr. Res.* **26**, 1451.

Young, J.F. (1983) *JME.* **3,** 402.

Young, J.F. (1988). *J. Am. Ceram. Soc.* **71**, C118.

Young, R. *The Rietveld Method,* International Union of Crystallography, Oxford University Press, Oxford (1996).

Zachariasen, W.H. *Theory of X-ray Diffraction in Crystals,* Dover publications, New York (1945).